Visualizing Protein Biogenesis at the ER Membrane

Doctoral thesis

Visualizing Protein Biogenesis at the ER Membrane

Maximilian Gemmer

Structural Biochemistry

Bijvoet Centre for Biomolecular Research, Faculty of Science

Utrecht University, the Netherlands

Visualizing Protein Biogenesis at the ER Membrane
Visualisatie van Eiwit Biogenese aan het ER-Membraan
(met een samenvatting in het Nederlands)

Proefschrift

ter verkrijging van de graad van doctor aan de
Universiteit Utrecht
op gezag van de
rector magnificus, prof.dr. H.R.B.M. Kummeling,
ingevolge het besluit van het college voor promoties
in het openbaar te verdedigen op

maandag 16 oktober 2023 des ochtends te 10.15 uur

door

Maximilian Gemmer

geboren op 16 april 1992
te Dachau, Duitsland

Promotor
Prof. dr. F.G. Förster

Beoordelingscommissie
Prof. dr. L.J. Braakman
Prof. dr. A. Briegel
Prof. dr. A. Perrakis
Dr. Z. Zeev Ben Mordehai
Prof. dr. R. Zimmermann

Dit proefschrift werd mogelijk gemaakt met financiële steun van de European Research Council.

Table of Contents

CHAPTER 1

General introduction

Max Gemmer[1]

[1]Structural Biochemistry, Bijvoet Center for Biomolecular Research, Utrecht University, 3584 CG Utrecht, The Netherlands

Secretory pathway

Subcellular compartmentalization is essential to separate various cellular functions into distinct organelles, for maintaining cellular homeostasis and preventing interference between different metabolic pathways, ultimately contributing to the overall functionality of the cell. To ensure cellular trafficking, i.e., the transport of proteins, lipids, and carbohydrates, compartments form a dynamic endomembrane system. This organelle system enables the delivery of proteins to their correct subcellular destination, also known as the secretory pathway, which is essential for cellular health.

The secretory pathway commences at the endoplasmic reticulum (ER) [1,2]. At the cytosolic face of the ER membrane, proteins are synthesized by the ribosome and enter the ER, where they undergo extensive processing, modification, folding and assembly [3]. In the Golgi apparatus, the sorting-hub of the endomembrane system, proteins continue to mature, are packaged into vesicles, and directed to distinct compartments [4]. While secretory proteins are destined for secretion into the extracellular space via exocytosis, other soluble or transmembrane proteins are targeted to specific organelles via an array of different signals based on specific features of the secretory pathway proteins themselves [5].

Probably the most prominent signal is the signal peptide (SP), which acts at the earliest point of the secretory pathway. SPs are cleavable peptides located at the N-terminus of precursor proteins, responsible for targeting to the endoplasmic reticulum (ER) membrane [6]. The N-terminal transmembrane helix (TMH) of a multispanning membrane protein or the C-terminal TMH of a tail-anchored protein can also serve as signal to target proteins to the ER membrane co-translationally or post-translationally, respectively [7,8]. Within the endomembrane system, proteins which reside in distinct organelles, comprise additional sorting signals. ER-resident proteins for instance contain a C-terminal retention motif, which is essential for the retrograde transport from the Golgi to the ER [9]. Sorting signals of lysosomal proteins are based on carbohydrate modifications or cytosolic sorting sequences [10], while Golgi-resident proteins feature a variety of signals based on protein conformation, amino acid sequence-based sorting signals, and transmembrane domain properties in Golgi-specific lipid compositions [11].

Protein biogenesis

Biogenesis of most proteins commences in the cytosol of the cell. Here, ribosomes translate the information stored in the mRNA into an amino acid sequence. In order to decode the mRNA and synthesize the polypeptide chain, the ribosome undergoes a series of conformational changes and cooperates with elongation factors and

tRNAs [12,13]. The ternary complex of elongation factor 1a (eEF1a) and amino acid-bound tRNA (aa-tRNA) delivers amino acids to the ribosome [14]. When the anticodon of the tRNA matches the codon sequence of the mRNA, the ribosome catalyzes the peptide bond formation of two amino acids, thereby extending the nascent polypeptide chain [15]. Finally, elongation factor 2 (eEF2) then facilitates translocation of the mRNA-tRNA entity, thereby promoting movement of the ribosome to the next codon position [14]. The ribosome continues to cycle through the three phases of decoding, peptidyl transfer, and translocation until it encounters a stop codon and completes protein synthesis.

Secretory and membrane proteins are targeted to the ER membrane, the entry point of the secretory pathway, and are translocated across or inserted into the ER membrane by complex insertion machineries. While some proteins are post-translationally targeted to the ER by the post-translocon (Sec61-Sec62-Sec63) [16-19] or the tail-anchored protein insertion machinery (TRC40/CAML) [20,21], most secretory pathway proteins undergo co-translational translocation or insertion by the ribosome-associated ER translocon complex [22]. Most of these co-translational precursor proteins contain an N-terminal SP, which recruits the SRP to the ribosome, stalls mRNA translation, and targets the ribosome-nascent-chain complex (RNC) to the ER membrane [23,24]. There, the SP and nascent chain are inserted into the protein-conducting channel Sec61, while the ribosome remains in contact with the translocon complex and continues synthesizing the polypeptide chain [25-27]. Sec61 has a lateral gate, which is essential for SPs and TMHs to access the lipid bilayer, as well as a central pore to translocate the nascent protein chain across the membrane into the ER lumen.

To handle the large variety of proteins entering the ER, Sec61 cooperates with numerous accessory factor complexes, specialized in translocation of specific protein subsets. The assembly of Sec61 and stably bound accessory factors is referred to as the ER translocon complex. It comprises the translocon-associated protein (TRAP) complex, which is a near-stoichiometric translocon component and affects SP insertion and topogenesis of membrane proteins [28-32]. In addition, the oligosaccharyltransferase A (OSTA) complex and its orthologous variant OSTB mediate co-translational and post-translational N-glycosylation [33,34], respectively, while ER-resident lectin chaperones, such as malectin [35-38] and calnexin [39-41], enhance glycoprotein folding. The signal peptidase complex (SPC) is transiently recruited to the translocon to cleave the N-terminal SP when the nascent chain reaches a critical length [6,42]. While insertion of the first TMH of multispanning membrane proteins can be initiated by the endoplasmic reticulum membrane (EMC) complex [43-47], multi-TMHs are inserted by the multipass translocon. This translocon comprises three obligate sub-complexes: the GET- and EMC-like (GEL), protein associated with translocon (PAT), and back-of-Sec61 (BOS)

complex [48-52]. Some accessory factors, such as TRAM1 [53,54] and RAMP4 [55-58], have been shown to be constitutively associated with the translocon but they are structurally and functionally not well characterized. Other transient interaction partners, such as the Sec63 subunit of the post-translocon, are also known to be recruited upon distinct translocation events of specific protein substrates, such as the prion protein [59,60]. Many of these translocon components have been structurally studied using cryo-electron microscopy (cryo-EM) and are further discussed in chapter 2 'a clearer picture of the ER translocon complex' [61].

Electron microscopy

Understanding the physiological function of biological structures, such as cells, organelles, their subcompartments, macromolecular assemblies, and biomolecules, requires visualization across different scales. The resolution of light microscopy, however, is limited to approx. 200 nm, rendering interpretation at molecular resolution level impossible. While structure determination techniques, such as x-ray crystallography and NMR spectroscopy, provide high resolution information of proteins or complexes at atomic detail, they are typically limited to highly purified and relatively small macromolecules. In contrast, electron microscopy (EM) allows for imaging of heterogenous biological samples and can provide both, high-resolution information at molecular detail, as well as the visualization of the cellular organization.

The early developments of electron microscopes were accompanied by studies of the subcellular compartments and ultimately led to the discovery of the secretory pathway by Palade and coworkers [1]. Traditionally, examining the ultrastructural organization of cellular specimens required chemical fixation, dehydration, resin embedding, sectioning, and staining using heavy-metal salts [62-64]. Heavy-metal salts have also been used to study isolated macromolecules or viral particles to generate high contrast images of air-dried samples by 'negative stain'-EM [65-67]. While these techniques were sufficient to resolve membrane compartments and the overall shape of some large macromolecular assemblies, they entail dehydration and denaturation of the sample; artefacts which render interpretation at molecular resolution detail impossible [68,69]. In contrast, the work on cryo-fixation by Dubochet and coworkers to overcome these obstacles led to the development of cryogenic electron microscopy (cryo-EM). Rapid cooling of hydrated biological specimens fixed them in amorphous ice, which has been shown to preserve biomolecules in their near-native state. Plunge-freezing allows visualization and interpretability of a variety of biological samples, such as macromolecules, isolated organelles, or whole-cell specimen at molecular resolution [70].

Cryo-electron microscopy

Over the years, two cryo-EM modalities have emerged as the main methods for determining the structures of large macromolecules: cryo-EM single particle analysis (SPA) [71,72] and cryo-electron tomography (cryo-ET) [73,74]. SPA involves the imaging of thousands of identical particles embedded in a thin (~10-100 nm) vitreous ice layer. Computational statistical analysis of individual particle images generates a 3D reconstruction of high resolution, meanwhile typically ranging from 2 to 3 Å or better. Cryo-ET involves acquiring a series of projection images of a specimen at different tilt angles. These tilt series are the basis for the reconstruction of a 3D tomogram of the biological sample, for example informing on the 3D arrangement of macromolecules. The thickness of a tomogram typically ranges from 100-500 nm and the resolution of the raw tomograms is in the range of 30-50 Å when measures from SPA are applied [75]. To get higher resolution into specific types of macromolecules, typically the realm of structural biology, individual particles from a tomogram (subtomograms) are computationally localized, extracted, and aligned to generate an average of higher resolution. Although the resolution of subtomogram reconstructions is typically lower than that of SPA reconstructions, cryo-ET has the advantage of preserving their physiological 3D organization or even cellular context, when applied to unperturbed cells.

The rise of cryo-EM techniques was empowered by dramatic improvements over the past decades that helped to overcome substantial challenges. A fundamental problem in EM is strong radiation damage. Since it limits the exposure of the sample, electron micrographs of the sensitive biological samples are very noisy and exhibit poor contrast. However, the past decades have seen rapid developments in the cryo-EM field to overcome these challenges [76-78]. For instance, advances of electron sources, such as field emission guns (FEGs) [79], improve spatial and temporal coherence of the electron beam. Improved specimen stages reduce specimen motion, allowing to keep the specimen centered during the tilt process and accelerating data acquisition. Post-column energy filters increase image contrast by removing inelastically scattered electrons [80], which is particularly important in cryo-ET because the amount of inelastic scattering, which blurs EM images due to large chromatic errors of EMs, correlates with specimen thickness [81]. Probably the most important development in cryo-EM leading to its 'resolution revolution' is a new generation of detectors [82,83]. Direct electron detectors have a high detective quantum efficiency, resulting in dramatically higher signal-to-noise ratio and improved image quality compared to CCD cameras and film, which were used previously. Moreover, the high framerate of direct detectors allows detection of single electron events and dose-fractionated imaging, which is important to remove beam-induced motion.

In addition to EM instrumentation, automated acquisition and processing of cryo-EM data has significantly advanced for both SPA and cryo-ET. Dose-fractionated acquisition of movies allows for correction of beam-induced motion (subtle non-rigid transformations of the sample during irradiation) and dramatically increases image resolution [84]. Template-matching or deep learning-based detection algorithms enable automated particle localization in SPA and cryo-ET [85,86], while unsupervised 3D classification algorithms are essential for unbiased sorting of heterogeneous particle sets. Bundling these algorithms in user-friendly processing packages readily increases accessibility of cryo-EM SPA and cryo-ET. In cryo-ET, an important recent milestone is an SPA-like approach to subtomogram averaging, where global motion and local deformation of individual tilt projections are optimized to generate high-resolution reconstructions of macromolecules in cells [87,88].

The developments in the cryo-EM field paved the way for high-resolution structure determination of isolated assemblies as well as intracellular structures, and increasingly push the resolution boundaries and macromolecule size limitations. The translation process and ER have often been the target of cryo-EM studies. Large assemblies such as ribosomes are 'easy' targets for SPA and have provided valuable mechanistic insights into bacterial and eukaryotic elongation [89-95] and hibernation [96-99], or antibiotic-induced ribosomal stalling [100-102], for example. Recently, the structure of a bacterial ribosome was determined at record-breaking resolution of 1.55 Å [103]. Furthermore, SPA of detergent-solubilized complexes, such as ribosome-associated Sec61 [25,26], the OSTA complex [34,104-106], or the SPC [42], revealed structural and functional details of ER-resident membrane proteins at molecular resolution, while cryo-ET succeeded to visualize the ribosome-associated ER translocon complex embedded in its native membrane environment [27,107]. On the cellular level, *in situ* cryo-ET, often in conjunction with cryogenic correlative light-electron microscopy (cryo-CLEM), recently provided insights into the organization of ER subcompartments [108,109], contact sites of the ER to mitochondria [110] and lysosome [111], degradation microcompartments at the ER membrane [112], ribosome-associated vesicles [113] (RAVs, which are different from purified microsomes), and ER stress-activated IRE1α oligomerization [114]. The integrative combination of SPA and cryo-ET enables high-resolution structure determination in cellular contexts.

Scope of this Thesis

The previous cryo-ET structure of the ribosome-bound ER translocon revealed the organization of the protein-conducting channel Sec61 with the major accessory factors TRAP and OSTA [27,107]. These structural studies as well as earlier functional

studies are traditionally based on ER-derived vesicles (microsomes) purified from pancreatic tissue [115,116], which commonly renders ER-bound ribosomes translationally idle [25,27], and is associated with challenging genetic and biochemical modifiability, as well as reproducibility and throughput. Moreover, since the publication of this work [27] more than 5 years have passed, in which cryo-ET processing has seen dramatic improvements [87,88].

This thesis aims to explore the near-native molecular landscape of the ribosome-associated ER translocon in ER-derived vesicles isolated from a human HEK293 cell line. Using cryo-ET in conjunction with SPA and mass spectrometry (MS), I dissect ribosomal intermediate states, visualize different translocon variants and reveal their organization at the ER membrane. Going beyond previous cryo-ET studies, I now obtain higher resolutions, reveal novel translocon components and interaction partners, and observe higher translation activity, indicating a close-to-physiological state.

In chapter 2, I outline the structurally and biochemically characterized molecular toolbox for protein biogenesis at the ER. I focus on the protein translocation and folding machinery associated with the ER translocon.

In chapter 3, I combine cryo-ET with high-resolution cryo-EM and mass spectrometry to study ribosomal intermediate states at resolutions ranging from 6-8 Å at the ER membrane and in solution. The study reveals eight actively translating ribosome intermediates of the elongation cycle and two hibernating ribosome states, as well as their polysomal organization at the ER. Moreover, the analysis shows a previously unknown intermediate associated with elongation factor 1a in the extended conformation.

In chapter 4, I dissect the downstream translocon machinery of ER-bound ribosomes using cryo-ET and subtomogram analysis. Beside one soluble ribosome population, 3D classification reveals three major translocon variants: Sec61-TRAP, Sec61-TRAP-OSTA, and the Sec61-multipass translocon. In addition to Sec61, the multipass translocon recruits TRAP in a substoichiometric manner. Subtomogram segmentation and 3D neighborhood analysis characterized the organization of the associated polysomes and indicate clustering of Sec61-TRAP-OSTA or the multipass translocon with distinct polysome chains. Integrating Alphafold and Colabfold predictions, we built a near-complete model of the most abundant translocon variant, Sec61-TRAP-OSTA, including the first atomistic structure of the TRAP complex, which reveals specific interactions with other translocon components. Moreover, the data reveal two unidentified OSTA-associated proteins, which are likely luminal chaperones that enhance glycoprotein folding at the translocon.

In chapter 5, I extended the subtomgram analysis of the multipass translocon from chapter 4 and characterize its composition in the context of translational activity. The results reveal that TRAP and PAT are variable components. Moreover, TRAP interacts with a structurally unidentified subunit of the multipass translocon, most likely NOMO, pointing to a hitherto unknown role of TRAP in multipass membrane protein biogenesis.

In chapter 6, I comprehensively discuss the findings from all chapters in context with recent literature and formulate hypotheses that provide a basis for future investigations.

References

1 **G. Palade.** Intracellular aspects of the process of protein synthesis. *Science* **189**, 867 (1975).
2 **C. K. Barlowe & E. A. Miller.** Secretory protein biogenesis and traffic in the early secretory pathway. *Genetics* **193**, 383-410 (2013).
3 **I. Braakman & D. N. Hebert.** Protein folding in the endoplasmic reticulum. *Cold Spring Harbor perspectives in biology* **5**, a013201 (2013).
4 **M. A. De Matteis & A. Luini.** Exiting the Golgi complex. *Nature reviews Molecular cell biology* **9**, 273-284 (2008).
5 **M. J. Chrispeels.** Sorting of proteins in the secretory system. *Annual review of plant biology* **42**, 21-53 (1991).
6 **B. Martoglio & B. Dobberstein.** Signal sequences: more than just greasy peptides. *Trends Cell Biol* **8**, 410-415 (1998).
7 **P. J. Chitwood & R. S. Hegde.** The Role of EMC during Membrane Protein Biogenesis. *Trends Cell Biol* **29**, 371-384 (2019).
8 **N. Borgese & E. Fasana.** Targeting pathways of C-tail-anchored proteins. *Biochim Biophys Acta* **1808**, 937-946 (2011).
9 **H. R. Pelham.** The retention signal for soluble proteins of the endoplasmic reticulum. *Trends Biochem Sci* **15**, 483-486 (1990).
10 **J. S. Bonifacino & L. M. Traub.** Signals for sorting of transmembrane proteins to endosomes and lysosomes. *Annu Rev Biochem* **72**, 395-447 (2003).
11 **D. K. Banfield.** Mechanisms of protein retention in the Golgi. *Cold Spring Harb Perspect Biol* **3**, a005264 (2011).
12 **V. Ramakrishnan.** Ribosome structure and the mechanism of translation. *Cell* **108**, 557-572 (2002).
13 **R. M. Voorhees & V. Ramakrishnan.** Structural basis of the translational elongation cycle. *Annu Rev Biochem* **82**, 203-236 (2013).
14 **G. R. Andersen, P. Nissen & J. Nyborg.** Elongation factors in protein biosynthesis. *Trends Biochem Sci* **28**, 434-441 (2003).
15 **M. Beringer & M. V. Rodnina.** The ribosomal peptidyl transferase. *Mol Cell* **26**, 311-321 (2007).
16 **S. Itskanov & E. Park.** Structure of the posttranslational Sec protein-translocation channel complex from yeast. *Science* **363**, 84-87 (2019).
17 **X. Wu, C. Cabanos & T. A. Rapoport.** Structure of the post-translational protein translocation machinery of the ER membrane. *Nature* **566**, 136-139 (2019).
18 **S. Itskanov, K. M. Kuo, J. C. Gumbart & E. Park.** Stepwise gating of the Sec61 protein-conducting channel by Sec63 and Sec62. *Nat Struct Mol Biol* **28**, 162-172 (2021).
19 **T. H. Weng, W. Steinchen, B. Beatrix, O. Berninghausen, T. Becker, G. Bange, J. Cheng & R. Beckmann.** Architecture of the active post-translational Sec translocon. *EMBO J* **40**, e105643 (2021).
20 **M. A. McDowell, M. Heimes, F. Fiorentino, S. Mehmood, A. Farkas, J. Coy-Vergara, D. Wu, J. R. Bolla, V. Schmid, R. Heinze, K. Wild, D. Flemming, S. Pfeffer, B. Schwappach, C. V. Robinson & I. Sinning.** Structural Basis of Tail-Anchored Membrane Protein Biogenesis by the GET Insertase

Complex. *Mol Cell* **80**, 72-86 e77 (2020).
21 **Y. Yamamoto & T. Sakisaka.** Molecular machinery for insertion of tail-anchored membrane proteins into the endoplasmic reticulum membrane in mammalian cells. *Mol Cell* **48**, 387-397 (2012).
22 **Y. Nyathi, B. M. Wilkinson & M. R. Pool.** Co-translational targeting and translocation of proteins to the endoplasmic reticulum. *Biochimica et Biophysica Acta (BBA)-Molecular Cell Research* **1833**, 2392-2402 (2013).
23 **K. Wild, M. Halic, I. Sinning & R. Beckmann.** SRP meets the ribosome. *Nat Struct Mol Biol* **11**, 1049-1053 (2004).
24 **D. Akopian, K. Shen, X. Zhang & S. O. Shan.** Signal recognition particle: an essential protein-targeting machine. *Annu Rev Biochem* **82**, 693-721 (2013).
25 **R. M. Voorhees, I. S. Fernandez, S. H. Scheres & R. S. Hegde.** Structure of the mammalian ribosome-Sec61 complex to 3.4 A resolution. *Cell* **157**, 1632-1643 (2014).
26 **R. M. Voorhees & R. S. Hegde.** Structure of the Sec61 channel opened by a signal sequence. *Science* **351**, 88-91 (2016).
27 **S. Pfeffer, L. Burbaum, P. Unverdorben, M. Pech, Y. Chen, R. Zimmermann, R. Beckmann & F. Forster.** Structure of the native Sec61 protein-conducting channel. *Nat Commun* **6**, 8403 (2015).
28 **R. D. Fons, B. A. Bogert & R. S. Hegde.** Substrate-specific function of the translocon-associated protein complex during translocation across the ER membrane. *J Cell Biol* **160**, 529-539 (2003).
29 **N. Sommer, T. Junne, K. U. Kalies, M. Spiess & E. Hartmann.** TRAP assists membrane protein topogenesis at the mammalian ER membrane. *Biochim Biophys Acta* **1833**, 3104-3111 (2013).
30 **D. Nguyen, R. Stutz, S. Schorr, S. Lang, S. Pfeffer, H. H. Freeze, F. Forster, V. Helms, J. Dudek & R. Zimmermann.** Proteomics reveals signal peptide features determining the client specificity in human TRAP-dependent ER protein import. *Nat Commun* **9**, 3765 (2018).
31 **T. Kriegler, G. Kiburg & T. Hessa.** Translocon-Associated Protein Complex (TRAP) is Crucial for Co-Translational Translocation of Pre-Proinsulin. *J Mol Biol* **432**, 166694 (2020).
32 **T. Kriegler, S. Lang, L. Notari & T. Hessa.** Prion Protein Translocation Mechanism Revealed by Pulling Force Studies. *J Mol Biol* **432**, 4447-4465 (2020).
33 **D. J. Kelleher & R. Gilmore.** An evolving view of the eukaryotic oligosaccharyltransferase. *Glycobiology* **16**, 47R-62R (2006).
34 **A. S. Ramirez, J. Kowal & K. P. Locher.** Cryo-electron microscopy structures of human oligosaccharyltransferase complexes OST-A and OST-B. *Science* **366**, 1372-1375 (2019).
35 **S. Y. Qin, D. Hu, K. Matsumoto, K. Takeda, N. Matsumoto, Y. Yamaguchi & K. Yamamoto.** Malectin forms a complex with ribophorin I for enhanced association with misfolded glycoproteins. *J Biol Chem* **287**, 38080-38089 (2012).
36 **Y. Chen, D. Hu, R. Yabe, H. Tateno, S. Y. Qin, N. Matsumoto, J. Hirabayashi & K. Yamamoto.** Role of malectin in Glc(2)Man(9)GlcNAc(2)-dependent quality control of alpha1-antitrypsin. *Mol Biol Cell* **22**, 3559-3570 (2011).
37 **C. Galli, R. Bernasconi, T. Solda, V. Calanca & M. Molinari.** Malectin participates in a backup glycoprotein quality control pathway in the mammalian ER. *PLoS One* **6**, e16304 (2011).
38 **T. Schallus, C. Jaeckh, K. Feher, A. S. Palma, Y. Liu, J. C. Simpson, M. Mackeen, G. Stier, T. J. Gibson, T. Feizi, T. Pieler & C. Muhle-Goll.** Malectin: a novel carbohydrate-binding protein of the endoplasmic reticulum and a candidate player in the early steps of protein N-glycosylation. *Mol Biol Cell* **19**, 3404-3414 (2008).
39 **J. J. Bergeron, M. B. Brenner, D. Y. Thomas & D. B. Williams.** Calnexin: a membrane-bound chaperone of the endoplasmic reticulum. *Trends Biochem Sci* **19**, 124-128 (1994).
40 **S. Lee, Y. Shin, K. Kim, Y. Song, Y. Kim & S. W. Kang.** Protein Translocation Acquires Substrate Selectivity Through ER Stress-Induced Reassembly of Translocon Auxiliary Components. *Cells* **9** (2020).
41 **A. K. Lakkaraju, L. Abrami, T. Lemmin, S. Blaskovic, B. Kunz, A. Kihara, M. Dal Peraro & F. G. van der Goot.** Palmitoylated calnexin is a key component of the ribosome-translocon complex. *EMBO J* **31**, 1823-1835 (2012).
42 **A. M. Liaci, B. Steigenberger, P. C. Telles de Souza, S. Tamara, M. Grollers-Mulderij, P. Ogrissek, S. J. Marrink, R. A. Scheltema & F. Forster.** Structure of the human signal peptidase complex reveals the determinants for signal peptide cleavage. *Mol Cell* **81**, 3934-3948 e3911 (2021).
43 **P. J. Chitwood, S. Juszkiewicz, A. Guna, S. Shao & R. S. Hegde.** EMC Is Required to Initiate Accurate Membrane Protein Topogenesis. *Cell* **175**, 1507-1519 e1516 (2018).

44 **L. Bai, Q. You, X. Feng, A. Kovach & H. Li.** Structure of the ER membrane complex, a transmembrane-domain insertase. *Nature* **584**, 475-478 (2020).

45 **T. Pleiner, G. P. Tomaleri, K. Januszyk, A. J. Inglis, M. Hazu & R. M. Voorhees.** Structural basis for membrane insertion by the human ER membrane protein complex. *Science* **369**, 433-436 (2020).

46 **A. M. Ngo, M. J. Shurtleff, K. D. Popova, J. Kulsuptrakul, J. S. Weissman & A. S. Puschnik.** The ER membrane protein complex is required to ensure correct topology and stable expression of flavivirus polyproteins. *Elife* **8** (2019).

47 **M. J. Shurtleff, D. N. Itzhak, J. A. Hussmann, N. T. Schirle Oakdale, E. A. Costa, M. Jonikas, J. Weibezahn, K. D. Popova, C. H. Jan, P. Sinitcyn, S. S. Vembar, H. Hernandez, J. Cox, A. L. Burlingame, J. L. Brodsky, A. Frost, G. H. Borner & J. S. Weissman.** The ER membrane protein complex interacts cotranslationally to enable biogenesis of multipass membrane proteins. *Elife* **7** (2018).

48 **S. A. Anghel, P. T. McGilvray, R. S. Hegde & R. J. Keenan.** Identification of Oxa1 Homologs Operating in the Eukaryotic Endoplasmic Reticulum. *Cell Rep* **21**, 3708-3716 (2017).

49 **P. T. McGilvray, S. A. Anghel, A. Sundaram, F. Zhong, M. J. Trnka, J. R. Fuller, H. Hu, A. L. Burlingame & R. J. Keenan.** An ER translocon for multi-pass membrane protein biogenesis. *Elife* **9** (2020).

50 **A. J. O. Lewis & R. S. Hegde.** A unified evolutionary origin for the ubiquitous protein transporters SecY and YidC. *BMC Biol* **19**, 266 (2021).

51 **L. Smalinskaite, M. K. Kim, A. J. O. Lewis, R. J. Keenan & R. S. Hegde.** Mechanism of an intramembrane chaperone for multipass membrane proteins. *Nature* **611**, 161-166 (2022).

52 **A. Sundaram, M. Yamsek, F. Zhong, Y. Hooda, R. S. Hegde & R. J. Keenan.** Substrate-driven assembly of a translocon for multipass membrane proteins. *Nature* **611**, 167-172 (2022).

53 **D. Gorlich, E. Hartmann, S. Prehn & T. A. Rapoport.** A protein of the endoplasmic reticulum involved early in polypeptide translocation. *Nature* **357**, 47-52 (1992).

54 **M. C. Klein, M. Lerner, D. Nguyen, S. Pfeffer, J. Dudek, F. Forster, V. Helms, S. Lang & R. Zimmermann.** TRAM1 protein may support ER protein import by modulating the phospholipid bilayer near the lateral gate of the Sec61-channel. *Channels (Austin)* **14**, 28-44 (2020).

55 **D. Gorlich & T. A. Rapoport.** Protein translocation into proteoliposomes reconstituted from purified components of the endoplasmic reticulum membrane. *Cell* **75**, 615-630 (1993).

56 **A. Yamaguchi, O. Hori, D. M. Stern, E. Hartmann, S. Ogawa & M. Tohyama.** Stress-associated endoplasmic reticulum protein 1 (SERP1)/Ribosome-associated membrane protein 4 (RAMP4) stabilizes membrane proteins during stress and facilitates subsequent glycosylation. *J Cell Biol* **147**, 1195-1204 (1999).

57 **O. Hori, M. Miyazaki, T. Tamatani, K. Ozawa, K. Takano, M. Okabe, M. Ikawa, E. Hartmann, P. Mai, D. M. Stern, Y. Kitao & S. Ogawa.** Deletion of SERP1/RAMP4, a component of the endoplasmic reticulum (ER) translocation sites, leads to ER stress. *Mol Cell Biol* **26**, 4257-4267 (2006).

58 **M. R. Pool.** A trans-membrane segment inside the ribosome exit tunnel triggers RAMP4 recruitment to the Sec61p translocase. *J Cell Biol* **185**, 889-902 (2009).

59 **B. J. Conti, P. K. Devaraneni, Z. Yang, L. L. David & W. R. Skach.** Cotranslational stabilization of Sec62/63 within the ER Sec61 translocon is controlled by distinct substrate-driven translocation events. *Mol Cell* **58**, 269-283 (2015).

60 **S. Sun, X. Li & M. Mariappan.** Signal sequences encode information for protein folding in the endoplasmic reticulum. *J Cell Biol* **222** (2023).

61 **M. Gemmer & F. Forster.** A clearer picture of the ER translocon complex. *J Cell Sci* **133** (2020).

62 **G. E. Palade.** A study of fixation for electron microscopy. *The Journal of experimental medicine* **95**, 285-298 (1952).

63 **K. Richardson, L. Jarett & E. Finke.** Embedding in epoxy resins for ultrathin sectioning in electron microscopy. *Stain technology* **35**, 313-323 (1960).

64 M. Hayat. *Fixation for electron microscopy*. (Elsevier, 2012).

65 **D. J. De Rosier & A. Klug.** Reconstruction of three dimensional structures from electron micrographs. *Nature* **217**, 130-134 (1968).

66 **M. Ohi, Y. Li, Y. Cheng & T. Walz.** Negative staining and image classification—powerful tools in modern electron microscopy. *Biological procedures online* **6**, 23-34 (2004).

67 **S. Brenner & R. Horne.** A negative staining method for high resolution electron microscopy of

viruses. *Biochimica et biophysica acta* **34**, 103-110 (1959).
68 **H. H. Mollenhauer.** Artifacts caused by dehydration and epoxy embedding in transmission electron microscopy. *Microscopy research and technique* **26**, 496-512 (1993).
69 **A. Bremer, C. Henn, A. Engel, W. Baumeister & U. Aebi.** Has negative staining still a place in biomacromolecular electron microscopy? *Ultramicroscopy* **46**, 85-111 (1992).
70 **J. Dubochet, M. Adrian, J.-J. Chang, J.-C. Homo, J. Lepault, A. W. McDowall & P. Schultz.** Cryo-electron microscopy of vitrified specimens. *Quarterly reviews of biophysics* **21**, 129-228 (1988).
71 **M. Van Heel, B. Gowen, R. Matadeen, E. V. Orlova, R. Finn, T. Pape, D. Cohen, H. Stark, R. Schmidt & M. Schatz.** Single-particle electron cryo-microscopy: towards atomic resolution. *Quarterly reviews of biophysics* **33**, 307-369 (2000).
72 **M. Wu & G. C. Lander.** How low can we go? Structure determination of small biological complexes using single-particle cryo-EM. *Current opinion in structural biology* **64**, 9-16 (2020).
73 **V. Lučić, A. Leis & W. Baumeister.** Cryo-electron tomography of cells: connecting structure and function. *Histochemistry and cell biology* **130**, 185-196 (2008).
74 **M. Turk & W. Baumeister.** The promise and the challenges of cryo-electron tomography. *FEBS letters* **594**, 3243-3261 (2020).
75 **S. Asano, Y. Fukuda, F. Beck, A. Aufderheide, F. Forster, R. Danev & W. Baumeister.** Proteasomes. A molecular census of 26S proteasomes in intact neurons. *Science* **347**, 439-442 (2015).
76 **X. C. Bai, G. McMullan & S. H. Scheres.** How cryo-EM is revolutionizing structural biology. *Trends Biochem Sci* **40**, 49-57 (2015).
77 **W. Kuhlbrandt.** Biochemistry. The resolution revolution. *Science* **343**, 1443-1444 (2014).
78 **E. Callaway.** Revolutionary cryo-EM is taking over structural biology. *Nature* **578**, 201-202 (2020).
79 **T. Kato, F. Makino, T. Nakane, N. Terahara, T. Kaneko, Y. Shimizu, S. Motoki, I. Ishikawa, K. Yonekura & K. Namba.** CryoTEM with a cold field emission gun that moves structural biology into a new stage. *Microscopy and Microanalysis* **25**, 998-999 (2019).
80 **A. Gubbens, M. Barfels, C. Trevor, R. Twesten, P. Mooney, P. Thomas, N. Menon, B. Kraus, C. Mao & B. McGinn.** The GIF Quantum, a next generation post-column imaging energy filter. *Ultramicroscopy* **110**, 962-970 (2010).
81 **K. Neselu, B. Wang, W. J. Rice, C. S. Potter, B. Carragher & E. Y. D. Chua.** Measuring the effects of ice thickness on resolution in single particle cryo-EM. *J Struct Biol X* **7**, 100085 (2023).
82 **S. Wu, J. P. Armache & Y. Cheng.** Single-particle cryo-EM data acquisition by using direct electron detection camera. *Microscopy (Oxf)* **65**, 35-41 (2016).
83 **G. McMullan, A. R. Faruqi & R. Henderson.** Direct Electron Detectors. *Methods Enzymol* **579**, 1-17 (2016).
84 **X. Li, P. Mooney, S. Zheng, C. R. Booth, M. B. Braunfeld, S. Gubbens, D. A. Agard & Y. Cheng.** Electron counting and beam-induced motion correction enable near-atomic-resolution single-particle cryo-EM. *Nature methods* **10**, 584-590 (2013).
85 **T. Wagner, F. Merino, M. Stabrin, T. Moriya, C. Antoni, A. Apelbaum, P. Hagel, O. Sitsel, T. Raisch & D. Prumbaum.** SPHIRE-crYOLO is a fast and accurate fully automated particle picker for cryo-EM. *Communications biology* **2**, 218 (2019).
86 **E. Moebel, A. Martinez-Sanchez, L. Lamm, R. D. Righetto, W. Wietrzynski, S. Albert, D. Larivière, E. Fourmentin, S. Pfeffer & J. Ortiz.** Deep learning improves macromolecule identification in 3D cellular cryo-electron tomograms. *Nature methods* **18**, 1386-1394 (2021).
87 **D. Tegunov, L. Xue, C. Dienemann, P. Cramer & J. Mahamid.** Multi-particle cryo-EM refinement with M visualizes ribosome-antibiotic complex at 3.5 A in cells. *Nat Methods* **18**, 186-193 (2021).
88 **J. Zivanov, J. Oton, Z. Ke, A. von Kugelgen, E. Pyle, K. Qu, D. Morado, D. Castano-Diez, G. Zanetti, T. A. M. Bharat, J. A. G. Briggs & S. H. W. Scheres.** A Bayesian approach to single-particle electron cryo-tomography in RELION-4.0. *Elife* **11** (2022).
89 **A. B. Loveland, G. Demo & A. A. Korostelev.** Cryo-EM of elongating ribosome with EF-Tu*GTP elucidates tRNA proofreading. *Nature* **584**, 640-645 (2020).
90 **S. Shao, J. Murray, A. Brown, J. Taunton, V. Ramakrishnan & R. S. Hegde.** Decoding Mammalian Ribosome-mRNA States by Translational GTPase Complexes. *Cell* **167**, 1229-1240 e1215 (2016).
91 **V. Bhaskar, A. Graff-Meyer, A. D. Schenk, S. Cavadini, O. von Loeffelholz, S. K. Natchiar, C. G. Artus-Revel, H. R. Hotz, G. Bretones, B. P. Klaholz & J. A. Chao.** Dynamics of uS19 C-Terminal Tail during the Translation Elongation Cycle in Human Ribosomes. *Cell Rep* **31**, 107473 (2020).

92 **T. V. Budkevich, J. Giesebrecht, E. Behrmann, J. Loerke, D. J. Ramrath, T. Mielke, J. Ismer, P. W. Hildebrand, C. S. Tung, K. H. Nierhaus, K. Y. Sanbonmatsu & C. M. Spahn.** Regulation of the mammalian elongation cycle by subunit rolling: a eukaryotic-specific ribosome rearrangement. *Cell* **158**, 121-131 (2014).

93 **Z. Guo & H. F. Noller.** Rotation of the head of the 30S ribosomal subunit during mRNA translocation. *Proc Natl Acad Sci U S A* **109**, 20391-20394 (2012).

94 **E. Behrmann, J. Loerke, T. V. Budkevich, K. Yamamoto, A. Schmidt, P. A. Penczek, M. R. Vos, J. Burger, T. Mielke, P. Scheerer & C. M. Spahn.** Structural snapshots of actively translating human ribosomes. *Cell* **161**, 845-857 (2015).

95 **J. Flis, M. Holm, E. J. Rundlet, J. Loerke, T. Hilal, M. Dabrowski, J. Burger, T. Mielke, S. C. Blanchard, C. M. T. Spahn & T. V. Budkevich.** tRNA Translocation by the Eukaryotic 80S Ribosome and the Impact of GTP Hydrolysis. *Cell Rep* **25**, 2676-2688 e2677 (2018).

96 **J. Barandun, M. Hunziker, C. R. Vossbrinck & S. Klinge.** Evolutionary compaction and adaptation visualized by the structure of the dormant microsporidian ribosome. *Nat Microbiol* **4**, 1798-1804 (2019).

97 **F. Leesch, L. Lorenzo-Orts, C. Pribitzer, I. Grishkovskaya, J. Roehsner, A. Chugunova, M. Matzinger, E. Roitinger, K. Belacic, S. Kandolf, T. Y. Lin, K. Mechtler, A. Meinhart, D. Haselbach & A. Pauli.** A molecular network of conserved factors keeps ribosomes dormant in the egg. *Nature* **613**, 712-720 (2023).

98 **J. N. Wells, R. Buschauer, T. Mackens-Kiani, K. Best, H. Kratzat, O. Berninghausen, T. Becker, W. Gilbert, J. Cheng & R. Beckmann.** Structure and function of yeast Lso2 and human CCDC124 bound to hibernating ribosomes. *PLoS Biol* **18**, e3000780 (2020).

99 **A. Brown, M. R. Baird, M. C. Yip, J. Murray & S. Shao.** Structures of translationally inactive mammalian ribosomes. *Elife* **7** (2018).

100 **Z. L. Watson, F. R. Ward, R. Meheust, O. Ad, A. Schepartz, J. F. Banfield & J. H. Cate.** Structure of the bacterial ribosome at 2 A resolution. *Elife* **9** (2020).

101 **Z. Zhang, C. E. Morgan, R. A. Bonomo & E. W. Yu.** Cryo-EM Determination of Eravacycline-Bound Structures of the Ribosome and the Multidrug Efflux Pump AdeJ of Acinetobacter baumannii. *mBio* **12**, e0103121 (2021).

102 **H. Khatter, A. G. Myasnikov, S. K. Natchiar & B. P. Klaholz.** Structure of the human 80S ribosome. *Nature* **520**, 640-645 (2015).

103 **S. A. Fromm, K. M. O'Connor, M. Purdy, P. R. Bhatt, G. Loughran, J. F. Atkins, A. Jomaa & S. Mattei.** The translating bacterial ribosome at 1.55 A resolution generated by cryo-EM imaging services. *Nat Commun* **14**, 1095 (2023).

104 **L. Bai, T. Wang, G. Zhao, A. Kovach & H. Li.** The atomic structure of a eukaryotic oligosaccharyltransferase complex. *Nature* **555**, 328-333 (2018).

105 **K. Braunger, S. Pfeffer, S. Shrimal, R. Gilmore, O. Berninghausen, E. C. Mandon, T. Becker, F. Forster & R. Beckmann.** Structural basis for coupling protein transport and N-glycosylation at the mammalian endoplasmic reticulum. *Science* **360**, 215-219 (2018).

106 **R. Wild, J. Kowal, J. Eyring, E. M. Ngwa, M. Aebi & K. P. Locher.** Structure of the yeast oligosaccharyltransferase complex gives insight into eukaryotic N-glycosylation. *Science* **359**, 545-550 (2018).

107 **S. Pfeffer, J. Dudek, M. Schaffer, B. G. Ng, S. Albert, J. M. Plitzko, W. Baumeister, R. Zimmermann, H. H. Freeze, B. D. Engel & F. Forster.** Dissecting the molecular organization of the translocon-associated protein complex. *Nat Commun* **8**, 14516 (2017).

108 **M. Turk & W. Baumeister.** The promise and the challenges of cryo-electron tomography. *FEBS Lett* **594**, 3243-3261 (2020).

109 **V. Lucic, A. Rigort & W. Baumeister.** Cryo-electron tomography: the challenge of doing structural biology in situ. *J Cell Biol* **202**, 407-419 (2013).

110 **M. R. Wozny, A. D. Luca, D. R. Morado, A. Picco, P. C. Hoffmann, E. A. Miller, S. Vanni & W. Kukulski.** Supramolecular architecture of the ER-mitochondria encounter structure in its native environment. *bioRxiv*, 2022.2004.2012.488000 (2022).

111 **S. Cai, Y. Wu, A. Guillen-Samander, W. Hancock-Cerutti, J. Liu & P. De Camilli.** In situ architecture of the lipid transport protein VPS13C at ER-lysosome membrane contacts. *Proc Natl Acad Sci U S A* **119**, e2203769119 (2022).

112 **S. Albert, W. Wietrzynski, C. W. Lee, M. Schaffer, F. Beck, J. M. Schuller, P. A. Salome, J. M. Plitzko, W. Baumeister & B. D. Engel.** Direct visualization of degradation microcompartments at the ER membrane. *Proc Natl Acad Sci U S A* **117**, 1069-1080 (2020).

113 **S. D. Carter, C. M. Hampton, R. Langlois, R. Melero, Z. J. Farino, M. J. Calderon, W. Li, C. T. Wallace, N. H. Tran, R. A. Grassucci, S. E. Siegmund, J. Pemberton, T. J. Morgenstern, L. Eisenman, J. I. Aguilar, N. L. Greenberg, E. S. Levy, E. Yi, W. G. Mitchell, W. J. Rice, C. Wigge, J. Pilli, E. W. George, D. Aslanoglou, M. Courel, R. J. Freyberg, J. A. Javitch, Z. P. Wills, E. Area-Gomez, S. Shiva, F. Bartolini, A. Volchuk, S. A. Murray, M. Aridor, K. N. Fish, P. Walter, T. Balla, D. Fass, S. G. Wolf, S. C. Watkins, J. M. Carazo, G. J. Jensen, J. Frank & Z. Freyberg.** Ribosome-associated vesicles: A dynamic subcompartment of the endoplasmic reticulum in secretory cells. *Sci Adv* **6**, eaay9572 (2020).

114 **N. H. Tran, S. D. Carter, A. De Maziere, A. Ashkenazi, J. Klumperman, P. Walter & G. J. Jensen.** The stress-sensing domain of activated IRE1alpha forms helical filaments in narrow ER membrane tubes. *Science* **374**, 52-57 (2021).

115 **P. Walter & V. R. Lingappa.** Mechanism of protein translocation across the endoplasmic reticulum membrane. *Annu Rev Cell Biol* **2**, 499-516 (1986).

116 **R. Zimmermann, S. Eyrisch, M. Ahmad & V. Helms.** Protein translocation across the ER membrane. *Biochim Biophys Acta* **1808**, 912-924 (2011).

CHAPTER 2

A clearer picture of the ER translocon complex

Max Gemmer[1], Friedrich Förster[1]

[1]Cryo-Electron Microscopy, Bijvoet Center for Biomolecular Research, Utrecht University, 3584 CH Utrecht, The Netherlands

Published in
M. Gemmer & F. Förster. A clearer picture of the ER translocon complex.
Journal of cell science **133** (2020)

Abstract

The endoplasmic reticulum (ER) translocon complex is the main gate into the secretory pathway, facilitating the translocation of nascent peptides into the ER lumen or their integration into the lipid membrane. Protein biogenesis in the ER involves additional processes, many of them occurring co-translationally while the nascent protein resides at the translocon complex, including recruitment of ER-targeted ribosome–nascent-chain complexes, glycosylation, signal peptide cleavage, membrane protein topogenesis and folding. To perform such varied functions on a broad range of substrates, the ER translocon complex has different accessory components that associate with it either stably or transiently. Here, we review recent structural and functional insights into this dynamically constituted central hub in the ER and its components. Recent cryo-electron microscopy (EM) studies have dissected the molecular organization of the co-translational ER translocon complex, comprising the Sec61 protein-conducting channel, the translocon-associated protein complex and the oligosaccharyl transferase complex. Complemented by structural characterization of the post-translational import machinery, key molecular principles emerge that distinguish co- and post-translational protein import and biogenesis. Further cryo-EM structures promise to expand our mechanistic understanding of the various biochemical functions involving protein biogenesis and quality control in the ER.

Introduction

The endoplasmic reticulum (ER) is the starting point of the secretory pathway [1]. Freshly synthesized proteins are translocated into the lumen of the ER or integrated into the ER membrane, in the case of membrane proteins, prior to their subsequent transport to the plasma membrane or to organelles of the endocytic and exocytic pathways. Approximately 30% of all eukaryotic proteins utilize the secretory pathway. Synthesis of secretory pathway proteins primarily occurs at the surface of the ER, where ER-bound ribosomes give rise to the 'rough' morphology of large parts of the ER [2].

Many secretory pathway proteins are targeted to the ER via a hydrophobic N-terminal signal peptide (SP) [3]. As the nascent SP emerges from the ribosome, it binds the soluble signal recognition particle (SRP), which mediates recruitment of the ribosome–nascent-chain (RNC) complex to the ER via the ER-membrane residing SRP receptor (SR) [4]. The ER-resident signal peptidase complex (SPC) eventually cleaves off the SP from the nascent peptide [5]. SP-equivalent N-terminal transmembrane helices that are not cleaved off can also target proteins to the ER through the same mechanism. In this SRP-dependent co-translational ER-targeting mode, ribosomes associate with the ER membrane via ER translocon complexes. These membrane protein complexes translocate nascent soluble proteins into the ER, integrate nascent membrane proteins into the ER membrane, mediate protein folding and membrane protein topogenesis, and modify them chemically. In addition to co-translational protein import and translocation, distinct ER translocon complexes enable post-translational translocation and membrane integration. This post-translational pathway is widespread in yeast [6], whereas higher eukaryotes primarily use it for relatively short peptides [7,8].

ER translocon complexes are dynamic entities, organized around an invariant core, the Sec61 protein-conducting channel. Sec61 is a trimeric membrane protein complex that is structurally and functionally highly conserved throughout all domains of life, known as SecYEG in bacteria and SecYEβ in archaea [9]. In the co-translational mode, the ribosome binds to the Sec61 complex, enabling the nascent unfolded peptide to enter the Sec61 channel. In higher eukaryotes, the translocon-associated protein (TRAP) complex binds constitutively to Sec61 and a ribosome [10-12], possibly to support the recruitment of specific SPs [13] and membrane topogenesis of some substrates [14]. The oligosaccharyl transferase complex (OST), which is responsible for glycosylation of specific asparagine residues (N-glycosylation), binds to the ribosome–Sec61–TRAP complex in near stoichiometric ratios [11,15], whereas other accessory components appear to rather bind transiently to the co-translational ER translocon in specific states in the biogenesis of specific proteins. These accessory factors include the SPC, ER-luminal chaperones and also members of the Oxa1/Alb3/YidC insertase family [16],

which cooperates with SecYEG or SecYEβ in the insertion of multi-transmembrane helix proteins into prokaryotic membranes [17].

In the post-translational mode, Sec61 forms a stable complex with the dimeric Sec62–Sec63 complex, and in fungi, additionally with Sec71 and Sec72 [18]. These accessory proteins facilitate the transient binding of chaperones, in particular heat-shock 70 (Hsp70) family proteins, to the cytosolic and luminal side of the ER post-translocon complex [19]. Hsp70 family proteins prevent misfolding of translocated substrates in the ER lumen.

Besides ER protein biogenesis, the ER translocon is also directly implicated in the unfolded protein response (UPR), the cellular mechanism to counteract abnormally high amounts of unfolded proteins in the ER. Inositol-requiring enzyme 1 (IRE1, also known as ERN1), which initiates one of the three UPR branches, has recently been found to bind to Sec61 and the ribosome [20].

Collectively, the ER translocon complex with its Sec61 core appears to be analogous to a 'Swiss army knife' that can adapt to different requirements with regard to substrates and cellular state (Fig. 1). The membrane-associated nature of the ER translocon complex has traditionally made it difficult to obtain structural insights into its functional and regulatory mechanisms. Advances in cryo-electron microscopy (cryo-EM) modalities have profoundly changed this situation [21]. Cryo-EM single-particle analysis (SPA) has provided numerous insights at near-atomic resolution into purified ER translocon complexes and their components. However, isolation-based approaches have their limits because the required solubilization tends to disrupt transient interactions and those involving lipids. Cryo-electron tomography (ET) complements studies of isolated components because it can image the ER translocon in its native ER environment – in the form of ER-derived vesicles or even in unperturbed cells [22]. Here, we review recent structural and mechanistic insights into the co- and post-translational ER translocon complex and the molecular principles that distinguish these modes.

Components and overall structure of the ER co-translocon complex

The development of cell-free assays allowed Blobel and co-workers to prove the 'signal hypothesis' [3], that is that the targeting of many proteins to the ER through an N-terminal SP. The combination of rabbit reticulocyte lysate with ER-derived microsomes from dog pancreas enabled the reconstitution of co-translational protein import and SP cleavage. Isolation of ribosome-associated membrane proteins (RAMPs) from solubilized pancreatic microsomes provided clues about the molecular composition of the ER translocon complex. Depending on the choice of detergent and salt concentration,

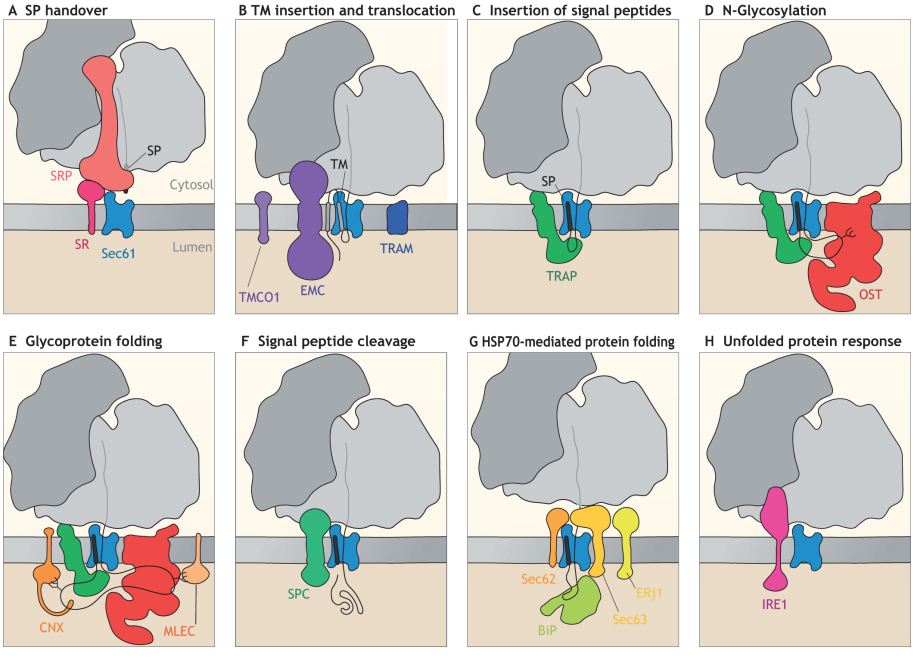

Fig. 1: Sec61 'Swiss army knife' and cofactors. (A) The SR recruits the RNC–SRP complex to the ER translocon and hands over the SP to Sec61. (B) Insertion of TMs is aided by insertases, such as EMC or possibly TMCO1, whereas TRAM helps to overcome pauses during translocation [23] (C) Insertion of some SPs requires TRAP. (D) As translocation continues, the OST N-glycosylates translocating peptides. (E) Processed glycans associate with lectin chaperones malectin (MLEC) and calnexin (CNX), which are transiently recruited for glycoprotein folding. (F) Eventually, the SP is cleaved off by the SPC. (G) Primarily in post-translational import, but also for some co-translational substrates, the Hsp70 BiP is recruited by the Sec62–Sec63 or ERj1. (H) The constitutive interaction of IRE1 with Sec61 directly links ER translocation and the UPR.

different proteins remained in these RAMP fractions. The most-detergent- and salt-resistant proteins are those belonging to the Sec61 complex, the translocating chain-associated membrane protein (TRAM1), the SPC and the protein RAMP4, later coined stress-associated endoplasmic reticulum protein 1 (SERP1) [24]. Additional components, such as the oligosaccharyl transferase complex (specifically its ribophorin subunits [25,26], the TRAP complex [27], the lectin calnexin [28], and the J-domain protein ERj1 (also known as DNAJC1) [29], were observed with the use of milder detergents or lower salt concentrations. Cross-linking prior to isolation revealed additional components such as p180 (also known as ribosome-binding protein 1, RRBP1) [30], and specific substrates such as the prion protein (PrP) indicated an association between the Sec62–Sec63 complex and the co-translational ER translocon complex [31]. However, these isolation studies did not address which of these components are indeed stoichiometric components, and the structural arrangement also remained unresolved.

Cryo-electron ET is uniquely suited to study the structures of macromolecular complexes under close-to-native conditions [22]. In particular, this approach is also applicable to transient interactions, which are inherently difficult to address by purification-based approaches. In combination with image processing methods to enhance the low signal of cryo-ET raw data by averaging approaches [32,33] and 'classify' distinct molecular configurations of assemblies [34,35], cryo-ET can reveal the structures of assemblies and relative abundances of complex types in native settings with sub-nanometer resolution. While the integral membrane proteins TRAM1 and SERP1 are difficult to detect by this approach because they can only be distinguished from the lipid membrane at resolutions notably better than 1 nm, all the other potential translocon components possess sufficiently large luminal or cytosolic domains to be detected. For instance, application of cryo-ET to ER-derived vesicles defined the mammalian core ER co-translocon complex; its main stoichiometric components are Sec61 and the TRAP complex, as determined by comparison of the wild-type translocon complex to that from knockdown cells [11] (Fig. 2A).

In mammals, the octameric OST complex is found in near-stoichiometric ratios associated with the ER co-translocon (Fig. 2A). For instance, in canine pancreatic ER-derived microsomes, ~70% of all ribosome–translocon complexes had OST bound [11], while in fibroblasts this proportion was 60–70% [10] and in HeLa [11] and HEK cells [36] ~40–

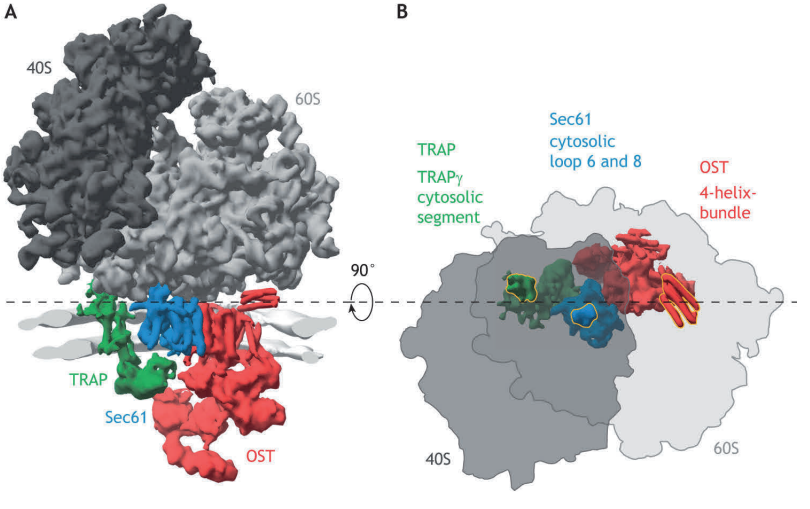

Fig. 2: Overview of the ribosome-bound ER translocon complex. (A) The overall structure of the native complex as determined by cryo-ET (EMDB 4315; PDB 6FTG) shows the molecular organization of Sec61 embedded in the ER membrane and associated to the ribosome and accessory factors TRAP and OST. (B) Schematic view of the ribosome ER translocon complex contacts (yellow contours) formed by TRAPγ, Sec61α and the OST subunit ribophorin 1 as seen from the top.

45%. By contrast, in the algae *Chlamydomas reinhardtii*, only ~15% of all ribosome–translocon complexes contain OST [10]. Thus, OST occupancy varies strongly depending on species and cell type, possibly reflecting different degrees of N-glycosylation.

In the subnanometer-resolution reconstruction of the *in situ* ribosome–Sec61–TRAP–OST complex [15,36], Sec61 binds to ribosomal proteins (uL23 and eL29) at the end of the ribosomal exit tunnel, as also observed in previous cryo-EM SPA of solubilized samples [37-39]. The transmembrane portion of TRAP is positioned near the C-terminal domain of Sec61, and its location is stabilized by associations with the ribosome through a cytosolic domain and to Sec61 through its luminal portion [15]. The transmembrane (TM) portion of OST binds to the N-terminal half of Sec61, and only its cytosolic domain binds the ribosome. Together, the ribosome-binding sites of TRAP, Sec61 and OST effectively form a line, stabilizing this giant molecular assembly (Fig. 2B).

SRP receptor

Co-translational translocation through the ER translocon complex requires the SRP, which is a complex of SRP RNA and six proteins (SRP9, SRP14, SRP19, SRP54, SRP68 and SRP72 [40]. SRP together with the heterodimeric SRP receptor (SRα and SRβ, encoded by *SRPRA* and *SRPRB*, hereafter SRαβ) are responsible for targeting ribosome–nascent-chain (RNC) complexes to the ER membrane and inserting the peptide chain into the Sec61 protein-conducting channel (Fig. 1A).

SRP and SRαβ have structurally related 'NG' GTPase domains in SRP54 and SRα, respectively [41]. Crystallographic structures indicate that the GTPase activity of these NG domains must be activated by a conformational switch in the SRP–SR complex [41,42]. This activation occurs concurrently with SP handover from the RNC–SRP–SRαβ to the ER translocon complex [43]. Thus, RNC–SRP–SRαβ exists in two ER-translocon-bound states: a pre-handover complex, where the RNC–SRP–SRαβ associates with the ER translocon, with the SP bound to the SRP, and an activated post-handover complex, where the SP is inserted into Sec61. Solubilized bacterial RNC–SRP–SRαβ–SecYEG complexes that were locked in a post-hydrolysis form with GDP-AlFx, representing a transient intermediate between the targeting and translocation states, have been analyzed by cryo-EM SPA [44]. The molecular interpretation of the obtained cryo-EM map suggests that a major structural remodeling of the ribosome–Sec61 complex occurs: Sec61 and the ribosome undergo a relative rotation of 180° in plane when transitioning from targeting to translocation [44] (Fig. S1). However, such dramatic conformational changes have to be confirmed in native settings.

Biochemical studies have also provided some glimpses into the molecular mechanisms underlying the switching of ER translocon complexes from their SRP-dependent co-translational mode to their post-translational one [45]. Both SRαβ and the ribosome individually induce the dissociation of Sec62 from Sec61, suggesting that the binding of SRαβ and ribosome sterically interferes with the binding of Sec62 to Sec61. Thus, the recruitment of RNC–SRP–SRαβ to Sec61 releases Sec62–Sec63 complexes from Sec61, suggesting that Sec62–Sec63 may only be involved in co-translational translocation at later stages, if at all.

Protein-conducting channel Sec61

Sec61 consists of the three transmembrane proteins Sec61α (note there are Sec61α1 and Sec61α2 forms in mammals), Sec61β and Sec61γ (Fig. 3A), and the prokaryotic homologs of Sec61α, Sec61β and Sec61γ are SecY, SecG and SecE (bacteria), and SecY, Secb and SecE (archaea), respectively. Crystallographic analysis of the archaeal SecY (Sec61α homolog) revealed that the two pseudo-symmetrical transmembrane domains of Sec61α form a narrow channel [46]. Contrary to previous hypotheses proposing a functional oligomerization of Sec61 complexes [47], the structure suggested that Sec61 may function as a single complex and conduct peptides through its central channel [46]. Furthermore, the structure also indicates that a lateral window to the lipid membrane might form at the interface of the two TM domains of Sec61α (Fig. 3B), possibly to facilitate insertion of transmembrane helices from the substrate into the ER membrane. Subsequent crystallographic structures of prokaryotic Sec61 homologs revealed a distinct conformation in which the repositioning of their two TM domains opens the lateral window [48,49]. In both 'open' structures, the cytosolic face of the Sec61α homolog SecY is in contact with another molecule, either the bacterial ATPase SecA [48] or a neighboring SecY molecule through crystal contacts [49]. A third observation was that a short helix forms a 'plug' in the ER lumen, thereby closing the translocation channel, which was hypothesized to open in the translocation process.

Cryo-EM SPA studies of solubilized RNC–Sec61 complexes confirmed that a single Sec61 complex acts as a translocation channel [37,39]. Notably, the conformational states of Sec61 appear heterogeneous in these studies. Whereas the C-terminal domain of Sec61α binds to the ribosome in a well-defined manner, the positioning of the N-terminal domain is variable. In those cryo-EM studies, analysis of minor, structurally well-defined classes that display defined translational states reveal better-resolved closed Sec61 conformers with the plug remaining in place. The finding of a closed Sec61 conformation is in contrast to that observed in the native non-solubilized ribosome-bound translocon; here, it is effectively exclusively observed in an open

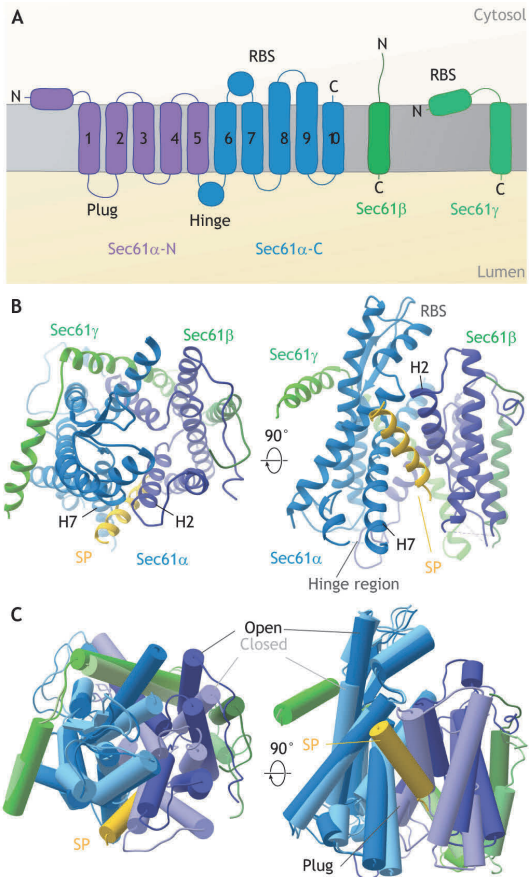

Fig. 3: Sec61 conformations and SP-binding. (A) Subunit composition and topology of the Sec61 complex. Ribosome-binding sites (RBS) are annotated. (B) The cryo-EM SPA structure of the 'open' SP-bound Sec61 conformation (PDB 3JC2) shows the central pore (left, top view) and the Sec61α helices H2 and H7, which delimit the lateral gate, accommodating the SP (right, side view). (C) Comparison of 'open' SP-bound conformation with the closed conformation observed in detergent-solubilized, idle ribosome–Sec61 complexes (PDB 3J7Q). The short 'plug' helix of Sec61α closes the protein-conducting channel formed by Sec61α.

conformation [15] (Fig. 3C). Interestingly, the map of the native translocon complex displays a rod-like density at the lateral gate [15]. This initially unassigned density co-localizes with the SP, as determined later on in the structure of solubilized RNC–Sec61 complexes with a non-cleaved SP [50], as well as a crystal structure of the prokaryotic homolog [51]. In these high-resolution structures, the SPs (the SP of pre-prolactin and OmpA, respectively) bind almost identically to helix 2 of the open Sec61α/SecY. In the RNC–Sec61–SP structure, the plug is not resolved, suggesting that it becomes unstructured [50], whereas, in the SecY–SP crystal structure, it undergoes a secondary structure change, which makes way for the SP [51]. Remarkably, a narrow pore ring

in the protein-conducting channel encloses the nascent peptide and maintains a permeability barrier for ions [51].

It is somewhat puzzling that the predominant form of ribosome-bound Sec61 complexes in the native membrane appears to be an open conformation with an SP bound [15], whereas major biochemical efforts are required to stabilize this conformation in isolated, solubilized complexes [50]. Thus, the SP appears prone to being released from its binding site in the lateral gate upon treatment with detergent. The cryo-ET experiments, at this point, cannot conclusively address whether the SPs bound to the native Sec61 are still predominantly bound to a nascent chain, or whether SPC cleavage has readily occurred, because the resolution is insufficient to distinguish nascent chains.

From prokaryotes, it is well established that the insertion of many multi-transmembrane helix proteins into membranes requires cooperation of SecYEG/SecYEβ with YidC [17]. This protein is part of the YidC/Alb3/Oxa1 membrane protein family, which is conserved in all kingdoms of life [52]. Its members function as insertases in bacterial (YidC), thylakoid (Alb3) and mitochondrial membranes (Oxa1). A unique structural feature of these proteins is a hydrophilic, positively charged groove open to the membrane interior, which may transport acidic portions of proteins across the membrane, while inserting TM segments into the membrane [17]. The structure of domain of unknown function 106 (DUF106) recently expanded the YidC/Alb3/Oxa1 protein family [53]. Based on the presence of DUF106, which interestingly binds to RNCs *in vitro*, three ER-residing eukaryotic members YidC/Alb3/Oxa1 family could be identified (Fig. 1B): TMCO1, the Get1 subunit of the Get1–Get2 complex and the subunit EMC3 of the ER membrane complex (EMC) [16,54]. Whereas the Get complex is thought to function independently of the ER translocon complex in the insertion of tail-anchored proteins, the EMC is considered to cooperate co-translationally with the ER translocon complex for the integration of multi-transmembrane helix proteins [55]. However, the precise function of TMCO1 and its possible interactions with the ER translocon complex remain to be elucidated.

Translocon-associated protein complex

The ER translocon complex of metazoans comprises the hetero-oligomeric TRAP complex as a constitutive subunit (Figs 1C and 4A). In animals, it is a hetero-tetramer assembled by the transmembrane proteins TRAPα, TRAPβ, TRAPγ and TRAPδ (also known as SSR1, SSR2, SSR3 and SSR4, respectively) [27], whereas in plants it is a dimer, TRAPα–TRAPβ [10]. The TRAP complex is required by specific substrates for the initiation

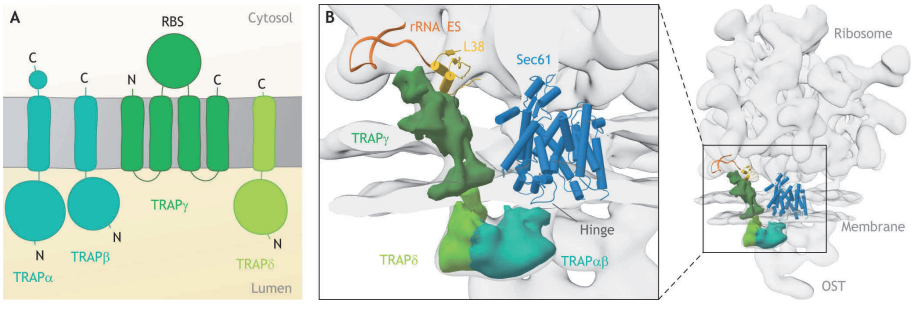

Architecture of the TRAP complex. (A) Mammalian TRAP subunits and their membrane topology with the ribosome-binding site (RBS) indicated. (B) Molecular arrangement of TRAP within the native ER translocon complex. The cytosolic TRAPγ domain mediates binding to the ribosome, whereas TRAPα–TRAPβ contacts the hinge region of Sec61 (EMDB 4315).

of translocation [56]. Proteomics analysis suggests that TRAP might be essential for the translocation of substrates that have SPs with low helical propensity due to high glycine and proline content [13]. Furthermore, mutations of the TRAP complex in glycosylation-deficient patients suggest its involvement in the N-glycosylation of specific substrates [57].

Comparative cryo-ET studies of mammalian cells and plants show that the animal-specific cytosolic TRAPγ domain associates with the large ribosome subunit via the protein L38 and a rRNA expansion segment (ES) [10] (Fig. 4B). The evolutionarily conserved luminal domains in TRAPα and TRAPβ bind to each other to form a heterodimer, which associates with the hinge region of Sec61 [10]. The cryo-ET structure of the ER translocon complex from cells of a TRAPδ-deficient patient, who suffers from congenital glycosylation defects, shows that the luminal domain of TRAPδ is positioned in proximity with OST subunit ribophorin 2 [10]. However, higher-resolution structures are required to mechanistically explain the function of TRAP in SP integration (possibly through TRAPα–TRAPβ) and its involvement in N-glycosylation, which might be mediated through TRAPδ.

Oligosaccharyltransferase complex

For many nascent proteins of the secretory pathway, glycosylation of asparagine residues (N-glycosylation) is essential. The initially transferred glycan is identical for all N-glycosylations and subsequent action of glycosidases and glycosyltransferases in ER and Golgi yields great chemical variation. The hetero-oligomeric OST complex catalyzes the transfer of $Glc_3Man_9GlcNAc_2$ glycans from a pre-formed lipid-linked oligosaccharides (LLOs) to specific asparagine residues of proteins in the lumen of

the ER [58] (Fig. 1D). Whereas OST is a monomeric enzyme in prokaryotes, its eukaryotic homolog STT3 is integrated into a larger oligomeric complex (Fig. 5A). Higher eukaryotes have two distinct catalytic paralogs, STT3a and STT3b, while simpler eukaryotes such as yeast only have a single ortholog (STT3). The modular composition and assembly of the yeast OST complex and the STT3b-containing mammalian complex are analogous; subcomplex 1 contains OST1 (ribophorin 1 in mammals) and OST5 (transmembrane protein 258, TMEM258), subcomplex 2 comprises STT3 (STT3b), OST3 or OST6 (TUSC3 or IAP) and OST4 (OST4), whereas subcomplex 3 involves OST2 (DAD1), WBP1 (OST48) and SWP1 (ribophorin 2) [59]. The STT3a-containing OST complex has the additional subunits DC2 (OSTC) and KCP2, while it lacks TUSC3 and IAP.

Gene silencing experiments indicate that there is a preference of the STT3a-containing OST for co-translational N-glycosylation, compared to the prevalent post-translational glycosylation mediated by STT3b [60]. Cryo-ET studies of cells in which STT3a and STT3b had been knocked out, showed that there is indeed a strict separation of co- and post-translational N-glycosylation, in that only the STT3a-containing OST associates with the ribosome-bound ER translocon [36].

Two independent cryo-EM SPA studies provided the atomic structure of the yeast OST [61,62]. The structure of the active subunit STT3 is similar to its prokaryotic counterparts [63,64] with conservation of the residues involved in substrate binding and oligosaccharyl transfer [61,62]. Thus far, specific enzymatic functions have only been assigned to the orthologs OST3 (TUSC3) and OST6 (IAP), which function as oxidoreductases in the (post-translational) OST to facilitate the breakage of disulfide bridges in folded domains, which might prevent N-glycosylation [65]. In the SPA structures, only the TM domain of OST3 is resolved, which localizes in immediate proximity to the LLO, as inferred from the prokaryotic STT3 homolog [66]. The large luminal domains of OST1 (ribophorin 1), WBP1 (OST48) and SWP1 (ribophorin 2) mostly form immunoglobulin G-like β-sandwich folds that are thought to serve as docking platforms for accessory proteins and possibly have chaperone function [61,62]. Of note, ribophorin 2 has an additional N-terminal domain located further distally from the membrane, which is not present in yeast and algae [10].

Complementary studies of the native mammalian ribosome-bound co-translational OST by cryo-ET and solubilized RNC–Sec61–OST by SPA have provided insights into the structure and function of the cytosolic domains and some of its TM regions [36] (Fig. 5B). A four-helix bundle at the C-terminus of Rpn1 mediates the interaction with the large ribosomal subunit by contacting ribosomal RNA helices H19, H20 and H25, and ribosomal protein eL28. Compared to its paralog STT3a, STT3b has an additional cytosolic N-terminal domain, which would be positioned in such a way that it likely interferes with ribosome binding.

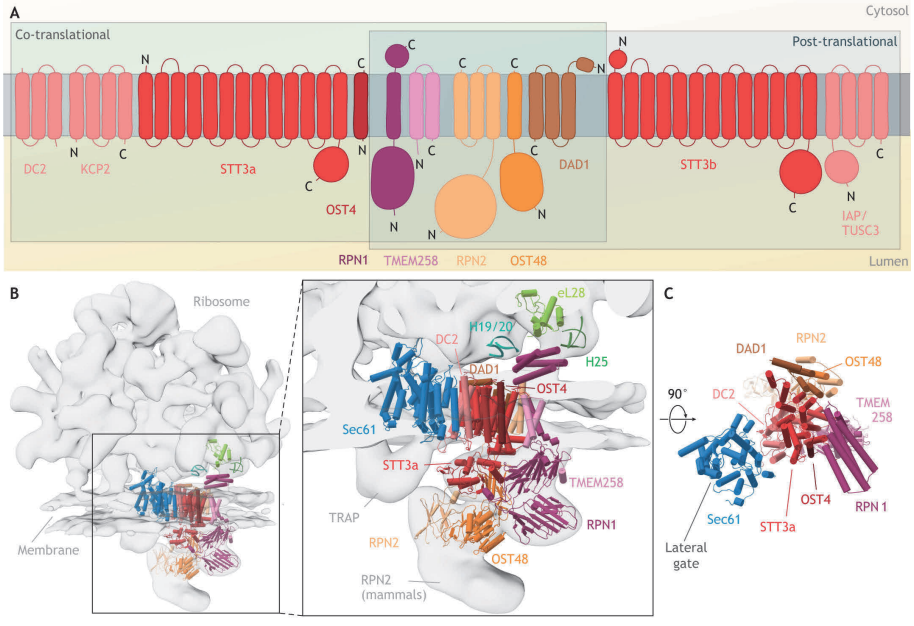

Composite atomic model of yeast and mammalian OST. (A) Mammalian co- and post-translational OST paralogs, consisting of a common (RPN1, TMEM258, RPN2, OST48 and DAD1) and paralog-specific set of subunits (STT3a and DC2 and KCP2; STT3b and IAP or TUSC3). The STT3a-containing complex associates with the ER co-translocon. (B) A composite atomic model of the mammalian co-translational OST (PDB 6FTG) fragment complemented with luminal domains of the yeast OST complex (PDB 6EZN) is positioned into the filtered density map of the ribosome-associated translocon (EMDB 4315). The central panel shows a magnified view of the complex and its interacting sites in the ribosome and translocon. (C) Top view from the cytosol where the ER membrane resides in the paper plane.

The OST subunit DC2, which has three TM regions, positions between STT3a and Sec61, and associates with the latter via its amphipathic N-terminus that projects near the Sec61 hinge [36]. Remarkably, the SPA maps reveal two distinct relative orientations of OST and Sec61, while the native conformation seen by cryo-ET differs from both. Therefore, the integration of OST into the ER translocon through only two major contact sites provides specificity, while at the same time accommodating for flexibility with regard to how Sec61 and OST are arranged relative to each other, which might be important for OST function and its regulation.

In ER protein biogenesis, N-glycans play an essential role in glycoprotein folding and quality control in the ER. N-glycans are sequentially trimmed by processing α-glucosidase I and processed glycans are bound by lectin chaperones malectin (MLEC) and calnexin (CNX) (Fig. 1E). Both, MLEC and CNX, associate with the ER co-translocon [67,68]. Recruitment of CNX is dependent on TRAP, whereas MLEC associates with OST subunit Rpn1 [67,69]. The interplay between MLEC and Rpn1 regulates the

subcellular distribution of MLEC and attenuates secretion of misfolded proteins [69,70], highlighting its importance in the early steps of the glycoprotein folding pathway. Further structural studies are important to understand how the chaperones are organized at the ER translocon.

Signal peptidase complex

The SPC is responsible for cleavage of the SP. The SPC acts on a broad range of substrates, but also has to distinguish signal peptides from TM segments. The highly specific binding mode of the SP to Sec61 [50,51] may be key to substrate selectivity.

The SPC evolved from a monomeric membrane-bound signal peptidase in prokaryotes (SPase I). The structure of the soluble domain of *E.coli* SPase I reveals that it is a serine protease with an unusual Ser-His dyad instead of the conventional Ser-His-Asp triad found in this class of enzymes [71]. This active site is embedded into a large hydrophobic surface, which is thought to be proximal to the membrane to facilitate cleavage of the SP. Mammals possess two SPase I paralogs, SPC18 (also known as SEC11A) and SPC21 (also known as SEC11C), which are complemented by three non-catalytic subunits SPC12 (SPCS1), SPC22 or SPC23 (both encoded by *SPCS3*), and SPC25 [5]. Yeast only has the single ortholog Sec11 [72], suggesting that mammals may have two distinct SPCs, either containing SPC18 or SPC21, analogous to the single OST complex in yeast and the two variants in mammals.

Although mammalian SPC co-purifies with the ER translocon complex [24], it was not found to be a (near) stoichiometric component [11]. Thus, SPC likely associates only transiently with the translocon in order to cleave off Sec61-bound SP. In line with this, cell-free assays demonstrated that the SPC has access to the nascent chain later than the OST (Fig. 1) [73]. Furthermore, pre-prolactin constructs have to translate at least for a ~80 residues further after their successful incorporation into Sec61 in order for their SP to be cleaved from the nascent chain [74]. The exact mechanisms underlying SPC association and cleavage are still poorly understood, and structures of both SPC alone and with the ER translocon complex will be insightful.

ER post-translocon complex

Sec61 also facilitates SRP-independent protein translocation. Whereas co-translational translocation is powered by GTP hydrolysis of the ribosome, the ATP-dependent Hsp70-type chaperone binding immunoglobulin protein (BiP, also known as HSPA5, Kar2 in yeast), which is the most abundant ER-luminal protein, assists in post-

translational translocation. BiP is thought to catalyze the directional translocation by binding the polypeptide chain that is translocated through Sec61, which prevents its backward movement into the cytosol. To acquire its full ATPase activity, the N-terminal ATPase domain of Hsp70 proteins associate with J-domains of their Hsp40-type co-chaperones, termed ERj proteins [75]. While yeast has only a single membrane-bound ERj (Sec63), humans have seven; ERj3–ERj6 (DNAJB11, DNAJB9, DNAJC10, DNAJC3) are soluble proteins, whereas ERj1 (DNAJC1), Sec63 (ERj2; SEC63) and ERj7 (DNAJC25) are membrane-resident.

In yeast, the Sec61–Sec62–Sec63–Sec71–Sec72 (Sec) complex (Fig. 6A) facilitates post-translational import together with the transiently bound BiP [18,19]. Recently, the cryo-EM SPA structure of the Sec complex has been solved [76,77] (Fig. 6B). Sec63 localizes opposite of the lateral gate and is tightly associated with Sec61, which involves cytosolic, transmembrane and luminal segments of all three Sec61 subunits [76,77]. In contrast to what is found in cryo-EM studies of the solubilized, idle ER translocon complex [39], Sec61 adopts its open conformation in the idle Sec complex, likely owing the extensive contacts with Sec63. Although the resolution of Sec62 was insufficient to build an atomic model, the localization of the cytosolic domain of Sec62 in proximity to the lateral gate of Sec61 in the low-resolution nevertheless supports its involvement in membrane protein insertion and topogenesis [78,79].

Superimposing the yeast Sec complex and the mammalian ribosome-associated translocon complex indicates that the entire cytosolic domain of Sec63 clashes with the large ribosomal subunit. Furthermore, the TM helices of Sec63 and OST overlap in their Sec61-binding site (Fig. 6C). In addition, the luminal domain of Sec63 interferes with the luminal domain of TRAPα–TRAPβ, which binds to the hinge region of Sec61 (Fig. 6C,D). Collectively, these steric considerations suggest that there is a strict separation of SRP-dependent co- and post-translational translocation using distinct complexes, the ER co-translocon and Sec complex, respectively. This notion is in agreement with earlier biochemical studies [45].

Mammals have the simpler Sec61–Sec62–Sec63 complex [80]. Interestingly, in mammalian systems, the Sec62–Sec63 dimer has been implicated in co-translational translocation of specific substrates, such as the prion protein [31,81]. One possibility to reconcile these findings with the steric clashes between the ribosome and Sec62–Sec63, as indicated above, is by assuming that the prion protein already folds in the cytosol, thereby causing a partial release of the ribosome from Sec61, together with recruitment of Sec62–Sec63 and possible dissociation of TRAP [31]. Recently, it has been suggested that the yeast Sec complex is also involved in co-translational translocation through a cytosolic Hsp70, which might also mediate the unfolding of the nascent

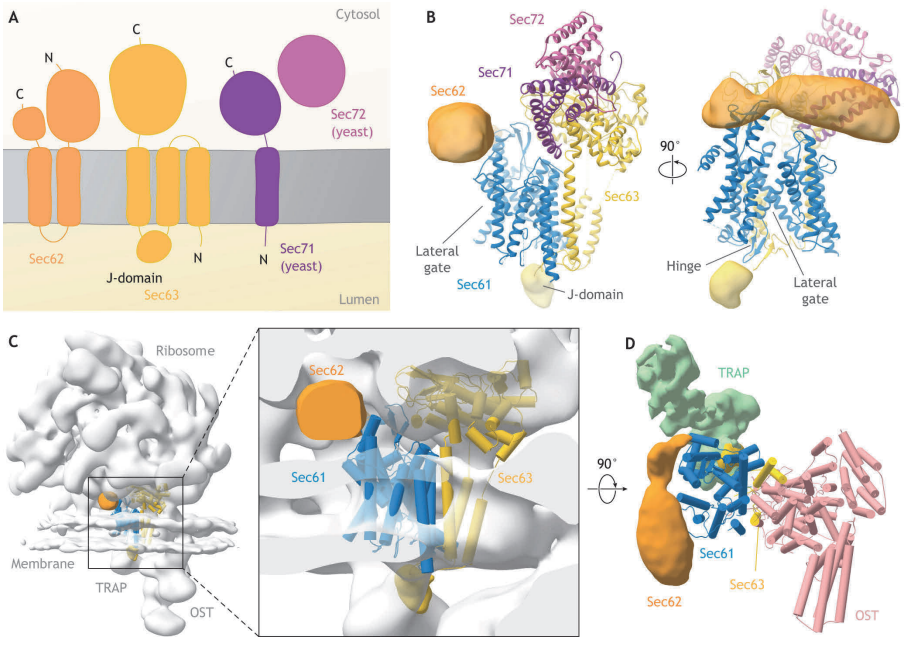

Structure of the yeast Sec complex. (A). In addition to Sec61, the Sec complex comprises the essential subunits Sec62 and Sec63, which recruit the Hsp70 BiP through its J-domain. The yeast Sec complex furthermore contains the non-essential subunits Sec71 and Sec72. (B) The cryo-EM SPA structure of the yeast Sec complex (EMDB 0336; PDB 6N3Q) reveals the atomic model of Sec63, Sec71 and Sec72 located opposite to the lateral gate of Sec61, as well as poorly resolved density of Sec62. (C) Superposition of the cryo-ET map of native mammalian ribosome-bound ER-translocon complex (gray, EMDB 4315) and the cryo-EM SPA yeast Sec translocon structure (colored, PDB 6FTG) illustrating the steric clashes of Sec63 with the ribosome and TRAP. (D) A top view of the ER translocon complex subunits (TRAP and OST) surrounding Sec61 compared with Sec translocon subunits Sec62 and Sec63 indicating that recruitment of Sec63 and the OST complex to Sec61 are mutually exclusive. Ribosome, membrane and cytosolic Sec63 densities are clipped to provide a better overview.

chain after its release from the ribosomal exit tunnel and prior to insertion into Sec61 [82]. Further structural studies will be required to investigate the precise mechanism of Sec62–Sec63-mediated co-translational translocation of specific substrates, as well as the structural basis of BiP-dependent regulation of translation by ERj1 [29,83-85].

Unfolded protein response machinery

The unfolded protein response (UPR) reduces the load of translated ER proteins and increases the ER-folding capacity upon stress through the initiation of a transcription program that increases the protein-folding capacity and decreases further protein influx [86,87]. In yeast, the ER-resident kinase inositol-requiring protein 1 (IRE1) initiates

this signaling cascade, whereas mammalian UPR exhibits two additional kinase branches [PERK (also known as EIF2AK3) and ATF6]. The mammalian protein IRE1α controls translation of the transcription factor X box-binding protein 1 (XBP1). IRE1α forms constitutive, but highly sub-stoichiometric complexes with Sec61, to which its substrate, *XBP1* mRNA, is recruited by a pseudo-SP of the XBP nascent chain [20]. At moderate stress levels, IRE1α is bound to Sec61 and active, while at higher levels of stress, it is released from Sec61 and forms high-order oligomers [88]. Consistent with these findings, IRE1α has also been found to directly associate with the ER-bound ribosome [89]. Thus, the co-translational translocation machinery and the IRE1α branch of the UPR are intimately linked, although this remains to be structurally elucidated in detail. In this endeavor, the intrinsically low abundance of IRE1α compared to other ER translocon complex constituents is a major challenge for cryo-EM approaches that are essentially statistics-based and thus rely on the analysis of a large number of complexes.

ER-associated protein degradation

The ER does not possess its own proteases for the degradation of (misfolded) proteins. Instead, the ER makes use of the cytosolic ubiquitin-proteasome system (UPS); this so-called ER-associated degradation (ERAD) process requires the retro-translocation of substrates into the cytosol, where they are ubiquitylated and eventually degraded by the 26S proteasome [90]. Some viruses, such as cytomegalovirus (CMV), hijack ERAD to evade the immune system as they encode for viral factors that target MHC-I complexes, which are involved in triggering an immune response, for degradation [91]. Affinity purification experiments that made use of the CMV genes US2 and US11 demonstrated that Sec61 interacts with ERAD substrates [91]. Moreover, in yeast, a physical interaction between Sec61 and ERAD components has also been demonstrated [92]. Although an earlier hypothesis that Sec61 serves as a retrotranslocation channel is no longer favored [93], the relevance of the physical interaction between the ER translocon and ERAD complexes remains to be elucidated, possibly with the help of structural exploration.

Conclusions and outlook

Recent structural studies using different cryo-EM modalities have advanced the mechanistic understanding of ER translocation and protein biogenesis in the ER. Central to these processes is the Sec61 protein-conducting channel, which appears to function almost like a Swiss army knife; with the help of a large number of accessory

components associated with it, its core translocation function can be complemented by a variety of co-translational tasks. Structural analysis revealed that binding of many of these accessory ER translocon complex components is mutually exclusive. For example, the formation of the Sec translocon is incompatible with the association of Sec61 with TRAP and OST.

Future research will reveal the precise interaction mode of further Sec61 interactors, such as YidC-like integrases complexes, SR, SPC and IRE1α, as well as the functional regulation of their association. Cryo-EM SPA in combination with affinity purification of native complexes from yeast has been the basis of many structural studies in the past (e.g. OST, ER post-translocon) and gene editing will extend this success to other organisms. Nevertheless, a fundamental limitation in the analysis of membrane-associated complexes by SPA is that their purification requires solubilization. While the effect of solubilization on protein–protein interactions within single protein complexes such as the OST may be moderate, interactions between complexes involving lipids become significantly distorted as illustrated for the RNC–translocon super-complex. Thus, cryo-ET may be the most efficient route to get a high-resolution structure of the ER translocon complex, including its currently poorly resolved transmembrane components, such as TRAP or TRAM. Ongoing rapid developments to increase the data throughput of cryo-ET [94] together with improved processing [95] will be key to substantially increase resolution. Similarly, less-abundant super-complexes involved in ERAD and the UPR will likely only be resolved in their native membranes. Efficient structural characterization may involve enrichment in (functional) membrane fractions or ultimately imaging in the cell, combined with the identification of specific events by correlative super-resolution light microscopy [96].

Acknowledgements

This work was supported by the European Research Council under the European Union's Horizon2020 Programme (ERC Consolidator Grant Agreement 724425 - BENDER). The authors thank all members of the Förster lab for fruitful discussions.

Competing interests

The authors declare no competing or financial interests.

Supplementary figures

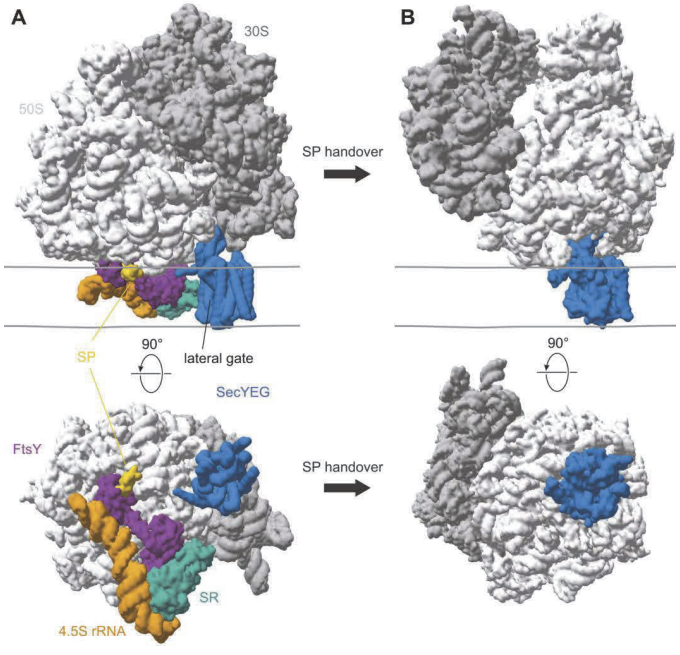

Fig. S1. Hypothetical model for SP handover based on cryo-EM SPA of solubilized RNC-SRP-SR-SecYEG complexes. (A) Surface representation of the *E. coli* pre-handover complex shows a quaternary complex comprising RNC, SRP, SR and SecYEG (PDB 5NCO) [44]. (B) Surface representation of the atomic model of RNC in complex with a translocating SecYEG (PDB 5GAE) suggests that the ribosome undergoes a 180° rotation upon handover of SP. Top panels: side view with ER membrane indicated. Bottom panels: view from the ER luminal side.

References

1 **A. E. Johnson & M. A. van Waes.** The translocon: a dynamic gateway at the ER membrane. *Annu Rev Cell Dev Biol* **15**, 799-842 (1999).

2 **G. Palade.** Intracellular aspects of the process of protein synthesis. *Science* **189**, 347-358 (1975).

3 **G. Blobel & B. Dobberstein.** Transfer of proteins across membranes. I. Presence of proteolytically processed and unprocessed nascent immunoglobulin light chains on membrane-bound ribosomes of murine myeloma. *The Journal of cell biology* **67**, 835-851 (1975).

4 **P. F. Egea, R. M. Stroud & P. Walter.** Targeting proteins to membranes: structure of the signal recognition particle. *Curr Opin Struct Biol* **15**, 213-220 (2005).

5 **E. A. Evans, R. Gilmore & G. Blobel.** Purification of microsomal signal peptidase as a complex. *Proc Natl Acad Sci U S A* **83**, 581-585 (1986).

6 **S. Panzner, L. Dreier, E. Hartmann, S. Kostka & T. A. Rapoport.** Posttranslational protein transport in yeast reconstituted with a purified complex of Sec proteins and Kar2p. *Cell* **81**, 561-570 (1995).

7 **S. Shao & R. S. Hegde.** A calmodulin-dependent translocation pathway for small secretory proteins. *Cell* **147**, 1576-1588 (2011).

8 **G. Schlenstedt & R. Zimmermann.** Import of frog prepropeptide GLa into microsomes requires ATP but does not involve docking protein or ribosomes. *Embo J* **6**, 699-703 (1987).

9 **T. A. Rapoport, L. Li & E. Park.** Structural and Mechanistic Insights into Protein Translocation. *Annu Rev*

Cell Dev Biol (2017).

10 **S. Pfeffer, J. Dudek, M. Schaffer, B. G. Ng, S. Albert, J. M. Plitzko, W. Baumeister, R. Zimmermann, H. H. Freeze, B. D. Engel & F. Förster.** Dissecting the molecular organization of the translocon-associated protein complex. *Nature communications* **8**, 14516 (2017).

11 **S. Pfeffer, J. Dudek, M. Gogala, S. Schorr, J. Linxweiler, S. Lang, T. Becker, R. Beckmann, R. Zimmermann & F. Förster.** Structure of the mammalian oligosaccharyl-transferase complex in the native ER protein translocon. *Nature communications* **5**, 3072 (2014).

12 **J. F. Menetret, R. S. Hegde, M. Aguiar, S. P. Gygi, E. Park, T. A. Rapoport & C. W. Akey.** Single copies of Sec61 and TRAP associate with a nontranslating mammalian ribosome. *Structure* **16**, 1126-1137 (2008).

13 **D. Nguyen, R. Stutz, S. Schorr, S. Lang, S. Pfeffer, H. H. Freeze, F. Förster, V. Helms, J. Dudek & R. Zimmermann.** Proteomics reveals signal peptide features determining the client specificity in human TRAP-dependent ER protein import. *Nature communications* **9**, 3765 (2018).

14 **N. Sommer, T. Junne, K. U. Kalies, M. Spiess & E. Hartmann.** TRAP assists membrane protein topogenesis at the mammalian ER membrane. *Biochim Biophys Acta* **1833**, 3104-3111 (2013).

15 **S. Pfeffer, L. Burbaum, P. Unverdorben, M. Pech, Y. Chen, R. Zimmermann, R. Beckmann & F. Förster.** Structure of the native Sec61 protein-conducting channel. *Nature communications* **6**, 8403 (2015).

16 **S. A. Anghel, P. T. McGilvray, R. S. Hegde & R. J. Keenan.** Identification of Oxa1 Homologs Operating in the Eukaryotic Endoplasmic Reticulum. *Cell Rep* **21**, 3708-3716 (2017).

17 **D. J. du Plessis, N. Nouwen & A. J. Driessen.** The Sec translocase. *Biochim Biophys Acta* **1808**, 851-865 (2011).

18 **R. J. Deshaies, S. L. Sanders, D. A. Feldheim & R. Schekman.** Assembly of yeast Sec proteins involved in translocation into the endoplasmic reticulum into a membrane-bound multisubunit complex. *Nature* **349**, 806-808 (1991).

19 **S. L. Sanders, K. M. Whitfield, J. P. Vogel, M. D. Rose & R. W. Schekman.** Sec61p and BiP directly facilitate polypeptide translocation into the ER. *Cell* **69**, 353-365 (1992).

20 **R. Plumb, Z. R. Zhang, S. Appathurai & M. Mariappan.** A functional link between the co-translational protein translocation pathway and the UPR. *eLife* **4** (2015).

21 **E. Callaway.** The revolution will not be crystallized: a new method sweeps through structural biology. *Nature* **525**, 172-174 (2015).

22 **M. Beck & W. Baumeister.** Cryo-Electron Tomography: Can it Reveal the Molecular Sociology of Cells in Atomic Detail? *Trends Cell Biol* **26**, 825-837 (2016).

23 **R. S. Hegde, S. Voigt, T. A. Rapoport & V. R. Lingappa.** TRAM regulates the exposure of nascent secretory proteins to the cytosol during translocation into the endoplasmic reticulum. *Cell* **92**, 621-631 (1998).

24 **D. Gorlich & T. A. Rapoport.** Protein translocation into proteoliposomes reconstituted from purified components of the endoplasmic reticulum membrane. *Cell* **75**, 615-630 (1993).

25 **G. Kreibich, M. Czako-Graham, R. Grebenau, W. Mok, E. Rodriguez-Boulan & D. D. Sabatini.** Characterization of the ribosomal binding site in rat liver rough microsomes: ribophorins I and II, two integral membrane proteins related to ribosome binding. *J Supramol Struct* **8**, 279-302 (1978).

26 **G. Kreibich, B. L. Ulrich & D. D. Sabatini.** Proteins of rough microsomal membranes related to ribosome binding. I. Identification of ribophorins I and II, membrane proteins characteristics of rough microsomes. *The Journal of cell biology* **77**, 464-487 (1978).

27 **E. Hartmann, D. Gorlich, S. Kostka, A. Otto, R. Kraft, S. Knespel, E. Burger, T. A. Rapoport & S. Prehn.** A tetrameric complex of membrane proteins in the endoplasmic reticulum. *Eur J Biochem* **214**, 375-381 (1993).

28 **E. Chevet, H. N. Wong, D. Gerber, C. Cochet, A. Fazel, P. H. Cameron, J. N. Gushue, D. Y. Thomas & J. J. M. Bergeron.** Phosphorylation by CK2 and MAPK enhances calnexin association with ribosomes. *Embo Journal* **18**, 3655-3666 (1999).

29 **J. Dudek, M. Greiner, A. Muller, L. M. Hendershot, K. Kopsch, W. Nastainczyk & R. Zimmermann.** ERj1p has a basic role in protein biogenesis at the endoplasmic reticulum. *Nat Struct Mol Biol* **12**, 1008-1014 (2005).

30 **P. G. Collins & R. Gilmore.** Ribosome binding to the endoplasmic reticulum: a 180-kD protein identified by crosslinking to membrane-bound ribosomes is not required for ribosome binding activity.

The Journal of cell biology **114**, 639-649 (1991).

31 **B. J. Conti, P. K. Devaraneni, Z. Yang, L. L. David & W. R. Skach.** Cotranslational stabilization of Sec62/63 within the ER Sec61 translocon is controlled by distinct substrate-driven translocation events. *Molecular cell* **58**, 269-283 (2015).

32 **F. Förster & R. Hegerl.** Structure determination in situ by averaging of tomograms. *Methods in cell biology* **79**, 741-767 (2007).

33 **J. A. Briggs.** Structural biology in situ--the potential of subtomogram averaging. *Curr Opin Struct Biol* **23**, 261-267 (2013).

34 **Y. Chen, S. Pfeffer, J. J. Fernandez, C. O. Sorzano & F. Förster.** Autofocused 3D classification of cryoelectron subtomograms. *Structure* **22**, 1528-1537 (2014).

35 **F. Förster, S. Pruggnaller, A. Seybert & A. S. Frangakis.** Classification of cryo-electron sub-tomograms using constrained correlation. *Journal of structural biology* **161**, 276-286 (2008).

36 **K. Braunger, S. Pfeffer, S. Shrimal, R. Gilmore, O. Berninghausen, E. C. Mandon, T. Becker, F. Förster & R. Beckmann.** Structural basis for coupling protein transport and N-glycosylation at the mammalian endoplasmic reticulum. *Science* **360**, 215-219 (2018).

37 **M. Gogala, T. Becker, B. Beatrix, J. P. Armache, C. Barrio-Garcia, O. Berninghausen & R. Beckmann.** Structures of the Sec61 complex engaged in nascent peptide translocation or membrane insertion. *Nature* **506**, 107-110 (2014).

38 **T. Becker, S. Bhushan, A. Jarasch, J. P. Armache, S. Funes, F. Jossinet, J. Gumbart, T. Mielke, O. Berninghausen, K. Schulten, E. Westhof, R. Gilmore, E. C. Mandon & R. Beckmann.** Structure of monomeric yeast and mammalian Sec61 complexes interacting with the translating ribosome. *Science* **326**, 1369-1373 (2009).

39 **R. M. Voorhees, I. S. Fernandez, S. H. Scheres & R. S. Hegde.** Structure of the Mammalian ribosome-sec61 complex to 3.4 a resolution. *Cell* **157**, 1632-1643 (2014).

40 **P. Walter & G. Blobel.** Signal recognition particle contains a 7S RNA essential for protein translocation across the endoplasmic reticulum. *Nature* **299**, 691-698 (1982).

41 **D. M. Freymann, R. J. Keenan, R. M. Stroud & P. Walter.** Structure of the conserved GTPase domain of the signal recognition particle. *Nature* **385**, 361-364 (1997).

42 **S. Padmanabhan & D. M. Freymann.** The conformation of bound GMPPNP suggests a mechanism for gating the active site of the SRP GTPase. *Structure* **9**, 859-867 (2001).

43 **K. Shen, S. Arslan, D. Akopian, T. Ha & S. O. Shan.** Activated GTPase movement on an RNA scaffold drives co-translational protein targeting. *Nature* **492**, 271-275 (2012).

44 **A. Jomaa, Y. H. Fu, D. Boehringer, M. Leibundgut, S. O. Shan & N. Ban.** Structure of the quaternary complex between SRP, SR, and translocon bound to the translating ribosome. *Nat Commun* **8**, 15470 (2017).

45 **B. Jadhav, M. McKenna, N. Johnson, S. High, I. Sinning & M. R. Pool.** Mammalian SRP receptor switches the Sec61 translocase from Sec62 to SRP-dependent translocation. *Nature communications* **6**, 10133 (2015).

46 **B. Van den Berg, W. M. Clemons, Jr., I. Collinson, Y. Modis, E. Hartmann, S. C. Harrison & T. A. Rapoport.** X-ray structure of a protein-conducting channel. *Nature* **427**, 36-44 (2004).

47 **R. Beckmann, C. M. Spahn, J. Frank & G. Blobel.** The active 80S ribosome-Sec61 complex. *Cold Spring Harb Symp Quant Biol* **66**, 543-554 (2001).

48 **J. Zimmer, Y. Nam & T. A. Rapoport.** Structure of a complex of the ATPase SecA and the protein-translocation channel. *Nature* **455**, 936-943 (2008).

49 **P. F. Egea & R. M. Stroud.** Lateral opening of a translocon upon entry of protein suggests the mechanism of insertion into membranes. *Proceedings of the National Academy of Sciences of the United States of America* **107**, 17182-17187 (2010).

50 **R. M. Voorhees & R. S. Hegde.** Structure of the Sec61 channel opened by a signal sequence. *Science* **351**, 88-91 (2016).

51 **L. Li, E. Park, J. Ling, J. Ingram, H. Ploegh & T. A. Rapoport.** Crystal structure of a substrate-engaged SecY protein-translocation channel. *Nature* **531**, 395-399 (2016).

52 **S. W. Hennon, R. Soman, L. Zhu & R. E. Dalbey.** YidC/Alb3/Oxa1 Family of Insertases. *J Biol Chem* **290**, 14866-14874 (2015).

53 **M. T. Borowska, P. K. Dominik, S. A. Anghel, A. A. Kossiakoff & R. J. Keenan.** A YidC-like Protein in the Archaeal Plasma Membrane. *Structure* **23**, 1715-1724 (2015).

54 **A. Guna, N. Volkmar, J. C. Christianson & R. S. Hegde.** The ER membrane protein complex is a transmembrane domain insertase. *Science* **359**, 470-473 (2018).

55 **M. J. Shurtleff, D. N. Itzhak, J. A. Hussmann, N. T. Schirle Oakdale, E. A. Costa, M. Jonikas, J. Weibezahn, K. D. Popova, C. H. Jan, P. Sinitcyn, S. S. Vembar, H. Hernandez, J. Cox, A. L. Burlingame, J. L. Brodsky, A. Frost, G. H. Borner & J. S. Weissman.** The ER membrane protein complex interacts cotranslationally to enable biogenesis of multipass membrane proteins. *eLife* **7** (2018).

56 **R. D. Fons, B. A. Bogert & R. S. Hegde.** Substrate-specific function of the translocon-associated protein complex during translocation across the ER membrane. *The Journal of cell biology* **160**, 529-539 (2003).

57 **M. E. Losfeld, B. G. Ng, M. Kircher, K. J. Buckingham, E. H. Turner, A. Eroshkin, J. D. Smith, J. Shendure, D. A. Nickerson, M. J. Bamshad, G. University of Washington Center for Mendelian & H. H. Freeze.** A new congenital disorder of glycosylation caused by a mutation in SSR4, the signal sequence receptor 4 protein of the TRAP complex. *Human molecular genetics* **23**, 1602-1605 (2014).

58 **D. J. Kelleher & R. Gilmore.** An evolving view of the eukaryotic oligosaccharyltransferase. *Glycobiology* **16**, 47R-62R (2006).

59 **S. Mueller, A. Wahlander, N. Selevsek, C. Otto, E. M. Ngwa, K. Poljak, A. D. Frey, M. Aebi & R. Gauss.** Protein degradation corrects for imbalanced subunit stoichiometry in OST complex assembly. *Mol Biol Cell* **26**, 2596-2608 (2015).

60 **C. Ruiz-Canada, D. J. Kelleher & R. Gilmore.** Cotranslational and posttranslational N-glycosylation of polypeptides by distinct mammalian OST isoforms. *Cell* **136**, 272-283 (2009).

61 **R. Wild, J. Kowal, J. Eyring, E. M. Ngwa, M. Aebi & K. P. Locher.** Structure of the yeast oligosaccharyltransferase complex gives insight into eukaryotic N-glycosylation. *Science* (2018).

62 **L. Bai, T. Wang, G. Zhao, A. Kovach & H. Li.** The atomic structure of a eukaryotic oligosaccharyltransferase complex. *Nature* **555**, 328-333 (2018).

63 **C. Lizak, S. Gerber, S. Numao, M. Aebi & K. P. Locher.** X-ray structure of a bacterial oligosaccharyltransferase. *Nature* **474**, 350-355 (2011).

64 **S. Matsumoto, A. Shimada, J. Nyirenda, M. Igura, Y. Kawano & D. Kohda.** Crystal structures of an archaeal oligosaccharyltransferase provide insights into the catalytic cycle of N-linked protein glycosylation. *Proceedings of the National Academy of Sciences of the United States of America* **110**, 17868-17873 (2013).

65 **E. Mohorko, R. L. Owen, G. Malojcic, M. S. Brozzo, M. Aebi & R. Glockshuber.** Structural basis of substrate specificity of human oligosaccharyl transferase subunit n33/tusc3 and its role in regulating protein N-glycosylation. *Structure* **22**, 590-601 (2014).

66 **M. Napiorkowska, J. Boilevin, T. Sovdat, T. Darbre, J. L. Reymond, M. Aebi & K. P. Locher.** Molecular basis of lipid-linked oligosaccharide recognition and processing by bacterial oligosaccharyltransferase. *Nat Struct Mol Biol* (2017).

67 **A. K. Lakkaraju, L. Abrami, T. Lemmin, S. Blaskovic, B. Kunz, A. Kihara, M. Dal Peraro & F. G. van der Goot.** Palmitoylated calnexin is a key component of the ribosome-translocon complex. *Embo J* **31**, 1823-1835 (2012).

68 **S. Y. Qin, D. Hu, K. Matsumoto, K. Takeda, N. Matsumoto, Y. Yamaguchi & K. Yamamoto.** Malectin forms a complex with ribophorin I for enhanced association with misfolded glycoproteins. *J Biol Chem* **287**, 38080-38089 (2012).

69 **K. Takeda, S. Y. Qin, N. Matsumoto & K. Yamamoto.** Association of malectin with ribophorin I is crucial for attenuation of misfolded glycoprotein secretion. *Biochem Biophys Res Commun* **454**, 436-440 (2014).

70 **Q. P. Yang, M. F. Fu, H. Gao, K. Yamamoto, D. Hu & S. Y. Qin.** Subcellular distribution of endogenous malectin under rest and stress conditions is regulated by ribophorin I. *Glycobiology* **28**, 374-381 (2018).

71 **M. Paetzel, R. E. Dalbey & N. C. Strynadka.** Crystal structure of a bacterial signal peptidase in complex with a beta-lactam inhibitor. *Nature* **396**, 186-190 (1998).

72 **J. M. van Dijl, A. de Jong, J. Vehmaanpera, G. Venema & S. Bron.** Signal peptidase I of Bacillus subtilis: patterns of conserved amino acids in prokaryotic and eukaryotic type I signal peptidases. *Embo J* **11**, 2819-2828 (1992).

73 **I. M. Nilsson & G. von Heijne.** Determination of the distance between the oligosaccharyltransferase active site and the endoplasmic reticulum membrane. *J Biol Chem* **268**, 5798-5801 (1993).

74 **W. Mothes, S. Prehn & T. A. Rapoport.** Systematic probing of the environment of a translocating secretory protein during translocation through the ER membrane. *Embo J* **13**, 3973-3982 (1994).

75 **S. Lang, S. Pfeffer, P. H. Lee, A. Cavalie, V. Helms, F. Förster & R. Zimmermann.** An Update on Sec61 Channel Functions, Mechanisms, and Related Diseases. *Frontiers in physiology* **8**, 887 (2017).

76 **X. Wu, C. Cabanos & T. A. Rapoport.** Structure of the post-translational protein translocation machinery of the ER membrane. *Nature* (2018).

77 **S. Itskanov & E. Park.** Structure of the posttranslational Sec protein-translocation channel complex from yeast. *Science* **363**, 84-87 (2019).

78 **J. H. Reithinger, J. E. Kim & H. Kim.** Sec62 protein mediates membrane insertion and orientation of moderately hydrophobic signal anchor proteins in the endoplasmic reticulum (ER). *J Biol Chem* **288**, 18058-18067 (2013).

79 **S. J. Jung, J. E. Kim, J. H. Reithinger & H. Kim.** The Sec62-Sec63 translocon facilitates translocation of the C-terminus of membrane proteins. *J Cell Sci* **127**, 4270-4278 (2014).

80 **H. A. Meyer, H. Grau, R. Kraft, S. Kostka, S. Prehn, K. U. Kalies & E. Hartmann.** Mammalian Sec61 is associated with Sec62 and Sec63. *The Journal of biological chemistry* **275**, 14550-14557 (2000).

81 **S. Lang, J. Benedix, S. V. Fedeles, S. Schorr, C. Schirra, N. Schauble, C. Jalal, M. Greiner, S. Hassdenteufel, J. Tatzelt, B. Kreutzer, L. Edelmann, E. Krause, J. Rettig, S. Somlo, R. Zimmermann & J. Dudek.** Different effects of Sec61alpha, Sec62 and Sec63 depletion on transport of polypeptides into the endoplasmic reticulum of mammalian cells. *J Cell Sci* **125**, 1958-1969 (2012).

82 **A. Tripathi, E. C. Mandon, R. Gilmore & T. A. Rapoport.** Two alternative binding mechanisms connect the protein translocation Sec71-Sec72 complex with heat shock proteins. *J Biol Chem* **292**, 8007-8018 (2017).

83 **J. Benedix, P. Lajoie, H. Jaiswal, C. Burgard, M. Greiner, R. Zimmermann, S. Rospert, E. L. Snapp & J. Dudek.** BiP modulates the affinity of its co-chaperone ERj1 for ribosomes. *J Biol Chem* **285**, 36427-36433 (2010).

84 **J. Dudek, J. Volkmer, C. Bies, S. Guth, A. Muller, M. Lerner, P. Feick, K. H. Schafer, E. Morgenstern, F. Hennessy, G. L. Blatch, K. Janoscheck, N. Heim, P. Scholtes, M. Frien, W. Nastainczyk & R. Zimmermann.** A novel type of co-chaperone mediates transmembrane recruitment of DnaK-like chaperones to ribosomes. *Embo J* **21**, 2958-2967 (2002).

85 **M. Blau, S. Mullapudi, T. Becker, J. Dudek, R. Zimmermann, P. A. Penczek & R. Beckmann.** ERj1p uses a universal ribosomal adaptor site to coordinate the 80S ribosome at the membrane. *Nat Struct Mol Biol* **12**, 1015-1016 (2005).

86 **C. Hetz.** The unfolded protein response: controlling cell fate decisions under ER stress and beyond. *Nat Rev Mol Cell Biol* **13**, 89-102 (2012).

87 **P. Walter & D. Ron.** The unfolded protein response: from stress pathway to homeostatic regulation. *Science* **334**, 1081-1086 (2011).

88 **A. Sundaram, R. Plumb, S. Appathurai & M. Mariappan.** The Sec61 translocon limits IRE1alpha signaling during the unfolded protein response. *eLife* **6** (2017).

89 **D. Acosta-Alvear, G. E. Karagoz, F. Frohlich, H. Li, T. C. Walther & P. Walter.** The unfolded protein response and endoplasmic reticulum protein targeting machineries converge on the stress sensor IRE1. *eLife* **7** (2018).

90 **M. M. Hiller, A. Finger, M. Schweiger & D. H. Wolf.** ER degradation of a misfolded luminal protein by the cytosolic ubiquitin-proteasome pathway. *Science* **273**, 1725-1728 (1996).

91 **E. J. Wiertz, D. Tortorella, M. Bogyo, J. Yu, W. Mothes, T. R. Jones, T. A. Rapoport & H. L. Ploegh.** Sec61-mediated transfer of a membrane protein from the endoplasmic reticulum to the proteasome for destruction. *Nature* **384**, 432-438 (1996).

92 **A. Schafer & D. H. Wolf.** Sec61p is part of the endoplasmic reticulum-associated degradation machinery. *Embo J* (2009).

93 **P. Carvalho, A. M. Stanley & T. A. Rapoport.** Retrotranslocation of a misfolded luminal ER protein by the ubiquitin-ligase Hrd1p. *Cell* **143**, 579-591 (2010).

94 **G. Chreifi, S. Chen, L. A. Metskas, M. Kaplan & G. J. Jensen.** Rapid tilt-series acquisition for electron cryotomography. *Journal of structural biology* **205**, 163-169 (2019).

95 **B. A. Himes & P. Zhang.** emClarity: software for high-resolution cryo-electron tomography and subtomogram averaging. *Nat Methods* **15**, 955-961 (2018).

96 **M. W. Tuijtel, A. J. Koster, S. Jakobs, F. G. A. Faas & T. H. Sharp.** Correlative cryo super-resolution light and electron microscopy on mammalian cells using fluorescent proteins. *Sci Rep* **9**, 1369 (2019).

CHAPTER 3

Molecular snapshots of human ribosome intermediate states at the ER membrane

Max Gemmer[1], Marten L. Chaillet[1], Joyce van Loenhout[1], Dimitrios Vismpas[1], Fujiet A. Koh[2], Pascal Albanese[3,4], Richard Scheltema[3,4], Stuart C. Howes[1], Abhay Kotecha[2], Juliette Fedry[1], Friedrich Förster[1]

[1] Structural Biochemistry, Bijvoet Center for Biomolecular Research, Utrecht University, 3584 CG Utrecht, The Netherlands
[2] Thermo Fisher Scientific, Eindhoven, The Netherlands
[3] Biomolecular Mass Spectrometry and Proteomics Group, Utrecht Institute for Pharmaceutical Sciences, Utrecht University, 3584 CH Utrecht, The Netherlands
[4] Netherlands Proteomics Center, Utrecht University, Utrecht University, 3584 CH Utrecht, The Netherlands

Modified from

M. Gemmer, M. L. Chaillet, J. van Loenhout, D. Vismpas, F. A. Koh, P. Albanese, R. Scheltema, S. C. Howes, A. Kotecha, J Fedry, F. Förster. Visualization of translation and protein biogenesis at the ER membrane. *Nature* **614**, 160-167 (2023).

Abstract

The human ribosome facilitates protein synthesis in the cytosol of the cell. To mediate polypeptide elongation, the ribosome cycles through a series of structural rearrangement and cooperates with tRNAs and elongation factors. While ribosome intermediate states have been extensively studied in isolation and *ex vivo*, high-resolution structure determination typically requires extensive purification, which potentially induces disruption of interactions to ribosome binding partners. Here, we rapidly isolated ribosome-decorated ER-derived vesicles to capture ribosomal intermediates using cryo-electron tomography (cryo-ET) and subtomogram analysis. We distinguish ten classes, seven of which were assigned to intermediates of the elongation cycle, while two of the classes adopt a hibernation state. Spatial 3D analysis of the ribosome neighborhood demonstrates that elongating particles tend to form polysomes at the ER membrane and in solution, whereas hibernating particles are unorganized. We identify a highly abundant classical pre-translocation intermediate with eEF1a in an extended conformation, suggesting that eEF1a may remain ribosome-associated after GTP-hydrolysis during proofreading. Collectively, we visualize human ribosome intermediate states and their polysome organization at the ER membrane *ex vivo*.

Main

Biosynthesis of most proteins is facilitated by the ribosome in the cytosol. The ribosome decodes the information of mRNAs and translates the genetic code into a polypeptide chain [1]. Protein synthesis is divided into four phases: Initiation elongation, termination, and ribosome recycling. To elongate the polypeptide chain, ribosomes cycle through a series of conformational rearrangements and cooperate with elongation factors and tRNAs, a process which is referred to as the elongation cycle.

The elongation cycle comprises three main steps: mRNA decoding, peptidyl transfer, and tRNA translocation. Aminoacyl (aa)-tRNAs are delivered to the ribosome by GTP-bound elongation factor 1a (eEF1a) [2-5]. When the tRNA anticodon matches the mRNA codon sequence, the aa-tRNA positions in the noncanonical A/T-site and eEF1a contacts the sarcin-ricin-loop (SRL) of the 28S rRNA. These interactions induce conformational changes in the domain 3 of eEF1a, stimulating its GTPase activity. Upon GTP-hydrolysis, eEF1a undergoes drastic domain movements switching from its compact to an extended conformation and triggering rapid release of eEF1a from the ribosome, while the aa-tRNA is accommodated in the canonical aminoacyl (A)-site. eEF1a has also been suggested to contribute to proofreading during mRNA decoding by preventing accommodation of near-cognate tRNAs, thereby increasing the accuracy of translation [5-8]. Next, the polypeptide chain is transferred from the peptidyl (P)-tRNA to the A-tRNA-bound amino acid, thereby elongating the nascent polypeptide chain by one amino acid [9]. Finally, after peptidyl transfer has occurred, eEF2 translocates the mRNA-tRNA moiety, allowing initiation of the next cycle [10].

To investigate the mechanisms underlying ribosomal elongation, structural studies often utilize non-hydrolyzable GTP analogs or antibiotics to arrest intermediates, which provided valuable insights into mRNA decoding or tRNA translocation [4,11-13]. However, stalling, as well as the subsequent enrichment and purification steps, can introduce artifacts or disrupt interactions to binding partners. While one study succeeded to visualize ribosome states of human polysomes *ex vivo* [14], studies investigating the molecular landscape of ribosomal elongation intermediates in human remained scarce. However, with the rapid advancement of cryo-electron microscopy (cryo-EM) techniques, particularly cryo-electron tomography, structural analysis of near-native, heterogeneous ribosome intermediates *ex vivo* or *in situ* are becoming increasingly feasible. We employed electron cryogenic tomography (cryo-ET) to visualize the elongating ribosome at the ER membrane.

Subtomogram analysis of ribosome complexes

To analyze the elongation cycle of ER-bound ribosomes we rapidly (~1 h) isolated ER-derived vesicles (microsomes) from HEK-293F cells for subsequent cryo-ET imaging (Supplementary Fig. 1 and 2). We acquired a large dataset (869 tilt series) of frozen-hydrated vesicles and employed a regularized single particle analysis approach to analyze the membrane-associated ribosome particles [15] (Supplementary Fig. 2). Extensive subtomogram analysis reveals ten classes at a resolution ranging from 4 to 10 Å, which allows for identification of ribosomal intermediate states based on high-resolution structures of isolates (Supplementary Fig. 3, Supplementary Table 1).

Ribosomal intermediates and 3D distribution

We first dissected the translational states of the ribosome pool consisting of membrane-bound and residual soluble particles. Focusing on the orientation of the SSU and association of tRNAs and elongation factors, we classified the particles into ten distinct states (Supplementary Fig. 2C, 3). To assess their translational activity, we examined the relative 3D distribution of the particles from the classes using a reciprocal neighborhood probability analysis, which is indicative of integration into polysomes (Fig. 1, Supplementary Fig. 4). Particles from eight classes (89%) show probability hotspots proximal to the ribosomal mRNA entrance and exit sites characteristic for membrane-bound and cytosolic ribosomes and consistent with previous lower-resolution analyses [16,17]. In contrast, two classes show a featureless neighbor distribution implying that these particles are not involved in polysomes. The reconstructions of these two classes do not have tRNA bound in the P-site and resemble known hibernating ribosome complexes bound to eEF2 [18].

To assess the physiological relevance of our preparation, we analyzed the distribution of ribosomal intermediate states *in situ* using focused ion beam (FIB) milled human cells. While the lower yield of this approach resulted in substantially fewer particles (5,818) and reduced classification depth, it confirmed the high abundance of factor-bound classes (~70%), and their presence on polysomes (Supplementary Fig. 5). The ~66% factor-bound ribosome complexes *ex vivo* exceed the abundance in previous ribosomal purification from HEK cells involving size exclusion chromatography (~8% in ref. [14]) (Supplementary Fig. 5F). Consistent with this previous cryo-EM analysis [14] and the high abundance eEF1a and eEF2 in proteomics data of the sample (Supplementary Fig. 6) we identify eEF1a and eEF2 as ribosome-binding factors. Nevertheless, we stress that lysis and the isolation conditions may affect intermediate complexes and their abundance, which may eventually be overcome when higher resolution is achievable for cryo-FIB/ET studies of human cells.

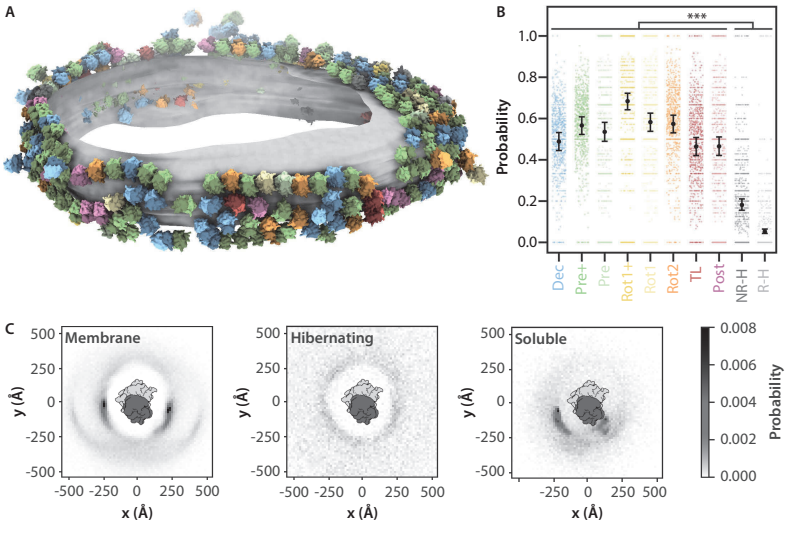

Fig. 1: Spatial distribution of ribosome intermediate states. (A) Different ribosome states mapped back onto one exemplary ER-derived vesicle (n=869 tomograms from 1 experiment, two independent replicates in Supplementary Fig. 5). (B) Probabilities of ribosome states to be present in polysomes. Black circles show the modelled mean with the 95% confidence interval as error bars fitted to n=132,371 ribosomes with the 869 tomograms included as a random effect. Hochberg adjusted p-values were determined with a two-sided Wald-test. p-values for comparison between hibernating and elongating states were all smaller than 2×10^{-16}. The small scattered points represent the frequencies of events per tomogram. (C) Definition of leading and trailing neighbors in polysome. Neighbor distribution of ER membrane-bound, hibernating, and soluble ribosome particles. The membrane resides in the paper plane.

Elongation cycle intermediates

To further analyze the polysome-associated ribosomal classes, we attempted to position them in the context of the elongation cycle as modelled based on knowledge from previous *in vitro* reconstitution work [4,6,10,13,14] (Fig. 2). While one class could not be conclusively assigned functionally (Supplementary Fig. 7), the remaining 7 states are consistent with prior structural or biochemical data. The elongation cycle model commences with delivery of aminoacyl (aa)-tRNAs to the ribosome by GTP-bound eEF1a (decoding state, Fig. 2). Approximately 22% of ribosomes in our data adopt an unrotated state, with clear densities for the tRNAs in the P- and E-sites and the eEF1a-tRNA ternary complex, which we assigned to a decoding population [12] (Fig. 3). The position of eEF1a in our decoding map differs slightly from a previously reported decoding state in polysomes purified from HEK cells [14] , which may be due to differences in the preparation protocols. The position of eEF1A in our decoding complex rather resembles a codon sampling state obtained by inhibiting eEF1a GTP hydrolysis [12] (Supplementary Fig. 8A,B). We speculate that the decoding population

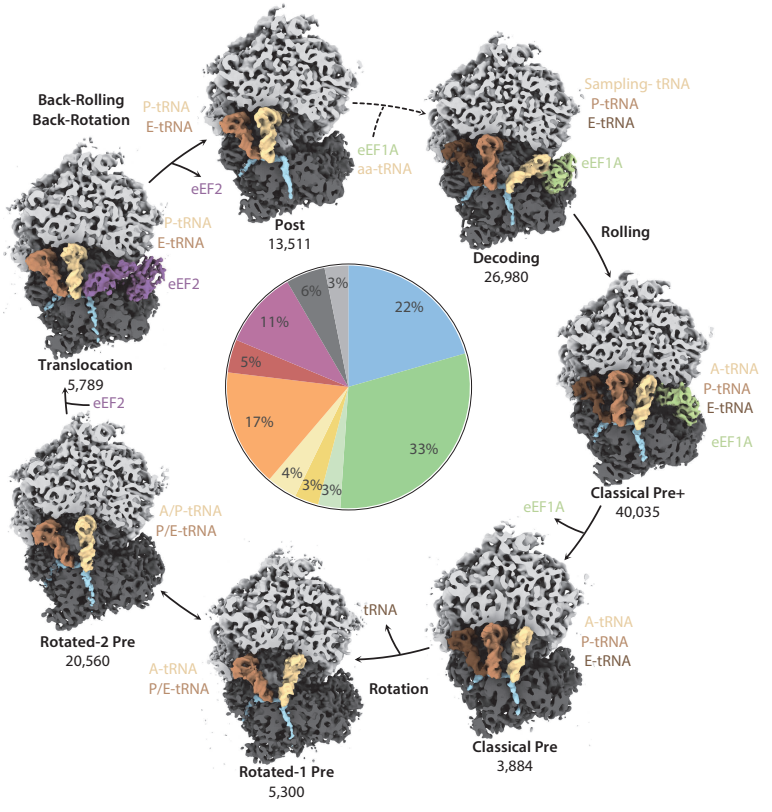

Fig. 2: Observed active intermediates arranged according to the model of the human elongation cycle. All reconstructions were filtered to 7 Å resolution. The ribosome is clipped for visualization. A, P, and E indicate ribosomal aminoacyl, peptidyl, and exit sites, respectively, and aa-tRNA is aminoacylated tRNA. The tRNAs are color-coded with respect to a complete cycle. Abundance of each state is indicated. Color code as in Fig. 1A.

observed in our data may be explained by ribosomes testing non-cognate tRNAs that do not trigger GTP hydrolysis and occur more frequently than cognate tRNAs in the cell.

Next, we observe a highly abundant intermediate (33%) that has not been described previously: while the tRNA is accommodated in the canonical aminoacyl (A)-site and the SSU 'rolls' into the classical pre-configuration, eEF1a is bound to the ribosome in an extended conformation, which matches crystal structures of purified eEF1A•GDP [5] and its bacterial homolog EF-Tu•GDP [3] (Fig. 3, Supplementary Fig. 8C,D). To analyze the PRE+ state at higher resolution, we rapidly isolated soluble ribosomes and imaged them with cryo-EM single particle analysis (SPA). Approximately 30% of particles were in the pre+ state yielding a focused reconstruction of eEF1a with specific side chains

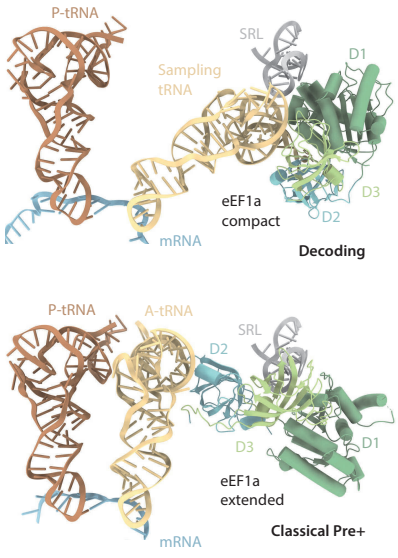

Fig. 3: Structures of human elongation factor eEF1a. Close-up view of ribosome-bound compact eEF1a in the decoding-sampling state (PDB 4CXG) and in the classical pre+ state (4C0S). D1-3 indicate the eEF1a domains 1-3 and SRL the sarcin-ricin loop.

of domain 3 (~3.5 Å resolution) unambiguously identifying eEF1a (Supplementary Fig. 9). In the classical-pre+ state, eEF1a domains 1 and 3 interact with the sarcin-ricin loop (SRL) of the 28S rRNA (Supplementary Fig. 9H), while domain 2 blocks the A/T site and contacts the A-site tRNA. In a human model elongation cycle, we propose that the classical PRE+ state may follow the decoding state, where eEF1a still adopts a compact conformation. While we cannot rule out that other factors observed at this site *in situ* could have been displaced by eEF1A (Supplementary Fig. 5) during the purification, the occurrence of the eEF1A bound classical pre+ state in purified samples indicates the possibility that eEF1a may remain bound to the ribosome during conformational switching to the extended form. This observation is different from bacteria, where no factors are observed *in situ* on the abundant PRE-like A,P state [19] and suggests differences in eukaryote post-hydrolysis proofreading, possibly involving eEF1A [7,20,21]. The functional relevance of a possible eEF1a-bound classical pre+ state remains to be further investigated with complementary methods.

Next, we observe a previously described classical pre state, which we propose to occur after eEF1a fully dissociates from the ribosome, as the SSU and tRNAs remain unchanged (3%). We then identified 2 rotated states in our data: the rotated-1 pre state resulting from dissociation of a tRNA (4%), and the much higher populated rotated-2 pre state with the tRNAs in hybrid A/P and P/E positions (17%). In contrast to previous studies of cytosolic polysomes [14], we found 5% of ribosomes in a state resembling a

translocation intermediate (TI) associated with eEF2 and tRNAs in the canonical P- and E-sites. GTP hydrolysis seems to have occurred as indicated by the disordered switch I loop (Supplementary Fig. 10). This state resembles the late TI-post-3 state[13], which would be consistent with kinetic studies in the bacterial system [22]. We finally observe a similar state with P- and E-tRNAs and without eEF2, which is in good agreement with the post translocation (POST) state (Fig. 2).

Finally, we note that the assigned positions of the 3 most abundant states we observe are consistent with the elongation rate-limiting steps: decoding and pre+ correspond to proof-reading steps, while rotated-2 precedes translocation.

Hibernating ribosomes and ER stress

Membrane-bound hibernating ribosomes group into two major populations (Fig. 4). A non-rotated state with a tRNA bound at the exit (E)-site and the protein CCDC124 occupying the P-site (7%) differs from a similar structure of the cytosolic hibernating ribosome [18] by eEF2 binding. We also detected a second rotated ribosome state (5%), which features eEF2, and from which CCDC124 is absent, analogous to the cytosolic hibernating ribosome [18]. To investigate the physiological role of hibernating ribosomes we also imaged microsomes from dithiothreitol (DTT)-treated HEK cells, where elongation activity should be reduced [23]. Strikingly, we almost exclusively observe hibernating ribosomes upon treatment with DTT (Supplementary Fig. 11). Thus, the abundance of ER-bound hibernating ribosomes strongly depends on cell state, and possibly also on cell density as observed for cytosolic hibernating ribosomes [18]. We cannot rule out induction of some hibernating ribosomes by lysis, which must be considered when interpreting the relative abundances.

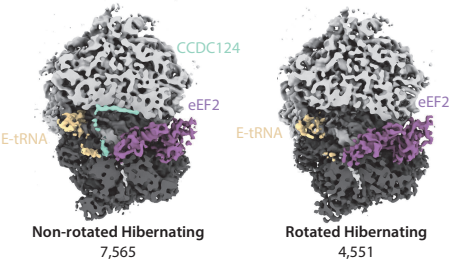

Fig. 4: Reconstructions of hibernating ribosomes. Reconstructions of two distinct ribosome states lacking tRNA at the P-site (hibernating states).

Conclusions

Collectively, subtomogram analysis visualizes elongating and hibernating intermediate states of ER membrane-bound and soluble ribosomes under normal and ER stress condition. Our data complement previous structural studies and provide a basis for future investigations to advance our understanding of eEF1a in proofreading. Moreover, the separation of active and inactive ER-bound ribosomes allows us to study the downstream ER translocon machinery in context of translational activity, which will be addressed in chapter 4 and 5.

Materials and Methods

Cell culture

HeLa and U2OS cells (from ATCC, CVCL_0042 and CVCL_0030 in Cellosaurus.org, respectively) were grown in standard tissue culture conditions (37°, 5% CO2) in DMEM Glutamax (Gibco). HEK 293-F cells (ThermoFisher Scientific, R79007) were grown in suspension in FreeStyle medium with 120 rpm agitation. Cell lines were not authenticated and were tested for negative mycoplasma.

ER-vesicle preparation

HEK 293-F WT or CCDC47 KO cells (0.5–1 × 10^6 cells/ml, 50 mL) were harvested and washed (3 × with PBS, at 300 *g*, 5 min, 4 °C). HEK 293-F cells used for ER stress studies were treated with 10 mM DTT for 2 h before harvesting. Cells were resuspended in lysis buffer (2–4 ml, 10 mM HEPES-NaOH pH 7.4, 250 mM sucrose, 2 mM $MgCl_2$, 0.5 mM DTT, protease inhibitor cocktail [Roche]) and lysed using a Isobiotec cell cracker (5–10 passes, 14 µm clearance, on ice). The lysate was cleared (1,500 *g*, 2–3 x 5 min, 4 °C, in 2 mL tubes) using a cooled tabletop centrifuge. Vesicles were pelleted (10,000 *g*, 10 min, 4 °C,) and washed with resuspension buffer (10 mM HEPES, 250 mM sucrose, 1 mM $MgCl_2$, 0.5 mM DTT). The pellet was resuspended at a concentration of ~50 mg/mL determined by A_{280}, frozen in liquid nitrogen and stored at -80 °C until further use. The supernatant was used for proteomics as control.

20 µg of microsomes were used for SDS-PAGE followed by immunoblotting using antibodies against Sec61α (Abcam, ab15575; 1:1000), TRAPγ (Sigma Aldrich, hpa014906; 1:1000) and CCDC47 (Abcam, ab241608; 1:1000).

Mass spectrometry data acquisition

Approximately 100 µg of the isolated ER-microsome and cytosolic fraction (supernatant) were digested using an S-Trap™ micro-MS column (protifi) according to vendor's protocol.

Proteins were solubilized in Lysis buffer (10% SDS, 100 mM Tris, pH 8), reduced (100 mM TCEP), alkylated (400 mM CAA in isopropanol) and denatured (27.5 % phosphoric acid). For protein trapping, samples were flown over an S-Trap micro spin column, (10,000 g, 30 sec) and further washed with binding buffer (100 mM TEA, in 90% methanol). Protein digestion was achieved with an overnight incubation at 37 °C using a waterbath (Grant Instruments, JB Academy) after the addition of digestion buffer (10% Trypsin, 2% Lysine, 50mM Tris). Protein peptides were retrieved by washing with elution buffer (50 mM Tris), using a table-top centrifuge (10,000 g, 1 min).

Eluted peptides were lyophilized and dissolved in 2% formic acid prior to LC-MS/MS data acquisition. MS data were acquired using an Ultimate 3000 RSLC nano system (Thermo Scientific) coupled to an Exploris 480 (Thermo Scientific). Three technical replicates of each sample were measured. Peptides are first trapped in a pre-column (Dr. Maisch Reprosil C18, 3 µm, 2 cm × 100 µm) prior to separation on the analytical column packed in-house (Poroshell EC-C18, 2.7 µm, 50 cm × 75 µm), both columns were kept at 40 ˚C in the built-in oven. Trapping was performed for 10 min in solvent A (0.1% v/v formic acid in water), and the elution gradient profile was as follows: 0 – 10% solvent B (0.1% v/v formic acid in 80% v/v ACN) over 5 min, 13 - 44% solvent B over 37 min, 44-100% solvent B over 4 min, and finally 100% B for 4 min before re-equilibration in 100% A for 8 min. The mass spectrometer was operated in a data-dependent mode. Full-scan MS spectra were collected in a mass range of m/z 350 – 1,300 *Th* in the Orbitrap at a resolution of 60,000 after accumulation to an AGC target value of 1e6 with a maximum injection time of 50 ms. In-source fragmentation was activated and set to 15 eV. The cycle time for the acquisition of MS/MS fragmentation scans was set to 1 s. Dynamic exclusion properties were set to n = 1 and to an exclusion duration of 10 s. HCD fragmentation (MS/MS) was performed with a fixed normalized collision energy of 27% and the mass spectra acquired in the Orbitrap at a resolution of 30,000 after accumulation to an AGC target value of 1e5 with an isolation window of m/z = 1.4 *Th*.

Raw data were processed using the MaxQuant software [24] version 2.0.1.0 with standard settings applied. Briefly, the extracted peak lists were searched against the reviewed Human UniProtKB database (date 15-07-2021; 20353 entries), with an allowed precursor mass deviation of 4.5 ppm and an allowed fragment mass deviation of 20 ppm. Cysteine carbamidomethylation was set as static modification, and methionine oxidation, N-terminal acetylation as variable modifications (maximum 5 modifications per peptide allowed). Both LFQ quantification and "match between runs" were enabled. The iBAQ values in Figure S4B are approximate absolute abundances of the identified proteins derived by the normalization of the summed peptide intensities by the number of theoretically observable peptides for a given protein. Raw data

were processed using the MaxQuant software [24] version 2.0.1.0 with standard settings applied. Briefly, the extracted peak lists were searched against the reviewed Human UniProtKB database (date 15-07-2021; 20353 entries), with an allowed precursor mass deviation of 4.5 ppm and an allowed fragment mass deviation of 20 ppm. Cysteine carbamidomethylation was set as static modification, and methionine oxidation, N-terminal acetylation as variable modifications (maximum 5 modifications per peptide allowed). Both LFQ quantification and "match between runs" were enabled. The iBAQ values in Figure S4B are approximate absolute abundances of the identified proteins derived by the normalization of the summed peptide intensities by the number of theoretically observable peptides for a given protein.

Grid preparation

ER-vesicles were diluted in resuspension buffer to a concentration of 2–3 mg/mL and 2 µl were applied onto a glow-discharged lacey carbon grid (Quantifoil). 4 µl of BSA-conjugated gold beads (10 nm, UMC Utrecht) diluted in resuspension buffer without sucrose were added and mixed with the sample on grid. Grids were immediately blotted from the backside for 5–6 s and plunged into a mix of liquid ethane and propane using a manual plunger.

For the adherent cell lines (Hela and U2OS), cells were seeded on R2/2 holey carbon on gold grids (Quantifoil) coated with fibronectin in a Mattek dish and incubated for 24h. The suspension 293HEKF cells were grown to mid-log phase, and the cells were then directly pipetted onto glow discharged R2/1 Carbon on Copper grids (Quantifoil). Grids were immediately blotted from the back for 10s and plunged into liquid ethane propane mix using a manual plunger.

Lamella preparation

Lamellae were prepared using an Aquilos FIB-SEM system (Thermo Fisher Scientific). Grids were sputtered with an initial platinum coat (10 s) followed by a 10 s gas injection system (GIS) to add an extra protective layer of organometallic platinum. Samples were tilted to an angle of 15° to 22° and 12 µm wide lamellae were prepared. The milling process was performed with an ion beam of 30 kV energy in 3 steps: (*i*) 500 pA, gap 3 µm with expansion joints, (*ii*) 300 pA, gap 1 µm, (*iii*) 100 pA, gap 500 nm. Lamellae were finally polished at 30-50 pA with a gap of 200 nm.

Data acquisition

869 tilt series were acquired on a Talos Arctica (Thermo Fisher Scientific) operated at an acceleration voltage of 200 kV and equipped with a K2 summit direct electron detector and energy filter (Gatan). Images were recorded in movies of 7–8 frames at a target

defocus of 3 µm and an object pixel size of 1.72 Å. Tilt series were acquired in SerialEM (3.8) [25] using a grouped dose-symmetric tilt scheme [26] covering a range of ±54° with an angular increment of 3°. The cumulative dose of a series did not exceed 80 $e^-/Å^2$.

Lamella data used in this analysis has been collected in one session on a pool of grids of human cell lines. 27 tilt series were acquired on 6 different lamellae on a Talos Arctica (same instrument as above). Images were recorded in movies of 5-8 frames at a target defocus of 4 µm and an object pixel size of 2.17 Å. Tilt series were acquired in SerialEM using a grouped dose-symmetric tilt scheme covering a range of ±60° with a pre tilt of ±10° and an angular increment of 3°. The cumulative dose of a series did not exceed 70 e-/Å2.

Reconstruction and particle localization

Movie files of individual projection images were motion-corrected in Warp (1.0.9) [27] and combined into stacks of tilt series with the determined CTF parameters. The combined stacks were aligned using the gold fiducials in IMOD (4.10.25) [28]. Per-tilt CTF estimation for entire tilt series was performed in Warp and full deconvoluted tomograms were reconstructed by weighted back projection at a pixel size of 20 Å. Ice thickness was determined manually for a subset of 50 tomograms and results in an average thickness of 156 nm. Particle coordinates were determined by template matching against a reconstruction of a human 80S ribosome filtered to 40 Å and downsampled to match the tomogram pixel size (20 Å) using pyTOM (0.994) [29]. Most false positive hits were manually removed in pyTOM. The determined positions of ribosomes were used to extract subtomograms and their corresponding CTF volumes at a pixel size of 3.45 Å (2 × binned) in Warp. Movie files of individual projection images were motion-corrected in Warp [27] and combined into stacks of tilt series with the determined CTF parameters. The combined stacks were aligned using the gold fiducials in IMOD [28]. Per-tilt CTF estimation for entire tilt series was performed in Warp and full deconvoluted tomograms were reconstructed by weighted back projection at a pixel size of 20 Å. Ice thickness was determined manually for a subset of 50 tomograms and results in an average thickness of 156 nm. Particle coordinates were determined by template matching against a reconstruction of a human 80S ribosome filtered to 40 Å and downsampled to match the tomogram pixel size (20 Å) using pyTOM [29]. Most false positive hits were manually removed in pyTOM. The determined positions of ribosomes were used to extract subtomograms and their corresponding CTF volumes at a pixel size of 3.45 Å (2 × binned) in Warp.

Lamellae data were processed as above with slight variations. Movie files of individual projection images were motion- and CTF-corrected in Warp and combined into stacks of tilt series. The combined stacks were aligned using patch tracking in IMOD.

CTF estimation for entire tilt series was performed in Warp and full tomograms were reconstructed by weighted back projection at a pixel size of 17.36 Å. Ice thickness was determined manually and was found to be <200nm for all lamellae. Particle coordinates were determined by template matching against a reconstruction of a human 80S ribosome filtered to 40 Å using downsampled to match the tomogram pixel size (17.36 Å) pyTOM. The determined positions of ribosomes were used to extract subtomograms and corresponding CTF volumes at a pixel size of 8.68 Å (4 × binned) in Warp.

Subtomogram analysis

The extracted subtomograms were aligned in RELION (3.1.1) [30] using a spherical mask with a diameter of 300 Å against a reference of an 80S ribosome obtained from a subset of the same data. The extracted subtomograms were aligned in RELION (3.1.1) [30] using a spherical mask with a diameter of 300 Å against a reference of an 80S ribosome obtained from a subset of the same data. The aligned particles were refined in M (1.0.9) [15] using the reconstructions of the two half maps as a reference and a tight soft mask focused on the LSU at a pixel size of 3.45 Å. Particles were subjected to 2-3 rounds of refining image warp grid, particle poses, stage angles, volume warp grid, defocus and pixel size. After refinements, new subtomograms and their corresponding CTF volumes were extracted at a pixel size of 6.9 Å (4 × binned) and subjected to 3D classification (without mask, without reference, T=4 and classes=50) to sort out remaining false positives, poorly aligned particles and lone LSUs. The remaining 134,350 particles were used for subsequent focused classification steps to dissect ribosomal intermediate states or translocon-variants.

Classification of ribosomal intermediates

Ribosomal intermediate states were obtained by hierarchical classification focused on the rotation of the SSU and on the tRNA and elongation factor binding sites. First, all 134,350 particles were classified into classes of ribosomes with non-rotated and rotated SSU (with reference, with soft tight mask focused on SSU, T=4, classes=2). Subsequently, non-rotated and rotated particles were each subjected to two rounds of classification (with reference, with mask focused on tRNA and elongation factor binding site, T=10-20, classes=10-20). Classes with fragmented densities, such as pre/pre+, rotated-1/rotated-1+, non-rotated idle/translocation, were separated in the second round of classification (with reference, with mask focused on tRNA and elongation factor binding site, T=10-20, classes=2-4).

Classification of intermediate states was first performed for individual populations of ER translocon-bound or soluble ribosomes, which revealed similar results for

each population. However, to improve performance of classification, especially for translocon-associated populations with a low number of particles, we pooled all translocon and soluble populations and performed classification of intermediates on the entire data set. Subsequently, particle sets of individual intermediate states were dissected according to the translocon-associated and soluble ribosome populations.

The classification workflow was repeated 4 times to assess the technical uncertainties of 3D classification, which was determined at 5% to 15% and correlates inversely with class size. To assess experimental reproducibility, we combined two smaller data sets of ER-derived vesicles (31 tomograms, 6,101 particles; 58 tomograms, 3,836 particles) with the large data set (869 tomograms, 134,350 particles) and processed them as described above. After obtaining classes of intermediate states, particle numbers were determined for each data set and class.

The classification workflow was applied to *in situ* data with slight variations: Extracted subtomograms were used for 3D classification with image alignment against a low pass filtered 80S ribosome map as reference in RELION to exclude false positive. The remaining 5,818 ribosome subtomograms were refined in RELION and reextracted in Warp at a pixel size of 4.34 Å (2x binned). 2x-binned subtomograms were refined in RELION with a mask on the LSU prior to a first round of 3D classification without image alignment with a mask on the SSU to separate rotated from non-rotated ribosomes. A second round of classification was performed using a mask positioned on the tRNA and elongation factors sites, optimizing the mask extension and class number to this data in order to yield stable classes despite limited resolution and particle number. The different classes were finally subjected to iterative refinement in M.

Refinement of intermediate states

Classes of ribosomal intermediate states were simultaneously refined in M at a pixel size of 1.72 Å (unbinned) using tight masks focused on the entire 80S ribosome, tRNAs and elongation factors, which were individually generated for each intermediate. Refinement of image warp grid, particle poses, stage angles, volume warp grid, defocus and pixel size was performed iteratively (2-3 iterations). Globally or locally filtered and sharpened maps were generated by M and used for visualization or model building.

Single particle analysis

Suspension 293-F HEK cells were grown to mid log phase (0.5–1 $\times$ 10^6 cells/ml, 50 ml). Cells were pelleted at 500g for 5 min and washed twice in ice cold PBS and resuspended in 10 mM Hepes KOH, pH 7.5, 250 mM sucrose, 2 mM MgAc, 0.5 mM DTT, 0.5 mM PMSF, protease inhibitor tablets). Cells were lysed with 30 passages through

a 21-gauge needle. The lysate was cleared by centrifugation steps at 1,000g for 10 min, 1,500g for 15 min and 20,000g for 20 min. The final supernatant was loaded onto a 1 M sucrose cushion and spun at 300,000g for 1 h. The final ribosomal pellet was resuspended in lysis buffer and snap frozen in liquid nitrogen. For grid preparation, 3.5 µl of the ribosome preparation was pipetted onto glow discharged R3.5/1 2 nm C holey grids (Quantifoil) and blotted for 2.5 s at force 0 using a Vitrobot (Thermo Fisher Scientific) before subsequent plunging into liquid ethane.

Single particle cryo-EM data were acquired on a Titan Krios (Thermo Fisher Scientific) equipped with a cold FEG, Falcon 4i detector and Selectris X energy filter 10 eV slit at a pixel size of 0.729 Å/px. 17,000 movies were acquired with EPU 3 (Thermo Fisher Scientific) in EER format. A cumulative dose of 40 e-/Å^2 was used.

The data was processed in Relion 3.1.1. Movies were motion-corrected and CTF was estimated. Particles were picked with the logpicker and reconstructed at a pixel size of 6 Å/px for subsequent 2D classification, followed by 3D classification with image alignment to exclude false-positive and low-quality particles. 66,000 particles were then subjected to 3D classification without image alignment using a mask on the A-tRNA site and the GTPase center. 19,000 particles were selected in a class corresponding to the classical PRE+ state, refined, re-extracted at 1.0 Å/px and refined again. CtfRefine was performed followed by another round of refinement. Masks on the A tRNA site and elongation factor, as well as on the peptidyl transferase center were used for particle subtraction and focused refinements to improve the quality of the maps in these regions.

For model building, a previous crystallographic structure of eEF1A in the extended GDP bound conformation (PDB 4c0s) was used as starting model and was first briefly refined in real space in the higher resolution crystallographic electron density map using Isolde and phenix refine, in order to improve the starting geometry of the model. The resulting model was then refined in our map through iterative cycling between phenix refine [31], Isolde [32] and Coot [33]. The model was validated using Coot [33] and Molprobity [34].

Polysome analysis

For the neighborhood analysis, ribosome positions and orientations were read from the RELION star files resulting from subtomogram alignment in a python script (Python 3.8.11, Numpy 1.20.3, Scipy 1.7.1). For each ribosome we determined distance vectors between itself and its n closest neighbors (n=4), excluding neighbors further than 100 Å. The vectors were rotated with the inverse orientation of the respective ribosome, resulting in the coordinates of neighbors in the coordinate system of an ER-

bound ribosome with the xy-plane corresponding to the ER membrane. These vectors were sampled on a 3D-histogram with voxels corresponding to 15^3 Å^3 and divided by the total number of analyzed neighbors to indicate the probability of finding a neighboring ribosome particle in each voxel. The plots were projected on the xy-plane to visualize the density of neighbors surrounding ER-bound and soluble ribosomes.

A threshold was chosen to identify clusters for trailing and leading neighbors. For ER-bound neighbors a binary mask was created in the 3D-histogram above a probability of p=0.0005, while for soluble ribosomes the threshold was put at p=0.0003. Both masks were dilated by 2 voxels. The soluble and ER-bound trailing masks were combined in a trailing mask for the whole dataset, and the same procedure was performed for the leading mask. The masks were used to annotate associations of ribosome pairs in a polysome. A trailing/leading connection was confirmed if the neighbor localized in the trailing/leading mask area and the analyzed ribosome also positioned in the leading/trailing area of the respective neighbor (i.e., the inverse calculation).

The trailing/leading states of neighbors were used in R to fit a multinomial mixed-effects logistic regression model (mclogit 0.9.4.2 [35] in R 3.6.1). The ribosome's state was used to predict probabilities of leading and trailing states, where the tomogram index was used as a random effect to account for sample and imaging variation. We used the same model to predict probabilities of translation states in polysome chains. For visualization, the probabilities were extracted with their 95% confidence interval, representing the region of 95% certainty that the modeled mean is the population mean. Variation between tomograms was shown by calculating the frequency of certain events per tomogram, e.g., the 42nd tomogram might have 7 Pre+ ribosomes of which 6 are associated in polysomes resulting in a frequency of 0.86. Random association probability was calculated by fractional abundance of each state in the dataset. For the plots showing the fold-increase, the modeled mean and confidence interval lower and upper bounds were divided by the random association probability and displayed with logarithmic y-axis. Statistical significance for the fitted logistic parameters was determined with a two-sided Wald-test (as reported by mclogit) and used to annotate plots. P-values were adjusted for multiple comparisons with the Hochberg method as implemented in R with p.adjust (method='hochberg').

Data availability

Data generated in this study are available in the main article, supplementary materials or in public repositories: nos. EMD-15871, EMD-15872, EMD-15873, EMD-15874, EMD-15875, EMD-15876, EMD-15877, EMD-15878, EMD-15879, EMD-15880, EMD-15893 of EMDB and PDB-8B6Z of PDB.

The mass spectrometry proteomics data have been deposited to the ProteomeXchange Consortium via the PRIDE[36] partner repository with the dataset identifier PXD035475.

In addition, we made use of a previously published atomic models from the PDB (accession codes 5AJO, 4CXG, 4UJE, 6Y0G, 6Y57, 6GZ5, 6Z6L, 6Z6M, 5LZS, 4C0S, 5LZT, 5IZK, 6O85, 5LZZ, 6GZ3, 6GZ4, 6GZ5, 6SXO, 1BN5, 6W6L, 6ENY, 6S7O, 3JC2). Moreover, we used the following EM densities from the EMDB for analyses: EMDB-2904, EMDB-2908.

Code availability

Python-code for polysome analysis is available at https://github.com/McHaillet/polysome-stats.

Acknowledgements

This work was supported by the European Research Council under the European Union's Horizon2020 Program (ERC Consolidator Grant Agreement 724425 - BENDER) and the Nederlandse Organisatie voor Wetenschappelijke Onderzoek (Vici 724.016.001 to FF, Veni 212.152 to JF, and National Roadmap for Large-Scale Research Infrastructure (NEMI) 184.034.014). We thank Gijs van der Schot, Mihajlo Vanevic, and Robert Englmeier for help with data processing, as well as Rutger Hermsen for advice on statistical analysis. We are grateful to Stefan Pfeffer, Bert Janssen, Matthias Feige, Emmanuelle Schmitt, Yves Mechulam, Sven Lang, and Richard Zimmermann for stimulating discussions and critical comments on the manuscript.

Author contributions

M.G, J.F. and F.F. conceived the project. M.G. performed microsome sample preparation, cryo-ET data acquisition and image analysis, M.G. and J.F. carried out model building. M.C. analysed polysomes. J.v.L., S.C.H. and J.F. performed *in situ* cryo-ET of human cells. D.V., M.G., P.A. and R.S. analysed samples using mass-spectrometry. J.F. performed cryo-EM SPA sample preparation and data processing, F.A.K. and A.K. collected cryo-EM SPA data. M.G., M.C., J.F. and F.F. analysed the data and wrote the manuscript.

Competing interests

Abhay Kotecha and Fujiet A. Koh are employees of Thermo Fisher Scientific. The other authors declare no competing interests.

Supplementary figures

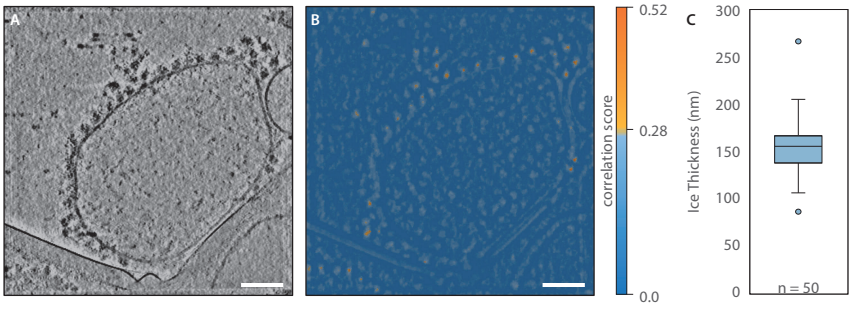

Supplementary Fig. 1: Cryo-tomogram of ER-derived vesicles from HEK-293 cells. (A) 2D slice (thickness 2.0 nm) of a representative tomogram. The scalebar corresponds to 100 nm. (B) PyTom correlation scores resulting from template matching [37]. Particles with scores of 0.28-0.56 were selected for subsequent subtomogram analysis. Scores are color-coded as indicated. (C) Distribution of ice thickness of n = 50 randomly selected tomograms. Median thickness (156 nm) is indicated, the box defines the lower (138 nm) and upper (167 nm) quartile, whiskers define the minimum (106 nm) and maximum (206 nm) thickness. Outliers are indicated.

► **Supplementary Fig. 2: Cryo-ET data analysis workflow**. Template matching in PyTom [37] generates candidates for ribosomal particles, which are further analyzed in RELION [30] and M [15]. Initial coarse 3D classification allowed removal of false positives, poorly aligned particles, and isolated LSUs. (A) The remaining ~135,000 80S ribosome subtomograms were subjected to focused classification on the area at the ribosomal tunnel exit (mask 1). Repeated classification is required to distinguish subtle differences of Sec61-multipass-, Sec61-multipass-TRAP translocon, and Sec61-TRAP. (B) The center of the reconstruction of the ribosome-Sec61-TRAP-OSTA population was shifted to the center of the translocon. After refinement, recentered subtomograms were subjected to 3D classification focused on a luminal mask near OSTA (mask 4). (C) To obtain the best statistics for analysis of ribosomal processing states all subtomograms were pooled again. The particles were hierarchically classified, first according to the rotation state of the SSU (mask 2) and then further focused using masks including the tRNA and eEF binding sites (mask 3). A minor population of <2k particles could not be assigned unambiguously to a translation state (ND = not defined). (D) Previously annotated particles from classification focused on the translocon (A) were extracted from classes obtained by classification of ribosomal intermediate states (C).

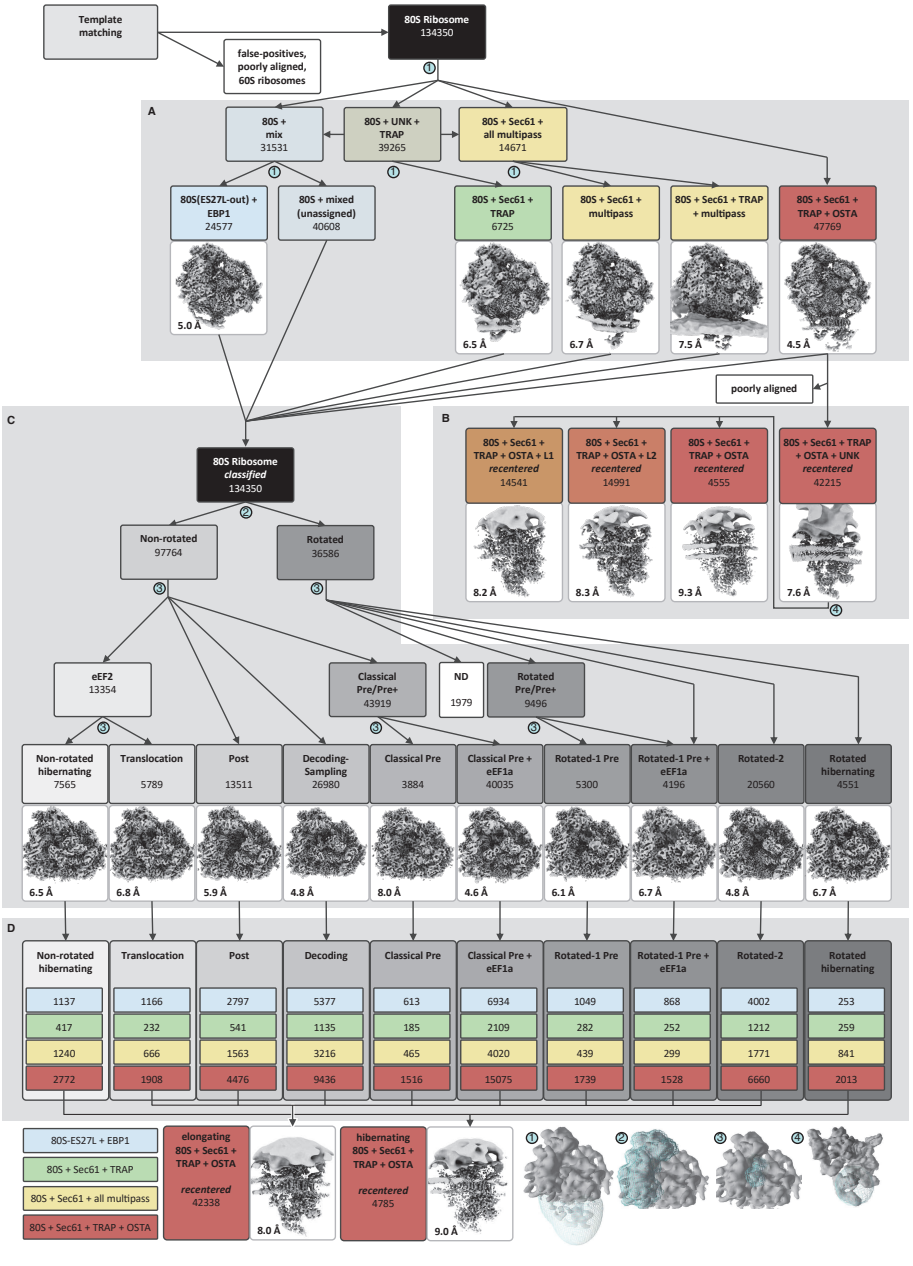

Supplementary Fig. 2: Cryo-ET data analysis workflow. See previous page for caption.

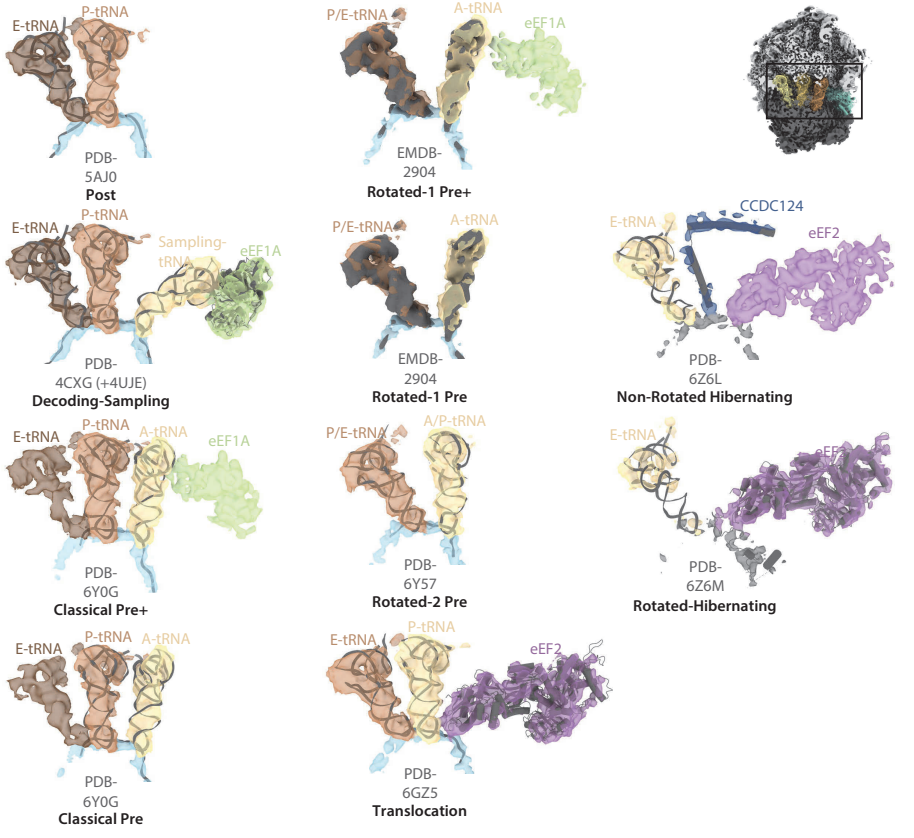

Supplementary Fig. 3: Identification of ribosomal intermediate states. Large ribosomal subunits of models or maps of previously characterized intermediate states were fitted into our reconstructions from Fig. 2, of which we only show the tRNAs and elongation factors for clarity. Structures of mRNAs, tRNAs, elongation factors and the small ribosomal subunit from the models indicated by their PDB or EMDB codes are superposed onto the respective segmented densities from our reconstructions.

► **Supplementary Fig. 4: Neighborhood analysis of ER membrane-bound and soluble ribosomes and their intermediate states.** (A) Side view (top panels) and top view (bottom panels) of filtered reconstructions of ER-membrane bound, soluble and hibernating ribosome populations depicted at low contour level. Densities of leading and trailing ribosome neighbors are visible adjacent to the centered ribosome. (B) Neighborhood analysis illustrates the arrangement of ribosomes and is consistent with the subtomogram averages from (A). Neighborhood analysis was performed in 3D, whereas 2D heat maps show the results projected onto a plane parallel to the membrane. (C) Masks were generated in 3D from results of the neighborhood analysis of membrane-bound and soluble populations combined. (D) Columns represent the modelled mean neighbor probability with 95% confidence interval as error bars analysis based on the neighborhood analysis from (B,C) for each ribosomal intermediate state. Statistics determined from n = 132,371 ribosomes with the 869 tomograms included as a random effect. The random association probability (gray hatched bars) is the overall abundance of the ribosome populations. (E) Columns represent the mean logarithmic fold increase of observed vs. random probability with 95% confidence interval as error bars of the data from (D).

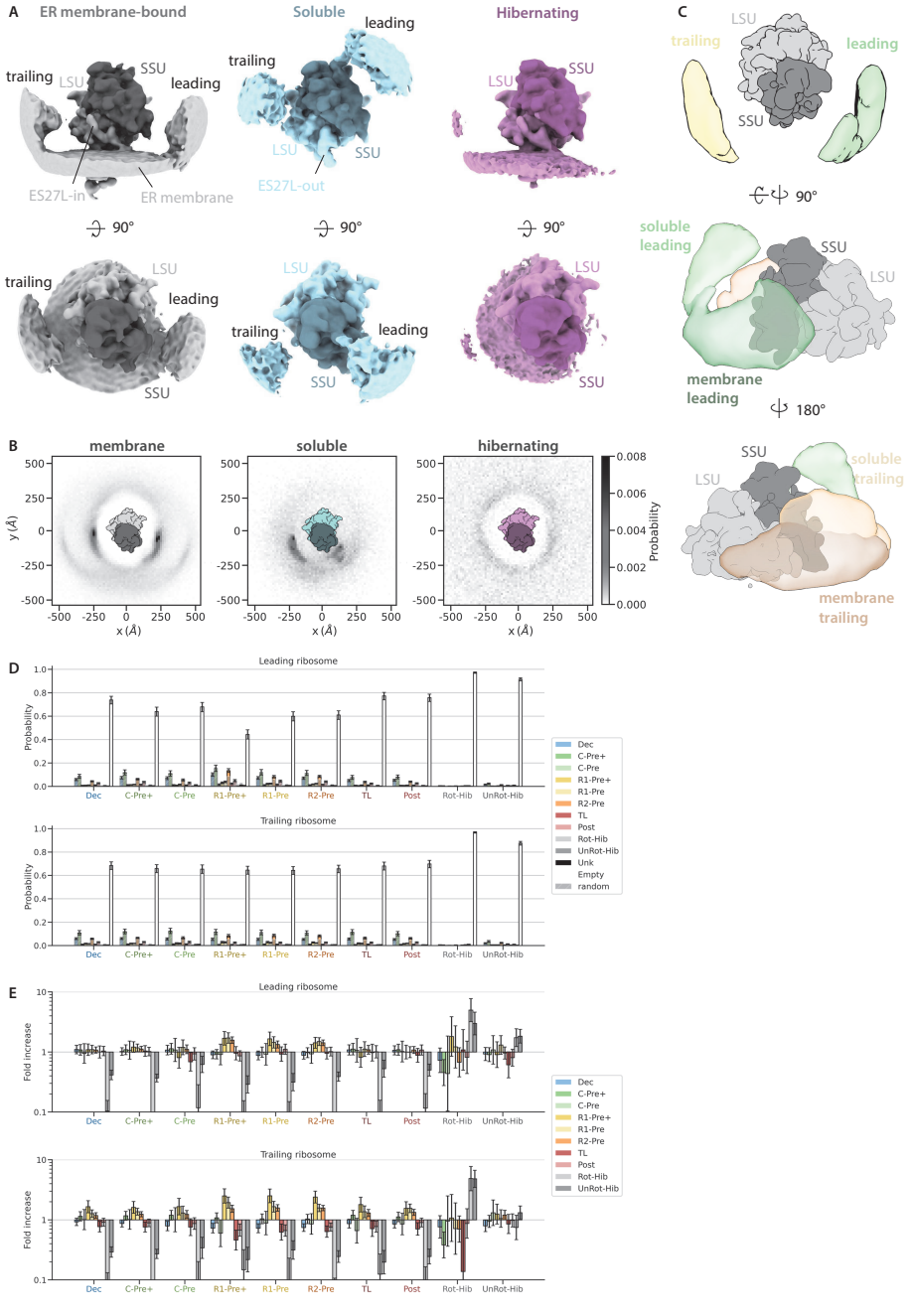

Supplementary Fig. 4: Neighborhood analysis of ER membrane-bound and soluble ribosomes and their intermediate states. See previous page for caption.

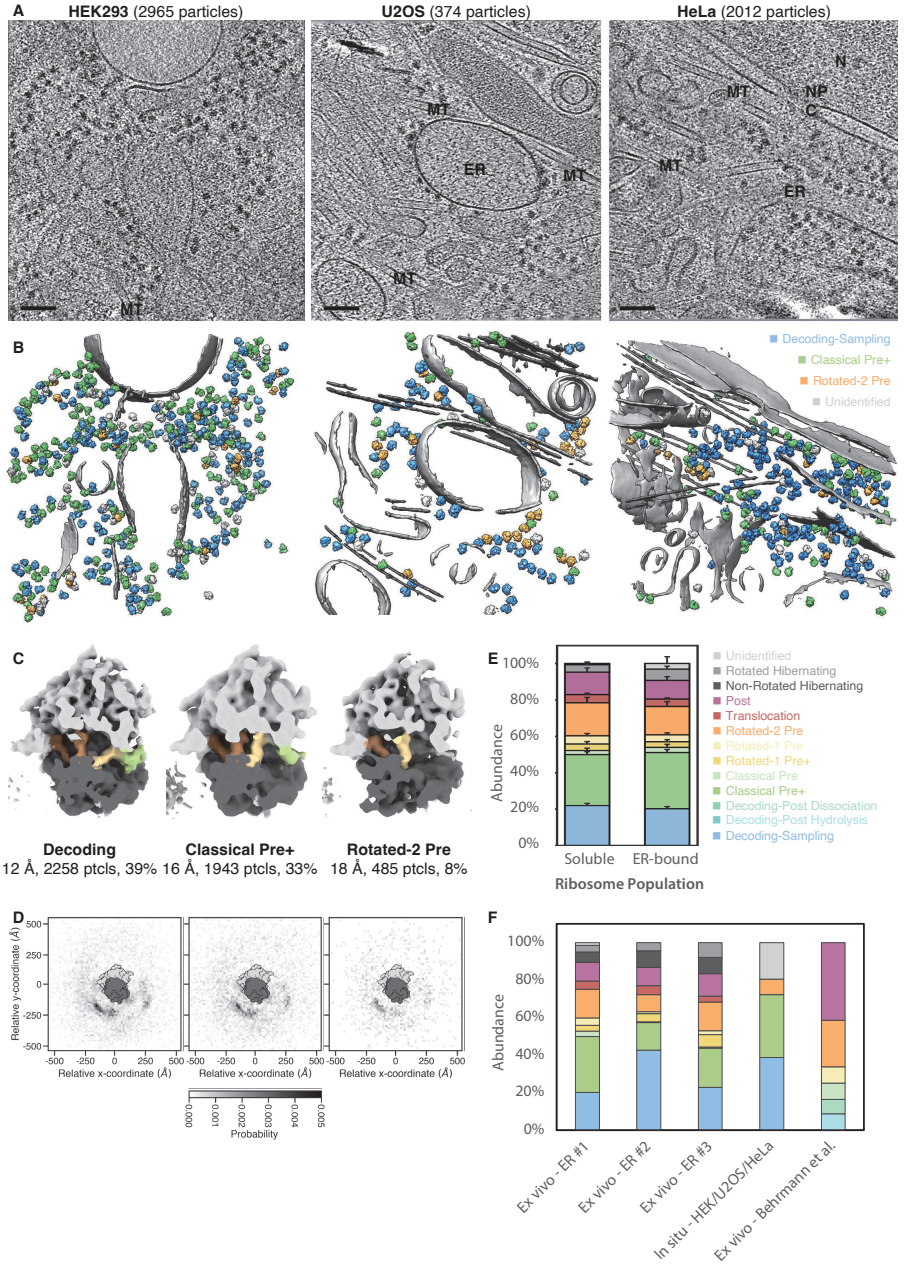

Supplementary Fig. 5: Ribosome states *in situ* and comparison to *ex vivo* abundances. See next page for caption.

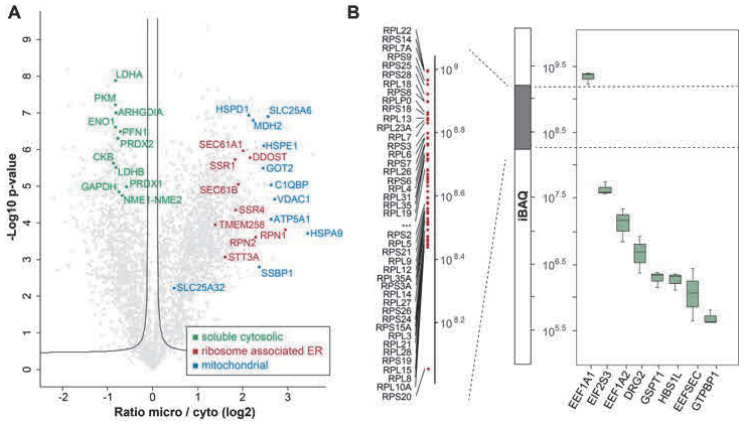

Supplementary Fig. 6: Proteomics characterization of microsome preparation. (A) Enrichment of ribosome-associated ER and mitochondrial proteins and depletion of cytosolic proteins when comparing microsome enriched samples to cytosolic supernatant. The y-axis of the volcano plot was made using a two-sided T-test, where the false positive rate was controlled to 5% based on 250 randomizations of the data. (B) Dynamic range of the detected absolute abundances for the measured proteome (central bar labeled with intensity-based quantification, iBAQ). Ribosomal proteins occupy a narrow band of absolute abundances (left bar). Among ribosome-binding GTPases, eEF1a the most abundant (right boxplot). Data points show n=3 technical replicates of 1 experiment. Median of logarithmic of IBAQ values is indicated, the box represents lower and upper quartile, whiskers represent minimum and maximum.

◄ **Supplementary Fig. 5: Ribosome states *in situ* and comparison to *ex vivo* abundances.** (A) Central slice (thickness 1.7 nm) of representative tomograms of cryo-FIB milled HEK293, U2OS and HeLa cells. Scale bar: 100 nm. (B) Segmented representation of tomograms from (A). Subtomogram averages of the ribosome were mapped back into the reconstruction and color-coded according to their ribosomal state. (C) Ribosomal states obtained by 3D classification of *in situ* data. (D) Neighborhood analysis of the intermediate states from (C). (E) Distribution of ribosomal states from soluble or membrane-bound ribosomes. Statistics determined from n = 132,371 ribosomes with 869 tomograms modeled as random effect. Stacked columns show the modelled mean with the 95% confidence interval as error bars. (F) Distribution of ribosomal states from 3 separate ER vesicles preparations (*ex vivo* - ER #1-3), *in situ* data, and cytosolic polysomes from Behrmann et al [14]. n(ER #1) = 132,731 particles in 869 tomograms, n(ER #2) = 6,101 particles in 31 tomograms, n(ER #3) = 3,836 particles in 58 tomograms, each from 1 experiment, n(in situ) = 5,351 (HEK293 = 2,965, U2OS = 374, HeLa = 2,012) particles in 27 tomograms from 3 independent experiments.

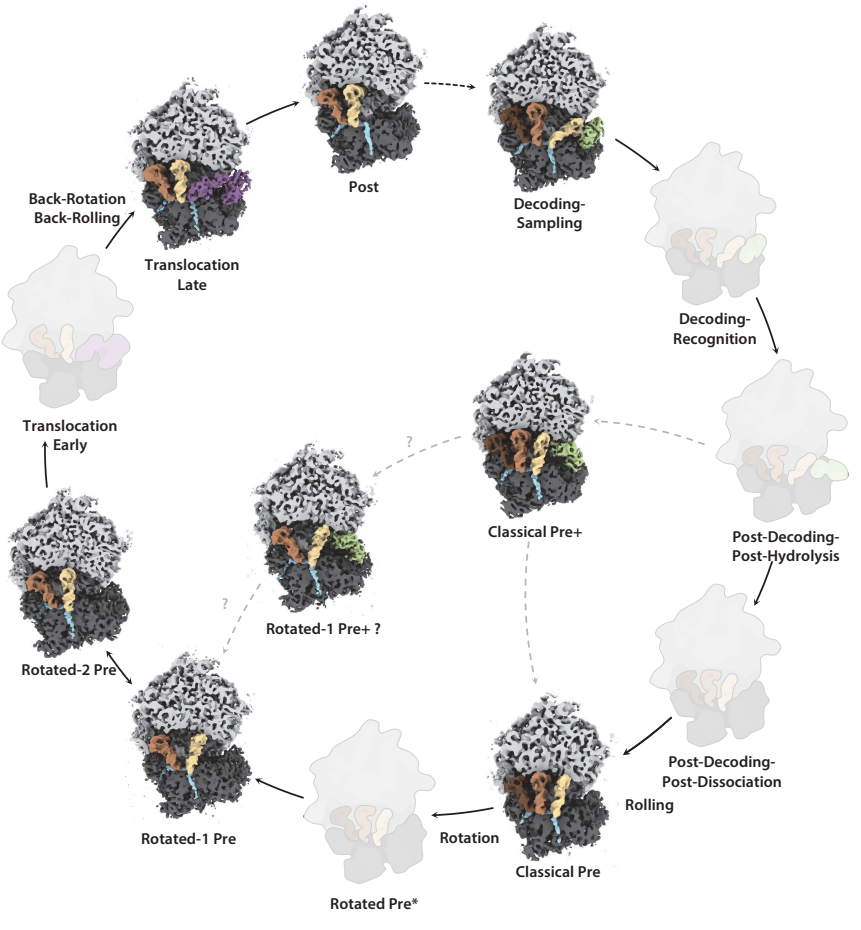

Supplementary Fig. 7: Observed active intermediates in the context of the complete model of human elongation cycle. Different from Figure 1D all observed ribosomal states are positioned in a model recapitulating structurally characterized states beyond the most abundant ones detected in our study. States that are not detected are grayed out. The solid arrows indicate the cycle from [14], while the transitions to states only detected in our study are broken lines. The Rotated-1 Pre+ state had not been assigned in Fig. 2 due to its missing support from *in situ* data.

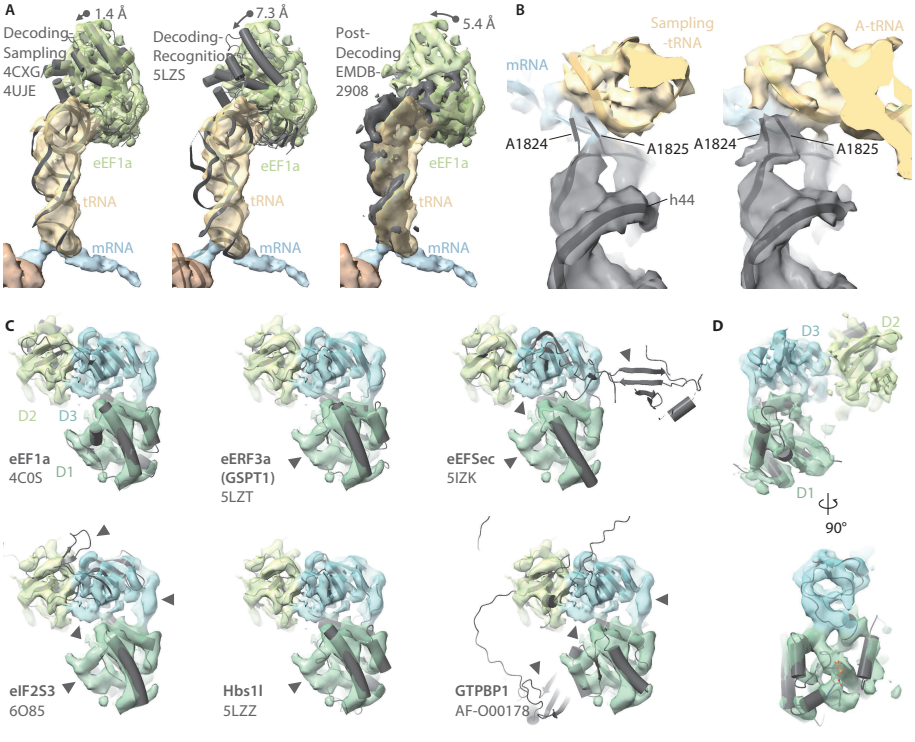

Supplementary Fig. 8: Identification of elongation factor-bound ribosomal intermediate states. (A) Superposition of the decoding-sampling (4CXG+4UJE), decoding-recognition (5LZS) and post-decoding (EMDB-2908) state (dark grey cartoon representations) onto our reconstruction (semi-transparent colored maps) of the ribosome-bound eEF1a-tRNA ternary complex. Arrows indicate structural differences. (B) Close-up of the decoding center of the decoding-recognition state (5LZS) superposed onto our segmented reconstructions (semi-transparent maps) of our decoding state (left) or the subsequent classical pre state (right) for comparison. Densities of the nucleobases A1824 and A1825 are clearly visible in the flipped-out conformation in the classical pre state (right) but flipped-in in the decoding state (left), indicating that tRNA recognition has not yet occurred. tRNA, mRNA, and 18S rRNA segment h44 were segmented and tRNAs were clipped for better overview. (C) Comparison of eEF1a and structurally related candidates fitted into the segmented density of the classical pre+ state. Arrowheads indicate structural differences. (D) Structure of eEF1A in extended conformation (4C0S) fitted into the segmented density of the classical pre+ state. Domain 1, 2 and 3 (D1-3) were fitted individually.

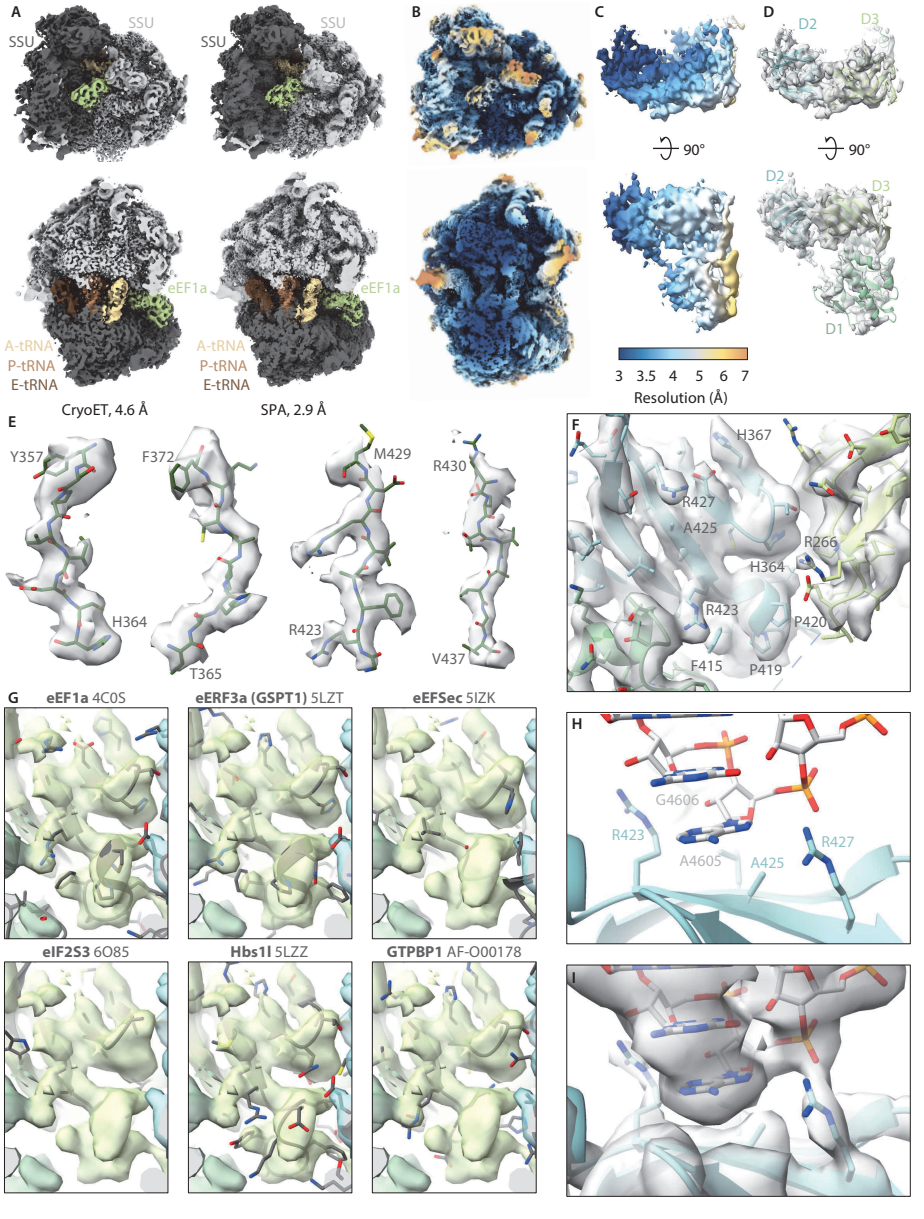

Supplementary Fig. 9: Single particle analysis of the ribosome in the classical pre+ state. (A) Comparison of cryo-ET and SPA reconstructions of the ribosome in the classical pre+ state filtered to local resolution. Ribosomes were clipped in top views (bottom panels). (B) SPA reconstruction color-coded according to local resolution. (C) Close-up view of eEF1a color-coded according to local resolution explained in the colorbar. (D) Refined atomic model of eEF1a placed into the SPA density map. Domains 1-3 (D1-3) are indicated. (E) Segments of eEF1a superposed on density maps with well-resolved side chains. (F) Refined model of eEF1a fitted into the locally refined reconstruction of domain 3. The SRL is not depicted for clarity. (G) Candidate GTPases fitted into the high-resolution density. The SRL binding site of domain 3 is displayed. (H) Interaction site of eEF1a with the SRL of the LSU. (H) Same view as in (H) with the density map.

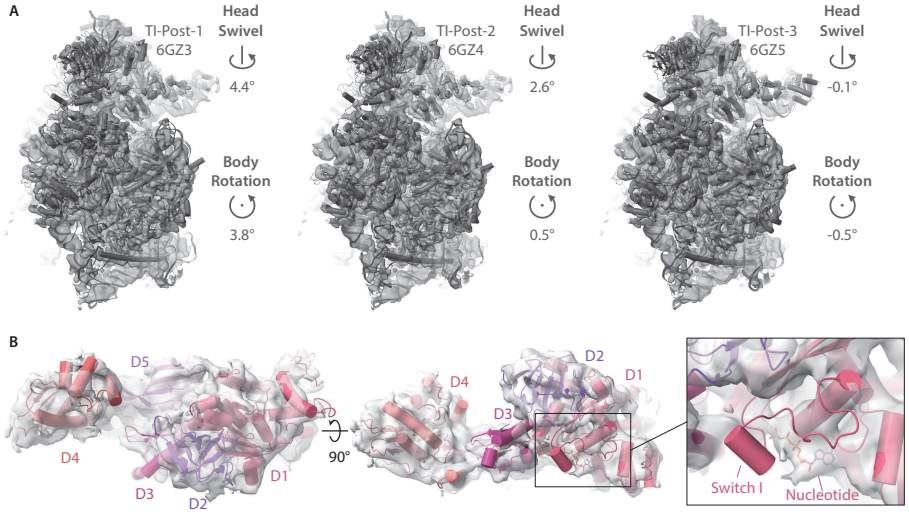

Supplementary Fig. 10: Identification of elongation factor-bound ribosomal translocation intermediate states. (A) Large ribosomal subunits of the TI (translocation intermediate)-Post-1 (6GZ3), TI-Post-2 (6GZ4) and TI-Post-3 (6GZ5) states were fitted into our reconstruction of the 'translocation' intermediate from Fig. 2 and the structure of the small ribosomal subunit was superposed onto our reconstruction. Rotational differences of the SSU head and body with respect to our reconstruction are indicated. (B) Domains of eEF2 (6GZ5) fitted into the translocation intermediate. Domains D1, D2, D4 and D5 fit well into the reconstruction, domain D3 is positioned slightly differently. The switch I loop is disordered in our reconstruction indicating a GDP-bound state.

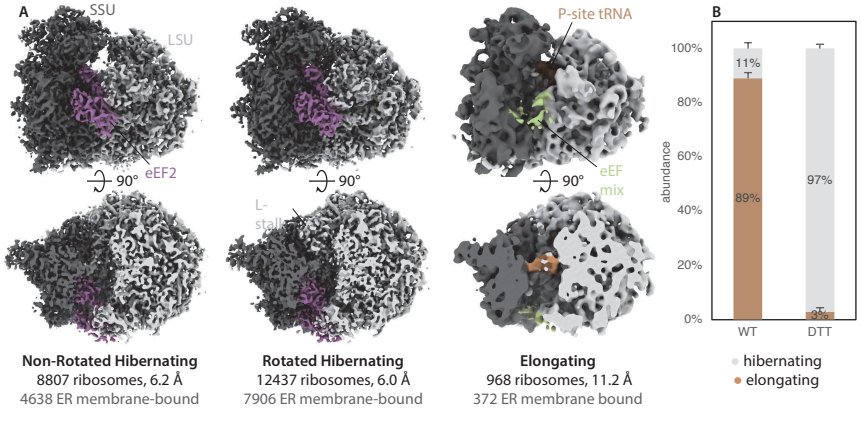

Supplementary Fig. 11: Cryo-ET analysis of ER membrane-bound ribosomes obtained from stressed cells. (A) Side views (top row) and top views (bottom row) of intermediate states of soluble and ER membrane-associated ribosomes under condition of oxidative stress. (B) Abundance of elongating and hibernating ER membrane-bound ribosomes in WT and DTT-treated vesicles. n(WT) = 132,371 particles in 869 tomograms from 1 experiment, n(DTT) = 26,512 particles in 212 (174 and 38) tomograms from 2 independent experiments. Stacked columns show the modelled mean with the 95% confidence interval as error bars.

Supplementary tables

Supplementary table 1: Cryo-EM data collection, refinement and validation statistics of ribosome and translocon classes.

	#1 Decoding-Sampling State (EMDB-15871)	#2 Classical Pre+ State (EMDB-15872)	#3 Classical Pre State (EMDB-15873)	#4 Rotated-1 Pre+ State (EMDB-15874)	#5 Rotated-1 Pre State (EMDB-15875)
Data collection and processing					
Magnification	79000	79000	79000	79000	79000
Voltage (kV)	200	200	200	200	200
Electron exposure (e–/Å^2)	<80	<80	<80	<80	<80
Defocus range (μm)	3	3	3	3	3
Pixel size (Å)	1.724	1.724	1.724	1.724	1.724
Symmetry imposed	-	-	-	-	-
Initial particle images (no.)	134350	134350	134350	134350	134350
Final particle images (no.)	26980	40035	3884	4196	5300
Map resolution (Å) FSC threshold	4.8 0.143	4.6 0.143	8.0 0.143	6.7 0.143	6.1 0.143
Map resolution range (Å)	3.6-51.7	3.6-34.5	4.3-51.7	4.3-51.7	4.1-51.7

Supplementary table 1 continued.

	#6 Rotated-2 Pre State (EMDB-15876)	#7 Translocation State (EMDB-15877)	#8 Post State (EMDB-15878)	#9 Non-Rotated Hibernating State (EMDB-15879)	#10 Rotated Hibernating State (EMDB-15880)
Data collection and processing					
Magnification	79000	79000	79000	79000	79000
Voltage (kV)	200	200	200	200	200
Electron exposure (e–/Å^2)	<80	<80	<80	<80	<80
Defocus range (μm)	3	3	3	3	3
Pixel size (Å)	1.724	1.724	1.724	1.724	1.724
Symmetry imposed	-	-	-	-	-
Initial particle images (no.)	134350	134350	134350	134350	134350
Final particle images (no.)	20560	5789	13511	7565	4551
Map resolution (Å) FSC threshold	4.8 0.143	6.8 0.143	5.9 0.143	6.5 0.143	6.7 0.143
Map resolution range (Å)	3.6-51.7	3.6-51.7	3.6-51.7	4.3-51.7	4.1-51.7

Supplementary table 1 continued.

	#11 SPA reconstruction Classical Pre+ State (EMDB-15893) (PDB-8B6Z)
Data collection and processing	
Magnification	
Voltage (kV)	300
Electron exposure (e–/Å^2)	40
Defocus range (μm)	
Pixel size (Å)	0.729
Symmetry imposed	-
Initial particle images (no.)	66041
Final particle images (no.)	19046
Map resolution (Å) FSC threshold	2.9 0.143
Map resolution range (Å)	2.3-22.7
Refinement	
Initial model used (PDB code)	4C0S
Model resolution (Å) FSC threshold	3.2 0.5
Model resolution range (Å)	-
Map sharpening B factor (Å^2)	0
Model composition Non-hydrogen atoms Protein residues Ligands (RNA)	 3581 442 8
B factors (Å^2) Protein Ligand (RNA)	 47.78 51.17
R.m.s. deviations Bond lengths (Å) Bond angles (°)	 0.002 0.505
Validation MolProbity score Clashscore Poor rotamers (%)	 0.70 0.59 0.27%
Ramachandran plot Favored (%) Allowed (%) Disallowed (%)	 98.64% 1.36% 0%

Supplementary table 2: Most abundant proteins determined by mass-spectrometry analysis of ER-derived microsomes and its supernatant from HEK293 cells. Full dataset deposited on PRIDE database with identifier PXD035475.

Protein IDs	Gene names	iBAQ supernatent	iBAQ microsomes	Category
P63261	ACTG1	4.8E+09	8.39E+09	
A0A0G2JIW1	HSPA1B	7.3E+09	3.46E+09	
P68104	EEF1A1	3.5E+09	2.47E+09	translation factor
P10809	HSPD1	1.2E+07	4.96E+09	mitochondrial
P62937	PPIA	3.2E+09	1.36E+09	
Q8N257	HIST3H2BB	1.3E+08	4.57E+09	
P06733	ENO1	3.6E+09	6.19E+08	
P61604	HSPE1	1.3E+07	4.26E+09	mitochondrial
K7ERI7	RPL22	6.4E+08	9.87E+08	ribosomal
P68363	TUBA1B	2.7E+09	5.48E+08	
A0A5F9ZHM4	LDHB	2.6E+09	4.39E+08	
P46781	RPS9	4.8E+08	9.25E+08	ribosomal
P07900	HSP90AA1	2.5E+09	4.31E+08	
Q5JR95	RPS8	5.8E+08	7.9E+08	ribosomal
Q06830	PRDX1	1.9E+09	5.66E+08	
P62263	RPS14	5.8E+08	9.9E+08	ribosomal
P68371	TUBB4B	2.2E+09	4.16E+08	
P04406	GAPDH	1.7E+09	3.83E+08	
P62424	RPL7A	3.7E+08	9.85E+08	ribosomal
P14625	HSP90B1	2.6E+08	2.17E+09	ER-resident
P23396	RPS3	4.7E+08	6.28E+08	ribosomal
Q71DI3	HIST2H3A	0	2.35E+09	
G3V203	RPL18	2.1E+08	7.91E+08	ribosomal
C9J9K3	RPSA	4.2E+08	5.48E+08	ribosomal
P62701	RPS4X	4.8E+08	6.59E+08	ribosomal
Q71UI9	H2AFV	4.2E+07	2.1E+09	
P05388	RPLP0	4.2E+08	7.3E+08	ribosomal
P18124	RPL7	2.7E+08	6.76E+08	ribosomal
P26641	EEF1G	1.2E+09	6.97E+08	translation factor
Q02878	RPL6	3.6E+08	6.08E+08	ribosomal
P62857	RPS28	3.6E+08	8.35E+08	ribosomal
P08670	VIM	1.2E+09	7.93E+08	
M0QZC5	RPS11	5E+08	5.15E+08	ribosomal
P07737	PFN1	1.6E+09	2.8E+08	
P62899	RPL31	2.5E+08	5.4E+08	ribosomal
P62269	RPS18	2.4E+08	7.19E+08	ribosomal
Q16777	HIST2H2AC	1.5E+07	1.73E+09	
P62753	RPS6	2.8E+08	5.76E+08	ribosomal
P11021	HSPA5	5.5E+07	1.65E+09	ER-resident
Q5VVC8	RPL11	2.8E+08	4.79E+08	ribosomal
P62081	RPS7	3.5E+08	6.06E+08	ribosomal
Q07021	C1QBP	1950200	1.68E+09	mitochondrial
P62244	RPS15A	3.1E+08	3.23E+08	ribosomal
P36578	RPL4	2.8E+08	5.39E+08	ribosomal
C9JXB8	RPL24	2.3E+08	4.48E+08	ribosomal
P62851	RPS25	1.1E+08	8.96E+08	ribosomal
P12277	CKB	1.4E+09	2.15E+08	
P16403	HIST1H1C	4E+07	1.46E+09	
Q04837	SSBP1	0	1.6E+09	mitochondrial
P46776	RPL27A	2.6E+08	4.4E+08	ribosomal
B5MDF5	RAN	1.1E+09	3.54E+08	
P23284	PPIB	3.3E+07	1.44E+09	ER-resident

Supplementary table 2 continued

Protein IDs	Gene names	iBAQ supernatent	iBAQ microsomes	Category
Q15084	PDIA6	4.7E+07	1.45E+09	ER-resident
E7ETK0	RPS24	2.6E+08	3.25E+08	ribosomal
P62249	RPS16	2.7E+08	4.26E+08	ribosomal
P25705	ATP5A1	0	1.49E+09	mitochondrial
P62277	RPS13	2.4E+08	4.8E+08	ribosomal
P06576	ATP5B	0	1.44E+09	
P26373	RPL13	1.6E+08	7E+08	ribosomal
E9PK54	HSPA8	8.7E+08	4.36E+08	
Q59GN2	RPL39P5	1.7E+08	8.66E+08	ribosomal
P21796	VDAC1	0	1.42E+09	mitochondrial
B8ZZQ6	PTMA	1.2E+09	1.33E+08	
P35232	PHB	0	1.42E+09	
A0A2R8Y6J3	RPL5	2.7E+08	3.93E+08	ribosomal
P12236	SLC25A6	0	1.39E+09	mitochondrial
P40429	RPL13A	2.3E+08	4.81E+08	ribosomal
P08238	HSP90AB1	1.1E+09	1.97E+08	
P27797	CALR	7.8E+07	1.24E+09	ER-resident
P61956	SUMO2	6.3E+08	6.46E+08	
P46778	RPL21	2.7E+08	2.97E+08	ribosomal
P63244	GNB2L1	2.6E+08	3.6E+08	
F8VZJ2	NACA	7.1E+08	3.43E+08	
P13639	EEF2	8.3E+08	2.39E+08	translation factor
P05387	RPLP2	2.5E+08	4.79E+08	ribosomal
P42677	RPS27	2.4E+08	4.66E+08	ribosomal
P25398	RPS12	2.2E+08	4.28E+08	ribosomal
P0CG48	UBC	5.7E+08	5.31E+08	
P62805	HIST1H4A	0	1.23E+09	
J3KPX7	PHB2	0	1.24E+09	
P60174	TPI1	1E+09	1.57E+08	
P60842	EIF4A1	6.6E+08	3.27E+08	translation factor
D6RAN4	RPL9	2.8E+08	3.77E+08	ribosomal
P23528	CFL1	7.1E+08	5.13E+08	
H0Y8D1	PRSS1	0	2.51E+08	
J3QRI7	RPL26	1.2E+08	5.81E+08	ribosomal
P62829	RPL23	2.1E+08	4.45E+08	ribosomal
P07437	TUBB	9.9E+08	1.99E+08	
P38646	HSPA9	0	1.21E+09	mitochondrial
E7EQV9	RPL15	1.3E+08	2.81E+08	ribosomal
E7EPB3	RPL14	1.1E+08	3.38E+08	ribosomal
P15880	RPS2	2E+08	4.11E+08	ribosomal
A0A3B3ITT5	RPL29	1.7E+08	4.78E+08	ribosomal
P61353	RPL27	1.4E+08	3.31E+08	ribosomal
P10599	TXN	9.5E+08	1.51E+08	
P13667	PDIA4	3.2E+07	1.1E+09	ER-resident
H7BY10	RPL23A	8.6E+07	6.92E+08	ribosomal
P30050	RPL12	1.5E+08	3.63E+08	ribosomal
P00338	LDHA	9.6E+08	1.53E+08	
P39023	RPL3	2E+08	3.11E+08	ribosomal
P61247	RPS3A	1.8E+08	3.51E+08	ribosomal
P62917	RPL8	1.3E+08	2.79E+08	ribosomal
P40926	MDH2	1282100	1.09E+09	mitochondrial
Q8WVC2	RPS21	2.3E+08	3.8E+08	ribosomal
P18077	RPL35A	1.9E+08	3.56E+08	ribosomal
P84098	RPL19	1.1E+08	5.22E+08	ribosomal

Supplementary table 2 continued

Protein IDs	Gene names	iBAQ supernatent	iBAQ microsomes	Category
P53999	SUB1	5.3E+08	4.42E+08	
P07237	P4HB	2.9E+07	9.45E+08	ER-resident
P30101	PDIA3	1.7E+07	9.46E+08	ER-resident
P14618	PKM	8.1E+08	1.01E+08	
P51149	RAB7A	6.2E+07	8.66E+08	
P17066	HSPA6	5.5E+08	3.24E+08	
K7ELL7	PRKCSH	4.9E+07	8.59E+08	
P16989	YBX3	2E+08	2.94E+08	
H0YMF4	RPL28	1.7E+08	2.91E+08	ribosomal
Q562R1	ACTBL2	9.2E+08	0	
P39019	RPS19	1.7E+08	2.87E+08	ribosomal
Q32Q12	NME1-NME2	7.3E+08	1.6E+08	
P22626	HNRNPA2B1	1.7E+08	4.89E+08	
P62906	RPL10A	1.2E+08	2.74E+08	ribosomal
P11142	HSPA8	5.6E+08	2.79E+08	
P09211	GSTP1	7.2E+08	1.3E+08	
P27824	CANX	8759400	8.16E+08	ER-resident
Q8NC51	SERBP1	1.3E+08	1.8E+08	
P45880	VDAC2	0	8.36E+08	
P19338	NCL	4.2E+08	3.85E+08	
H0Y8G5	HNRNPD	2.5E+08	2.5E+08	
P38117	ETFB	0	8E+08	mitochondrial
P14174	MIF	6.6E+08	1.29E+08	
Q9UQ80	PA2G4	2E+08	1.73E+08	
E9PR30	FAU	9.3E+07	4.16E+08	
Q00688	FKBP3	1.3E+08	1.94E+08	
P00403	MT-CO2	0	7.39E+08	
P62258	YWHAE	4.5E+08	2.53E+08	
P09651	HNRNPA1	1.6E+08	3.14E+08	
F2Z388	RPL35	4.3E+07	5.35E+08	ribosomal
P50990	CCT8	4.9E+08	1.88E+08	
F8W7C6	RPL10	9.6E+07	2.26E+08	ribosomal
P13797	PLS3	3.2E+08	3.47E+08	
P63241	EIF5A	4.8E+08	1.25E+08	translation factor
P30048	PRDX3	0	6.78E+08	
P52565	ARHGDIA	5.7E+08	85275000	
P67809	YBX1	1.6E+08	2.25E+08	
A0A3B3IUA2	NHP2L1	5E+08	96659000	
P84077	ARF1	4.2E+08	2.12E+08	
P00505	GOT2	0	6.25E+08	mitochondrial
P00441	SOD1	4.9E+08	1.07E+08	
P32119	PRDX2	4.8E+08	85405000	
P09936	UCHL1	5.7E+08	29213000	
P62820	RAB1A	7.3E+07	5.17E+08	
P13804	ETFA	0	5.92E+08	
Q9NZI8	IGF2BP1	1.1E+08	1.75E+08	
P05386	RPLP1	0	4.51E+08	ribosomal
P04075	ALDOA	4.7E+08	73747000	
A6NLH6	CNIH4	3.4E+07	5.49E+08	
E5RI99	RPL30	1.3E+08	1.93E+08	ribosomal
Q9Y3U8	RPL36	3.4E+07	4.56E+08	ribosomal
P68032	ACTC1	1.6E+08	4.13E+08	
F8VNT9	CD63	0	5.64E+08	
P49411	TUFM	0	5.7E+08	mitochondrial

Supplementary table 2 continued

Protein IDs	Gene names	iBAQ supernatent	iBAQ microsomes	Category
Q13162	PRDX4	1.6E+07	5.22E+08	
P30041	PRDX6	4.4E+08	72288000	
M0R0F0	RPS5	5.7E+07	2.2E+08	ribosomal
Q96AG4	LRRC59	0	5.08E+08	
P05141	SLC25A5	0	5.03E+08	
P48643	CCT5	3.8E+08	1.13E+08	
Q5W0H4	TPT1	1.2E+08	2.53E+08	
Q9H9B4	SFXN1	0	4.97E+08	
B4DDC6	PTGES3	4.5E+08	38353000	
P78371	CCT2	3.4E+08	1.37E+08	
R4GN19	RPL36A	0	0	ribosomal
F5GWH5	TMEM258	0	4.89E+08	ER-resident
Q5H8X8	UTS2	2E+07	4.47E+08	
Q00325	SLC25A3	0	4.72E+08	mitochondrial
P12956	XRCC6	2E+08	1.7E+08	
P49207	RPL34	5.8E+07	1.64E+08	ribosomal
P0DP25	CALM2	2.7E+08	1.96E+08	
P11940	PABPC1	1.1E+08	1.05E+08	
P26038	MSN	7.2E+07	3.88E+08	
Q99832	CCT7	3.5E+08	95201000	
P04844	RPN2	885160	4.52E+08	ER-resident
G3V4C1	HNRNPC	5.7E+07	2.67E+08	
P61978	HNRNPK	1.8E+08	2.18E+08	
P50454	SERPINH1	1.3E+07	4.33E+08	
Q04760	GLO1	3.9E+08	51169000	
P09429	HMGB1	1.8E+08	2.51E+08	
P62854	RPS26	2.3E+07	3.26E+08	ribosomal
P40227	CCT6A	3.3E+08	1.07E+08	
P51148	RAB5C	5E+07	3.98E+08	
P00558	PGK1	3.7E+08	54466000	
Q00839	HNRNPU	1.5E+08	1.59E+08	
Q15366	PCBP2	2.2E+08	1.18E+08	
Q14697	GANAB	1.9E+07	4.1E+08	
P24534	EEF1B2	2.5E+08	1.32E+08	translation factor
D6R9P3	HNRNPAB	1E+08	1.75E+08	
P30086	PEBP1	3.7E+08	41781000	
P04843	RPN1	377820	4.17E+08	ER-resident
P29692	EEF1D	1.4E+08	2.15E+08	translation factor
P35637	FUS	6.2E+07	1.72E+08	
Q99497	PARK7	2.9E+08	1.19E+08	
O75390	CS	0	4.1E+08	
Q15907	RAB11B	7.6E+07	3.32E+08	
P06748	NPM1	2E+08	1.69E+08	
P17987	TCP1	3E+08	97293000	
B1AKQ8	GNB1	1.4E+07	3.92E+08	
P00387	CYB5R3	4203100	3.96E+08	
O43852	CALU	6999100	3.92E+08	
P13073	COX4I1	0	4.03E+08	
P22234	PAICS	3.6E+08	24321000	
P12004	PCNA	2.9E+08	95135000	

References

1 **V. Ramakrishnan.** Ribosome structure and the mechanism of translation. *Cell* **108**, 557-572 (2002).

2 **T. Pape, W. Wintermeyer & M. V. Rodnina.** Complete kinetic mechanism of elongation factor Tu-dependent binding of aminoacyl-tRNA to the A site of the E. coli ribosome. *EMBO J* **17**, 7490-7497 (1998).

3 **H. Song, M. R. Parsons, S. Rowsell, G. Leonard & S. E. Phillips.** Crystal structure of intact elongation factor EF-Tu from Escherichia coli in GDP conformation at 2.05 A resolution. *J Mol Biol* **285**, 1245-1256 (1999).

4 **S. Shao, J. Murray, A. Brown, J. Taunton, V. Ramakrishnan & R. S. Hegde.** Decoding Mammalian Ribosome-mRNA States by Translational GTPase Complexes. *Cell* **167**, 1229-1240 e1215 (2016).

5 **T. Crepin, V. F. Shalak, A. D. Yaremchuk, D. O. Vlasenko, A. McCarthy, B. S. Negrutskii, M. A. Tukalo & A. V. El'skaya.** Mammalian translation elongation factor eEF1A2: X-ray structure and new features of GDP/GTP exchange mechanism in higher eukaryotes. *Nucleic Acids Res* **42**, 12939-12948 (2014).

6 **A. B. Loveland, G. Demo & A. A. Korostelev.** Cryo-EM of elongating ribosome with EF-Tu*GTP elucidates tRNA proofreading. *Nature* **584**, 640-645 (2020).

7 **J. C. Morse, D. Girodat, B. J. Burnett, M. Holm, R. B. Altman, K. Y. Sanbonmatsu, H. J. Wieden & S. C. Blanchard.** Elongation factor-Tu can repetitively engage aminoacyl-tRNA within the ribosome during the proofreading stage of tRNA selection. *Proc Natl Acad Sci U S A* **117**, 3610-3620 (2020).

8 **T. V. Budkevich, A. A. Timchenko, E. I. Tiktopulo, B. S. Negrutskii, V. F. Shalak, Z. M. Petrushenko, V. L. Aksenov, R. Willumeit, J. Kohlbrecher, I. N. Serdyuk & A. V. El'skaya.** Extended conformation of mammalian translation elongation factor 1A in solution. *Biochemistry* **41**, 15342-15349 (2002).

9 **M. Beringer & M. V. Rodnina.** The ribosomal peptidyl transferase. *Mol Cell* **26**, 311-321 (2007).

10 **R. M. Voorhees & V. Ramakrishnan.** Structural basis of the translational elongation cycle. *Annu. Rev. Biochem.* **82**, 203-236 (2013).

11 **V. Bhaskar, A. Graff-Meyer, A. D. Schenk, S. Cavadini, O. von Loeffelholz, S. K. Natchiar, C. G. Artus-Revel, H. R. Hotz, G. Bretones, B. P. Klaholz & J. A. Chao.** Dynamics of uS19 C-Terminal Tail during the Translation Elongation Cycle in Human Ribosomes. *Cell Rep* **31**, 107473 (2020).

12 **T. V. Budkevich, J. Giesebrecht, E. Behrmann, J. Loerke, D. J. Ramrath, T. Mielke, J. Ismer, P. W. Hildebrand, C. S. Tung, K. H. Nierhaus, K. Y. Sanbonmatsu & C. M. Spahn.** Regulation of the mammalian elongation cycle by subunit rolling: a eukaryotic-specific ribosome rearrangement. *Cell* **158**, 121-131 (2014).

13 **J. Flis, M. Holm, E. J. Rundlet, J. Loerke, T. Hilal, M. Dabrowski, J. Burger, T. Mielke, S. C. Blanchard, C. M. T. Spahn & T. V. Budkevich.** tRNA Translocation by the Eukaryotic 80S Ribosome and the Impact of GTP Hydrolysis. *Cell Rep* **25**, 2676-2688 e2677 (2018).

14 **E. Behrmann, J. Loerke, T. V. Budkevich, K. Yamamoto, A. Schmidt, P. A. Penczek, M. R. Vos, J. Burger, T. Mielke, P. Scheerer & C. M. Spahn.** Structural snapshots of actively translating human ribosomes. *Cell* **161**, 845-857 (2015).

15 **D. Tegunov, L. Xue, C. Dienemann, P. Cramer & J. Mahamid.** Multi-particle cryo-EM refinement with M visualizes ribosome-antibiotic complex at 3.5 A in cells. *Nat Methods* **18**, 186-193 (2021).

16 **S. Pfeffer, F. Brandt, T. Hrabe, S. Lang, M. Eibauer, R. Zimmermann & F. Förster.** Structure and 3D Arrangement of Endoplasmic Reticulum Membrane-Associated Ribosomes. *Structure* **20**, 1508-1518 (2012).

17 **F. Brandt, L. A. Carlson, F. U. Hartl, W. Baumeister & K. Grunewald.** The three-dimensional organization of polyribosomes in intact human cells. *Mol Cell* **39**, 560-569 (2010).

18 **J. N. Wells, R. Buschauer, T. Mackens-Kiani, K. Best, H. Kratzat, O. Berninghausen, T. Becker, W. Gilbert, J. Cheng & R. Beckmann.** Structure and function of yeast Lso2 and human CCDC124 bound to hibernating ribosomes. *PLoS Biol.* **18**, e3000780 (2020).

19 **L. Xue, S. Lenz, M. Zimmermann-Kogadeeva, D. Tegunov, P. Cramer, P. Bork, J. Rappsilber & J. Mahamid.** Visualizing translation dynamics at atomic detail inside a bacterial cell. *Nature* **610**, 205-211 (2022).

20 **W. Liu, D. Kavaliauskas, J. M. Schrader, K. Poruri, V. Birkedal, E. Goldman, H. Jakubowski, W. Mandecki, O. C. Uhlenbeck, C. R. Knudsen, Y. E. Goldman & B. S. Cooperman.** Labeled EF-Tus for rapid kinetic studies of pretranslocation complex formation. *ACS Chem Biol* **9**, 2421-2431 (2014).

21 **K. W. Ieong, U. Uzun, M. Selmer & M. Ehrenberg.** Two proofreading steps amplify the accuracy of genetic code translation. *Proc Natl Acad Sci U S A* **113**, 13744-13749 (2016).

22 **M. R. Wasserman, J. L. Alejo, R. B. Altman & S. C. Blanchard.** Multiperspective smFRET reveals rate-determining late intermediates of ribosomal translocation. *Nat Struct Mol Biol* **23**, 333-341 (2016).

23 **G. D. Pavitt & D. Ron.** New insights into translational regulation in the endoplasmic reticulum unfolded protein response. *Cold Spring Harb Perspect Biol* **4** (2012).

24 **J. Cox & M. Mann.** MaxQuant enables high peptide identification rates, individualized p.p.b.-range mass accuracies and proteome-wide protein quantification. *Nat Biotechnol* **26**, 1367-1372 (2008).

25 **D. N. Mastronarde.** Automated electron microscope tomography using robust prediction of specimen movements. *J Struct Biol.* **152**, 36-51. (2005).

26 **W. J. Hagen, W. Wan & J. A. Briggs.** Implementation of a cryo-electron tomography tilt-scheme optimized for high resolution subtomogram averaging. *J Struct Biol* (2016).

27 **D. Tegunov & P. Cramer.** Real-time cryo-electron microscopy data preprocessing with Warp. *Nat Methods* **16**, 1146-1152 (2019).

28 **J. R. Kremer, D. N. Mastronarde & J. R. McIntosh.** Computer visualization of three-dimensional image data using IMOD. *J Struct Biol* **116**, 71-76 (1996).

29 **T. Hrabe, Y. Chen, S. Pfeffer, L. K. Cuellar, A. V. Mangold & F. Förster.** PyTom: a python-based toolbox for localization of macromolecules in cryo-electron tomograms and subtomogram analysis. *J. Struct. Biol.* **178**, 177-188 (2012).

30 **S. H. Scheres.** RELION: implementation of a Bayesian approach to cryo-EM structure determination. *J. Struct. Biol.* **180**, 519-530 (2012).

31 **D. Liebschner, P. V. Afonine, M. L. Baker, G. Bunkoczi, V. B. Chen, T. I. Croll, B. Hintze, L. W. Hung, S. Jain, A. J. McCoy, N. W. Moriarty, R. D. Oeffner, B. K. Poon, M. G. Prisant, R. J. Read, J. S. Richardson, D. C. Richardson, M. D. Sammito, O. V. Sobolev, D. H. Stockwell, T. C. Terwilliger, A. G. Urzhumtsev, L. L. Videau, C. J. Williams & P. D. Adams.** Macromolecular structure determination using X-rays, neutrons and electrons: recent developments in Phenix. *Acta Crystallogr D Struct Biol* **75**, 861-877 (2019).

32 **T. I. Croll.** ISOLDE: a physically realistic environment for model building into low-resolution electron-density maps. *Acta Crystallogr D Struct Biol* **74**, 519-530 (2018).

33 **P. Emsley & K. Cowtan.** Coot: model-building tools for molecular graphics. *Acta Crystallogr. D Biol. Crystallogr.* **60**, 2126-2132 (2004).

34 **C. J. Williams, J. J. Headd, N. W. Moriarty, M. G. Prisant, L. L. Videau, L. N. Deis, V. Verma, D. A. Keedy, B. J. Hintze, V. B. Chen, S. Jain, S. M. Lewis, W. B. Arendall, 3rd, J. Snoeyink, P. D. Adams, S. C. Lovell, J. S. Richardson & D. C. Richardson.** MolProbity: More and better reference data for improved all-atom structure validation. *Protein Sci.* **27**, 293-315 (2018).

35 **M. Elff** Social divisions, party positions, and electoral behaviour. *Electoral Studies* **28**, 297-308 (2009).

36 **Y. Perez-Riverol, J. Bai, C. Bandla, D. Garcia-Seisdedos, S. Hewapathirana, S. Kamatchinathan, D. J. Kundu, A. Prakash, A. Frericks-Zipper, M. Eisenacher, M. Walzer, S. Wang, A. Brazma & J. A. Vizcaino.** The PRIDE database resources in 2022: a hub for mass spectrometry-based proteomics evidences. *Nucleic Acids Res* **50**, D543-D552 (2022).

37 **Y. Chen, T. Hrabe, S. Pfeffer, O. Pauly, D. Mateus, N. Navab & F. Förster.** in *Biomedical Imaging (ISBI), 2012 9th IEEE International Symposium on* 1373 - 1376 (IEEE, Barcelona, 2012).

CHAPTER 4

Visualizing protein translocation at the ER membrane

Max Gemmer[1], Marten L. Chaillet[1], Rodrigo Cuevas Arenas[1], Mariska Gröllers-Mulderij[1], Juliette Fedry[1], Friedrich Förster[1]

[1] Structural Biochemistry, Bijvoet Center for Biomolecular Research, Utrecht University, 3584 CG Utrecht, The Netherlands

Modified from
M. Gemmer, M. L. Chaillet, J. van Loenhout, D. Vismpas, F. A. Koh, P. Albanese, R. Scheltema, S. C. Howes, A. Kotecha, J Fedry, F. Förster. Visualization of translation and protein biogenesis at the ER membrane. *Nature* **614**, 160-167 (2023).

Abstract

The dynamic ribosome-translocon complex, which resides at the endoplasmic reticulum (ER) membrane, produces a major fraction of the human proteome [1,2]. It governs the synthesis, translocation, membrane insertion, N-glycosylation, folding and disulfide-bond formation of nascent proteins. While individual components of this machine have been studied at high resolution in isolation [3-7], insights into their interplay in the native membrane remain limited. Here, we use electron cryo-tomography (cryo-ET), extensive classification and molecular modeling to capture molecular resolution snapshots of protein biogenesis at the ER membrane. We visualize how distinct polysomes bind to different ER-translocons specialized in the synthesis of proteins with signal peptides (SPs) or multipass transmembrane proteins with the translocon-associated protein complex (TRAP) present in both. The near-complete atomic model of the most abundant ER translocon variant comprising the protein-conducting channel Sec61, TRAP and the oligosaccharyltransferase complex A (OSTA) reveals specific interactions of TRAP with other translocon components. Associated with OSTA we observe stoichiometric and sub-stoichiometric cofactors, likely including protein isomerases. Collectively, we visualize ER-bound polysomes with their coordinated downstream machinery.

Main

In mammalian cells, the vast majority of membrane proteins, secreted proteins and soluble proteins of most organelles are synthesized at the endoplasmic reticulum (ER) membrane. A cleavable N-terminal signal peptide (SP) emerging from the ribosome targets most secretory pathway proteins to the ER [1,2], where the nascent chain (NC) elongation is continued concomitant with its translocation across or insertion into the ER membrane.

Ribosomes bind to the dynamic ER translocon complex [2]. Its invariant core module, the heterotrimeric protein-conducting channel Sec61, faces the ribosomal exit tunnel. To facilitate protein transport and to accommodate the SP, Sec61 can switch from closed to open conformations [8,9]. Sec61 associates with distinct cofactors that reflect the requirements of different substrates. The translocon-associated protein complex (TRAP), a hetero-tetrameric transmembrane (TM) protein complex supporting the insertion of many SPs [10,11], is a near-stoichiometric ER translocon component [12]. Low-resolution studies revealed interactions of TRAP with ribosome rRNA expansion segments and ribosomal subunit protein 38e (RPL38e) [13], but molecular details remain unresolved without an atomic TRAP model. The oligosaccharyl transferase complex A (OSTA), which is responsible for co-translational N-glycosylation of substrates, is observed in 50% of translocon particles in mammalian cells [14]. While OSTA's structure and its specific association with the ribosome and Sec61 have been studied extensively [13], its native interactions, including those with biogenesis cofactors such as ER chaperones remain elusive. In addition to the Sec61-TRAP and Sec61-TRAP-OSTA translocons, a ribosome-bound translocon specialized in the insertion of multipass TM proteins, has recently been isolated and analyzed structurally [15,16]. We employed electron cryogenic tomography (cryo-ET) to visualize the elongating ribosome at the ER membrane and its downstream translocation and biogenesis machinery.

Native ER translocon distribution

We analyzed the 869 tilt series of ER-derived vesicles described in chapter 2 to obtain structural insights into the ER translocon complexes in the native membrane. Subtomogram analysis focused on the features at the ribosomal tunnel exit revealed five different classes: one soluble and four membrane-bound ribosome populations at a resolution ranging from 6 to 10 Å (Supplementary Table 1) (Fig. 1A). Approximately 30% of particles, mostly 'top views', were not assigned to any of these distinct five classes due to insufficient signal or the missing wedge. Soluble ribosomes are associated with EBP1 embraced by expansion segment (ES) 27L at the exit tunnel

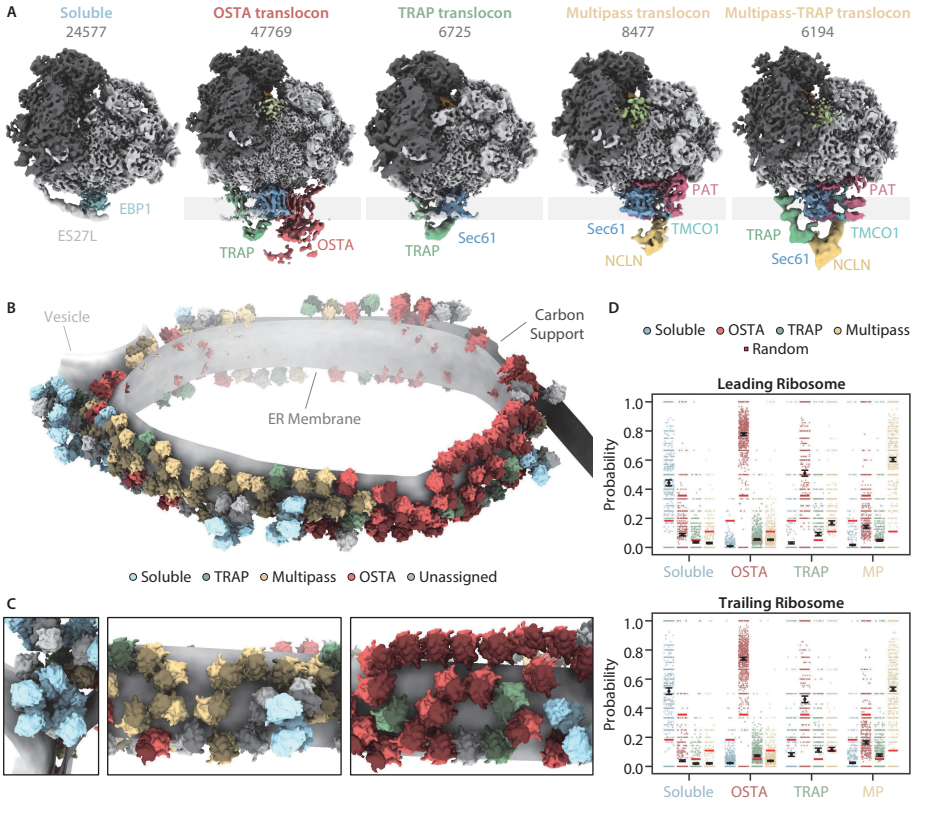

Fig. 1: Organization of soluble and ER membrane-associated ribosome populations. (A) Locally filtered reconstructions of different soluble and ER membrane-associated ribosome populations resulting from 3D-classification focused near the exit tunnel. (B) Segmented representation of one tomogram of an ER-derived vesicle (n=869 tomograms from 1 experiment). Populations from (A) are mapped back into the reconstruction and colored accordingly. (C) Close-up views of the segmentation from (B). (D) Probability of encountering ER-associated ribosomes from (A) as leading or trailing neighbor. The black circles show the modelled mean with the 95% confidence interval as error bars fitted to n=45,751 ribosomes with the 869 tomograms included as a random effect. The small, scattered points represent the frequencies of events per tomogram. The random association probability (bright red lines) is the overall abundance of the ribosome populations.

(Supplementary Fig. 1) [17], while membrane-bound ribosomes (64,208 particles) contact four distinct ER-translocon complexes (Fig. 1A): the most populated Sec61-OSTA-TRAP (69% of ER-bound particles) and Sec61-TRAP translocons (10%) have previously been identified in cryo-ET datasets of dog pancreatic ER-derived microsomes [14]. The ER translocons in the remaining two classes (21%) have a common larger component, with one of them also harboring TRAP. The common density has been observed but not identified previously in ER microsomes from 293T HEK cells upon knock-out of OSTA subunit STT3a [7]. This translocon component resembles a recently discovered TM

protein complex responsible for insertion of multipass transmembrane proteins [15]. In addition to Sec61, the multipass translocon comprises the insertase TMCO1, the PAT complex and the Nicalin-TMEM147-NOMO complex [16,18]. To confirm the assignment of our density to the multipass (TMCO1-PAT-Nicalin-TMEM147-NOMO) translocon, we knocked out CCDC47, a component of the PAT complex. Indeed, cryo-ET data of the ΔCCDC47 microsomes did not display the density at the position of the protein in the isolated multipass translocon [15] (Supplementary Fig. 2A,B). Thus, the major translocon types in wildtype HEK ER microsomes are Sec61-multipass, Sec61-multipass-TRAP, Sec61-OSTA-TRAP and Sec61-TRAP (Fig. 1A).

Mapping back the particles of these different ribosome-translocon populations in the original tomograms indicate clustering according to their translocon type (Fig. 1C). To further examine their polysomal organization, we employed our neighbor probability analysis in context of leading and trailing ribosome neighbors, which reflect late and early stages of translation, respectively (Fig. 1D, Supplementary Fig. 3). This statistical approach indicates a strong segregation of ribosomes bound to OSTA-containing and multipass translocons, as well as soluble EBP1 (Fig. 1D). Interestingly, Sec61-TRAP translocons have less tendency to pair among themselves. They also neighbor OSTA-containing and multipass translocons, where they are preferably found as a trailing polysome neighbor (Supplementary Fig. 3C,D). Thus, nascent peptides preferentially encounter Sec61-TRAP translocons early in their biogenesis. Later, the membrane-bound translocon machineries specialize, which is consistent with recent studies on different model substrates during the revision of this work [19].

Architecture of Sec61-OSTA-TRAP translocon

Ribosome-centered refinement of the most abundant population, the Sec61-OSTA-TRAP translocon, yielded a 4.2 Å-resolution structure (focused on LSU) with poorly-resolved transmembrane helices (TMHs) (7-10 Å). Recentering on the ER luminal domains resolved those at improved resolution (6–8 Å) (Fig. 2A,B, Supplementary Fig. 4A-D). A composite of both densities allowed us to build a near-complete atomic model using AlphaFold [20].

The heterotrimeric protein-conducting channel Sec61 opens its lateral gate to the lipid membrane (Fig. 3A,B, Supplementary Fig. 4D) [8,9]. Like in previous cryo-ET studies [12], the lateral gate accommodates a pronounced helical density, which matches the position of the SP in isolates [6,21] and may represent an average of the SPs of the different proteins synthesized at the ER membrane. Moreover, a density is discernable near the ribosomal exit tunnel that may correspond to an average of NCs (Supplementary

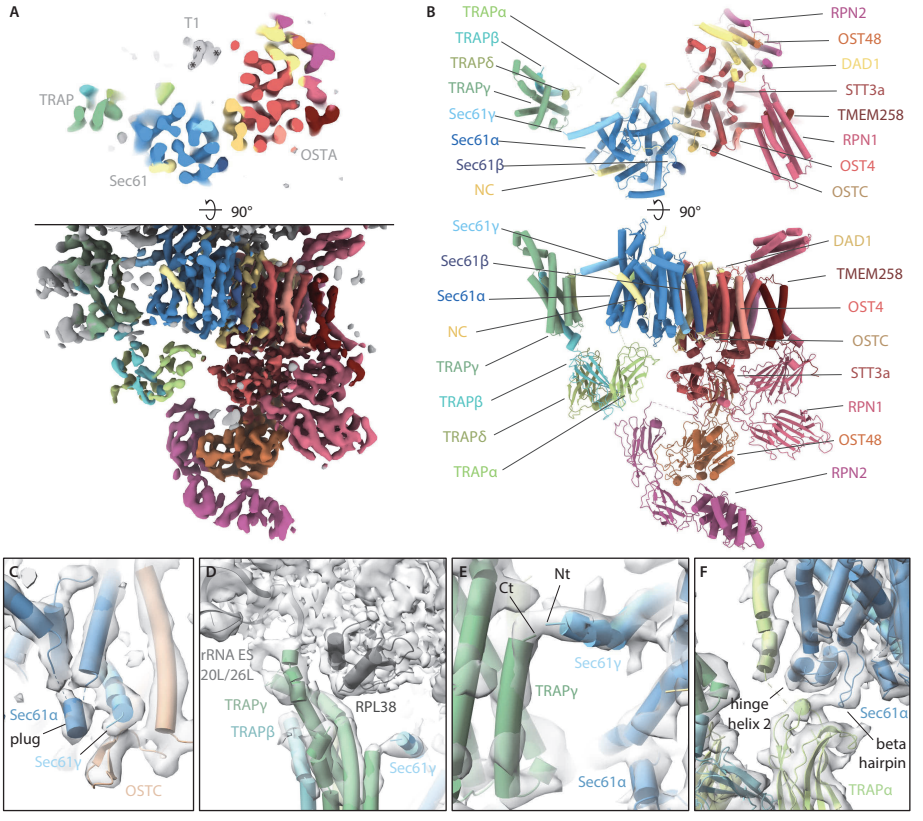

Fig. 2: Atomic model of the most abundant ER translocon. (A) Top view (top panel) and side view (bottom panel) of the translocon-centered reconstruction of Sec61-TRAP-OSTA. (B) Atomic model of the ER translocon built from cryo-EM structures (3JC2, 6S7O) and AlphaFold predictions. (C-F) Close-ups showing the molecular model placed into the segmented density maps. (C) The plug helix of Sec61α contacts the Sec61γ C-terminus and the luminal OSTC beta hairpin. Sec61α TMH4 and Sec61β were removed for clarity. (D) The cytosolic TRAPγ domain associates with rRNA expansion segment ES20L/ES26L and ribosomal protein L35. (E) The TRAPγ C-terminus contacts the N-terminus of Sec61γ. (F) The luminal TRAPα domain interacts with a β-hairpin of the Sec61α hinge region and the TRAPα TMH contacts the second helix of the hinge region. Sec61α TMH7-10 were removed for clarity.

Fig. 4E). The luminal part of Sec61 reveals a short α-helix, which we assigned to the Sec61α plug (Fig. 3C, Supplementary Fig. 4F,G). This hallmark feature of Sec61 was not resolved in lower resolution cryo-ET studies [12] and higher resolution structures of solubilized ribosome-Sec61 complexes [6,7]. Here, we observe the plug in a displaced conformation stabilized by Sec61γ and OSTC. This arrangement resembles the yeast post-translocon, where Sec63 stabilizes the plug [22].

To investigate structural deviations of Sec61-TRAP-OSTA when bound to hibernating ribosomes we reconstructed the inactive Sec61-TRAP-OSTA from the DTT-stressed

microsomes. While the Sec61 plug closes in the inactive complex, the density still reveals an open lateral gate accommodating a helical density (Supplementary Fig. 5). Since SPs can be cleaved co-translationally [23] this helix might correspond to a pool of cleaved SPs or to an unknown specific peptide.

An AlphaFold-based model of TRAP could be fitted unambiguously into the Sec61-OSTA-TRAP translocon map, requiring only minor repositioning of single TMHs and removal of low-confidence segments (Supplementary Fig. 6A-C). The assembly model does not display notable clashes and density in the lumen coincides with predicted N-glycosylation sites of TRAPα and TRAPβ, further supporting our assignment (Supplementary Fig. 6D).

As previously observed [16], TRAPγ's cytosolic domain tethers TRAP to RPL38e and the rRNA expansion segments ES20L and ES26L (Fig. 2D). Our results reveal the position of the TRAPα TMH, separated by a 2-3.5 nm lipid density from the major transmembrane part of TRAP, which comprises TRAPβ, TRAPγ and TRAPδ. In addition, we visualize a contact between the previously unresolved TRAPγ's C-terminus and the amphipathic Sec61γ N-terminal helix at the cytosolic face of the membrane (Fig. 2E, Supplementary Fig. 6E). The fibronectin-fold domains of TRAPα, TRAPβ and TRAPγ form the luminal part of TRAP, where they may interact with nascent proteins in a confined space. Near the luminal end of its TMH, the TRAPα fibronectin-like domain's FG and BC loops associate with the Sec61α hinge-region (Fig. 2F), which bridges Sec61's pseudo-symmetric N- and C-terminal halves. Finally, we observe that TRAP association is not restricted to laterally open Sec61 as the Sec61-multipass-TRAP translocon displays a closed lateral gate, in the presence of CCDC47 as recently shown [24], but also in the absence of CCDC47 (Supplementary Fig. 2H,I).

Cellular and biochemical studies indicate that TRAP is required for the biogenesis of proteins that exhibit SPs with weak helical propensity due to glycine and proline residues [11]. Preproteins with pronounced hydrophobic helical SPs are subject to stronger pulling forces than TRAP-dependent preproteins of, e.g., prion protein [25,26], presumably due to the lower affinity of their SPs for the lateral gate. While the structure of TRAP-Sec61 does not provide an obvious mechanism of action for the TRAP complex, it allows to formulate a hypothesis. When SPs traverse Sec61 head-on and enter the lumen, they contact the luminal TRAPα domain [27]. We speculate that the growing nascent chain pushing against the Sec61 hinge-bound TRAPα domain might then open the Sec61 lateral gate via an allosteric mechanism and expose its hydrophobic surface to accommodate the SP. Alternatively, it was suggested during the revision of this work that lipid bilayer modulation induced by TRAP, which can indeed be observed in our membrane-embedded structure, could promote insertion

of SPs [28]. Further studies will be required to evaluate the mechanistic function of the TRAP interactions revealed in this study.

Native OSTA and its associated factors

The cryo-ET structure is in excellent agreement with the cryo-EM SPA structure of solubilized OSTA [4], which lacks the RPN2 N-terminal domain (Supplementary Fig. 7A). To complete the atomic model, we fitted the corresponding AlphaFold models into the most membrane-distal part of our map (Supplementary Fig. 7B,C). However, the Sec61-TRAP-OSTA model does not explain a ~15 kDa TMH structure (T1), which comprises 3 TMHs and a characteristic amphipathic helix facing the cytosol (Fig. 2A, Supplementary Fig. 7D-F). T1 is intercalated between STT3a TMH9 and the C-terminus of the TRAPα TMH resulting in the formation of a lipid-filled cavity near the hinge region of Sec61. In line with OSTA association and cavity formation, T1 was only observed in the OSTA-containing ER translocon (Supplementary Fig. 7G,H). The glucosyltransferases acting upstream of OSTA or the dolichyldiphosphatase I acting downstream of OSTA are candidates for T1 [29], but neither atomic model provides an acceptable fit. Thus, further investigation will be required to determine the molecular identity of T1.

We observed weak density associated with the luminal domain of STT3a. To get higher resolution insights into possible sub-stoichiometric binding partners we performed classification focused on the Sec61-proximal luminal face of the OSTA, which revealed three distinct populations: (*i*) OSTA without accessory factors (11%), (*ii*) OSTA in complex with a ~35 kDa globular density (L1, 54%), and (*iii*) OSTA in complex with a ~60 kDa density (L2, 35%) (Fig. 3A,B, Supplementary Fig. 7I-L). L1 associates with the C-terminal ~50 mostly negatively charged residues of STT3a. L2 comprises four approximately equally sized domains (Fig. 3B), of which domains L2-1 and L2-2 compete for the same binding site with L1. Domain L2-4 binds the N-terminal domain of RPN2, and L2-3 does not interact with OSTA. While L2-1 and L2-2 reveal secondary structure elements, L2-3 and L2-4, bind the flexible RPN2 N-terminal domain, are poorly resolved.

L1 and L2 have not been observed in OSTA complexes purified from HEK cells [4] and likely represent transiently binding proteins. The ER contains many chaperones assisting protein biogenesis, which are prime candidates for L1 and L2 [30]. Among the ER chaperones, prolyl isomerase cyclophilin B is most abundant in the sample (Supplementary Table 2) and has the best agreement in shape and size with L1, which is, however, too small and globular for unambiguous assignment. Protein disulfide isomerases (PDIs) [31] explain the characteristic four-domain structure of the larger L2 well (Fig. 3D, Supplementary Fig. 7M-P). The negative charges at the interacting site of

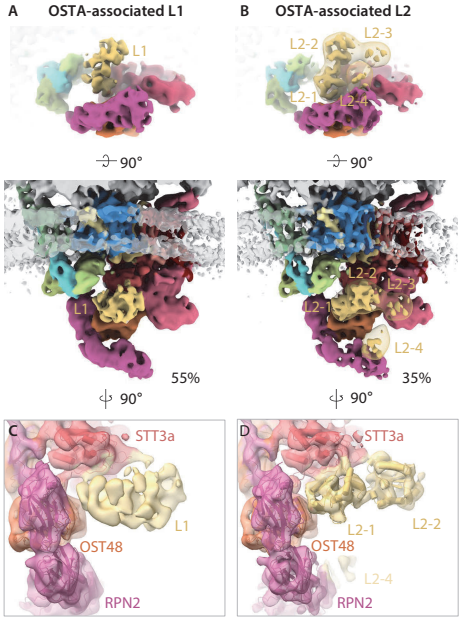

Fig. 3: Co-translational ER biogenesis factors. (A,B) Top view (top panel) and front view (bottom panel) of accessory factors L1 (A) and L2 (B) associated with the Sec61-TRAP-OSTA-translocon. The transparent map represents L2 filtered to a resolution of 20 Å. (C,D) Close-up view of the interaction site between STT3a and L1 (C) or L2 (D). Domain a and b of L2 candidate protein PDIR were placed into domain L2-1 and L2-2, respectively.

STT3a would be consistent with the interaction pattern observed for PDIs with calnexin and calreticulin (Supplementary Fig. 7Q) [32]. PDIs are highly abundant in the sample (Chapter 3, Supplementary Table 2) with glycoprotein-specific family member PDIA3 (ERp57) most likely representing L2 [33]. The transient recruitment of an oxidoreductase to OSTA is plausible as its post-translational counterpart OSTB features a constitutive oxidoreductase (N33/Tusc3) [34].

Conclusions

In summary, extensive classification of cryo-ET data visualizes the dynamic recruitment of protein biogenesis factors in the context of polysomes. This study on the ensemble of secretory proteins synthesized in the cell complements biochemical analyses [19,24] and is the basis for future investigation of the biogenesis of specific proteins and the change of the machinery in distinct cellular states and diseases.

Materials and Methods

CRISPR/Cas9 knock-out of CCDC47

FreeStyle™ 293-F cells (ThermoFisher Scientific, R79007) were transfected with the plasmid pSpCas9(BB)-2A-Puro (PX459) V2.0 from F. Zhang Lab (Addgene plasmid 62988) containing the 20-bp single guide RNA (sgRNA) target sequence 5'-CACCGGTACACGGTGAACTCGTGCG-3', PAM: AGG or 5'-CACCGGGAGGAAGCGGGCGAGGTGC-3', PAM:GGG. Transfection was performed using Lipofectamine 2000 (ThermoFisher Scientifiic, 11668019) according to the manufacturer's instructions using 1 µg DNA/mL of culture at a cell density of 1 × 10^6 cells/mL. Cells were cultured for 48 h in FreeStyle™ 293 expression medium (ThermoFisher Scientific, 12338018) on an orbital shaker (120 RPM) at 37 °C and supplemented with 5% CO_2. Two days post-transfection, cells were harvested and resuspended in complete Dulbecco's Modified Eagle Medium (DMEM) (ThermoFisher Scientific, 11966025) (supplemented with 10% fetal bovine serum (Thermofisher Scientific, 10100147) and GlutaMAX-I (ThermoFisher Scientific, 35050061)) with 0.5 µg/mL Puromycin (InvivoGen, ant-pr-1). Subsequently, cells were plated in T175 flasks (ThermoFisher Scientific, 159910) and grown for 7 days in complete DMEM with 0.5 µg/mL Puromycin with periodical medium exchange or sub-culturing when confluency was reached.

After 7 days of Puromycin selection, surviving cells were dislodged, harvested, and resuspended at 5 cells/mL in conditioned complete DMEM. 150 µl/well of cell suspension was plated into sterile 96well plates and cultured for 14 days. Cell colonies derived from single cells were used for further cell expansion. After 14 days in culture, conditioned complete DMEM was exchanged for FreeStyle medium and cell colonies transferred into 24well plates. Subsequently, cells were grown to confluency and further expanded into 6-well plates and 10-cm dishes prior to analysis.

Cell culture

HEK 293-F cells (ThermoFisher Scientific, R79007) were grown in suspension in FreeStyle medium with 120 rpm agitation. Cell lines were not authenticated and were tested for negative mycoplasma.

ER-vesicle preparation

HEK 293-F WT or CCDC47 KO cells (0.5–1 × 10^6 cells/ml, 50 mL) were harvested and washed (3 × with PBS, at 300 *g*, 5 min, 4 °C). HEK 293-F cells used for ER stress studies were treated with 10 mM DTT for 2 h before harvesting. Cells were resuspended in lysis buffer (2–4 ml, 10 mM HEPES-NaOH pH 7.4, 250 mM sucrose, 2 mM $MgCl_2$, 0.5

mM DTT, protease inhibitor cocktail [Roche]) and lysed using a Isobiotec cell cracker (5–10 passes, 14 µm clearance, on ice). The lysate was cleared (1,500 *g*, 2–3 x 5 min, 4 °C, in 2 mL tubes) using a cooled tabletop centrifuge. Vesicles were pelleted (10,000 *g*, 10 min, 4 °C,) and washed with resuspension buffer (10 mM HEPES, 250 mM sucrose, 1 mM $MgCl_2$, 0.5 mM DTT). The pellet was resuspended at a concentration of ~50 mg/mL determined by A_{280}, frozen in liquid nitrogen and stored at -80 °C until further use. The supernatant was used for proteomics as control.

20 µg of microsomes were used for SDS-PAGE followed by immunoblotting using antibodies against Sec61α (Abcam, ab15575; 1:1000), TRAPγ (Sigma Aldrich, hpa014906; 1:1000) and CCDC47 (Abcam, ab241608; 1:1000).

Grid preparation

ER-vesicles were diluted in resuspension buffer to a concentration of 2–3 mg/mL and 2 µl were applied onto a glow-discharged lacey carbon grid (Quantifoil). 4 µl of BSA-conjugated gold beads (10 nm, UMC Utrecht) diluted in resuspension buffer without sucrose were added and mixed with the sample on grid. Grids were immediately blotted from the backside for 5–6 s and plunged into a mix of liquid ethane and propane using a manual plunger.

Data acquisition

869 tilt series were acquired on a Talos Arctica (Thermo Fisher Scientific) operated at an acceleration voltage of 200 kV and equipped with a K2 summit direct electron detector and energy filter (Gatan). Images were recorded in movies of 7–8 frames at a target defocus of 3 µm and an object pixel size of 1.72 Å. Tilt series were acquired in SerialEM (3.8) [35] using a grouped dose-symmetric tilt scheme [36] covering a range of ±54° with an angular increment of 3°. The cumulative dose of a series did not exceed 80 $e^-/Å^2$.

Reconstruction and particle localization

Movie files of individual projection images were motion-corrected in Warp (1.0.9) [37] and combined into stacks of tilt series with the determined CTF parameters. The combined stacks were aligned using the gold fiducials in IMOD (4.10.25) [38]. Per-tilt CTF estimation for entire tilt series was performed in Warp and full deconvoluted tomograms were reconstructed by weighted back projection at a pixel size of 20 Å. Ice thickness was determined manually for a subset of 50 tomograms and results in an average thickness of 156 nm. Particle coordinates were determined by template matching against a reconstruction of a human 80S ribosome filtered to 40 Å and downsampled to match the tomogram pixel size (20 Å) using pyTOM (0.994) [39]. Most false positive hits were manually removed in pyTOM. The determined positions of

ribosomes were used to extract subtomograms and their corresponding CTF volumes at a pixel size of 3.45 Å (2 × binned) in Warp. Movie files of individual projection images were motion-corrected in Warp [37] and combined into stacks of tilt series with the determined CTF parameters. The combined stacks were aligned using the gold fiducials in IMOD [38]. Per-tilt CTF estimation for entire tilt series was performed in Warp and full deconvoluted tomograms were reconstructed by weighted back projection at a pixel size of 20 Å. Ice thickness was determined manually for a subset of 50 tomograms and results in an average thickness of 156 nm. Particle coordinates were determined by template matching against a reconstruction of a human 80S ribosome filtered to 40 Å and downsampled to match the tomogram pixel size (20 Å) using pyTOM [39]. Most false positive hits were manually removed in pyTOM. The determined positions of ribosomes were used to extract subtomograms and their corresponding CTF volumes at a pixel size of 3.45 Å (2 × binned) in Warp.

Subtomogram analysis

The extracted subtomograms were aligned in RELION (3.1.1) [40] using a spherical mask with a diameter of 300 Å against a reference of an 80S ribosome obtained from a subset of the same data. The extracted subtomograms were aligned in RELION (3.1.1) [40] using a spherical mask with a diameter of 300 Å against a reference of an 80S ribosome obtained from a subset of the same data. The aligned particles were refined in M (1.0.9) [41] using the reconstructions of the two half maps as a reference and a tight soft mask focused on the LSU at a pixel size of 3.45 Å. Particles were subjected to 2-3 rounds of refining image warp grid, particle poses, stage angles, volume warp grid, defocus and pixel size. After refinements, new subtomograms and their corresponding CTF volumes were extracted at a pixel size of 6.9 Å (4 × binned) and subjected to 3D classification (without mask, without reference, T=4 and classes=50) to sort out remaining false positives, poorly aligned particles and lone LSUs. The remaining 134,350 particles were used for subsequent focused classification steps to dissect ribosomal intermediate states or translocon-variants.

Classification of ER ribosome populations

All 134,350 particles were subjected to 3D classification (without reference, with soft mask, T=4, classes=20) in RELION, focused on the area at the ribosomal tunnel exit including the membrane and translocon. Particles were sorted into Sec61-TRAP-bound, Sec61-TRAP-OST-bound, Sec61-multipass-bound, EBP1- bound ribosomes and a combined class of ribosomes with ambiguous densities. Ribosomes with ambiguous densities were subjected to two further classification rounds and sorted the respective class from above until no further separation could be achieved. Ribosomes that associated with the EBP1 were designated 'soluble', ribosomes associated with

translocon variants were designated 'membrane-bound' and ribosomes associated with ambiguous densities were designated 'unidentified'.

Subtomograms of the multipass-translocon were recentered by 17 nm from the center of the ribosome towards Sec61 and extracted in M at a voxel size of 6.9 Å. Subsequently, subtomograms were classified focused on the luminal domains of TRAP and NCLN (with reference of all multipass-translocons, with soft mask, T=4, classes=3) or focused on the cytosolic domain of CCDC47 (with reference, with mask, T=3, classes=2). The TRAP-multipass-translocon was further refined using local angular searches in RELION or, to obtain ribosome-centered reconstructions of the multipass-translocon populations, subtomograms were recentered again by 17 nm towards the center of the ribosome in M and subjected to another round of refinement.

Refinement of the Sec61-TRAP-OSTA-translocon

The 42,215 best-correlating particles (5,554 particles were poorly aligned) of the OST-bound ribosome were used for refinement focused on the LSU in M using the same parameters as above at a pixel size of 1.72 Å (unbinned), which resulted in a reconstruction at an overall resolution of ~4 Å. However, densities of OST or TRAP in the ER lumen were poorly resolved. To improve local resolution of the translocon components, the reconstruction was recentered by 19.5 nm from the center of the ribosome towards the OST-translocon and subtomograms were extracted in M at a pixel size of 3.45 Å. The particles were aligned in RELION using the average of the recentered reconstruction of the OST-translocon as reference and a tight soft mask focused on Sec61, TRAP and OST. Subsequently, the aligned particles were refined in M as above at a pixel size of 1.72 Å resulting in a reconstruction at an overall resolution of 8 Å. Local resolutions estimated using M [41] ranged from 6–7 Å for the OST and 8–9 Å for TRAP and the N-terminal domain of RPN2, indicating flexibility. Local refinement focused on the TRAP complex did not improve its resolution, presumably because the protein complex was too small to provide sufficient signal for reliable refinement.

After refinement in M, translocon-centered OST-particles were extracted at a pixel size of 6.9 Å and subjected to classification in RELION (without reference, with mask, T=10, classes=4) focused on the chaperone binding site. The resulting classes were refined in M as above using masks focusing on Sec61, TRAP, OST, and chaperone.

Model building

Initial models for each chain of Sec61 and the OST were downloaded from the Alphafold database [42]. A poly-alanine helical stretch was manually built to account for the plug density. The OSTA chains were manually docked into the higher resolution

OSTA SPA map EMD-10110, followed by refinement through an iterative cycling between phenix (1.20.1) refine [43], isolde (1.0b5) [44] and Coot (0.9.8.2) [45]. The initial model for TRAP was built using AlphaFold Colab [20] and Coot [45]. The initial model for TRAP was built using AlphaFold Colab for multimeric complexes [46] and was divided into the transmembrane part and the luminal part. Each model was manually fitted into our subtomogram average (STA) density in UCSF Chimera (1.14.0) [47], followed by normal-mode guided refinement using iMODFIT (1.51) [48]. Long flexible loops not visible in our density were manually removed from the models. Sec61, OSTA and luminal TRAP domains were fitted and refined into a STA centered on the OST, while the TRAP transmembrane helices were fitted and refined into the original ribosome-centered STA, which they were better defined. Each model was refined using iterative cycling between phenix refine, Isolde and Coot. Models were then combined for one last round of refinement together in the OST centered STA. Validation was performed using Molprobity (4.5.1) [49]. UCSF ChimeraX (1.3.0) [47] was used for visualization of all models and reconstructions.

Sequence conservation

The degree of sequence conservation was determined using the ConSurf server [50] using 150 homologous sequences with a sequence identity ranging from 35%–95%. The conservation score was plotted onto the surface of the respective protein model in UCSF Chimera.

Polysome analysis

For the neighborhood analysis, ribosome positions and orientations were read from the RELION star files resulting from subtomogram alignment in a python script (Python 3.8.11, Numpy 1.20.3, Scipy 1.7.1). For each ribosome we determined distance vectors between itself and its n closest neighbors (n=4), excluding neighbors further than 100 Å. The vectors were rotated with the inverse orientation of the respective ribosome, resulting in the coordinates of neighbors in the coordinate system of an ER-bound ribosome with the xy-plane corresponding to the ER membrane. These vectors were sampled on a 3D-histogram with voxels corresponding to 15^3 Å^3 and divided by the total number of analyzed neighbors to indicate the probability of finding a neighboring ribosome particle in each voxel. The plots were projected on the xy-plane to visualize the density of neighbors surrounding ER-bound and soluble ribosomes.

A threshold was chosen to identify clusters for trailing and leading neighbors. For ER-bound neighbors a binary mask was created in the 3D-histogram above a probability of p=0.0005, while for soluble ribosomes the threshold was put at p=0.0003. Both masks were dilated by 2 voxels. The soluble and ER-bound trailing masks were combined

in a trailing mask for the whole dataset, and the same procedure was performed for the leading mask. The masks were used to annotate associations of ribosome pairs in a polysome. A trailing/leading connection was confirmed if the neighbor localized in the trailing/leading mask area and the analyzed ribosome also positioned in the leading/trailing area of the respective neighbor (i.e., the inverse calculation).

The trailing/leading states of neighbors were used in R to fit a multinomial mixed-effects logistic regression model (mclogit 0.9.4.2 [51] in R 3.6.1). The ribosome's state was used to predict probabilities of leading and trailing states, where the tomogram index was used as a random effect to account for sample and imaging variation. We used the same model to predict probabilities of translation states in polysome chains. For visualization, the probabilities were extracted with their 95% confidence interval, representing the region of 95% certainty that the modeled mean is the population mean. Variation between tomograms was shown by calculating the frequency of certain events per tomogram, e.g., the 42nd tomogram might have 7 Pre+ ribosomes of which 6 are associated in polysomes resulting in a frequency of 0.86. Random association probability was calculated by fractional abundance of each state in the dataset. For the plots showing the fold-increase, the modeled mean and confidence interval lower and upper bounds were divided by the random association probability and displayed with logarithmic y-axis. Statistical significance for the fitted logistic parameters was determined with a two-sided Wald-test (as reported by mclogit) and used to annotate plots. P-values were adjusted for multiple comparisons with the Hochberg method as implemented in R with p.adjust (method='hochberg').

Data availability

Data generated in this study are available in the main article, supplementary materials or in public repositories: nos. EMD-15870, EMD-15884, EMD-15885, EMD-15886, EMD-15887, EMD-15888, EMD-15889, EMD-15890, EMD-15891, EMD-15892 of EMDB and PDB-8B6L of PDB.

Code availability

Python-code for polysome analysis is available at https://github.com/McHaillet/polysome-stats.

Acknowledgements

This work was supported by the European Research Council under the European Union's Horizon2020 Program (ERC Consolidator Grant Agreement 724425 - BENDER) and the Nederlandse Organisatie voor Wetenschappelijke Onderzoek (Vici 724.016.001 to FF, Veni 212.152 to JF, and National Roadmap for Large-Scale Research Infrastructure (NEMI) 184.034.014). We thank Gijs van der Schot, Mihajlo Vanevic, and Robert Englmeier for help with data processing, as well as Rutger Hermsen for advice on statistical analysis. We are grateful to Stefan Pfeffer, Bert Janssen, Matthias Feige, Emmanuelle Schmitt, Yves Mechulam, Sven Lang, and Richard Zimmermann for stimulating discussions and critical comments on the manuscript.

Author contributions

M.G, J.F. and F.F. conceived the project. M.G. performed microsome sample preparation, cryo-ET data acquisition and image analysis, M.G. and J.F. carried out model building. M.C. analysed polysomes. R.C.A. and M.G.-M. cloned CRISPR-Cas9 constructs and generated monoclonal cells. M.G., M.C., J.F. and F.F. analysed the data and wrote the manuscript.

Competing interests

The authors declare no competing interests.

Supplementary figures

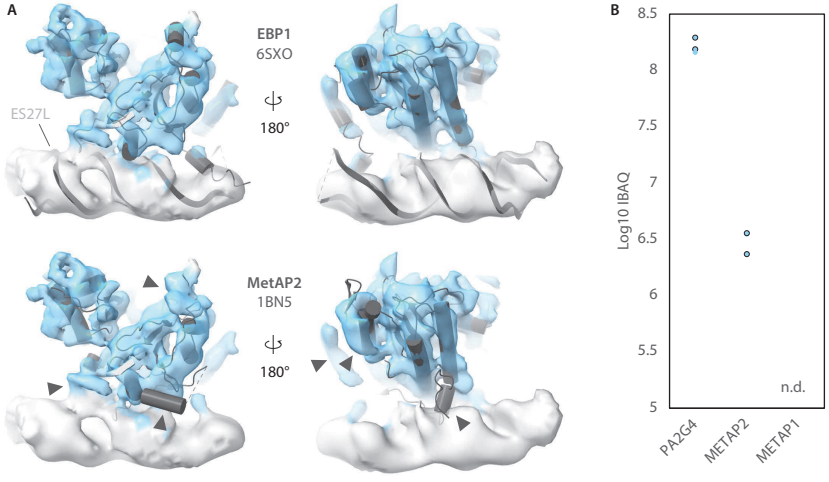

Supplementary Fig. 1: Identification of ribosome-associated EBP1. (A) Structures of EBP1 (6SXO, SPA structure) and MetAP2 (1BN5, crystal structure) fitted into our segmented reconstruction of soluble ribosomes. Arrowheads indicate structural differences between EBP1 and MetAP2 that are not explained by the reconstruction. (B) Abundance of the structurally related proteins EBP1 (PA2G4), MetAP1 and MetAP2 in our ER-vesicle preparation determined by mass spectrometry. n.d. – not determined. Data points show n=3 technical replicates of 1 experiment.

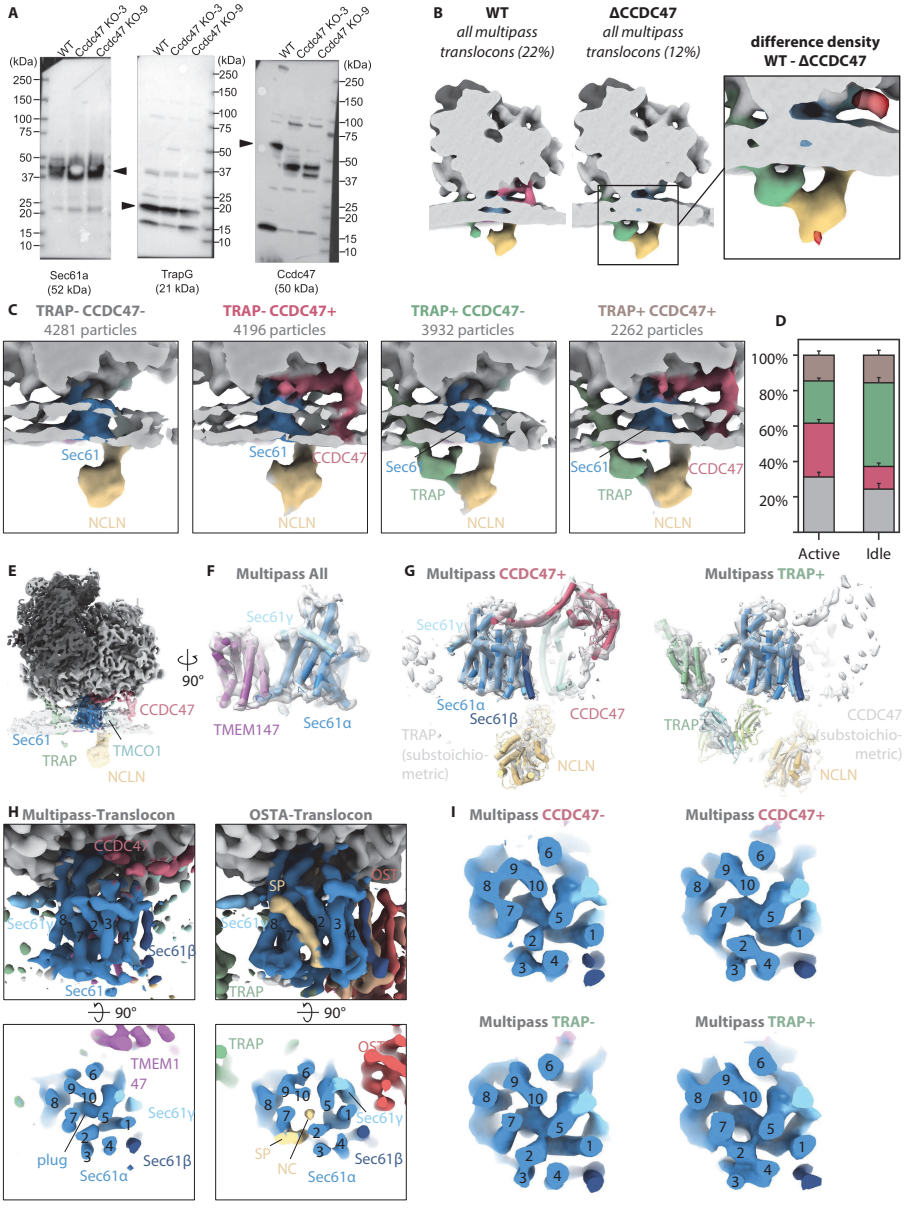

Supplementary Fig. 2: Reconstructions of multipass translocon populations. See next page for caption.

◄ **Supplementary Fig. 2: Reconstructions of multipass translocon populations.** (A) Western blots of ER-derived vesicles prepared from HEK293F WT and ΔCCDC47 cells. Samples of WT and knock-out (KO) clones 3 and 9 in different lanes derive from the same experiment. The membrane was cut vertically after blotting and its fragments were processed in parallel. Sec61α (Sec61a) and TRAPγ (TrapG) were used as ER marker. The depicted Western blot is a representative of two independent experiments. (B) Comparison between the multipass translocon population from WT and ΔCCDC47. The difference density is displayed at 2σ (red). n(ΔCCDC47) = 555 particles in 60 tomograms from 1 experiment (C) Multipass translocon populations obtained by classification focused on the ER luminal densities of TRAP and NCLN or on CCDC47. (D) Quantification of multipass translocon populations associated with elongating or hibernating ribosomes. Color-code as in (C). n = 14781 particles in 869 tomograms from 1 experiment. (E) Overall structure of the entire multipass translocon-associated ribosome filtered to 8 Å (opaque) and 20 Å (transparent) resolution. Densities of TRAP, NCLN, CCDC47 are highly fragmented due to flexibility or compositional heterogeneity. (F) Close-up view of Sec61 and TMEM147 (PDB: 6W6L) fitted into the segmented reconstruction from (E). (G) Components of the multipass translocon (PDB: 6W6L) fitted into the segmented densities of CCDC47-containing or TRAP-containing populations. Densities that are distant from the ribosome are fragmented due to flexibility. (H) Close-up views of Sec61 from the entire multipass-translocon population (left) compared to the OSTA-translocon (right). Numbering of TMHs of Sec61α is indicated. SP– signal peptide, NC – nascent chain. (I) Segmented density of Sec61 shown as in (H) of reconstructions from populations lacking or containing CCDC47 and lacking or containing TRAP.

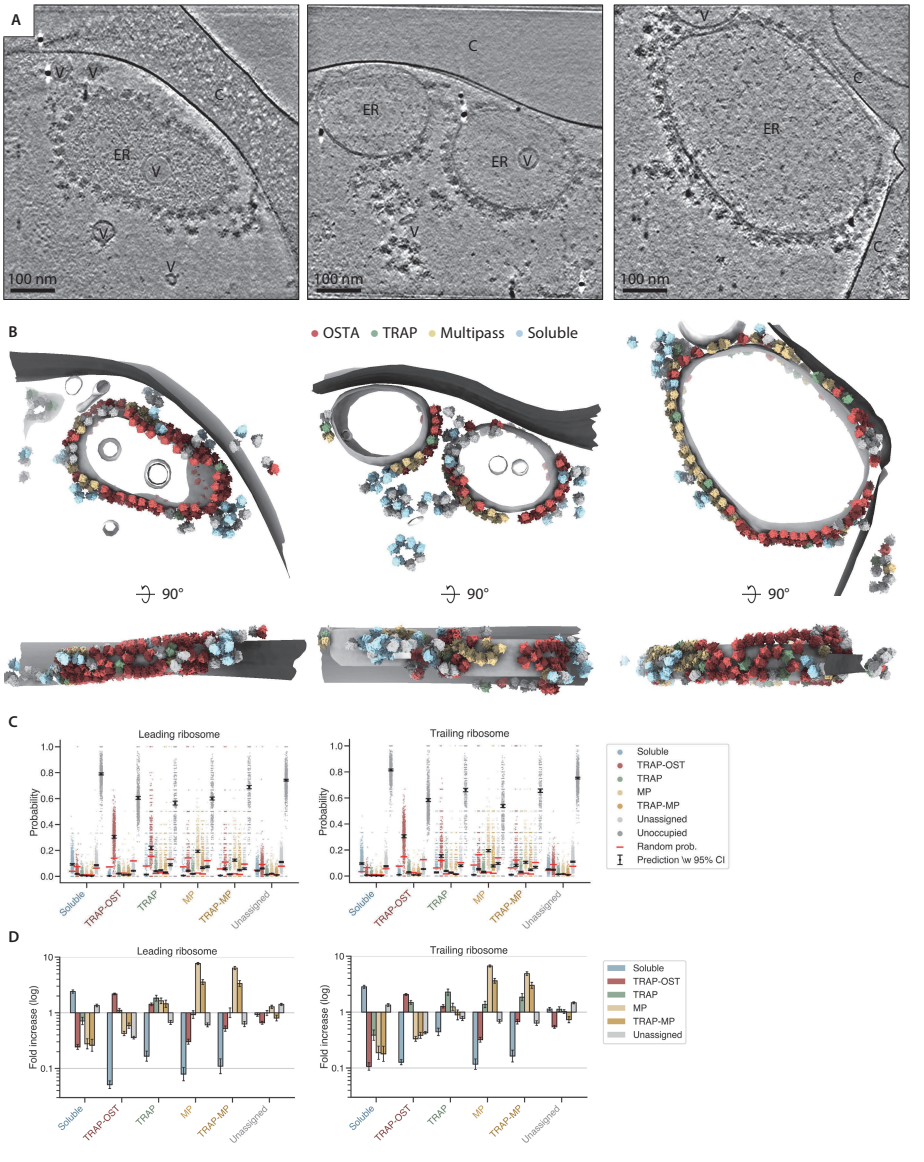

Supplementary Fig. 3: Neighbor probability analysis of soluble and ER translocon populations. See next page for caption.

◄ Supplementary Fig. 3: Neighbor probability analysis of soluble and ER translocon populations. (A) Central slices from representative filtered tomograms of ER-derived vesicles. ER (endoplasmic reticulum), V (vesicle), C (carbon support). (B) Segmented representation of tomograms from (A), including the ER membrane (grey), carbon support (black) and subtomogram averages of different ribosome populations mapped back into the tomogram. Ribosomes are color-coded according to their binding partners at the exit tunnel: soluble (blue), OSTA-translocon (red), TRAP-translocon (green), multipass-translocon (yellow), unassigned (grey); large ribosomal subunit (LSU, lighter shade), small ribosomal subunit (SSU, darker shade). (C) Probability of encountering soluble or ER-associated ribosomes from as leading or trailing neighbor. The black circles show the modelled mean with the 95% confidence interval as error bars fitted to n=134,350 ribosomes with the 869 tomograms included as a random effect. The small scattered points represents the frequencies of events per tomogram. The random association probability (bright red lines) is the overall abundance of the ribosome populations corrected for unoccupied positions. Neighbors are defined as 'unoccupied' if there is no particle in the defined neighborhood mask or its potential neighbor (e.g., a particle must have a trailing neighbor, which has this particle as a leading neighbor). (D) Columns represent the mean fold increase of observed vs random probability with 95% confidence interval as error bars of the data from (C).

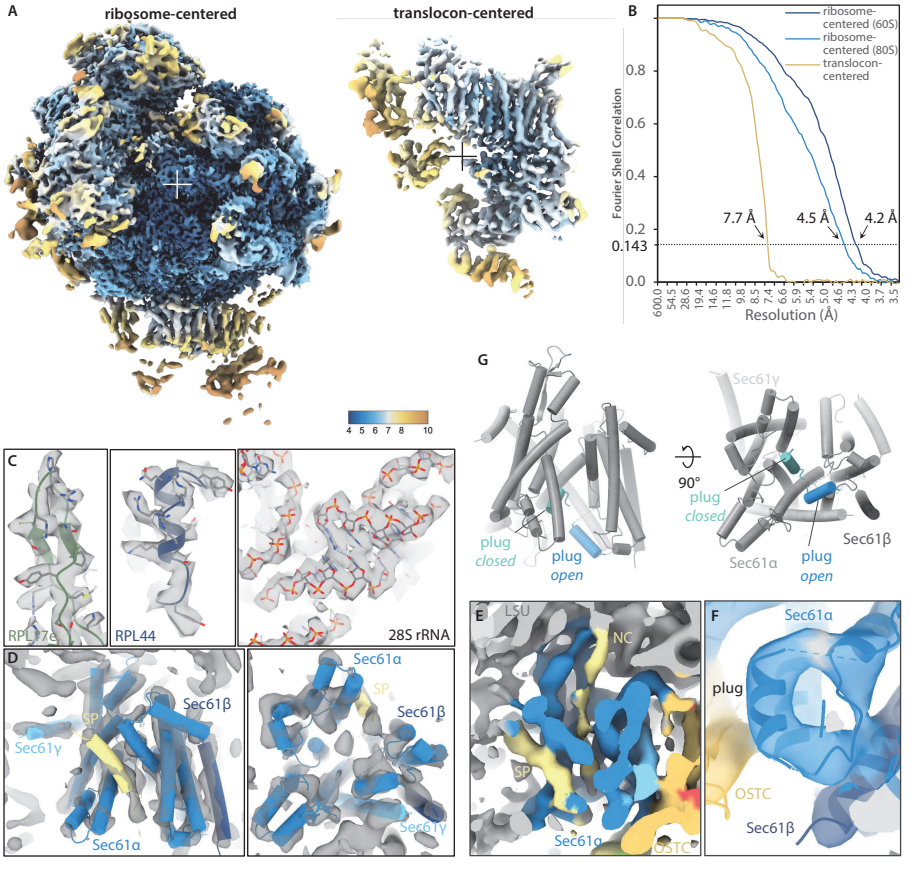

Supplementary Fig. 4: Reconstruction of the Sec61-TRAP-OSTA-translocon. (A) Ribosome- and translocon-centered reconstruction of the ribosome-Sec61-TRAP-OSTA-translocon color-coded by local resolution (color bar in Å). Centers of the respective reconstructions are indicated. (B) FSC curves of the ribosome- and translocon-centered reconstructions of the ribosome-Sec61-TRAP-OSTA-translocon. (C) Examples of 60S ribosomal proteins and 28S rRNA fitted into the ribosome-centered reconstruction filtered to local resolution of up to 3.5-Å. (D) Cryo-EM structures of Sec61 (3JC2) fitted into the translocon-centered reconstruction. (E) Density of the nascent chain (NC, light-yellow) is visible at the ribosomal tunnel exit, the Sec61 pore and in the lateral gate as signal peptide (SP, light-yellow). The front side of the ribosome and membrane were clipped for visualization purposes. (F) Close-up of the Sec61 plug placed into the density of the translocon-centered reconstruction. (G) Superposition of the plug in the closed (cyan, 3J7Q) and open (blue) conformation

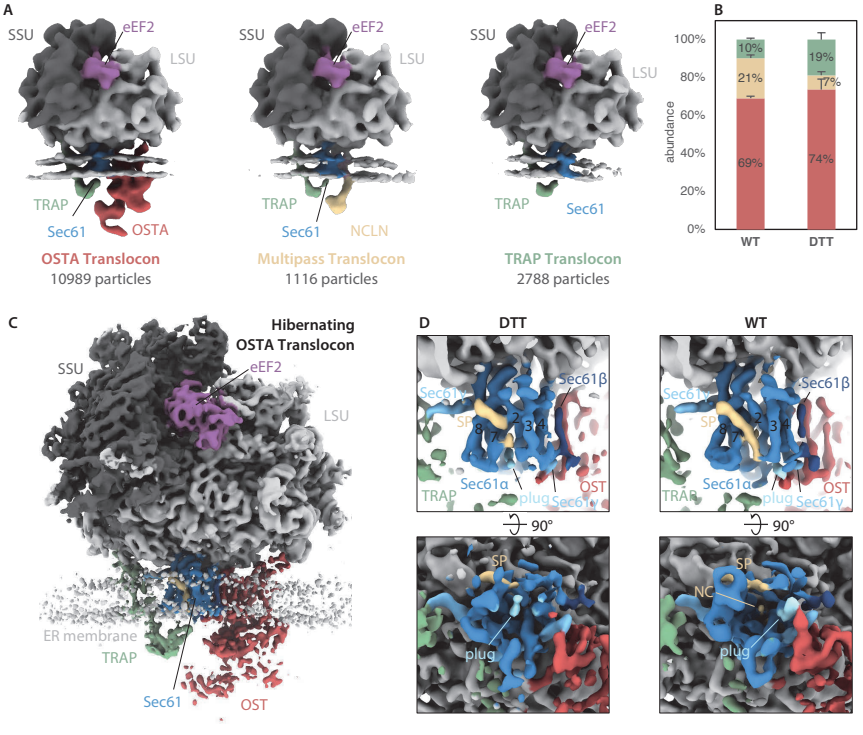

Supplementary Fig. 5: Cryo-ET analysis of ER membrane-bound ribosomes obtained from stressed cells. (A) Different populations of ER translocons from DTT-treated microsomes. (B) Distribution of ER translocon populations in WT and DTT-treated sample. n(WT) = 132,371 particles in 869 tomograms from 1 experiment, n(DTT) = 26,512 particles in 212 (174 and 38) tomograms from 2 independent experiments. Stacked columns show the modelled mean with the 95% confidence interval as error bars. (C) Structure of the hibernating ribosome-bound OSTA-translocon complex from DTT-treated samples at an overall resolution of 6.4 Å. (D) Side view (top row) and view from the ER lumen (bottom row) of the active WT (left) and inactive DTT-treated (right) OSTA-translocon. Both reconstructions were filtered to a resolution of 8 Å. SP: signal peptide, NC: nascent chain.

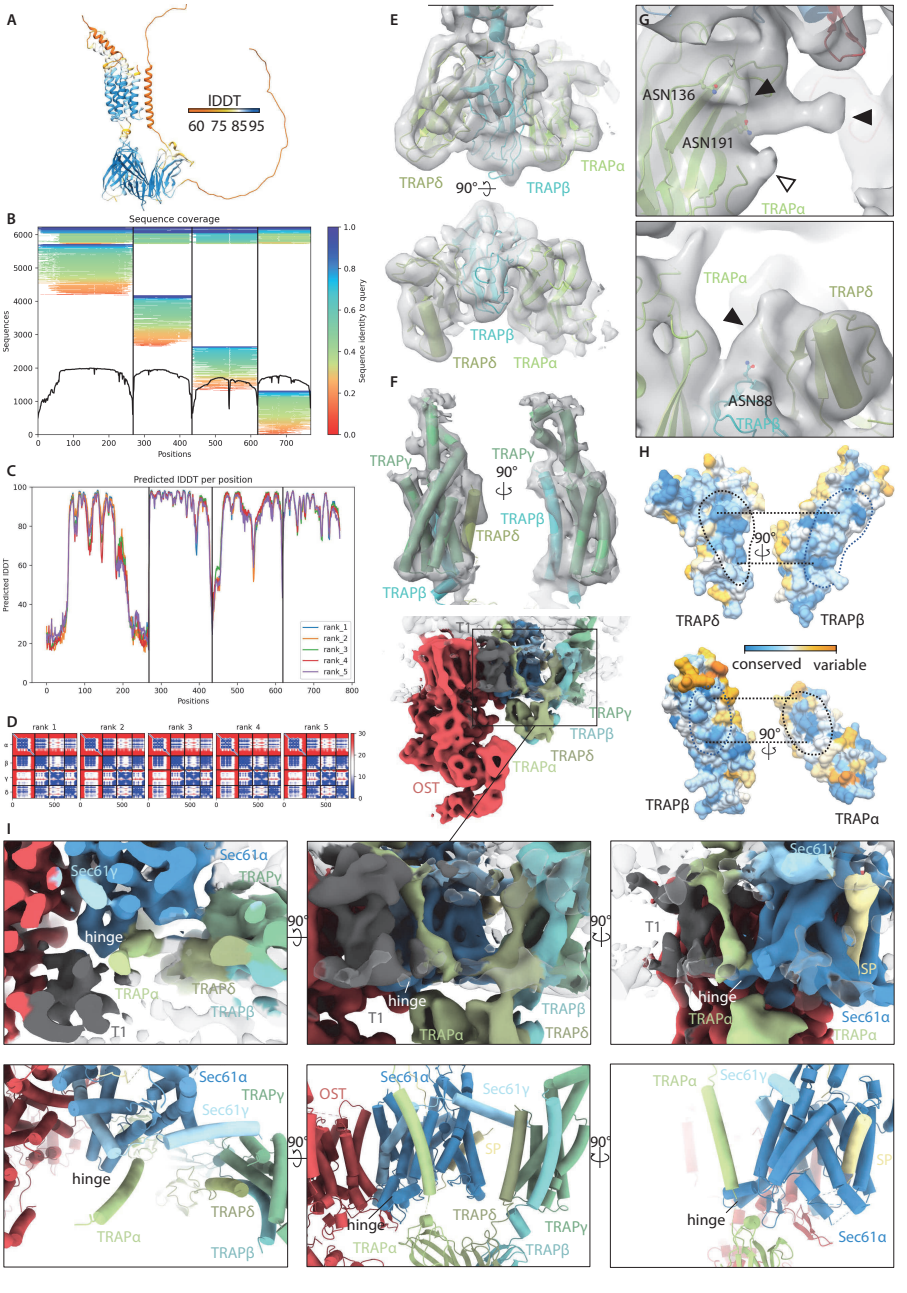

Supplementary Fig. 6: Model building of the TRAP complex. See next page for caption.

◄ **Supplementary Fig. 6: Model building of the TRAP complex**. (A) Prediction model of TRAP (P43307, P43308, Q9UNL2, P51571) obtained by Colabfold (v1.4)[52] using MMseqs2 and Alphafold2-multimer (v2) [46] color-coded according to predicted local distance difference test (pLDDT) score. Signal peptides were removed prior to prediction. (B) Sequence coverage obtained by sequence alignments generated by MMseqs2. (C) pLDDT scores per position of five model predictions. (D) Predicted aligned error (PAE) of five models predictions. (E) Prediction models of TRAPαβδ placed into the density of the locally filtered translocon-centered reconstruction. (F) Alphafold models of TRAPβγδ placed into the segmented density of the locally filtered ribosome-centered reconstruction. (G) Additional densities which are not explained by the prediction models reside near disordered terminal regions (white arrowhead) or glycosylation sites of TRAPαβ indicating partially ordered glycans (black arrowheads). Asparagine residues are displayed as ball/stick models and annotated according to residue number. (H) Sequence conservation score plotted onto the surface of TRAP subunits (blue: high conservation, orange: low conservation). Evolutionary conserved residues reside primarily at the interface areas, whereas peripheral residues are variable. The luminal TRAPα, TRAPβ, and TRAPδ domains possess large interaction interfaces (TRAPα-TRAP: β695 Å^2, TRAPβ-TRAPδ: 985 Å^2). (I) Top, back and side view of the reconstruction of the Sec61-TRAP-OSTA-translocon (top panels). Semi-transparent densities originate from residual membrane signal. Models generated from the density map at the same view (bottom panels).

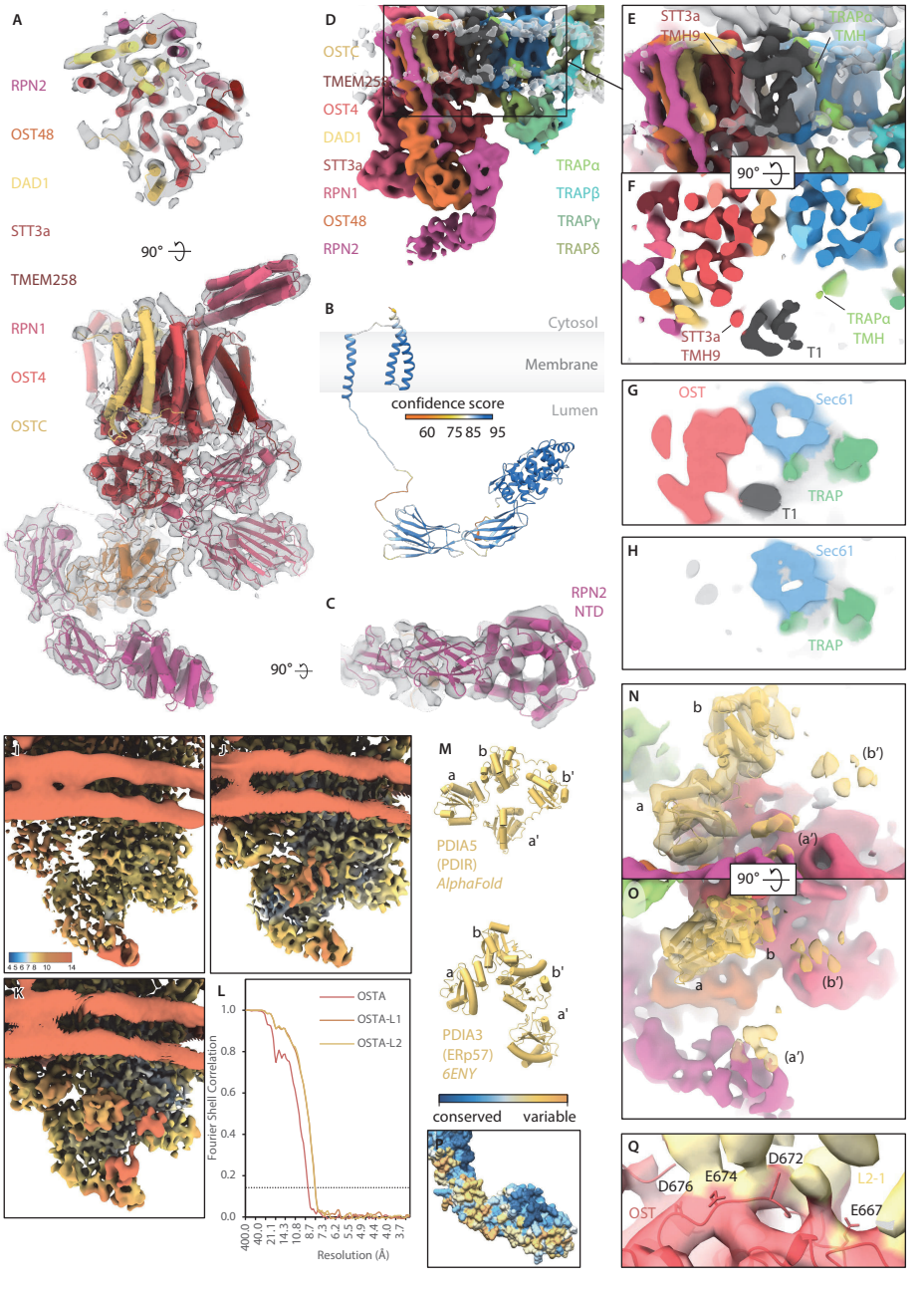

Supplementary Fig. 7: Native OSTA and its accessory factors. See next page for caption.

◄ **Supplementary Fig. 7: Native OSTA and its accessory factors.** (A) View from cytosol (top) and side view (bottom) of the OSTA complex (PDB 6S7O, AlphaFold P04844) fitted into the segmented map of the translocon-centered reconstruction of the OSTA-translocon. (B) AlphaFold model of RPN2 (P04844). The model is color-coded according to confidence score as indicated. (C) Close-up view of the N-terminal domain (NTD) of the RPN2 prediction model fitted into the reconstruction as in (A). (D) Side view of the OSTA-translocon opposite to the lateral gate. (E,F) Close-up side view (E) and top view from the cytosol (F) of T1 intercalated between TMHs of STT3a and TRAPα. (G,H) Membrane-resident translocon components (same view as in (F)) of the ribosome-centered reconstructions of the Sec61-TRAP-OSTA-translocon (G) and the Sec61-TRAP-translocon (H) filtered to a resolution of 15 Å. (I-K) Reconstructions of the OSTA-translocon without (I) or with accessory factor L1 (J) or L2 (K) color-coded according to local resolution as indicated. (L) FSC curves of the reconstructions from (I-K). (M) Models of L2-candidate proteins PDIA3 (6ENY) and PDIA5 (Q14554). Catalytic (a, a') and non-catalytic (b, b') thioredoxin domains are indicated. (N,O) PDI domains a and b fitted into the reconstruction of OSTA-L2. (P) Sequence conservation plotted onto the surface model of the RPN2 NTD. Highly conserved residues reside at the binding site of the a'-domain of PDI or other OST subunits. (Q) Close-up view of the interaction site of STT3A and L2-1.

Supplementary tables

Supplementary table 1: Cryo-EM data collection, refinement and validation statistics of ribosome and translocon classes.

	#1 Ribosome-Sec61-TRAP-OSTA (EMDB-15884)	#2 Ribosome-Sec61-TRAP (EMDB-15885)	#3 Ribosome-Sec61-TRAP-Multipass (EMDB-15886)	#4 Ribosome-Sec61-Multipass (EMDB-15887)	#5 Ribosome-EBP1 (EMDB-15888)
Data collection and processing					
Magnification	79000	79000	79000	79000	79000
Voltage (kV)	200	200	200	200	200
Electron exposure (e–/Å^2)	<80	<80	<80	<80	<80
Defocus range (μm)	3	3	3	3	3
Pixel size (Å)	1.724	1.724	1.724	1.724	1.724
Symmetry imposed	-	-	-	-	-
Initial particle images (no.)	134350	134350	134350	134350	134350
Final particle images (no.)	42215	6725	6194	8477	24577
Map resolution (Å) FSC threshold	4.5 0.143	6.5 0.143	7.5 0.143	6.7 0.143	5.0 0.143
Map resolution range (Å)	3.6-51.7	4.1-51.7	4.5-51.7	4.3-51.7	3.8-51.7

Supplementary table 1 continued.

	#16 Idle Ribosome-Sec61-TRAP-OSTA (EMDB-15889)	#17 Sec61-TRAP-OSTA-Translocon (EMDB-15890)	#18 Sec61-TRAP-OSTA-L1-Translocon (EMDB-15891)	#19 Sec61-TRAP-OSTA-L2-Translocon (EMDB-15892)
Data collection and processing				
Magnification	79000	79000	79000	79000
Voltage (kV)	200	200	200	200
Electron exposure (e–/Å^2)	<80	<80	<80	<80
Defocus range (μm)	3	3	3	3
Pixel size (Å)	1.724	1.724	1.724	1.724
Symmetry imposed	-	-	-	-
Initial particle images (no.)	134350	134350	134350	134350
Final particle images (no.)	9163	4555	14541	14991
Map resolution (Å) FSC threshold	6.4 0.143	9.3 0.143	8.2 0.143	8.3 0.143
Map resolution range (Å)	4.3-51.7	6.5-51.7	5.4-51.7	5.7-51.7

Supplementary table 1 continued.

	#20 Sec61-TRAP-OSTA-Translocon (all) (EMDB-15870) (PDB 8B6L)
Data collection and processing	
Magnification	79000
Voltage (kV)	200
Electron exposure (e–/Å^2)	<80
Defocus range (μm)	3
Pixel size (Å)	1.724
Symmetry imposed	-
Initial particle images (no.)	134350
Final particle images (no.)	42215
Map resolution (Å) FSC threshold	7.6 0.143
Map resolution range (Å)	5.4-51.7
Refinement	
Initial model used (PDB code)	AF and Colab models
Model resolution (Å) FSC threshold	6.0 0.5
Model resolution range (Å)	
Map sharpening B factor (Å^2)	
Model composition Non-hydrogen atoms Protein residues Ligands (RNA)	 29611 3798 0
B factors (Å^2) Protein Ligand (RNA)	 328.57 -
R.m.s. deviations Bond lengths (Å) Bond angles (°)	 0.003 0.594
Validation MolProbity score Clashscore Poor rotamers (%)	 1.26 2.19 0%
Ramachandran plot Favored (%) Allowed (%) Disallowed (%)	 96.11% 3.81% 0.08%

References

1 **R. M. Voorhees & R. S. Hegde.** Toward a structural understanding of co-translational protein translocation. *Curr. Opin. Cell Biol.* **41**, 91-99 (2016).

2 **M. Gemmer & F. Förster.** A clearer picture of the ER translocon complex. *Journal of cell science* **133** (2020).

3 **R. M. Voorhees & V. Ramakrishnan.** Structural basis of the translational elongation cycle. *Annu. Rev. Biochem.* **82**, 203-236 (2013).

4 **A. S. Ramirez, J. Kowal & K. P. Locher.** Cryo-electron microscopy structures of human oligosaccharyltransferase complexes OST-A and OST-B. *Science* **366**, 1372-1375 (2019).

5 **B. Van den Berg, W. M. Clemons, Jr., I. Collinson, Y. Modis, E. Hartmann, S. C. Harrison & T. A. Rapoport.** X-ray structure of a protein-conducting channel. *Nature* **427**, 36-44 (2004).

6 **R. M. Voorhees & R. S. Hegde.** Structure of the Sec61 channel opened by a signal sequence. *Science* **351**, 88-91 (2016).

7 **K. Braunger, S. Pfeffer, S. Shrimal, R. Gilmore, O. Berninghausen, E. C. Mandon, T. Becker, F. Förster & R. Beckmann.** Structural basis for coupling protein transport and N-glycosylation at the mammalian endoplasmic reticulum. *Science* **360**, 215-219 (2018).

8 **J. Zimmer, Y. Nam & T. A. Rapoport.** Structure of a complex of the ATPase SecA and the protein-translocation channel. *Nature* **455**, 936-943 (2008).

9 **P. F. Egea & R. M. Stroud.** Lateral opening of a translocon upon entry of protein suggests the mechanism of insertion into membranes. *Proc Natl Acad Sci U S A* **107**, 17182-17187 (2010).

10 **R. D. Fons, B. A. Bogert & R. S. Hegde.** Substrate-specific function of the translocon-associated protein complex during translocation across the ER membrane. *J. Cell Biol.* **160**, 529-539 (2003).

11 **D. Nguyen, R. Stutz, S. Schorr, S. Lang, S. Pfeffer, H. H. Freeze, F. Förster, V. Helms, J. Dudek & R. Zimmermann.** Proteomics reveals signal peptide features determining the client specificity in human TRAP-dependent ER protein import. *Nat. Commun.* **9**, 3765 (2018).

12 **S. Pfeffer, L. Burbaum, P. Unverdorben, M. Pech, Y. Chen, R. Zimmermann, R. Beckmann & F. Förster.** Structure of the native Sec61 protein-conducting channel. *Nat. Commun.* **6**, 8403 (2015).

13 **S. Pfeffer, J. Dudek, M. Schaffer, B. G. Ng, S. Albert, J. M. Plitzko, W. Baumeister, R. Zimmermann, H. H. Freeze, B. D. Engel & F. Förster.** Dissecting the molecular organization of the translocon-associated protein complex. *Nat. Commun.* **8**, 14516 (2017).

14 **S. Pfeffer, J. Dudek, M. Gogala, S. Schorr, J. Linxweiler, S. Lang, T. Becker, R. Beckmann, R. Zimmermann & F. Förster.** Structure of the mammalian oligosaccharyl-transferase complex in the native ER protein translocon. *Nat. Commun.* **5**, 3072 (2014).

15 **P. T. McGilvray, S. A. Anghel, A. Sundaram, F. Zhong, M. J. Trnka, J. R. Fuller, H. Hu, A. L. Burlingame & R. J. Keenan.** An ER translocon for multi-pass membrane protein biogenesis. *Elife* **9** (2020).

16 **R. S. Hegde & R. J. Keenan.** The mechanisms of integral membrane protein biogenesis. *Nat. Rev. Mol. Cell Biol.* (2021).

17 **K. Wild, M. Aleksic, K. Lapouge, K. D. Juaire, D. Flemming, S. Pfeffer & I. Sinning.** MetAP-like Ebp1 occupies the human ribosomal tunnel exit and recruits flexible rRNA expansion segments. *Nat Commun* **11**, 776 (2020).

18 **P. J. Chitwood & R. S. Hegde.** An intramembrane chaperone complex facilitates membrane protein biogenesis. *Nature* **584**, 630-634 (2020).

19 **A. Sundaram, M. Yamsek, F. Zhong, Y. Hooda, R. S. Hegde & R. J. Keenan.** Substrate-driven assembly of a translocon for multipass membrane proteins. *Nature* (2022).

20 **J. Jumper, R. Evans, A. Pritzel, T. Green, M. Figurnov, O. Ronneberger, K. Tunyasuvunakool, R. Bates, A. Zidek, A. Potapenko, A. Bridgland, C. Meyer, S. A. A. Kohl, A. J. Ballard, A. Cowie, B. Romera-Paredes, S. Nikolov, R. Jain, J. Adler, T. Back, S. Petersen, D. Reiman, E. Clancy, M. Zielinski, M. Steinegger, M. Pacholska, T. Berghammer, S. Bodenstein, D. Silver, O. Vinyals, A. W. Senior, K. Kavukcuoglu, P. Kohli & D. Hassabis.** Highly accurate protein structure prediction with AlphaFold. *Nature* **596**, 583-589 (2021).

21 **L. Li, E. Park, J. Ling, J. Ingram, H. Ploegh & T. A. Rapoport.** Crystal structure of a substrate-engaged SecY protein-translocation channel. *Nature* **531**, 395-399 (2016).

22 **S. Itskanov, K. M. Kuo, J. C. Gumbart & E. Park.** Stepwise gating of the Sec61 protein-conducting

channel by Sec63 and Sec62. *Nat. Struct. Mol. Biol.* **28**, 162-172 (2021).
23 **M. S. Wollenberg & S. M. Simon.** Signal sequence cleavage of peptidyl-tRNA prior to release from the ribosome and translocon. *J. Biol. Chem.* **279**, 24919-24922 (2004).
24 **L. Smalinskaitė, M. K. Kim, A. J. O. Lewis, R. J. Keenan & R. S. Hegde.** Mechanism of an intramembrane chaperone for multipass membrane proteins. *Nature* (2022).
25 **T. Kriegler, S. Lang, L. Notari & T. Hessa.** Prion Protein Translocation Mechanism Revealed by Pulling Force Studies. *J. Mol. Biol.* **432**, 4447-4465 (2020).
26 **T. Kriegler, G. Kiburg & T. Hessa.** Translocon-Associated Protein Complex (TRAP) is Crucial for Co-Translational Translocation of Pre-Proinsulin. *J. Mol. Biol.* **432**, 166694 (2020).
27 **M. Wiedmann, D. Goerlich, E. Hartmann, T. V. Kurzchalia & T. A. Rapoport.** Photocrosslinking demonstrates proximity of a 34 kDa membrane protein to different portions of preprolactin during translocation through the endoplasmic reticulum. *FEBS lett.* **257**, 263-268 (1989).
28 **S. Karki, M. Javanainen, D. Tranter, S. Rehan, J. T. Huiskonen, L. Happonen & V. O. Paavilainen.** Molecular view of ER membrane remodeling by the Sec61/TRAP translocon. *bioRxiv*, 2022.2009.2030.510141 (2022).
29 **M. Aebi.** N-linked protein glycosylation in the ER. *Biochim. Biophys. Acta* **1833**, 2430-2437 (2013).
30 **T. Gidalevitz, F. Stevens & Y. Argon.** Orchestration of secretory protein folding by ER chaperones. *Biochim. Biophys. Acta* **1833**, 2410-2424 (2013).
31 **G. Tian, S. Xiang, R. Noiva, W. J. Lennarz & H. Schindelin.** The crystal structure of yeast protein disulfide isomerase suggests cooperativity between its active sites. *Cell* **124**, 61-73 (2006).
32 **E. M. Frickel, R. Riek, I. Jelesarov, A. Helenius, K. Wuthrich & L. Ellgaard.** TROSY-NMR reveals interaction between ERp57 and the tip of the calreticulin P-domain. *Proc Natl Acad Sci U S A* **99**, 1954-1959 (2002).
33 **J. D. Oliver, H. L. Roderick, D. H. Llewellyn & S. High.** ERp57 functions as a subunit of specific complexes formed with the ER lectins calreticulin and calnexin. *Molecular biology of the cell* **10**, 2573-2582 (1999).
34 **E. Mohorko, R. L. Owen, G. Malojcic, M. S. Brozzo, M. Aebi & R. Glockshuber.** Structural basis of substrate specificity of human oligosaccharyl transferase subunit N33/Tusc3 and its role in regulating protein N-glycosylation. *Structure* **22**, 590-601 (2014).
35 **D. N. Mastronarde.** Automated electron microscope tomography using robust prediction of specimen movements. *J Struct Biol.* **152**, 36-51. (2005).
36 **W. J. Hagen, W. Wan & J. A. Briggs.** Implementation of a cryo-electron tomography tilt-scheme optimized for high resolution subtomogram averaging. *J Struct Biol* (2016).
37 **D. Tegunov & P. Cramer.** Real-time cryo-electron microscopy data preprocessing with Warp. *Nat Methods* **16**, 1146-1152 (2019).
38 **J. R. Kremer, D. N. Mastronarde & J. R. McIntosh.** Computer visualization of three-dimensional image data using IMOD. *J Struct Biol* **116**, 71-76 (1996).
39 **T. Hrabe, Y. Chen, S. Pfeffer, L. K. Cuellar, A. V. Mangold & F. Förster.** PyTom: a python-based toolbox for localization of macromolecules in cryo-electron tomograms and subtomogram analysis. *J. Struct. Biol.* **178**, 177-188 (2012).
40 **S. H. Scheres.** RELION: implementation of a Bayesian approach to cryo-EM structure determination. *J. Struct. Biol.* **180**, 519-530 (2012).
41 **D. Tegunov, L. Xue, C. Dienemann, P. Cramer & J. Mahamid.** Multi-particle cryo-EM refinement with M visualizes ribosome-antibiotic complex at 3.5 A in cells. *Nat Methods* **18**, 186-193 (2021).
42 **M. Varadi, S. Anyango, M. Deshpande, S. Nair, C. Natassia, G. Yordanova, D. Yuan, O. Stroe, G. Wood, A. Laydon, A. Zidek, T. Green, K. Tunyasuvunakool, S. Petersen, J. Jumper, E. Clancy, R. Green, A. Vora, M. Lutfi, M. Figurnov, A. Cowie, N. Hobbs, P. Kohli, G. Kleywegt, E. Birney, D. Hassabis & S. Velankar.** AlphaFold Protein Structure Database: massively expanding the structural coverage of protein-sequence space with high-accuracy models. *Nucleic Acids Res.* **50**, D439-D444 (2022).
43 **D. Liebschner, P. V. Afonine, M. L. Baker, G. Bunkoczi, V. B. Chen, T. I. Croll, B. Hintze, L. W. Hung, S. Jain, A. J. McCoy, N. W. Moriarty, R. D. Oeffner, B. K. Poon, M. G. Prisant, R. J. Read, J. S. Richardson, D. C. Richardson, M. D. Sammito, O. V. Sobolev, D. H. Stockwell, T. C. Terwilliger, A. G. Urzhumtsev, L. L. Videau, C. J. Williams & P. D. Adams.** Macromolecular structure determination using X-rays, neutrons and electrons: recent developments in Phenix. *Acta Crystallogr D Struct Biol* **75**,

861-877 (2019).

44 **T. I. Croll.** ISOLDE: a physically realistic environment for model building into low-resolution electron-density maps. *Acta Crystallogr D Struct Biol* **74**, 519-530 (2018).

45 **P. Emsley & K. Cowtan.** Coot: model-building tools for molecular graphics. *Acta Crystallogr. D Biol. Crystallogr.* **60**, 2126-2132 (2004).

46 **R. Evans, M. O'Neill, A. Pritzel, N. Antropova, A. Senior, T. Green, A. Žídek, R. Bates, S. Blackwell, J. Yim, O. Ronneberger, S. Bodenstein, M. Zielinski, A. Bridgland, A. Potapenko, A. Cowie, K. Tunyasuvunakool, R. Jain, E. Clancy, P. Kohli, J. Jumper & D. Hassabis.** Protein complex prediction with AlphaFold-Multimer. *bioRxiv*, 2021.2010.2004.463034 (2021).

47 **T. D. Goddard, C. C. Huang & T. E. Ferrin.** Visualizing density maps with UCSF Chimera. *J. Struct. Biol.* **157**, 281-287 (2007).

48 **J. R. Lopez-Blanco & P. Chacon.** iMODFIT: efficient and robust flexible fitting based on vibrational analysis in internal coordinates. *J. Struct. Biol.* **184**, 261-270 (2013).

49 **C. J. Williams, J. J. Headd, N. W. Moriarty, M. G. Prisant, L. L. Videau, L. N. Deis, V. Verma, D. A. Keedy, B. J. Hintze, V. B. Chen, S. Jain, S. M. Lewis, W. B. Arendall, 3rd, J. Snoeyink, P. D. Adams, S. C. Lovell, J. S. Richardson & D. C. Richardson.** MolProbity: More and better reference data for improved all-atom structure validation. *Protein Sci.* **27**, 293-315 (2018).

50 **H. Ashkenazy, S. Abadi, E. Martz, O. Chay, I. Mayrose, T. Pupko & N. Ben-Tal.** ConSurf 2016: an improved methodology to estimate and visualize evolutionary conservation in macromolecules. *Nucleic Acids Res.* **44**, W344-350 (2016).

51 **M. Elff** Social divisions, party positions, and electoral behaviour. *Electoral Studies* **28**, 297-308 (2009).

52 **M. Mirdita, K. Schutze, Y. Moriwaki, L. Heo, S. Ovchinnikov & M. Steinegger.** ColabFold: making protein folding accessible to all. *Nat Methods* **19**, 679-682 (2022).

CHAPTER 5

Exploring the molecular variability of the ER multipass translocon in its native membrane environment

Max Gemmer[1], Marten L. Chaillet[1], Friedrich Förster[1]

[1] Structural Biochemistry, Bijvoet Center for Biomolecular Research, Utrecht University, 3584 CG Utrecht, The Netherlands

Manuscript in preparation

Abstract

Ribosome-bound translocon complexes, which comprise the protein conducting-channel Sec61 bound to different sets of accessory factors, translocate nascent proteins into the ER lumen or insert them into the lipid membrane. Recent studies showed that the multipass translocon facilitates co-translational transmembrane helix (TMH) insertion and folding of multipass membrane protein clients. In addition to Sec61, the multipass translocon comprises the TMCO1-OPTI (GEL) complex, the NCLN-NOMO-TMEM147 (BOS) complex and the CCDC47-asterix (PAT) complex, as determined using cryo-EM single particle analysis of the detergent-solubilized, isolated complex. However, the multipass translocon subunit composition and variability in the native membrane remains unexplored. Here, we used cryo-electron tomography to identify the multipass translocon as abundant ER translocon variant in ER-derived vesicles from HEK cells and provide insights into its structural organization in the ER membrane. We show that PAT and the translocon associated protein complex (TRAP) are substoichiometric components of the multipass translocon whose recruitment is dependent on translational activity. While both factors appear to dynamically associate with the active translocon complex, the inactive multipass translocon features a decreased abundance of PAT and increased abundance of TRAP. Upon ER stress-induced inhibition of translation activity, we did not detect the PAT complex, whereas TRAP was present in a stoichiometric manner. The luminal domains of TRAP interact with the BOS complex via a previously unidentified partner, most likely NOMO, whereby this interaction is accompanied by re-orientation of the luminal segment of BOS. Collectively, our results visualize the interplay of accessory factors associated with multipass membrane protein biogenesis under near-native conditions.

Introduction

Biogenesis of most secretory and membrane proteins is facilitated by the ribosome-associated ER translocon complex [1]. The ribosome binds to the protein-conducting channel Sec61, a heterotrimeric ER membrane-embedded complex, which facilitates signal peptide (SP) insertion into its lateral gate and co-translational translocation of the nascent chain into the ER lumen through its central pore [2]. To meet the translocation requirements of the broad spectrum of nascent protein clients, Sec61 associates with various accessory factors specialized in functions such as SP insertion and cleavage, N-glycosylation, protein folding and maturation, transmembrane helix insertion, and ER stress response [1,3-6]. Sec61 assembles with different sets of accessory factors in ER translocon complexes. In all mammalian cells studied to date, the most abundant ribosome-bound ER translocon variant consists of the translocon-associated protein (TRAP) complex and the oligosaccharyltransferase A (OSTA) complex in addition to Sec61 [7]. A less abundant variant comprises only Sec61 and TRAP. The heterotetrameric TRAP complex facilitates insertion of SPs with below-average hydrophobicity and above-average glycine-and-proline content [8,9], while OSTA mediates co-translational N-glycosylation and recruitment of ER luminal chaperones [10,11].

In contrast to secretory proteins, biogenesis of multispanning membrane proteins relies on different translocon variants that are specialized in transmembrane helix (TMH) insertion, membrane protein topogenesis, folding and assembly [4]. Recently, Get1, EMC3, and TMCO1 have been identified as ER membrane-resident Oxa1 superfamily members, which are core components of different insertase complexes [12]. The guided entry of tail-anchored protein (GET) complex (TRC40-WBL-CAML in humans) is specialized in post-translational targeting and insertion of tail-anchored membrane proteins [13,14], while the ER membrane complex (EMC) and TMCO1-translocon facilitate co-translational TMH insertion of multispanning membrane proteins [12,15-18]. Recent biochemical, mass-spectrometry and cryo-electron microscopy (cryo-EM) studies of affinity-tagged TMCO1 isolates revealed the composition and architecture of a ribosome-bound TMCO1-containing complex [18-20], herein referred to as the multipass translocon. Besides Sec61, the multipass translocon comprises three obligate complexes: the GET- and EMC-like (GEL), the protein associated with the ER translocon (PAT), and the back-of-Sec61 (BOS) complex. GEL consists of TMCO1 and OPTI and facilitates TMH insertion [18-21]. The PAT complex consists of the intramembrane chaperone asterix to protect TMHs with exposed hydrophilic residues [22], and CCDC47 which forms contacts with the ribosome and impedes Sec61 opening [22,23]. BOS comprises TMEM147, nicalin (NCLN), and one of the three nearly identical paralogs of nodal modulator (NOMO) 1, NOMO2, or NOMO3, collectively referred to as NOMO [24-26]. While the function of BOS in humans remains poorly understood, their homologs

in other animals regulate assembly and subcellular localization of multi-subunit membrane protein complexes [27-29]. Together, the components of the multipass translocon form a lipid-filled cavity adjacent to Sec61, which mediates TMH insertion and folding of multi-spanning membrane proteins [18]. While cryo-EM studies revealed the structural organization of the multipass transocon, its compositional variation and regulation in the native membrane remains to be explored.

In chapter 3 and 4 [30], we visualized the molecular landscape of mRNA translation and protein translocation at the ER membrane, respectively. While our analysis revealed ribosomal intermediate states, major translocon variants, and OSTA-associated proteins, the composition and organization of the multipass translocon remained to be characterized. Here, we extended our subtomogram analysis of the multipass translocon and provide structural insights in the context of translational activity under near-native conditions.

Results

PAT and TRAP are variable multipass translocon components

We previously analyzed approx. 135,000 ribosome particles from human HEK cells and revealed the distribution of the major ER translocon variants. We have shown that approx. 14,700 ribosomes were associated with the multipass translocon variant. While refinement of the ribosome-multipass translocon yielded a reconstruction with a resolution of ~8 Å in the vicinity of Sec61, its associated accessory factors remained poorly resolved (Fig. S1). To reveal potential substoichiometric components or conformational heterogeneity, multipass translocon particles were subjected to two independent rounds of 3D classification focused either on PAT or on luminal densities of TRAP and BOS. This classification procedure yields four classes, comprising either TRAP only (TRAP+/PAT-, 27%), PAT only (TRAP-/PAT+, 29%), both (TRAP+/PAT+, 15%), or none (TRAP-/PAT-, 29%) (Fig. 1A,B). Hence, TRAP and PAT are both substoichiometric subunits of the multipass translocon.

Interestingly, we observed a slight but significant reduction of PAT levels in the presence of TRAP ($p=7.14*10^{-12}$), and, vice versa, a reduction of TRAP in the presence of PAT ($p=8.52*10^{-11}$) (Fig. 2A,B). To further investigate the correlation of TRAP and PAT associated with the multipass translocon, we analyzed cryo-ET data of microsomes isolated from ΔCCDC47 (PAT subunit) cells, which we previously used to identify the multipass translocon component [30]. Remarkably, in the ΔCCDC47 microsomes, we did not observe a TRAP-less multipass translocon population (Fig. 2C,D). Since TRAP and PAT reside at opposite sides of Sec61, they do not display any notable clashes (Fig.

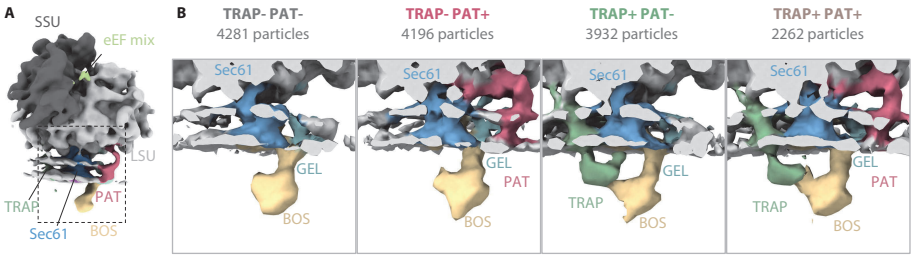

Fig. 1: Molecular composition of the multipass translocon in the native ER membrane. (A) Reconstruction of the entire multipass-population associated to the ribosome filtered to 20 Å. (B) Close up views of different multipass translocon populations. Membrane and ribosome were clipped for visual clarity.

S1) and thus do not compete for a mutual binding site. Taken together, TRAP is a stoichiometric component of the multipass translocon in the absence of PAT.

To explore translocation activity-dependent recruitment of TRAP and PAT, we analyzed the distribution of multipass translocon classes in context of the translation activity of their bound ribosomes. We previously separated active and inactive ribosomes by grouping the particles into elongating and hibernating populations using extensive classification of ribosomal intermediate states [30], which now allows us to distinguish the active and inactive multipass translocon in the native membrane. Strikingly, in inactive multipass translocon particles, we observed a strong increase of the TRAP+/PAT- class from 23% to 47%, accompanied by a strong reduction of the TRAP-/PAT+ class from 31% to 13% (Fig. 2C,D). Hence, TRAP is preferably recruited to the inactive particles, while PAT is found primarily in active multipass translocons.

To support our findings, we analyzed cryo-ET data of vesicles isolated from HEK cells, which were treated with the ER stress-inducing drug dithiothreitol (DTT). Induction of the unfolded protein response triggers a dramatic reduction of translational activity (Fig. 2C) [31]. Remarkably, we found TRAP stoichiometrically associated with the almost exclusively inactive multipass translocon (97 %), while PAT was not detected (Fig. 2C,D). Importantly, the KO of PAT subunit CCDC47 did not appear to affect ribosomal translation (Fig. 2C), precluding the possibility that the observed recruitment effects induced by the ΔCCDC47 are caused indirectly by reduced translational activity. Collectively, our results indicate a negative correlation of TRAP and PAT in the multipass translocon, which depends on the activity of the complex.

Recently, a cryo-EM single particle analysis (SPA) study revealed the architecture of the isolated, ribosome-bound Sec61-TRAP translocon [32]. The high resolution of the ribosome-TRAP interface in the map allowed identification of a short cytosolic, C-terminal stretch of the TRAPα subunit anchored to the 5.8S ribosomal RNA (rRNA)

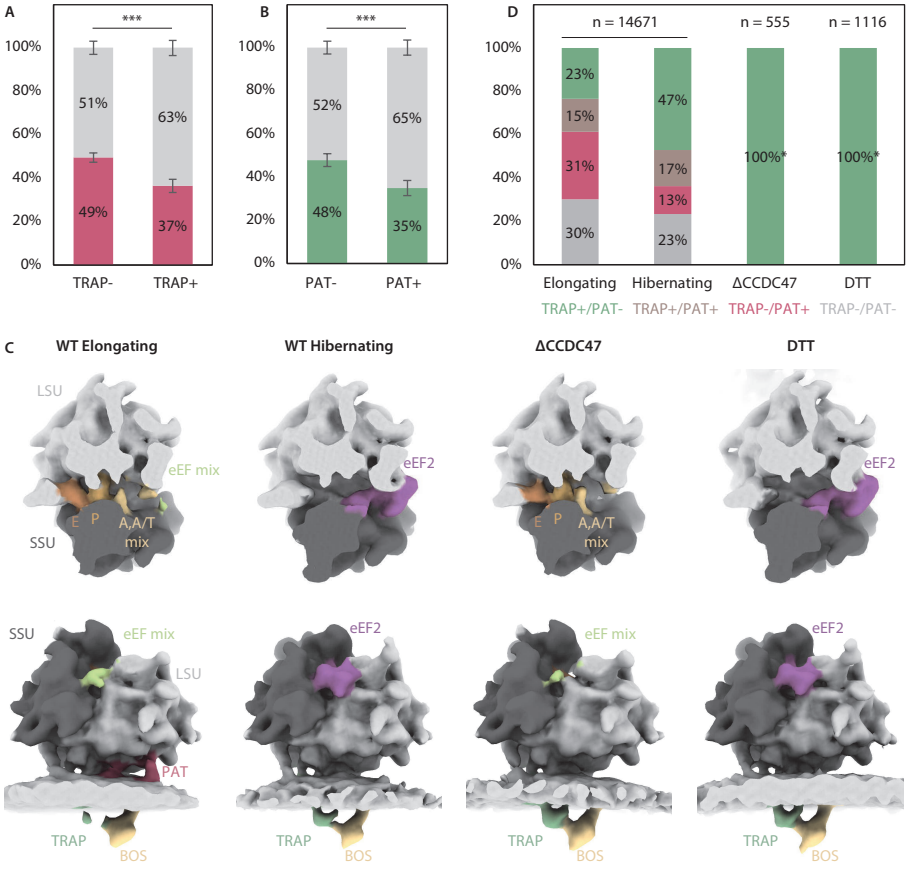

Fig. 2: Recruitment behavior of PAT and TRAP. (A) Relative abundance of PAT (magenta) in the TRAP-lacking (TRAP-) or -containing (TRAP+) multipass population with $p=7.14*10^{-12}$. (B) Relative abundance of TRAP (green) in the PAT-lacking (PAT-) or -containing (PAT+) multipass population with $p=8.52*10^{-11}$. (C) Reconstructions of multipass translocon-associated ribosomes obtained from HEK293F under unperturbed condition (WT) of elongating and hibernating classes, ΔCCDC47, and DTT-treated samples. Top row shows top views of the ribosomal binding cleft and elongation factor binding site. The ribosome was clipped for clarity. Bottom row shows the corresponding front views of the ribosome-associated translocon populations. The ER membrane was clipped for clarity. The subtomogram averages represent the entire multipass population in each class (hibernating and elongating) or sample (ΔCCDC47 and DTT). Note the varying occupancy of TRAP and PAT in the different classes. (D) Distribution of TRAP and PAT in the multipass populations from (C) color-coded as indicated. (*) PAT-containing or TRAP-lacking classes were not detected in ΔCCDC47 and DTT-treated samples.

of the large ribosomal subunit. Consistently, we spotted this anchor in subtomogram averages of membrane-bound ribosome classes (Sec61-TRAP-OSTA), but not in the soluble population (Fig. 3). Interestingly, we also observed a small density colocalizing with the TRAPα anchor in multipass variants regardless of the association of the core

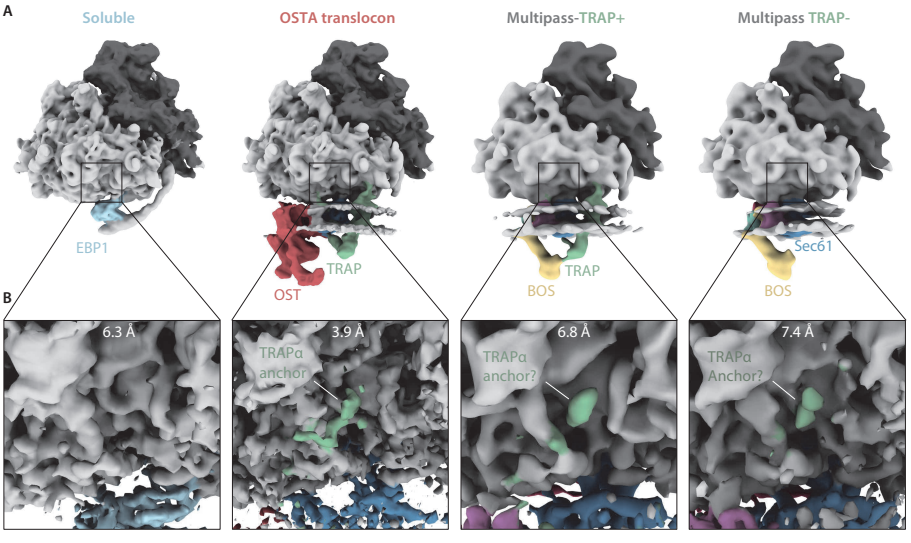

Fig. 3: Association of the TRAPα anchor domain with different ribosome populations. (A) Back side of the ribosome associated with different soluble or ER translocon variants. Reconstructions of soluble and OSTA translocon-bound ribosomes are filtered to 12 Å and multipass-bound ribosomes to 20 Å. (B) Close-up views of the TRAPα anchor binding site. Reconstructions are filtered to their overall resolution as indicated.

TRAP complex (Fig. 3). While the resolution is not sufficient to unambiguously identify this density, we believe it may correspond to the TRAPα anchor.

TRAP interacts with the BOS complex

In the multipass translocon, TRAP forms direct contacts with the luminal segment of the BOS complex. To examine the structural organization of both components, we obtained multipass translocon structures containing (8,477 particles) and lacking (6,194 particles) the TRAP complex. In the absence of TRAP, the luminal segment of BOS adopts a tilted conformation with respect to the membrane (Fig. 4). This conformation is consistent with the orientation observed in the cryo-EM structure of the isolated TMCO1 translocon (6W6L [18]), which also lacks the TRAP complex. In the presence of TRAP, BOS undergoes a 20° rotation and projects orthogonally from the membrane, in line with a cryo-EM structure of the multipass translocon in which TRAP remained bound to the multipass translocon (7TUT [19]) (Fig. 4).

Subtomogram recentering and local refinement focused on the luminal densities of TRAP and BOS yielded notably improved densities at a resolution of approximately 15 Å (Fig. 5A). While the atomic models of NCLN (AF-Q969V3) and TRAP (8B6L) could be fitted into the recentered reconstruction, two small densities, each with an approximate molecular weight of 10 kDa, remained unexplained. Both densities

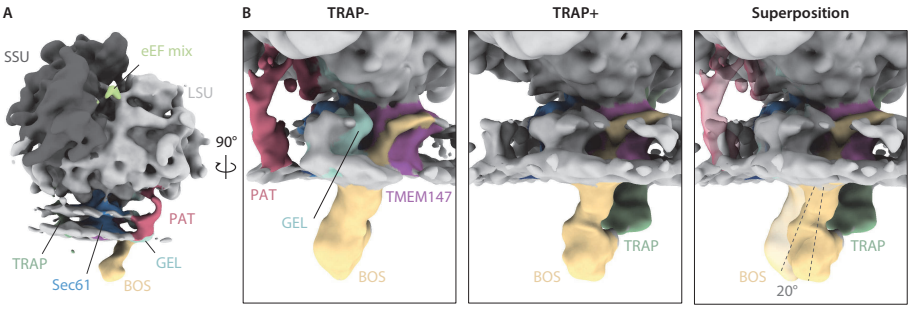

Fig. 4: Orientation of the BOS complex in different populations. (A) Overall structure of the ribosome-bound multipass-translocon filtered to 20 Å. (B) Close-up side views of the TRAP-lacking (TRAP-) and TRAP-containing (TRAP+) multipass translocon, and their superposition with TRAP- in transparent. The longitudinal axis of BOS is indicated as dashed line.

are bound to the luminal domain of NCLN, while the membrane-proximal density interacts with the luminal domains of TRAPβ and TRAPδ (Fig. 5A).

An obvious candidate for the unidentified densities is NOMO, a subunit of the BOS complex , which was shown to be highly abundant in isolates but could not be localized in the SPA structure of the multipass translocon [18]. Among the highly similar proteins NOMO1, NOMO2, and NOMO3, two paralogs, NOMO1 and NOMO3, were enriched in the isolated ribosome-associated TMCO1 translocon as detected by mass spectrometry. NOMO is a 60 kDa ER-resident single-pass membrane protein with a large luminal domain. NOMO and NCLN associate independently of TMEM147 while the domains that mediate their interaction reside in the ER lumen [25]. Nevertheless, NOMO was not modelled into the SPA reconstruction, presumably because the resolution of ER luminal densities was affected by flexibility [18]. Negative stain electron microscopy and sequence analysis of NOMO suggest an elongated shape, comprising 12 immunoglobulin (Ig)-like domains that are arranged like 'beads on a string' [33,34]. AlphaFold models of NOMO paralogs are consistent with this notion [34,35]. The two most C-terminal NOMO domains, which reside adjacent to the ER membrane-anchoring TMH, are prime candidates to explain the unknown densities and indeed fit well into the low-resolution cryo-ET reconstruction without major clashes to NCLN or TRAP (Fig. 5B). The failure to explain the remaining NOMO Ig-like domains might be due to their flexibility. To test the hypothesis that NOMOs C-terminal Ig domains constitute the unknown density, we built a prediction model of the NCLN-NOMO complex using Colabfold [36]. Intriguingly, this model positions the C-terminal NOMO1 domains almost identical to our fit into the cryo-ET structure with high confidence (PAE<10, pLDDT>85%) (Fig. 5C, S2). Although experimental validation of our assembly model will still be required, our results strongly suggests that the luminal domain of NOMO mediates association of TRAP and NCLN in the ER lumen.

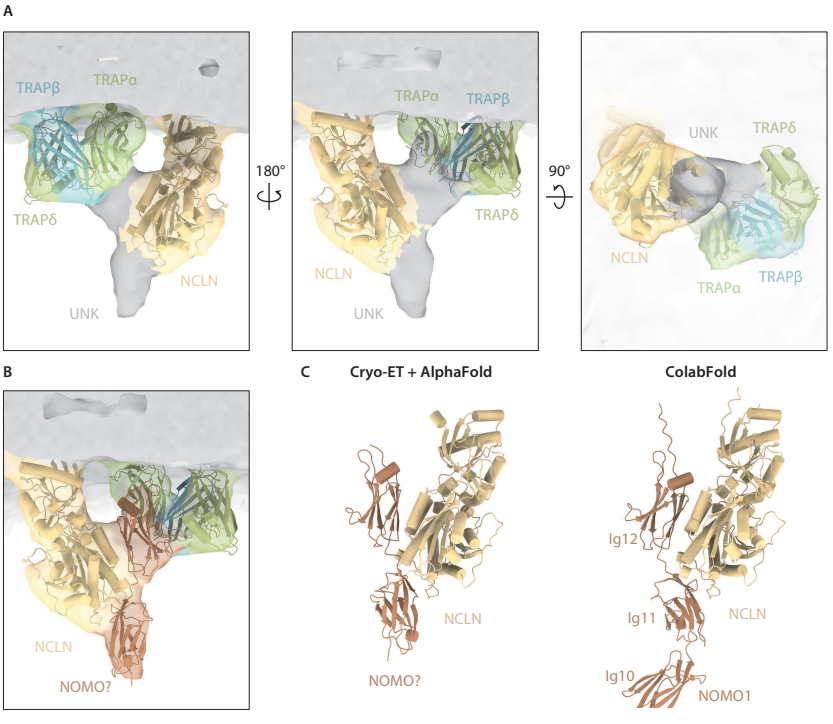

Fig. 5: TRAP interacts with the BOS complex. (A) Recentered and locally refined reconstruction of the TRAP-containing multipass translocon. Luminal domains of TRAP (8B6L, green) and NCLN (AF-Q969V3, yellow) fit well into the density map. Two unidentified densities (UNK, grey) have an approx. molecular weight of 10 kDa each. (B) Molecular model of the C-terminal Ig-like domain 11-12 of NOMO1 (AF-Q15155) placed into the map of the unidentified densities. (C) Comparison of our model and the ColabFold prediction model of the NCLN-NOMO1 complex.

Multipass translocon-associated Sec61 adopts a closed conformation

To analyze the structural features of the multipass translocon, we obtained a reconstruction of all combined multipass translocon populations at a resolution of approx. 8 Å in the TMH area of Sec61 and TMEM147 (Fig. 6A). The Sec61 lateral gate and plug helix both adopt a closed conformation that matches the structure of the isolated TMCO1 translocon [18] (Fig. 6B). Interestingly, this conformation is consistent in all multipass translocon populations, regardless of the variable accessory factors TRAP or PAT bound (Fig. S5). This contrasts the conformation of the cryo-ET reconstruction of the Sec61-TRAP-OSTA-translocon, where the Sec61 complex features an open plug and a lateral gate engaged by a helical peptide [30]. Thus, the fully closed Sec61 conformation is a characteristic feature of the multipass translocon complex in the native membrane.

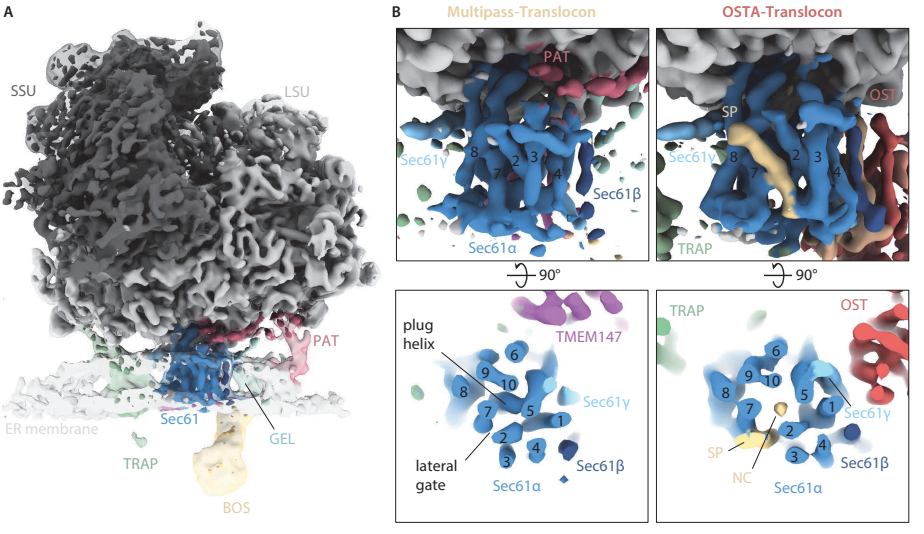

Fig. 6: Structure of the ribosome-associated multipass translocon. (A) Overall structure of the ribosome-bound multipass translocon filtered to 8 Å (opaque) and 20 Å (transparent). Densities of TRAP, the luminal BOS segment, and PAT are highly fragmented due to flexibility and compositional heterogeneity. (B) Close-up views of Sec61 from the multipass translocon (left) compared to the OSTA-translocon (right). Numbering of TMHs of Sec61α is indicated. SP – signal peptide, NC – nascent chain.

Discussion

Until recently, the Sec61 channel was considered the only protein-conducting unit of the ER translocon. However, bioinformatic and structural studies revealed an alternative translocon variant responsible for insertion of multispanning membrane proteins [12,18,21]. Our study aims to explore the near-native molecular organization, composition, and variability of the multipass translocon complex, which we previously identified in microsomes from human HEK cells.

Multi-TMH insertion is independent of Sec61 lateral gate and translocation pore

In our subtomogram reconstructions of the multipass translocon, we observed Sec61's lateral gate and plug domain in a closed conformation. This observation is consistent with previous structural studies of isolated multipass-translocons in complex with defined substrates and with the concept of TMH insertion by the specialized translocon machinery [18-20]: multi-TMHs are inserted by TMCO1 into the lipid-filled cavity adjacent to Sec61, rather than into the Sec61 lateral gate or translocation pore, to maximize folding and assembly assisted by intramembrane chaperones in a protected environment. This notion is further supported by experiments showing that biogenesis of multipass proteins is not affected by Sec61 inhibitors [19]. The Sec61

complex itself may however be required as a ribosome receptor. The cryoEM study of the isolated multipass translocon suggested CCDC47 to impede opening of Sec61 [19]. In the absence of PAT, the N-terminal half of Sec61, which mediates opening of the lateral gate, was observed to be flexible, indicating laterally open Sec61 conformations. In contrast, we observe Sec61 to be strictly closed in all multipass translocon variants, regardless of PAT, indicating that PAT is not the cause of Sec61 closure. Taken together, the Sec61 gate and plug do not appear to contribute to multipass-TMH insertion.

To facilitate translocation of large topological domains or loops carrying glycosylation sites, Sec61 cooperates again with other translocon variants [20]. Since association of the OSTA and multipass translocon is mutually exclusive, they are dynamically recruited during translocation. When multipass components are released, the nascent chain likely follows the conventional path through the Sec61 plug and lateral gate again [20]. Although multipass translocons cluster preferentially in distinct polysomes, our results do not contradict the idea of exchanging translocon variants. The majority of multipass-TMHs are linked via short loops [37] and likely undergo consecutive insertion mediated by the multipass translocon. Accordingly, multipass components may be retained at the translocon for a substantial amount of time over the course of translocation, explaining their clustered organization within polysomes. As an example, a putative multipass membrane protein with 4 TMHs consists of approx. 100 amino acid residues, which are translated from an mRNA sequence comprising 300 nucleotides. A 300 nucleotide-long mRNA molecule is approx. 100 nm long which is sufficient to cover four to five ER membrane-bound ribosomes, consistent with the clustering behavior observed in our data.

Composition of the multipass translocon is variable

While our analysis revealed the variable nature of TRAP and PAT, the determinants for recruitment of the two factors remain elusive. Since their association to the translocon is dependent on translation activity, we speculate that TRAP and PAT recruitment is regulated dependent on the presence of nascent protein clients. For example, the PAT complex specifically engages TMHs with exposed hydrophilic residues and releases its substrates upon correct folding [18]. Consequently, PAT may only associate with the translocon in the presence of partially hydrophilic TMHs and dissociate again upon substrate release. This recruitment behavior was reported previously [19] and is consistent with the substoichiometric nature of PAT and its strong reduction in inactive multipass translocons.

On the opposite side of the Sec61 complex, TRAP supports insertion of SPs with below-average hydrophobicity and above-average glycine-and-proline content and contributes to safeguarding membrane protein topogenesis [9,38]. However, a

role for TRAP in multipass membrane protein biogenesis has not been reported to date. Previously, TRAP was considered a strictly stoichiometric accessory factor of the ER translocon, since it was primarily studied in secreting cells, which synthesize comparably few membrane proteins [7]. The substoichiometric association of TRAP in context of the multipass translocon, however, suggests that its release may be required for multipass-TMH insertion. Considering the role of TRAP in SP insertion, release of TRAP seems plausible to prevent insertion of TMHs into the Sec61 lateral gate, and instead promote multi-TMH insertion via the specialized accessory factors. However, TRAP, PAT, and other multipass components appear to be able to coexist without sterically hindering each other. Thus, the requirements of TRAP release and recruitment remain to be investigated.

Interestingly, we observed a small ribosome-bound density which colocalizes with the recently described C-terminal TRAPα anchor [32]. The putative TRAPα anchor density is present in all multipass translocons, including TRAP-lacking variants, indicating that TRAP remains flexibly tethered to the ribosome, while the transmembrane and luminal TRAP segment detaches from the ribosome and translocon. This notion was previously proposed by Ban *et al.* and is consistent with our observations [32]. However, the resolution of our reconstructions is not sufficient to identify the density and classification errors must be considered when interpreting our results.

Although TRAP dynamically associates with the translocon throughout active translocation, it is preferentially recruited to the inactive translocon. During ER stress, where most particles are inactive (approx. 97%), we observe TRAP stoichiometrically bound to the mulitpass translocon, which we attributed to the preference of TRAP to associate with inactive translocons. However, the enhanced recruitment of TRAP may also be explained by ER stress-activated induction of all four TRAP subunits [39] and thus could be a direct result of ER stress.

TRAP interacts with NOMO in the ER lumen

The recruitment of TRAP is accompanied by formation of direct contacts with the BOS complex. This interaction is mediated by luminal domains of TRAPα, TRAPβ and presumably NOMO. NCLN, NOMO, and TMEM147, or their metazoan homologs, have been shown to regulate levels, subcellular localization, and subunit composition of different homo- and heterooligomeric multispanning membrane proteins [27-29,40], indicating a role in membrane protein biogenesis. Their precise function and interplay with other translocon accessory factors, however, remains poorly understood. We speculate, that the interaction of TRAP and BOS may be important for intermolecular communication, such as regulating the insertion process of TMHs into the membrane. For instance, conformational changes of BOS may trigger release of TRAP thereby

preventing Sec61-mediated insertion of multi-TMHs. Vice versa, recruitment of TRAP may induce conformational changes of the BOS complex which may be important to regulate multi-TMH insertion. While we can only speculate about the role of TRAP and NOMO in multipass membrane protein biogenesis, our structural insights provide a basis for future studies investigating the interplay between the components.

Conclusions

Taken together, the extensive and intricate interaction network formed by Sec61-embracing accessory factors in the multipass translocon constitute a dynamic frame allowing intermolecular communication. We suggest that it may regulate various processes during translocation of multispanning membrane proteins. While our results provide a comprehensive picture of the multipass translocon in its native membrane environment, further detailed functional and structural characterization in context of defined substrates is needed to understand the interplay of these specialized translocon components.

Materials and methods

Cell culture

HEK 293-F cells (ThermoFisher Scientific, R79007) were grown in suspension in FreeStyle medium with 120 rpm agitation. Cell lines were not authenticated and were tested for negative mycoplasma.

Sample preparation

Preparation of ER-derived vesicles (microsomes), grid preparation, and electron tomography data collection and processing were carried out and described before [30]. In brief, HEK293-F cells were washed 3 x with PBS and lysed using an Isobiotec cell cracker. After the lysate was cleared (1,500 *g*, 2–3 x 5 min), vesicles were pelleted (10,000 *g*, 10 min) and washed with resuspension buffer (10 mM HEPES, 250 mM sucrose, 1 mM $MgCl_2$, 0.5 mM DTT).

ER-vesicles were diluted in resuspension buffer and applied onto a glow-discharged lacey carbon grid (Quantifoil) together with BSA-conjugated gold beads (10 nm, UMC Utrecht). Grids were immediately blotted from the backside for 5–6 s and plunged into a mix of liquid ethane and propane using a manual plunger.

Data collection

869 tilt series were acquired on a Talos Arctica (Thermo Fisher Scientific) operated at an acceleration voltage of 200 kV and equipped with a K2 summit direct electron detector and energy filter (Gatan). Images were recorded in movies of 7–8 frames at a target defocus of 3 µm and an object pixel size of 1.72 Å. Tilt series were acquired in SerialEM (3.8) [41] using a grouped dose-symmetric tilt scheme [42] covering a range of ±54° with an angular increment of 3°. The cumulative dose of a series did not exceed 80 $e^-/Å^2$.

Reconstruction and particle localization

Movie files of individual projection images were motion-corrected in Warp (1.0.9) [43] and combined into stacks of tilt series with the determined CTF parameters. The combined stacks were aligned using the gold fiducials in IMOD (4.10.25) [44]. Per-tilt CTF estimation for entire tilt series was performed in Warp and full deconvoluted tomograms were reconstructed by weighted back projection at a pixel size of 20 Å.. Particle coordinates were determined by template matching against a reconstruction of a human 80S ribosome filtered to 40 Å and downsampled to match the tomogram pixel size (20 Å) using pyTOM (0.994) [45]. Most false positive hits were manually removed in pyTOM. The determined positions of ribosomes were used to extract subtomograms and their corresponding CTF volumes at a pixel size of 3.45 Å (2 × binned) in Warp.

Subtomogram analysis

The extracted subtomograms were aligned in RELION (3.1.1) [46] using a spherical mask with a diameter of 300 Å against a reference of an 80S ribosome obtained from a subset of the same data. The aligned particles were refined in M (1.0.9) [47] using the reconstructions of the two half maps as a reference and a tight soft mask focused on the LSU at a pixel size of 3.45 Å. Particles were subjected to 2-3 rounds of refining image warp grid, particle poses, stage angles, volume warp grid, defocus and pixel size. After refinements, new subtomograms and their corresponding CTF volumes were extracted at a pixel size of 6.9 Å (4 × binned) and subjected to 3D classification (without mask, without reference, T=4 and classes=50) to sort out remaining false positives, poorly aligned particles, and lone LSUs. The remaining 134,350 particles were used for subsequent focused classification steps.

Classification of ER translocon variants

All 134,350 particles were subjected to 3D classification (without reference, with soft mask, T=4, classes=20) in RELION, focused on the area at the ribosomal tunnel exit including the membrane and translocon. Particles were sorted into Sec61-TRAP-bound, Sec61-TRAP-OST-bound, Sec61-multipass-bound, EBP1-bound ribosomes and

a combined class of ribosomes with ambiguous densities. Ribosomes with ambiguous densities were subjected to two further classification rounds and sorted the respective class from above until no further separation could be achieved. Ribosomes that associated with the EBP1 were designated 'soluble', ribosomes associated with translocon variants were designated 'membrane-bound' and ribosomes associated with ambiguous densities were designated 'unidentified'.

Subtomograms of the multipass-translocon were recentered by 17 nm from the center of the ribosome towards Sec61 and extracted in M at a voxel size of 6.9 Å. Subsequently, subtomograms were classified focused on the luminal domains of TRAP and NCLN (with reference of all multipass-translocons, with soft mask, T=4, classes=3) or focused on the cytosolic domain of CCDC47 (with reference, with mask, T=3, classes=2). The TRAP-multipass-translocon was further refined using local angular searches in RELION. To obtain ribosome-centered reconstructions of TRAP-containing and -lacking and PAT-containing and -lacking multipass-translocon populations, subtomograms were recentered again by 17 nm towards the center of the ribosome in M and subjected to another round of refinement focused on the 60S ribosomal subunit.

Model fitting

The assembly of Sec61α, Sec61β, Sec61γ, TMEM147 of the cryo-EM structure of the multipasss translocon (6W6L) was rigid-body fitted into our reconstruction of the overall multipass translocon filtered to a resolution of 8 Å. Sec61 (6W6L), TMEM147 (6W6L), and the alphafold model of NCLN (AF-Q969V3) were rigid-body fitted into the PAT-containing, TRAP-containing, and TRAP-lacking multipass translocon. In addition, PAT (7TUT) was placed into the PAT-containing and TRAPα, TRAPβ, TRAPδ (8B6L) into the TRAP-containing translocon as well. Moreover, TRAPα, TRAPβ, TRAPδ (8B6L), NCLN (AF-Q969V3) and luminal Ig-like domains 11-12 of NOMO1 (AF-Q15155) were fitted into the density map of the recentered reconstruction of the Sec61-TRAP-multipass translocon.

The AlphaFold Colab [48] model prediction was build based on sequences of human NCLN (Q969V3) and NOMO1 (Q15155). The sequence of the signal peptide was removed from NCLN and NOMO prior to prediction. To meet computational limitations (<1000aa), we split NOMO1 into three models (Ig1-5, Ig5-9, Ig9-12+TMH).

Polysome analysis

Ribosome neighborhood and statistical analyses were previously described in chapter 3 and 4 [30].

Data availability

We made use of a previously published atomic models from the PDB (8B6L, 6W6L) and the AlphaFold Protein Structure Database (Q969V3, Q15155).

Acknowledgements

This work was supported by the European Research Council under the European Union's Horizon2020 Program (ERC Consolidator Grant Agreement 724425 - BENDER) and the Nederlandse Organisatie voor Wetenschappelijke Onderzoek (Vici 724.016.001, research program TA 741.018.201, and National Roadmap for Large-Scale Research Infrastructure NEMI 184.034.014).

Author contributions

M.G and F.F. conceived the project. M.G. performed microsome sample preparation, cryo-ET data acquisition and image analysis. M.C. analysed polysomes. M.G. and F.F. analysed the data and wrote the manuscript.

Competing interests

The authors declare no competing interests.

Supplementary Figures

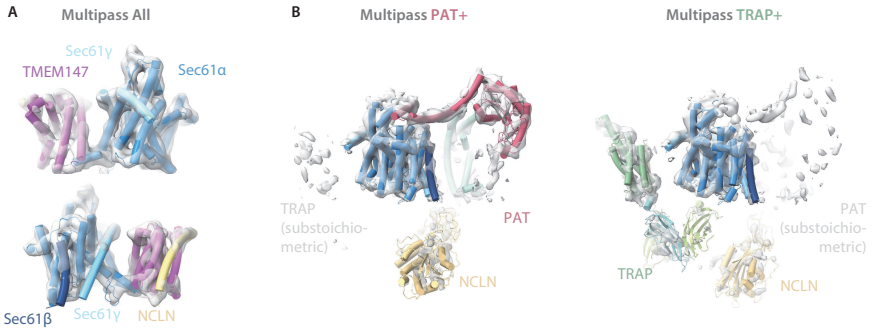

Supplementary Fig. 1: Model of the multipass translocon. (A) Rigid body fit of the isolated multipass translocon (6W6L) (Sec61 complex, TMEM147, NCLN-TMH) into the density map of the entire multipass population. (B) Rigid body fit of the isolated multipass translocon (6W6L) into the density map of the PAT-containing class and of the Sec61 complex (6W6L), NCLN (AF-Q969V3), and TRAP (8B6L) into the TRAP-containing class.

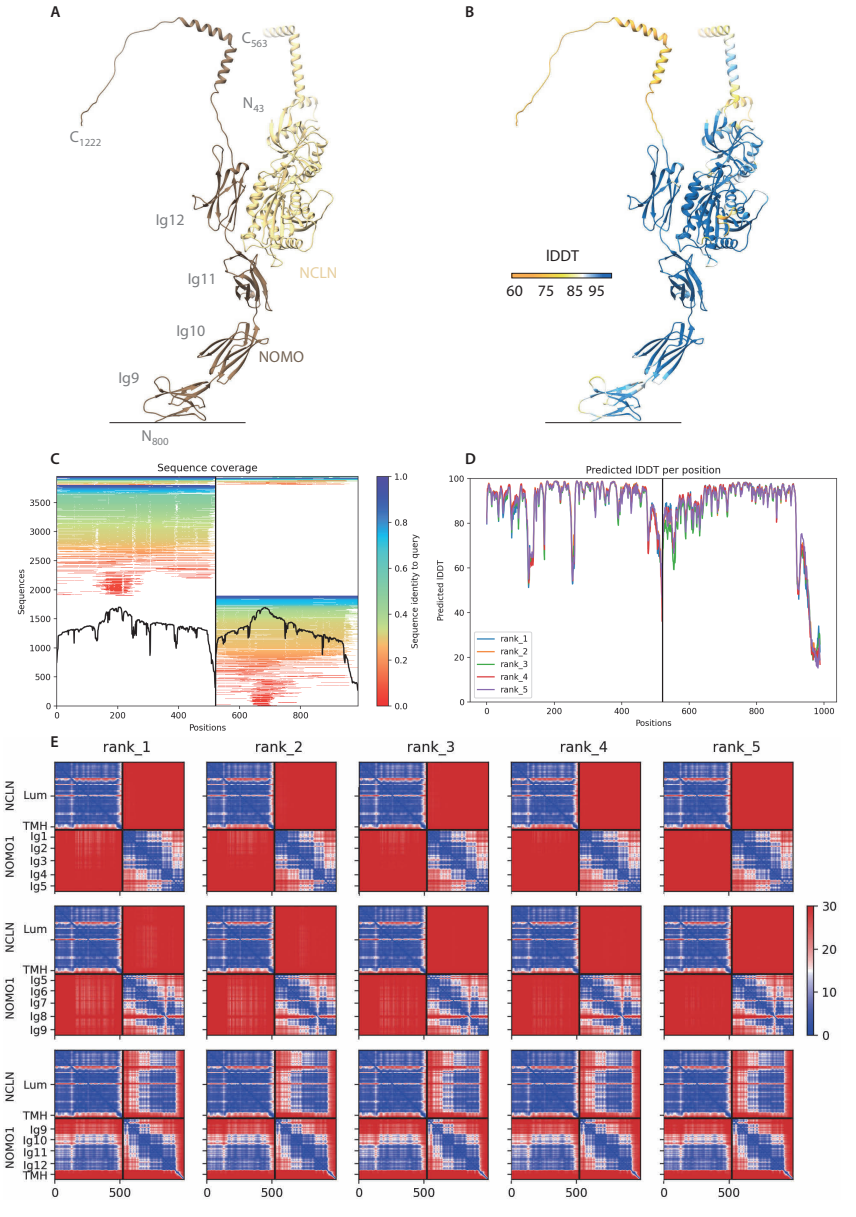

Supplementary Fig. 2: Colabfold model prediction of the NCLN-NOMO1 complex. (A) Colabfold prediction model of NCLN (full-length) in complex with NOMO1 (aa800-aa1222; Ig9-C-terminus) color-coded according to chain as indicated. N- and C-termini, corresponding residue numbering, and NOMO1 domain numbering is indicated. Signal peptides were removed prior to prediction. (B) Prediction model as in A color-coded according to predicted local distance difference test (pLDDT) score. (C) Sequence coverage obtained by sequence alignments generated by MMseqs2. (D) pLDDT scores per position of five model predictions. (E) Predicted aligned error (PAE) of five model predictions of NCLN-NOMO1$_{Ig1\text{-}5}$, NCLN-NOMO1$_{Ig5\text{-}9}$, and NCLN-NOMO1$_{Ig9\text{-}12}$.

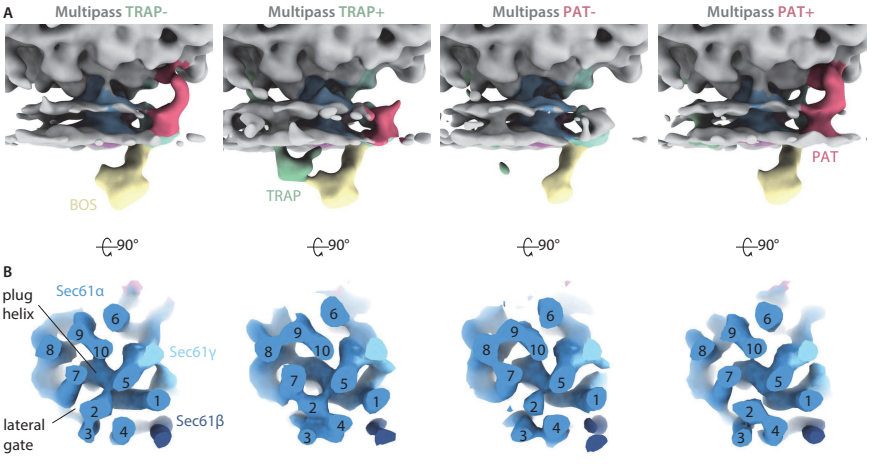

Supplementary Fig. 3: Sec61 conformational states of different multipass translocon populations. (A) Reconstructions of TRAP-lacking (TRAP-) and -containing (TRAP+), and CCDC47-lacking (CCDC47-) and -containing (CCDC47+) multipass translocon population filtered to 20 Å. (B) Top view of the corresponding map of Sec61 filtered to 8 Å. The membrane resides in the paper plane. The complex was clipped in the center of the membrane plane for visual clarity. TMH numbering is indicated.

References

1 **M. Gemmer & F. Forster.** A clearer picture of the ER translocon complex. *J Cell Sci* **133** (2020).

2 **E. Park & T. A. Rapoport.** Mechanisms of Sec61/SecY-mediated protein translocation across membranes. *Annu Rev Biophys* **41**, 21-40 (2012).

3 **A. M. Liaci & F. Forster.** Take Me Home, Protein Roads: Structural Insights into Signal Peptide Interactions during ER Translocation. *Int J Mol Sci* **22** (2021).

4 **R. S. Hegde & R. J. Keenan.** The mechanisms of integral membrane protein biogenesis. *Nat Rev Mol Cell Biol* **23**, 107-124 (2022).

5 **L. Bai & H. Li.** Cryo-EM is uncovering the mechanism of eukaryotic protein N-glycosylation. *FEBS J* **286**, 1638-1644 (2019).

6 **S. Lang, S. Pfeffer, P. H. Lee, A. Cavalie, V. Helms, F. Förster & R. Zimmermann.** An Update on Sec61 Channel Functions, Mechanisms, and Related Diseases. *Frontiers in physiology* **8**, 887 (2017).

7 **S. Pfeffer, L. Burbaum, P. Unverdorben, M. Pech, Y. Chen, R. Zimmermann, R. Beckmann & F. Förster.** Structure of the native Sec61 protein-conducting channel. *Nature communications* **6**, 8403 (2015).

8 **R. D. Fons, B. A. Bogert & R. S. Hegde.** Substrate-specific function of the translocon-associated protein complex during translocation across the ER membrane. *J Cell Biol* **160**, 529-539 (2003).

9 **D. Nguyen, R. Stutz, S. Schorr, S. Lang, S. Pfeffer, H. H. Freeze, F. Förster, V. Helms, J. Dudek & R. Zimmermann.** Proteomics reveals signal peptide features determining the client specificity in human TRAP-dependent ER protein import. *Nature communications* **9**, 3765 (2018).

10 **F. Schwarz & M. Aebi.** Mechanisms and principles of N-linked protein glycosylation. *Curr Opin Struct Biol* **21**, 576-582 (2011).

11 **R. Wild, J. Kowal, J. Eyring, E. M. Ngwa, M. Aebi & K. P. Locher.** Structure of the yeast oligosaccharyltransferase complex gives insight into eukaryotic N-glycosylation. *Science* **359**, 545-550 (2018).

12 **S. A. Anghel, P. T. McGilvray, R. S. Hegde & R. J. Keenan.** Identification of Oxa1 Homologs Operating in the Eukaryotic Endoplasmic Reticulum. *Cell Rep* **21**, 3708-3716 (2017).

13 **M. Schuldiner, J. Metz, V. Schmid, V. Denic, M. Rakwalska, H. D. Schmitt, B. Schwappach & J. S. Weissman.** The GET complex mediates insertion of tail-anchored proteins into the ER membrane. *Cell* **134**, 634-645 (2008).

14 **M. A. McDowell, M. Heimes, F. Fiorentino, S. Mehmood, A. Farkas, J. Coy-Vergara, D. Wu, J. R. Bolla, V. Schmid, R. Heinze, K. Wild, D. Flemming, S. Pfeffer, B. Schwappach, C. V. Robinson & I. Sinning.** Structural Basis of Tail-Anchored Membrane Protein Biogenesis by the GET Insertase Complex. *Mol Cell* **80**, 72-86 e77 (2020).

15 **P. J. Chitwood, S. Juszkiewicz, A. Guna, S. Shao & R. S. Hegde.** EMC Is Required to Initiate Accurate Membrane Protein Topogenesis. *Cell* **175**, 1507-1519 e1516 (2018).

16 **A. Guna, N. Volkmar, J. C. Christianson & R. S. Hegde.** The ER membrane protein complex is a transmembrane domain insertase. *Science* **359**, 470-473 (2018).

17 **M. J. Shurtleff, D. N. Itzhak, J. A. Hussmann, N. T. Schirle Oakdale, E. A. Costa, M. Jonikas, J. Weibezahn, K. D. Popova, C. H. Jan, P. Sinitcyn, S. S. Vembar, H. Hernandez, J. Cox, A. L. Burlingame, J. L. Brodsky, A. Frost, G. H. Borner & J. S. Weissman.** The ER membrane protein complex interacts cotranslationally to enable biogenesis of multipass membrane proteins. *Elife* **7** (2018).

18 **P. T. McGilvray, S. A. Anghel, A. Sundaram, F. Zhong, M. J. Trnka, J. R. Fuller, H. Hu, A. L. Burlingame & R. J. Keenan.** An ER translocon for multi-pass membrane protein biogenesis. *Elife* **9** (2020).

19 **L. Smalinskaite, M. K. Kim, A. J. O. Lewis, R. J. Keenan & R. S. Hegde.** Mechanism of an intramembrane chaperone for multipass membrane proteins. *Nature* **611**, 161-166 (2022).

20 **A. Sundaram, M. Yamsek, F. Zhong, Y. Hooda, R. S. Hegde & R. J. Keenan.** Substrate-driven assembly of a translocon for multipass membrane proteins. *Nature* **611**, 167-172 (2022).

21 **A. J. O. Lewis & R. S. Hegde.** A unified evolutionary origin for the ubiquitous protein transporters SecY and YidC. *BMC Biol* **19**, 266 (2021).

22 **P. J. Chitwood & R. S. Hegde.** An intramembrane chaperone complex facilitates membrane protein biogenesis. *Nature* **584**, 630-634 (2020).

23 **S. L. Meacock, F. J. Lecomte, S. G. Crawshaw & S. High.** Different transmembrane domains associate with distinct endoplasmic reticulum components during membrane integration of a polytopic protein. *Mol. Biol. Cell* **13**, 4114-4129 (2002).

24 **C. Haffner, U. Dettmer, T. Weiler & C. Haass.** The Nicastrin-like protein Nicalin regulates assembly and stability of the Nicalin-nodal modulator (NOMO) membrane protein complex. *J Biol Chem* **282**, 10632-10638 (2007).

25 **U. Dettmer, P. H. Kuhn, C. Abou-Ajram, S. F. Lichtenthaler, M. Kruger, E. Kremmer, C. Haass & C. Haffner.** Transmembrane protein 147 (TMEM147) is a novel component of the Nicalin-NOMO protein complex. *J Biol Chem* **285**, 26174-26181 (2010).

26 **C. Haffner, M. Frauli, S. Topp, M. Irmler, K. Hofmann, J. T. Regula, L. Bally-Cuif & C. Haass.** Nicalin and its binding partner Nomo are novel Nodal signaling antagonists. *EMBO J* **23**, 3041-3050 (2004).

27 **R. B. Almedom, J. F. Liewald, G. Hernando, C. Schultheis, D. Rayes, J. Pan, T. Schedletzky, H. Hutter, C. Bouzat & A. Gottschalk.** An ER-resident membrane protein complex regulates nicotinic acetylcholine receptor subunit composition at the synapse. *EMBO J* **28**, 2636-2649 (2009).

28 **S. Kamat, S. Yeola, W. Zhang, L. Bianchi & M. Driscoll.** NRA-2, a nicalin homolog, regulates neuronal death by controlling surface localization of toxic Caenorhabditis elegans DEG/ENaC channels. *J Biol Chem* **289**, 11916-11926 (2014).

29 **A. Christodoulou, G. Maimaris, A. Makrigiorgi, E. Charidemou, C. Luchtenborg, A. Ververis, R. Georgiou, C. W. Lederer, C. Haffner, B. Brugger & N. Santama.** TMEM147 interacts with lamin B receptor, regulates its localization and levels, and affects cholesterol homeostasis. *J Cell Sci* **133** (2020).

30 **M. Gemmer, M. L. Chaillet, J. van Loenhout, R. Cuevas Arenas, D. Vismpas, M. Grollers-Mulderij, F. A. Koh, P. Albanese, R. A. Scheltema, S. C. Howes, A. Kotecha, J. Fedry & F. Forster.** Visualization of translation and protein biogenesis at the ER membrane. *Nature* **614**, 160-167 (2023).

31 **P. Walter & D. Ron.** The unfolded protein response: from stress pathway to homeostatic regulation. *Science* **334**, 1081-1086 (2011).

32 **M. Jaskolowski, A. Jomaa, M. Gamerdinger, S. Shrestha, M. Leibundgut, E. Deuerling & N. Ban.** Molecular basis of the TRAP complex function in ER protein biogenesis. *bioRxiv*, 2022.2010.2004.510795 (2022).

33 **C. Amaya, C. J. F. Cameron, S. C. Devarkar, S. J. H. Seager, M. B. Gerstein, Y. Xiong & C. Schlieker.** Nodal modulator (NOMO) is required to sustain endoplasmic reticulum morphology. *J Biol Chem* **297**, 100937 (2021).

34 **J. Jumper, R. Evans, A. Pritzel, T. Green, M. Figurnov, O. Ronneberger, K. Tunyasuvunakool, R. Bates, A. Zidek, A. Potapenko, A. Bridgland, C. Meyer, S. A. A. Kohl, A. J. Ballard, A. Cowie, B. Romera-Paredes, S. Nikolov, R. Jain, J. Adler, T. Back, S. Petersen, D. Reiman, E. Clancy, M. Zielinski, M. Steinegger, M. Pacholska, T. Berghammer, S. Bodenstein, D. Silver, O. Vinyals, A. W. Senior, K. Kavukcuoglu, P. Kohli & D. Hassabis.** Highly accurate protein structure prediction with AlphaFold. *Nature* **596**, 583-589 (2021).

35 **M. Varadi, S. Anyango, M. Deshpande, S. Nair, C. Natassia, G. Yordanova, D. Yuan, O. Stroe, G. Wood, A. Laydon, A. Zidek, T. Green, K. Tunyasuvunakool, S. Petersen, J. Jumper, E. Clancy, R. Green, A. Vora, M. Lutfi, M. Figurnov, A. Cowie, N. Hobbs, P. Kohli, G. Kleywegt, E. Birney, D. Hassabis & S. Velankar.** AlphaFold Protein Structure Database: massively expanding the structural coverage of protein-sequence space with high-accuracy models. *Nucleic Acids Res.* **50**, D439-D444 (2022).

36 **M. Mirdita, K. Schutze, Y. Moriwaki, L. Heo, S. Ovchinnikov & M. Steinegger.** ColabFold: making protein folding accessible to all. *Nat Methods* **19**, 679-682 (2022).

37 **C. UniProt.** UniProt: the Universal Protein Knowledgebase in 2023. *Nucleic Acids Res* **51**, D523-D531 (2023).

38 **N. Sommer, T. Junne, K. U. Kalies, M. Spiess & E. Hartmann.** TRAP assists membrane protein topogenesis at the mammalian ER membrane. *Biochim Biophys Acta* **1833**, 3104-3111 (2013).

39 **K. Nagasawa, T. Higashi, N. Hosokawa, R. J. Kaufman & K. Nagata.** Simultaneous induction of the four subunits of the TRAP complex by ER stress accelerates ER degradation. *EMBO Rep* **8**, 483-489 (2007).

40 **E. Rosemond, M. Rossi, S. M. McMillin, M. Scarselli, J. G. Donaldson & J. Wess.** Regulation of M(3) muscarinic receptor expression and function by transmembrane protein 147. *Mol Pharmacol* **79**, 251-261 (2011).

41 **D. N. Mastronarde.** Automated electron microscope tomography using robust prediction of specimen movements. *J Struct Biol.* **152**, 36-51. (2005).
42 **W. J. Hagen, W. Wan & J. A. Briggs.** Implementation of a cryo-electron tomography tilt-scheme optimized for high resolution subtomogram averaging. *J Struct Biol* (2016).
43 **D. Tegunov & P. Cramer.** Real-time cryo-electron microscopy data preprocessing with Warp. *Nat Methods* **16**, 1146-1152 (2019).
44 **J. R. Kremer, D. N. Mastronarde & J. R. McIntosh.** Computer visualization of three-dimensional image data using IMOD. *J Struct Biol* **116**, 71-76 (1996).
45 **T. Hrabe, Y. Chen, S. Pfeffer, L. K. Cuellar, A. V. Mangold & F. Förster.** PyTom: a python-based toolbox for localization of macromolecules in cryo-electron tomograms and subtomogram analysis. *J. Struct. Biol.* **178**, 177-188 (2012).
46 **S. H. Scheres.** RELION: implementation of a Bayesian approach to cryo-EM structure determination. *J. Struct. Biol.* **180**, 519-530 (2012).
47 **D. Tegunov, L. Xue, C. Dienemann, P. Cramer & J. Mahamid.** Multi-particle cryo-EM refinement with M visualizes ribosome-antibiotic complex at 3.5 A in cells. *Nat Methods* **18**, 186-193 (2021).
48 **R. Evans, M. O'Neill, A. Pritzel, N. Antropova, A. Senior, T. Green, A. Žídek, R. Bates, S. Blackwell, J. Yim, O. Ronneberger, S. Bodenstein, M. Zielinski, A. Bridgland, A. Potapenko, A. Cowie, K. Tunyasuvunakool, R. Jain, E. Clancy, P. Kohli, J. Jumper & D. Hassabis.** Protein complex prediction with AlphaFold-Multimer. *bioRxiv*, 2021.2010.2004.463034 (2021).

CHAPTER 6

General discussion

Max Gemmer[1]

[1] Structural Biochemistry, Bijvoet Center for Biomolecular Research, Utrecht University, 3584 CG Utrecht, The Netherlands

In this thesis, I have dissected the variable molecular landscape of the human ribosome-associated endoplasmic reticulum (ER) translocon complex using cryo-electron tomography (cryo-ET). Extensive subtomogram analysis reveals ribosome states, including eight elongation intermediates and two hibernating states. At the ribosomal tunnel exit, I distinguished one soluble ribosome population and three major ER translocon variants, the Sec61-TRAP, Sec61-TRAP-OSTA, and multipass translocon. Using AlphaFold prediction models, we succeeded to build a near-complete atomic model of the most abundant variant, Sec61-TRAP-OSTA, revealing specific interactions of TRAP with the ribosome and other translocon components. Moreover, I detected a novel OSTA-specific intramembrane protein T1, as well as two novel OSTA-associated proteins L1 and L2 in the ER lumen. I characterized the composition of the multipass translocon in the context of translation activity and visualized interactions between TRAP and an unidentified component of the mulitpass translocon, most likely NOMO. Finally, I characterized the ultrastructural organization of ribosome intermediate states and ER translocon variants with polysomes at the ER membrane and in solution. In essence, I visualized the molecular toolbox required for manufacturing secretory pathway proteins at unprecedented detail (Fig. 1). My observations can largely be categorized into the four steps following the process of protein biogenesis: (i) protein biosynthesis, (ii) signal peptide (SP) insertion, (iii) multipass transmembrane helix (TMH) insertion, and (iv) glycoprotein folding. In this chapter, the implications of my findings are discussed in context with our understanding of protein biogenesis at the ER membrane.

Protein biosynthesis

To facilitate polypeptide synthesis, ribosomes recruit elongation factors and aminoacyl-tRNAs and undergo extensive conformational rearrangements. The process underlying polypeptide elongation is referred to as the elongation cycle [1]. Capturing high-resolution structures of ribosome intermediates often requires stalling of a particular state using chemical tools like non-hydrolyzable GTP analogs or antibiotics. Although such studies have provided valuable insights into the molecular mechanisms underlying the mammalian elongation cycle, such as mRNA decoding and tRNA translocation [2-5], these approaches typically require extensive purification and enrichment, procedures which potentially disrupt interactions between the ribosome and its binding partners. An earlier study characterized the distribution of elongation intermediates in polysomes *ex vivo* [6], which however was based on size-exclusion gel-filtration as well. Until recently, further structural studies visualizing the molecular landscape of intermediate states remained scarce. Now, the rapidly advancing cryo-electron microscopy (cryo-EM) techniques, especially cryo-ET, are increasingly used to dissect the heterogeneous mixture of co-existing ribosomal elongation intermediate states *ex vivo* and *in situ* [7-10].

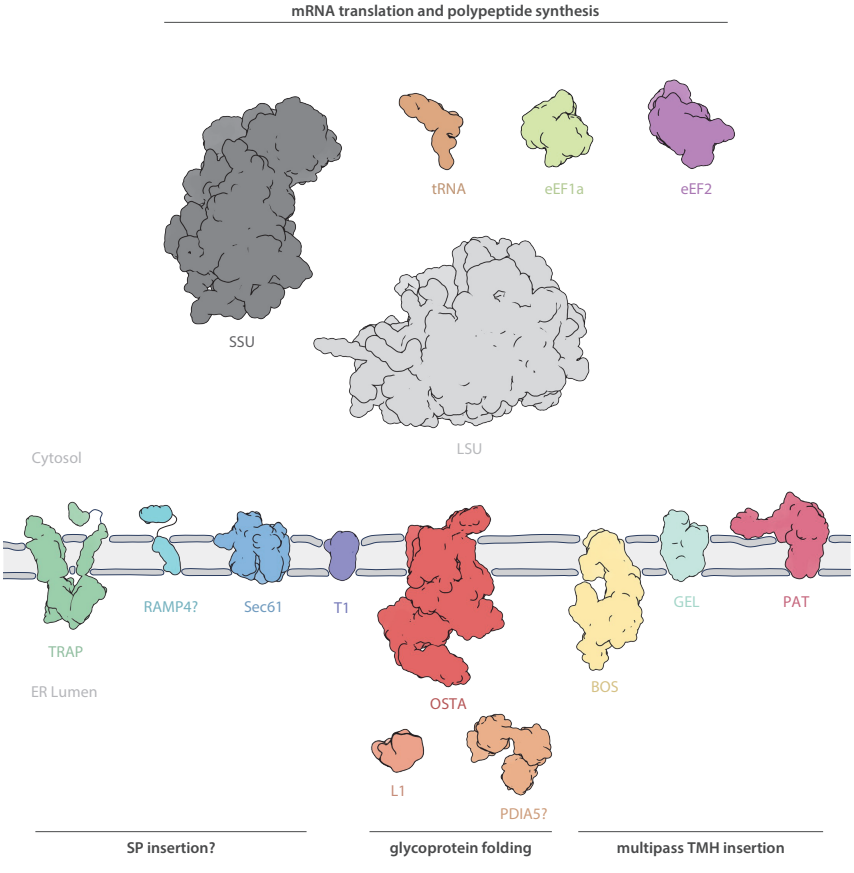

Fig. 1: The observed molecular toolbox for manufacturing secretory pathway proteins. Overview of cytosolic, membrane-resident, and ER luminal protein biogenesis factors observed in this study.

To structurally analyze human ribosome intermediate states, I used ER-derived vesicles, rapidly isolated from HEK293 cells with as minimal purification steps as possible [11]. Using cryo-ET and subtomogram analysis, I distinguished ten ribosome classes, seven classes of which I assigned to elongation cycle intermediates and two classes to hibernating states, based on previously published structures [2-4,6,12]. My assignment to elongating and hibernating particles is consistent with their polysomal organization. Remarkably, the abundance of intact, actively elongating ribosomes was substantially higher (90%) in my vesicle preparations from human HEK293 cells compared to preparations from canine (30%) [13] or porcine (13%) [14] pancreas. Although the ER enrichment of my preparations is generally lower than in the preparations from organs, the rapid isolation, genetic and biochemical modifiability, high throughput, and reproducibility demonstrate the advantage of the use of cell lines over tissue.

The occurrence of intermediates is largely consistent with mammalian *in situ* structural studies [9-11] and with the rate-limiting steps of the bacterial elongation cycle [15]. However, I observed significant differences in elongation factor recruitment compared to other cryo-EM studies. In our study, I found 66% of intermediates bound to elongation factors, while only 8% were observed to be factor-bound in the previous *ex vivo* analysis of purified polysomes [6], indicating dramatic differences based on purification procedures. To validate my *ex vivo* results, we analyzed a small *in situ* set from different human cell lines (HEK-293, U2-OS, HeLa) [11]. The abundance of *in situ* intermediates (70% factor-bound) is consistent with that of my *ex vivo* analysis and other *in situ* studies in human (66%) [10] and *Dictyostelium discoideum* (72%) [7] cells. However, I noted significant structural differences in ribosome-associated factors between these studies and ours. Specifically, I observed an intermediate in the classical-pre state bound to eEF1a in the extended conformation *ex vivo*. Our *in situ* analysis in human cell lines [11] and a follow-up study in murine (MEF) cells [9] also detected a factor bound to the classical-pre state, consistent with my *ex vivo* analysis. Although the resolution was not sufficient to identify the putative eEF1a density, it reveals strong differences to the recent *in situ* study in human cells (T-REx-293), which did not detect this factor-bound classical-pre state [10]. Such significant differences are surprising, considering the close relationship between some of the analyzed cell lines used in these studies (HEK-293 and T-REx-293). Thus, I reasoned that the distribution of intermediate states may be affected by the cellular state and environmental factors, such as growth medium and temperature. Classification error might also be an explanation, although considered unlikely by us. While *in situ* cryo-ET is considered the closest-to-native technique in the field, our results demonstrate that careful interpretation is warranted. In the future, the investigation of the prokaryotic and eukaryotic elongation cycle will benefit from increasingly higher accessibility of cryo-EM techniques, improved data processing and the increasing number of *in situ* studies in general. Analyzing ribosomal intermediates will become a routine approach to assess the cellular state of the vitrified specimen and may reveal cellular or environmental factors affecting elongation intermediates.

Signal peptide insertion

Secretory and membrane proteins employ the secretory pathway, i.e., they must enter the ER in order to reach their final subcellular destination. Most secretory pathway proteins comprise an N-terminal, cleavable SP which recruits the signal recognition particle (SRP) to the ribosome once the SP emerges from the ribosomal tunnel exit. The SRP pauses translation and targets the ribosome-nascent chain (RNC) complex to the ER membrane [16]. There, the SRP receptor (SR) and the SRP mediate handover of the SP to the Sec61 protein-conducting channel. The solubilized RNC-SRP-SR intermediate

has been structurally studied in isolation using non-hydrolyzable GTP analogs but it is not captured by my analysis likely due the short-lived nature of this intermediate [17].

The SP then inserts into the central pore of Sec61 head-on, with its N-terminus facing the ER lumen [18]. Upon insertion into the lateral gate, the SP flips its topology with the N-terminal now facing the cytosol. After dissociation of the SRP, mRNA translation continues while the polypeptide chain is co-translationally translocated through the central pore of Sec61 [19]. Various *in vitro* experiments show that the SP can be cleaved off co-translationally [20-24]. The cryo-EM structure of the SP-bound Sec61 has been determined in isolation using a truncated construct of the model substrate protein preprolactin, revealing structural details of SP accommodation [25].

Consistent with previous lower-resolution cryo-ET studies [13], I observed a helical SP-like density (SPLD) in the most abundant translocon variant, Sec61-TRAP-OSTA, residing at the same position as the SP, accommodated by the lateral gate of Sec61 (Fig. 2) [11]. Hence, one obvious hypothesis is that the SPLD represents a mixture of SPs from precursor proteins. A consequence of this interpretation would be that there is a long lag-time between SP accommodation and signal peptidase complex (SPC)-mediated cleavage, as SP-less Sec61 populations are not detected for the most abundant ER translocon class (Sec61-TRAP-OSTA). This observation could be explained by the steric inaccessibility of the SP to the SPC while the ER-translocon is bound to a ribosome. The cytosolic SPC domain would clash with the ribosome [26], requiring either transient release of the ribosome from the ER-translocon or permanent dissociation of the SP from the lateral gate.

Surprisingly, in addition to the actively translocating translocon, I also observed SPLD associated with inactive ribosome-translocon complexes under unperturbed conditions as well as under conditions of ER stress (Chapter 4). The transition of these particles into an inactive state is likely to have occurred much later after the completion of translocation [11]. Thus, if the SPLD indeed represented a mix of SPs, these observations would be difficult to reconcile with the model of co-translational SP cleavage. As discussed above, SP release is likely to occur prior to SP cleavage [22,26]. Hence, association of SPs with inactive particles is not plausible. Although some SPs are known to be cleaved post-translationally [27,28], SP cleavage is generally thought to occur very early during translocation [29], which is inconsistent with the stoichiometric SPLD observed in my reconstruction of inactive particles. Even the reconstruction of the active translocon complex, which is an average of translocons at all stages of the translocation process, would not be expected to feature a stoichiometrically bound SP mixture. Thus, I reasoned that instead of a heterogenous SP mixture, SPLD could correspond to a small, hitherto unknown translocon component.

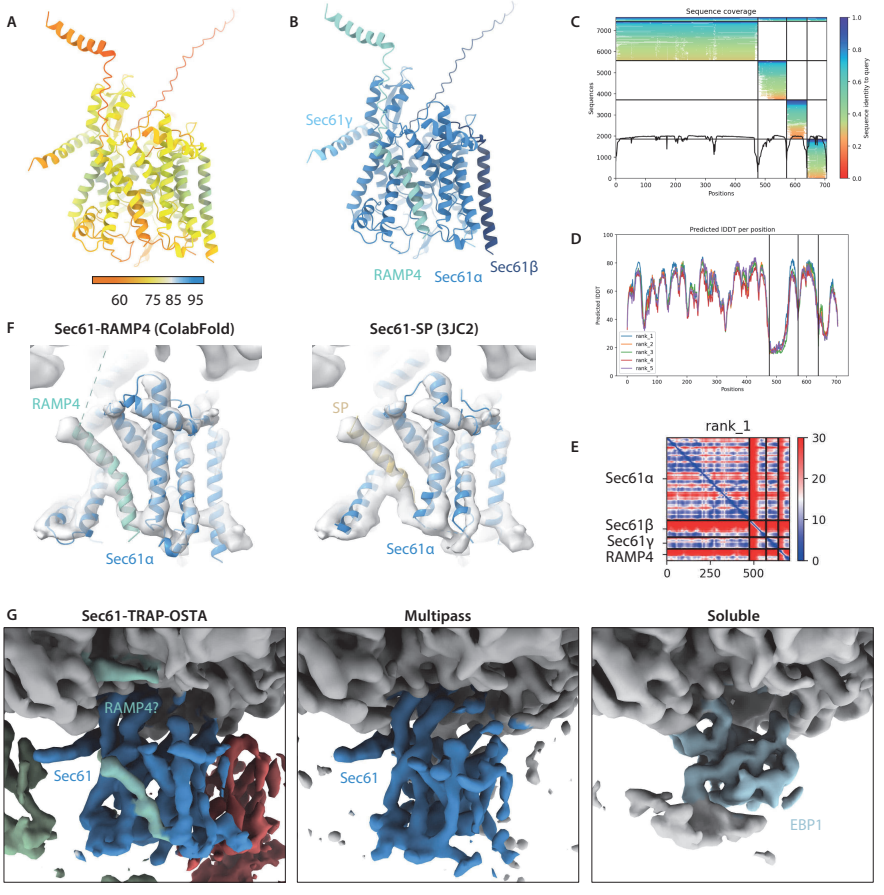

Fig. 2: A putative gate-occupying translocon component. (A) Colabfold prediction of Sec61α, Sec61β, Sec61γ, and RAMP4. The N-terminal helix and TMH comprise amino acid residues 1-22 and 40-65, respectively. The full-length sequence of each subunit was used for prediction. (B) Colabfold prediction as in (A) color-coded according to pLDDT as indicated. (C) Sequence coverage obtained by sequence alignments generated by MMseqs2. (D) pLDDT scores per position of five model predictions. (E) Predicted aligned error (PAE) of the best ranked model prediction. (F) Colabfold model of Sec61-RAMP4 or cryo-EM structure of Sec61-SP (3JC2) fitted into the reconstruction of the Ribosome-Sec61-SPLD-TRAP-OSTA translocon. (G) Comparison between reconstructions of Sec61-SPLD-TRAP-OSTA-, Sec61-multipass-, and EBP1-bound ribosomes. SPLD and RBHD are colored in cyan and may represent TMH and cytosolic helix of RAMP4, respectively. At the ribosome, putative RAMP4 helix contacts mostly the 28S rRNA, and RPL22, RPL19.

Among the biochemically characterized interaction partners of the ER translocon, ribosome-associated membrane protein 4 (RAMP4), also known as stress-associated endoplasmic reticulum protein 1 (SERP1), is a promising candidate for SPLD [30-34]. The protein was identified decades ago to be associated with Sec61 and TRAP in the ER translocon [30]. This protein is abundantly expressed in many cells comparable to the expression level of TRAP subunits [35]. However, it was not detected in the mass-

spectrometry analysis of my microsome preparations, which is likely due to the limited sensitivity for small membrane proteins. RAMP4 has a molecular weight of only 7 kDa and was predicted to comprise a single TMH and a small cytosolic domain [36], which is consistent with recent AlphaFold models [36,37]. However, structural studies that characterize its interaction with Sec61 are scarce. Biochemical experiments demonstrated that RAMP4 crosslinks to ribosomal protein 17 (RPL17) and Sec61β, both of which reside in proximity to the lateral gate [33]. The ColabFold [38] model of Sec61α, Sec61β, Sec61γ and RAMP4, which I generated after publishing the results of chapter 4, predicts the TMH of RAMP4 to associate with the lateral gate of Sec61 with moderate confidence (pLDDT ~75%, PAE ~15) (Fig. 2A-E). Strikingly, the prediction model of Sec61-RAMP4 is in excellent agreement with the reconstruction of the Sec61-TRAP-OSTA translocon and explains SPLD even better than the slightly shorter SP from the isolated preprolactin intermediate [25] (Fig. 2F). This result makes RAMP4 a strong candidate for SPLD. Moreover, I observed a ribosome-bound α-helical density (RBHD) proximal to the lateral gate, contacting RPL22, RPL19 and the 28S rRNA. RBHD could not be explained by previously published structures (4UG0) of the human ribosome [39]. Intriguingly, I observed RBHD only in the Sec61-TRAP-OSTA-bound ribosome, which also features SPLD, while it was absent in soluble or multipass-associated ribosome populations, which lack SPLD (Fig. 2G). Thus, I speculate that the unassigned RBHD and SPLD may be the same protein and could represent the cytosolic helix and TMH of RAMP4, respectively. The flexible linker between the two helices is long enough to bridge the gap between ribosome and the lateral gate. A continuous density observable at low contour level connecting RBHD and SPLD supports this notion. Collectively, I propose that a structurally unidentified component, likely RAMP4, associates with the lateral gate of the Sec61-TRAP-OSTA translocon and with the ribosome in the cytosol.

The presence of a gate-occupying translocon component would have significant implications on the process of Sec61-mediated SP and TMH insertion. In the arrangement with Sec61, SPLD would block access of the nascent protein to the lateral gate. SPs and TMHs that are engaging with a laterally occluded Sec61 would have to compete with SPLD for the lateral gate. Considering the diverse physicochemical properties of precursor proteins, many SPs or TMHs with weak affinity to the lateral gate, such as the SPs of TRAP clients [40,41], will likely not be able to replace SPLD on their own. Since the lateral gate contributes to the reorientation of SPs during insertion [19,25,42], the SPLD component may ultimately be able to regulate topogenesis of protein substrates. On a different note, SPLD may play a role in SP release from Sec61, a process which is thought to occur spontaneously and is poorly addressed in literature to this point.

Identification and functional characterization of the suggested novel translocon component is important to understand its role in protein biogenesis. Knockout (KO), knockdown (KD), or fusion tagging of candidate proteins, such as RAMP4, in conjunction with cryo-ET may allow unambiguous identification of the putative protein. Upon identification, further experiments using WT and KO cell lines of RAMP4 or other candidates may provide functional insights. Analyzing protein abundance using whole cell proteomics upon RAMP4 depletion in conjunction with biochemical validation experiments may reveal RAMP4-dependent protein clients. Cell-free *in vitro* translation experiments of defined insertion intermediates of such newly identified or previously known RAMP4 clients [32] may reveal the determinants of RAMP4 recruitment. Its effects on protein topogenesis may be examined using immunoblotting of client proteins carrying natural or artificially introduced glycosylation sites. Collectively, I detected a putative novel translocon component, which may become a pivotal aspect in our understanding of SP and TMH insertion.

TRAP complex

Although all SPs have a common secondary structure, the variability of SPs in precursor proteins is tremendously large, resulting in a variation of the physicochemical properties of SPs [22]. Some SPs require accessory factors to mediate insertion, such as the TRAP complex [41]. TRAP is a heterotetrameric, near-stoichiometric component of the translocon and was identified three decades ago [43], but its function and mechanism remained largely obscure. Biochemical assays and whole cell proteomics of TRAP KOs demonstrated that TRAP-dependent SPs feature lower-than-average hydrophobicity and higher-than-average glycine-and-proline content [40,41]. Cryo-EM single particle analysis (SPA) studies of TRAP-associated ribosomes failed to resolve atomistic details, since the resolution was insufficient for *de novo* model building, likely due to the flexibility of the complex. While cryo-ET revealed the domain architecture of TRAP, atomistic structure determination also failed due to limited resolution [13,44]. However, recent developments of the highly accurate protein prediction tools Alphafold and ColabFold [37,38,45], in conjunction with cryo-EM and cryo-ET studies, allowed us and three other research groups [46-48] to determine the molecular model of the TRAP complex. While the structure does not reveal an obvious molecular mechanism, it allows formulation of hypotheses about TRAP's mechanism in protein biogenesis.

As shown by a recent cryo-EM study published while chapter 4 was under review, TRAPα comprises a short C-terminal, cytosolic α-helix, flexibly linked to the TRAPα TMH, which serves as ribosome anchor and may promote tethering of ribosomes to the ER membrane prior to translocation [46]. Conversely, the TRAPα anchor may

keep TRAP flexibly tethered to the ribosome during translocation, even when the TRAP complex moves out of position next to the translocon [11,46]. TRAPα's luminal domain resides directly below the channel exit of Sec61 and binds to the β-hairpin loop of Sec61's hinge region. Since the conformation of this hinge does not show any alterations in cryo-EM structures of open and closed Sec61 complexes across different species [11,13,49-51], TRAP is likely not sufficient to open the lateral gate on its own. Thus, I speculate that TRAP allosterically cooperates with Sec61 when SPs with weak gating efficiencies engage the Sec61 pore and interact with the TRAPα luminal domain (allosteric model). The allosteric interaction of TRAP with Sec61 may decrease the energy barrier to open the lateral gate.

Other independent single-particle cryo-EM studies, which also provided structural insights into the TRAP complex, proposed alternative hypotheses on its molecular mechanism [46-48]. A hydrophobic cradle formed by the luminal domains of TRAPαβδ has been suggested to carry chaperone-like functions and may interact with the nascent chain [46]. Negatively charged residues in the disordered luminal TRAPα domain have also been speculated to interact with the nascent chain to prevent back-translocation into the cytosol [47]. The proposed contacts of TRAPα with the nascent chain would be consistent with earlier crosslinking studies [52]. Besides TRAPα, TRAPγ also comprises a binding site to the ribosome and contacts the N-terminus of Sec61γ at the cytosolic face of the membrane. The arrangement of TRAP and Sec61 forms a V-shaped transmembrane segment, which induces local curvature and thinning of the ER membrane at the site proximal to the lateral gate [11,47] . In conjunction with molecular dynamics (MD) simulations, this lipid nanocompartment was suggested to stabilize Sec61 in a laterally open conformation (stabilizing model) [47].

The observation of a lateral gate-associated SPLD in the majority of translocon complexes gives rise to a third, alternative model of TRAP (displacement model). I speculate that newly synthesized SPs that emerge from the ribosomal tunnel exit may encounter a laterally occupied Sec61. SPs with low affinity to the lateral gate, such as the SPs of TRAP clients, including preproinsulin and the prion protein [41,53-55], would fail to displace SPLD on their own. A model, in which TRAP cooperates with the translocon to trigger release of SPLD or to mediates its displacement by subsequent SPs would explain the putative role of TRAP in insertion of SPs equally well as the allosteric or stabilizing model.

In addition to Sec61 and the ribosome, I observed TRAP in association with other translocon components. In the ER membrane, the TRAPα TMH resides near an unidentified, OST-specific transmembrane protein that I named T1 (chapter 4). Attempts to identify T1 using crosslinking mass spectrometry (XL-MS) or by comparing

its architecture with Alphafold models of candidate proteins that are abundant according to mass-spectrometry analysis failed, and I can only speculate about its function. TRAPα, T1, Sec61, and OSTA form a lipid-filled cavity at a site proximal to the hinge region of Sec61, similar to the cavity formed by multipass translocon components [56,57]. Furthermore, the cryo-EM SPA structure of an insertion intermediate of the GPCR model substrate opsin indicated that Sec61 and OST subunit OSTC intercalate a TMH, which may correspond to the nascent chain [49]. This finding is supported by immunoprecipitation studies of other multipass insertion intermediates demonstrating that the OSTA-bound translocon can accommodate up to two TMHs, before it is displaced by the multipass translocon [58]. How the putative Sec61-OSTA-bound TMH is released is not known. Interestingly, the location of this unidentified helix is adjacent to the cavity formed by T1 and thus I speculate that this cavity may be involved in TMH accommodation, while the contacts to OSTA and TRAP may allow intermolecular communication. The role of T1 and its interplay with TRAP and OSTA remains to be explored.

TRAP contacts another unidentified protein of the multipass translocon. In chapter 5, I suggest that this protein is most likely NOMO. This direct interaction of TRAP with the multipass translocon observed in our reconstruction hints to a previously unknown role of TRAP in multipass membrane protein biogenesis. The results and their implications are discussed in the following section.

Collectively, I visualized TRAP and its intricate interaction network with the ribosome, Sec61α, Sec61β, T1 and presumably NOMO in its native membrane environment. While recent results allow to speculate about its mechanism, the interplay between TRAP and other translocon components remains poorly understood. However, the molecular model of TRAP will pave the way for future structure-based functional studies. Topology analysis of TRAP-dependent client proteins, such as the prion protein, in WT cells or TRAP mutants that disrupt specific interactions may provide further mechanistic details and reveal how TRAP cooperates with its binding partners. MD simulations of Sec61, TRAP or TRAP mutants, and different SPs with varying affinity to the lateral gate may further elucidate the mechanism of TRAP-mediated SP insertion.

Multipass membrane protein insertion

The Sec61-TRAP-OSTA translocon governs translocation of soluble and single-TMH proteins. In the presence of more than two TMHs of multispanning membrane proteins, the OSTA complex is displaced by another set of specialized translocon components, collectively termed multipass translocon [58]. The multipass translocon comprises

three obligate heterooligomeric complexes named GET- and EMC-like (GEL), protein associated with translocon (PAT), and back of Sec61 (BOS) [56-58]. GEL consists of the insertase TMCO1 and OPTI (previously known as C20Orf24) and is thought to mediate insertion of TMH pairs behind Sec61, while the loops that connect the two TMHs are moved through the membrane via a semihydrophilic groove. PAT comprises CCDC47 and the intramembrane chaperone asterix, which protects TMHs with exposed hydrophilic residues [59]. Finally, BOS consists of TMEM147, nicalin (NCLN), and one of the three nearly identical paralogs NOMO1, NOMO2, or NOMO3, collectively termed NOMO [60,61]. The function of BOS in humans is not known. GEL, BOS, and PAT form a lipid-filled cavity together with Sec61 to protect the nascent chain in a confined membrane compartment behind Sec61 opposite to the lateral gate.

While cryo-EM structures revealed the organization of multipass components, subtomogram analysis provides valuable insights into their composition in the native membrane environment (Chapter 5). The PAT complex is a variable component which is transiently recruited to the translocon in a translation-dependent manner. While PAT associates dynamically with the active translocon, it is reduced in inactive translocons and absent under ER stress condition, where the majority of ribosomes is inactive (97%). Since PAT specifically binds TMHs with exposed hydrophilic residues, I speculate that its recruitment is dependent on the presence of protein clients with such specific properties [59]. Thus, PAT may dissociate together with its client after translocation, explaining why it was not observed under ER stress condition. Biochemical analysis of different multipass insertion intermediates are consistent with this idea [57].

The TRAP complex is a second variable and novel component of the multipass translocon. Previously, TRAP was characterized as strictly stoichiometric translocon component [13]. However, in context of multipass protein biogenesis, TRAP is variable during active translocation and primarily associated with the inactive translocon. This observation suggests that release of TRAP may be a requirement for multi-TMH insertion. This notion is plausible considering that TRAP supports Sec61-mediated insertion of SPs and single-TMHs and thus would interfere with multi-TMH insertion by the multipass translocon at the backside of Sec61 [62]. In contrast to our results, cryo-EM SPA structures visualize TRAP associated with the substrate-bound state but not the apo state of the isolated multipass translocon [56,57]. Thus, the recruitment of TRAP and its interplay with the multipass translocon requires further investigation.

Based on the recentered and focused reconstruction of the multipass translocon (Chapter 5), colabfold model predictions [37,38], as well as biochemical [60,61] and MS data [56], I suggest that TRAP interacts with BOS subunit NOMO in the ER lumen. NOMO is a type II membrane protein with a large N-terminal segment predicted to comprise 12

consecutive immunoglobulin (Ig)-like domains. My results indicate that Ig-like domains 11 and 12 interact with NCLN, while domain 12 contacts TRAPβ and TRAPδ. The direct interaction between TRAP and NOMO further suggests a functional link between TRAP and multipass membrane protein biogenesis. While TRAP has been shown to affect insertion of single- or double-TMH proteins [62], its role in multipass protein biogenesis is unexplored. In contrast, human BOS subunits or their metazoan homologs have been shown to regulate subunit composition and subcellular distribution of membrane proteins, indicating a role in membrane protein assembly and quality control [63-66]. Considering TRAP's and BOS's connection to Sec61-mediated or multi-TMH insertion, respectively, it seems plausible that TRAP and BOS may cooperate to coordinate the insertion process.

While the interaction between TRAP and NOMO may allow intermolecular communication, the mechanism underlying TRAP release remains unclear. Sec61, TRAP and the multipass translocon complexes GEL, PAT, and BOS do not appear to sterically hinder each other at the translocon and have been shown to coexist [57,58]. Intriguingly, the subtomogram reconstructions of multipass translocon populations reveal different conformations of the BOS complex, that may explain TRAP release. In the absence of TRAP, BOS adopts a tilted orientation. Although the resolution is not sufficient to individually place NOMO and NCLN into the reconstruction, I speculate that NOMO domain 12 would clash with the luminal domain of TRAPα and thus would be incompatible with TRAP binding. In the presence of TRAP, BOS adopts a straight orientation and forms direct contacts to the TRAP complex. I hypothesize that conformational changes of the luminal BOS segment, possibly induced by yet undetermined translocation events, may trigger TRAP release by displacing its luminal domain at the Sec61 hinge region. In an alternative model, TRAP release and recruitment may induce conformational changes of the BOS complex to regulate the multi-TMH insertion process. Clearly, understanding the determinants for TRAP recruitment and release requires further investigation.

Both, the lateral gate and plug domain of the multipass-associated Sec61 channel adopt a closed conformation. Thus, multi-TMH insertion appears to be solely mediated by the specialized multipass components, while Sec61 may only be required for docking to the ribosome. Consistently, translocation of multipass membrane proteins is not affected by Sec61 inhibitors [57]. PAT complex subunit CCDC47 has been proposed to impede lateral opening of Sec61 by constraining the movement of Sec61's N-terminal half. In cryo-EM structures of solubilized isolates, only the PAT-bound translocon was observed to be closed, while the N-terminal half of Sec61 was flexible in the absence of PAT [57]. In the subtomogram reconstructions of the multipass translocon, however, I always observed Sec61 in a closed conformation, regardless of the associated factors

PAT or TRAP. These observations do not support the notion of CCDC47 causing gate closure.

Multipass-associated ribosomes, as well as Sec61-TRAP-OSTA-associated and soluble ribosomes tend to cluster with distinct polysome chains, reflecting the substrate-dependent translocon requirements of multispanning and SP-containing proteins, respectively [11]. However, multipass membrane proteins carrying glycosylation sites still rely on association of OSTA. Since multipass translocon components and OSTA are mutually exclusive, these factors are dynamically exchanged during translocation. Translocation of ER luminal or extracellular domains upstream or downstream of the membrane domain is again dependent on Sec61 [58].

Taken together, I characterized the structural organization and composition of the multipass translocon. I identified TRAP as novel, sub-stoichiometric multipass translocon component and interaction partner of a structurally unidentified subunit of the BOS complex, most likely NOMO. Validation of NOMO and the role of TRAP and BOS in multipass membrane protein biogenesis remains to be established. NOMO KO or KD coupled with cryo-ET will likely not be suitable for structural identification since BOS subunits are mutually dependent on each other [58,60,61]. In contrast, site-specific nanobodies or fusion-tagging may be feasible for structural identification of NOMO *ex vivo*, while immunoprecipitation of NCLN and WT or mutant NOMO will be important to validate their interaction. To gain functional insights into the BOS complex, whole cell proteomic analysis of KOs of NOMO, NCLN, or TMEM147 may reveal BOS-dependent client proteins. Analyzing abundance, oligomerization, localization, and topology of these identified clients in context of WT and mutated BOS subunits will provide valuable insights into their function and interplay with TRAP.

Glycoprotein folding

N-linked glycosylation is a post-translational modification essential for protein folding, quality control, sorting, secretion, signal transduction, and cell surface interactions [67-69]. In humans, co-translational N-glycosylation is facilitated by the heterooctameric OSTA complex [70]. Its catalytic subunit, STT3a, covalently attaches a $GlcNAc_2Man_9Glc_3$ glycan to an asparagine residue of the N-X-S/T motif (X = any amino acid except proline) of the nascent chain as it emerges from the Sec61 channel. Other subunits, such as OSTC and ribophorin 1 (RPN1) form contacts with Sec61 and the ribosome, respectively, mediating stable association with the ribosome-translocon complex [49,71]. Although structures of the yeast OST and human OSTA and its post-translational paralog OSTB have been solved, little is known about the functions of the other subunits RPN2,

OST48, OST4, DAD1, and TMEM258 [72,73]. It has been suggested that their luminal domains serve as docking platforms for ER-resident chaperones, such as malectin, a chaperone which associates with processed glycoproteins and specifically interacts with RPN1 [73-76]. Using cryo-ET, I observed two additional interaction partners of OSTA named L1 and L2. Both, L1 and L2, contact OST subunits STT3a and OST48, while L2 also interacts with RPN2.

The obtained resolution of 7-12 Å is insufficient to unambiguously identify L1 and L2 (Chapter 4). However, I speculate that the novel interaction partners are associated with the downstream glycoprotein folding pathway, known as the calnexin (CNX)/ calreticulin (CRT) cycle [77]. Many members of the CNX/CRT cycle are functionally and structurally well characterized [78], allowing for comparison of size and shape of these candidates with L1 and L2. While L1 is not sufficiently well defined to allow identification, L2's domain architecture is highly reminiscent of that of protein disulfide isomerases (PDIs).

The PDI family comprises more than 20 different members, most of which support protein folding by catalyzing cleavage, formation, or isomerization of disulfide bridges [79,80]. However, only two PDI members, PDIA3 and PDIA5 (also known as ERp57 and PDIR, respectively), have been shown to act specifically on glycoproteins by cooperating with the glycoprotein-binding chaperones CNX and CRT [81-84]. Unpublished XL-MS data of ER-derived vesicles (J. Fedry, T. Shamorkina, J. Snijder) revealed a crosslink between the third domain of PDIA5 and OSTA subunit RPN1. While more data are needed to confidently identify the L2 density, this observation is consistent with the arrangement of L2 and OSTA. Strikingly, the Colabfold [38] model of the assembly of PDIA5 and the luminal domains of OST subunits STT3a, OST48, and RPN2 matches almost precisely the arrangement of L2 with OSTA as observed in the cryo-ET reconstruction (Fig. 3A-F). While the prediction of PDIA5-STT3a-OST48-RPN2 generated a structure with very high confidence (PAE <10), Colabfold fails to predict a high-confidence model for OSTA subunits and PDIA3 (PAE ~30) (Fig. 3F), suggesting that PDIA5 but not PDIA3 is an interaction partner of OSTA. To further support this hypothesis, I computed the electrostatic potential onto the surface models of OSTA and PDI candidates [85]. The areas of OSTA at the interface to L2 are highly acidic, complementing the highly basic domains 1 and 4 of PDIA5 (Fig. 3G). In contrast, other PDIs, including PDIA3, are moderately to highly acidic and, hence, are not likely to bind to the OSTA complex (Fig. 3G). Although future validation experiments will be required, my results strongly suggest that PDIA5 associates co-translationally with the OSTA complex.

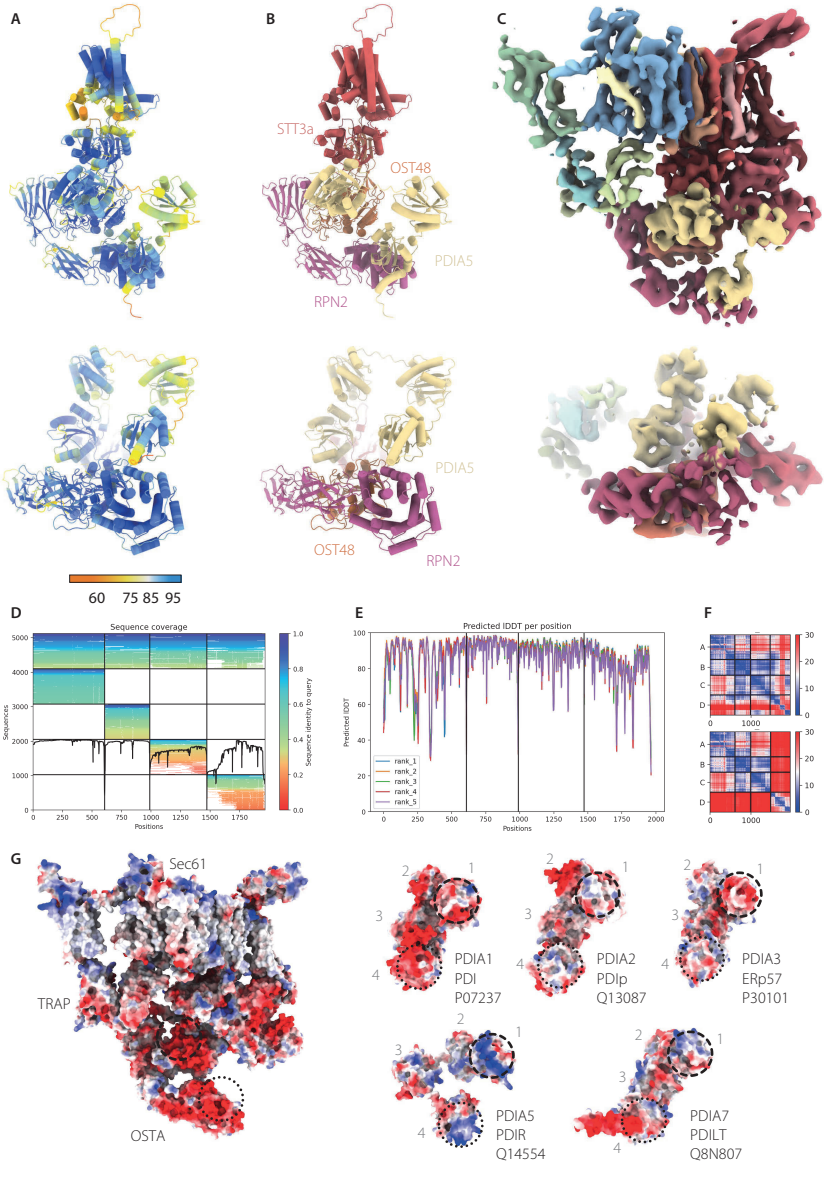

Fig. 3: Towards identification of an OSTA-associated chaperone. (A) Colabfold model of truncated domains of STT3a (aa38-264, aa324-705), OST48 (aa42-422), RPN2 (aa22-505), and PDIA5 (aa28-519) color-coded according to pLDDT. (B) Colabfold model as in (A) color-coded according to subunit domains. (C) Reconstruction of Sec61-TRAP-OSTA-L2. (D) Sequence coverage obtained by sequence alignments generated by MMseqs2 in the following order: STT3a, OST48, RPN2, PDIA5. (E) pLDDT scores per position of five model predictions. (F) Predicted aligned error (PAE) of the best ranked model prediction for STT3a (A), OST48 (B), RPN2 (C) and PDIA5 (D) (top) or PDIA3 (D) (bottom). (G) Electrostatic potential plotted onto the surface representation of Sec61-TRAP-OSTA and AlphaFold models of PDI members with a characteristic 4-domain-structure. Domain number and putative interaction sites between OSTA and PDI domains 1 (dashed) and 4 (dotted) are indicated.

Both L1 and L2 bind to the most membrane-distant luminal part of STT3a in proximity to OST48. Compared to STT3a, the catalytic subunit of the post-translational OSTB complex, STT3b, comprises a longer C-terminal region which interacts with OST48 and blocks access to L1 and L2 [73]. Hence, I speculate that recruitment of the observed chaperones is limited to the co-translational variant. This notion is plausible because OSTB comprises two paralogous, integral oxidoreductase subunits, MagT1 or TUSC3 [86]. In addition to STT3a and OST48, L2 associates with the N-terminal domain (NTD) of RPN2. Some lower eukaryotes such as yeast [72] or *Chlamydomonas* [44], lack this domain. Among those species that contain the RPN2-NTD, its binding site to L2 domain 4 is highly conserved [11], indicating that L2 may have co-evolved with RPN2-NTD.

Given that the interfaces between OSTA and L1 or L2 are small, I speculate that their binding affinity to OSTA may be relatively low. This notion may explain why the chaperones are not captured by high-resolution SPA, since they presumably dissociate upon isolation of the detergent-solubilized complex [73]. It has been speculated that chaperones bind transiently to the translocon only in the presence of a nascent substrate. However, the occupancy of the observed luminal densities does not appear to be affected by stress-induced reduction of translational activity (not shown), arguing against this notion. Alternatively, L1 and L2 may bind to OSTA in a concentration-dependent manner. While this idea may be plausible for L1, it is not consistent with the abundance of the hypothetical L2 candidate PDIA5. PDIA5 abundance is approximately one order of magnitude lower than that of the OST subunits at mRNA and protein level [11,35], indicating that the vast majority of PDIA5 proteins may be in association with OSTA. On a different note, the electrostatic interactions between OSTA and L1 or L2 may be sensitive to high salt concentration and were thus previously disrupted during purification of OSTA (using 400 mM NaCl) [73]. Clearly, further studies will be required to identify and characterize L1 and L2.

Collectively, my results define a new checkpoint along the path of the nascent protein chain at the ribosome-associated translocon to enhance glycoprotein folding. I visualized OSTA-bound proteins in their near-native environment which are likely sensitive to extensive purification. Although I cannot unambiguously identify L1 and L2, my results provide a structural basis for future investigations of the OSTA-associated chaperone network. KO or KD of candidate proteins, such as PDIA5, combined with cryo-ET may allow identification of L1 and L2, while SPA of the isolated OSTA complex purified at lower salt concentrations or reconstituted with excess of candidate chaperones may provide high-resolution details of the interaction sites. Analyzing expression levels and the degree of misfolding of L1- and L2-dependent proteins, such as the PDIA5 client protein ATF6 [87], will be useful to study the relevance of L1 and L2 recruitment to the OTA in glycoprotein folding.

Protein biogenesis during ER stress

Protein homeostasis, the balance of protein synthesis, folding, and degradation, is essential for cellular health. Imbalance in processes regulating proteostasis, for instance caused by environmental or physiological stresses, leads to accumulation of misfolded proteins and causes ER stress. In response to ER stress, a cellular program known as the unfolded protein response (UPR) is activated to enhance the protein folding capacity of the ER [88]. Generally, UPR mediates induction of the protein folding machinery, reduction of protein flux into the ER, and increase of the ER size. The UPR comprises three ER membrane-resident key regulators responsible for measuring the degree of misfolded proteins in the ER and for triggering the UPR signal: IRE1α, ATF6, and PERK [88].

Upon ER stress, PERK oligomerizes and inhibits mRNA translation by triggering phosphorylation of eukaryotic initiation factor 2a (eIF2a) [89,90]. Consistently, I observed a dramatic reduction of translational activity from 90% under normal condition down to 3% under DTT-induced ER stress condition [11]. While I cannot rule out formation of hibernating intermediates as a result of sample preparation, I am confident that the hibernating states observed in the DDT-treated sample are induced by ER stress, as indicated by the strong inhibition of translation compared to normal condition as control. While hibernating states from normal and stress condition are similar, I noted differences in recruitment of hibernation factors dependent on the cellular states.

Recently, many novel hibernating factors have been observed in different cellular contexts, such as sporulation, dormancy in the egg, or upon nutrient starvation [12,91-93]. In general, hibernation factors inhibit translation by blocking access to important binding sites at the ribosome, such as the mRNA tunnel, elongation factor binding sites or the P-site tRNA. Induction of hibernating ribosome by nutrient starvation results in two different states associated with either eEF2a and SERPB1, or CCDC124 [12]. While the subtomogram reconstructions are not sufficiently resolved to detect small factors like SERBP1, I found CCDC124 and eEF2 associated with hibernating ribosomes at the ER membrane *ex vivo* [11]. Intriguingly, I detected CCDC124 under normal condition, but not upon ER stress induction, indicating that hibernation factor recruitment is dependent on the cellular state. CCDC124 has been shown to promote ribosome splitting, which may be important for rapid ribosome recycling and reinitiation of mRNA translation [12]. While this mechanism may be required for efficient protein synthesis under steady state condition, it would be unfavorable during stress. Thus, I speculate that, in order to control the protein flux into the ER, hibernation factor recruitment is regulated in context of different cellular states.

Consistent with the reduction of mRNA translation, I observed a strong decrease of polysomes upon ER stress induction as well as a strong reduction of high-order polysome chains, which is in line with previous experiments (Fig. 4) [94]. As previously reported, ribosomes can remain in contact with the ER membrane despite translational inactivity [95,96]. During synthesis of cytosolic proteins, ribosomes either detach from the membrane or remain ER-bound independently of the nascent chain or mRNA [97]. After overcoming ER stress, ER-bound ribosomes can reengage in translation of mRNAs encoding for secretory pathway proteins, which are then translocated into the ER in an SRP-independent manner [96].

The ER stress-induced inhibition of translation allows for analysis of the molecular landscape of inactive translocon variants. Consistent with biochemical assays, abundance and composition of the major translocon components Sec61, TRAP, and OSTA are not affected by ER stress [95]. The architecture of Sec61-TRAP-OSTA is nearly identical to that under normal condition and only the Sec61 plug domain was observed to undergo conformational changes [11]. While open under steady state condition, the plug occludes the central pore of Sec61 in the inactive translocon upon ER stress. I speculate that regulation at the level of translocon components is largely redundant, as reduction of protein flux into the ER is mostly governed by the UPR and hibernation factors inhibiting polypeptide synthesis in the cytosol.

In contrast to the Sec61-TRAP-OSTA complex, the composition of the multipass translocon is significantly affected by ER stress. While TRAP and PAT are variably recruited to the active translocon, PAT is absent and TRAP is stably associated with the translocon under stress. Considering the recruitment tendencies of TRAP with inactive and PAT with active translocons under steady state condition [11], I assume that this observation may be a result of translation inhibition, rather than a direct effect of the ER stress response. On the other hand, a previous study reported induction of all four TRAP subunits upon ER stress [98], which would be consistent with our observation of increased TRAP abundance at the multipass translocon.

TRAP was recently reported to regulate quality control of N-glycosylated proteins during ER stress [99]. In patients, germline mutations of TRAP subunits have been associated with congenital disorder of glycosylation [100-103], further supporting a role of TRAP in mediating N-glycosylation. While a direct role of TRAP is possible, studies that investigate the insertion of disrupted glycoprotein clients into the ER and their resulting topology are lacking. The observed glycosylation defects upon TRAP depletion may simply be caused upstream by impaired translocation of TRAP-dependent glycoproteins. Thus, further studies will be required to understand TRAP's role in glycosylation.

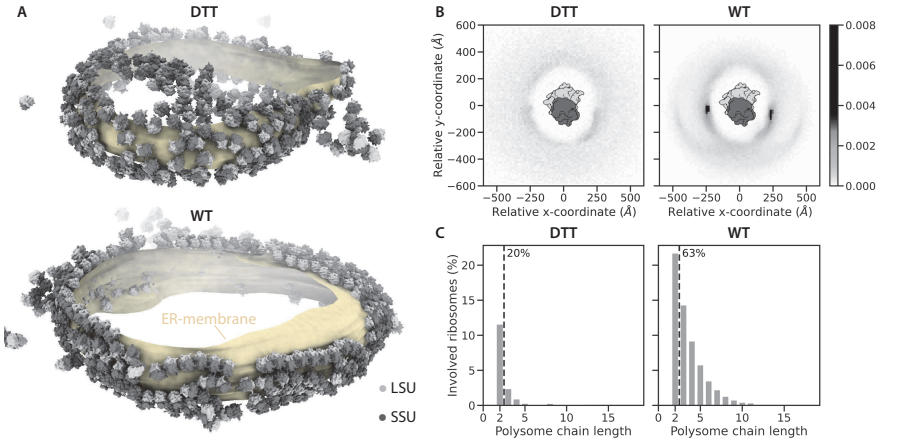

Fig. 4: ER-bound ribosomes under conditions of ER stress. (A) Segmentation of a tomogram from DTT-treated (DTT, top) or untreated (WT, bottom) specimens. (B) Spatial neighborhood probability of ER-associated ribosomes under stress (DTT) or normal condition (WT). (C) Proportion of ribosomes as function of polysome chain length in DTT and WT samples based on the spatial analysis from (B). Polysome chain length was determined by checking for presence of neighbors in the hot spot areas. Note that the percentage of ribosomes involved in polysomes strongly depends on mask thresholding. While they may not accurately represent the percentage of polysomal ribosomes, they allow comparison between the two samples.

Collectively, I visualized the ER-associated translation and translocation machinery under normal condition and condition of ER stress. While the molecular landscape of ribosome intermediates is strongly affected upon ER stress, composition, abundance, and architecture of ER translocon variants remain largely unchanged. I reasoned that the assembly of ribosome and translocon variants remain in stable association to efficiently reengage in protein synthesis once the cell overcomes ER stress.

Protein biogenesis in health and disease

Many of the translocon components characterized in this thesis are linked to various diseases [104,105], such as congenital disorder of glycosylation [44,99-102,106,107], facial dysmorphism and intellectual disability [108-115], cancer [87,116-120], glaucoma [121,122], and other diseases [108,110,123-127]. Moreover, many disease-related secretory pathway proteins undergo co-translational processing, modification, folding, and assembly at the ribosome-associated translocon, including proteins linked to neurodegenerative diseases, such as prion tauopathies [41,55,128] or Alzheimer's disease [129,130], viral infections, such as HIV [131,132] or SARS-CoV2 [133-135] infections, or cystic fibrosis [136-138]. Understanding the role of translocon components at high detail is therefore essential for the discovery of therapeutic targets.

Future perspectives

Structural biology will be a key technique to study the ER, its subcompartments and ER-resident proteins. As demonstrated by this work, cryo-ET enables structural investigation of membrane-embedded protein complexes at unprecedented detail and, in contrast to crystallography and SPA approaches, succeeds to capture interaction partners in the cytosol, membrane, and ER lumen, which are often disrupted upon purification. Developments of EM instrumentation and cryo-ET data acquisition and processing will pave the way for structural biology in the closest-to-native state, by preserving cellular context. While the resolution of cryo-ET reconstructions is generally low, the integrative combination of cryo-ET with high-resolution SPA, XL-MS, and protein structure prediction unfolds the full potential of these techniques. In this thesis, cryo-ET provided many unexpected observations which will inspire future functional studies.

References

1 **R. M. Voorhees & V. Ramakrishnan.** Structural basis of the translational elongation cycle. *Annu Rev Biochem* **82**, 203-236 (2013).

2 **V. Bhaskar, A. Graff-Meyer, A. D. Schenk, S. Cavadini, O. von Loeffelholz, S. K. Natchiar, C. G. Artus-Revel, H. R. Hotz, G. Bretones, B. P. Klaholz & J. A. Chao.** Dynamics of uS19 C-Terminal Tail during the Translation Elongation Cycle in Human Ribosomes. *Cell Rep* **31**, 107473 (2020).

3 **T. V. Budkevich, J. Giesebrecht, E. Behrmann, J. Loerke, D. J. Ramrath, T. Mielke, J. Ismer, P. W. Hildebrand, C. S. Tung, K. H. Nierhaus, K. Y. Sanbonmatsu & C. M. Spahn.** Regulation of the mammalian elongation cycle by subunit rolling: a eukaryotic-specific ribosome rearrangement. *Cell* **158**, 121-131 (2014).

4 **J. Flis, M. Holm, E. J. Rundlet, J. Loerke, T. Hilal, M. Dabrowski, J. Burger, T. Mielke, S. C. Blanchard, C. M. T. Spahn & T. V. Budkevich.** tRNA Translocation by the Eukaryotic 80S Ribosome and the Impact of GTP Hydrolysis. *Cell Rep* **25**, 2676-2688 e2677 (2018).

5 **S. Shao, J. Murray, A. Brown, J. Taunton, V. Ramakrishnan & R. S. Hegde.** Decoding Mammalian Ribosome-mRNA States by Translational GTPase Complexes. *Cell* **167**, 1229-1240 e1215 (2016).

6 **E. Behrmann, J. Loerke, T. V. Budkevich, K. Yamamoto, A. Schmidt, P. A. Penczek, M. R. Vos, J. Burger, T. Mielke, P. Scheerer & C. M. Spahn.** Structural snapshots of actively translating human ribosomes. *Cell* **161**, 845-857 (2015).

7 **P. C. Hoffmann, J. P. Kreysing, I. Khusainov, M. W. Tuijtel, S. Welsch & M. Beck.** Structures of the eukaryotic ribosome and its translational states in situ. *Nat Commun* **13**, 7435 (2022).

8 **L. Xue, S. Lenz, M. Zimmermann-Kogadeeva, D. Tegunov, P. Cramer, P. Bork, J. Rappsilber & J. Mahamid.** Visualizing translation dynamics at atomic detail inside a bacterial cell. *Nature* **610**, 205-211 (2022).

9 **J. Fedry, J. Silva, M. Vanevic, S. Fronik, Y. Mechulam, E. Schmitt, A. d. Georges, W. Faller & F. Förster.** Visualization of translation reorganization upon persistent collision stress in mammalian cells. *bioRxiv*, 2023.2003.2023.533914 (2023).

10 **H. Xing, R. Taniguchi, I. Khusainov, J. P. Kreysing, S. Welsch, B. Turoňová & M. Beck.** Translation dynamics in human cells visualized at high-resolution reveal cancer drug action. *bioRxiv*, 2023.2003.2002.529652 (2023).

11 **M. Gemmer, M. L. Chaillet, J. van Loenhout, R. Cuevas Arenas, D. Vismpas, M. Grollers-Mulderij, F. A. Koh, P. Albanese, R. A. Scheltema, S. C. Howes, A. Kotecha, J. Fedry & F. Forster.** Visualization of translation and protein biogenesis at the ER membrane. *Nature* **614**, 160-167 (2023).

12 **J. N. Wells, R. Buschauer, T. Mackens-Kiani, K. Best, H. Kratzat, O. Berninghausen, T. Becker, W. Gilbert, J. Cheng & R. Beckmann.** Structure and function of yeast Lso2 and human CCDC124 bound to hibernating ribosomes. *PLoS Biol* **18**, e3000780 (2020).
13 **S. Pfeffer, L. Burbaum, P. Unverdorben, M. Pech, Y. Chen, R. Zimmermann, R. Beckmann & F. Forster.** Structure of the native Sec61 protein-conducting channel. *Nat Commun* **6**, 8403 (2015).
14 **R. M. Voorhees, I. S. Fernandez, S. H. Scheres & R. S. Hegde.** Structure of the mammalian ribosome-Sec61 complex to 3.4 A resolution. *Cell* **157**, 1632-1643 (2014).
15 **M. R. Wasserman, J. L. Alejo, R. B. Altman & S. C. Blanchard.** Multiperspective smFRET reveals rate-determining late intermediates of ribosomal translocation. *Nat Struct Mol Biol* **23**, 333-341 (2016).
16 **R. J. Keenan, D. M. Freymann, R. M. Stroud & P. Walter.** The signal recognition particle. *Annu Rev Biochem* **70**, 755-775 (2001).
17 **A. Jomaa, Y. H. Fu, D. Boehringer, M. Leibundgut, S. O. Shan & N. Ban.** Structure of the quaternary complex between SRP, SR, and translocon bound to the translating ribosome. *Nat Commun* **8**, 15470 (2017).
18 **R. M. Voorhees & R. S. Hegde.** Toward a structural understanding of co-translational protein translocation. *Curr Opin Cell Biol* **41**, 91-99 (2016).
19 **R. Zimmermann, S. Eyrisch, M. Ahmad & V. Helms.** Protein translocation across the ER membrane. *Biochim Biophys Acta* **1808**, 912-924 (2011).
20 **G. Blobel & B. Dobberstein.** Transfer of proteins across membranes. I. Presence of proteolytically processed and unprocessed nascent immunoglobulin light chains on membrane-bound ribosomes of murine myeloma. *J Cell Biol* **67**, 835-851 (1975).
21 **R. C. Jackson & G. Blobel.** Post-translational cleavage of presecretory proteins with an extract of rough microsomes from dog pancreas containing signal peptidase activity. *Proc Natl Acad Sci U S A* **74**, 5598-5602 (1977).
22 **B. Martoglio & B. Dobberstein.** Signal sequences: more than just greasy peptides. *Trends Cell Biol* **8**, 410-415 (1998).
23 **W. Mothes, S. U. Heinrich, R. Graf, I. Nilsson, G. von Heijne, J. Brunner & T. A. Rapoport.** Molecular mechanism of membrane protein integration into the endoplasmic reticulum. *Cell* **89**, 523-533 (1997).
24 **B. Jungnickel & T. A. Rapoport.** A posttargeting signal sequence recognition event in the endoplasmic reticulum membrane. *Cell* **82**, 261-270 (1995).
25 **R. M. Voorhees & R. S. Hegde.** Structure of the Sec61 channel opened by a signal sequence. *Science* **351**, 88-91 (2016).
26 **A. M. Liaci, B. Steigenberger, P. C. Telles de Souza, S. Tamara, M. Grollers-Mulderij, P. Ogrissek, S. J. Marrink, R. A. Scheltema & F. Forster.** Structure of the human signal peptidase complex reveals the determinants for signal peptide cleavage. *Mol Cell* **81**, 3934-3948 e3911 (2021).
27 **Y. Li, J. J. Bergeron, L. Luo, W. J. Ou, D. Y. Thomas & C. Y. Kang.** Effects of inefficient cleavage of the signal sequence of HIV-1 gp 120 on its association with calnexin, folding, and intracellular transport. *Proc Natl Acad Sci U S A* **93**, 9606-9611 (1996).
28 **A. Land, D. Zonneveld & I. Braakman.** Folding of HIV-1 envelope glycoprotein involves extensive isomerization of disulfide bonds and conformation-dependent leader peptide cleavage. *FASEB J* **17**, 1058-1067 (2003).
29 **I. Braakman & D. N. Hebert.** Protein folding in the endoplasmic reticulum. *Cold Spring Harb Perspect Biol* **5**, a013201 (2013).
30 **D. Gorlich & T. A. Rapoport.** Protein translocation into proteoliposomes reconstituted from purified components of the endoplasmic reticulum membrane. *Cell* **75**, 615-630 (1993).
31 **A. Yamaguchi, O. Hori, D. M. Stern, E. Hartmann, S. Ogawa & M. Tohyama.** Stress-associated endoplasmic reticulum protein 1 (SERP1)/Ribosome-associated membrane protein 4 (RAMP4) stabilizes membrane proteins during stress and facilitates subsequent glycosylation. *J Cell Biol* **147**, 1195-1204 (1999).
32 **K. Schroder, B. Martoglio, M. Hofmann, C. Holscher, E. Hartmann, S. Prehn, T. A. Rapoport & B. Dobberstein.** Control of glycosylation of MHC class II-associated invariant chain by translocon-associated RAMP4. *EMBO J* **18**, 4804-4815 (1999).
33 **M. R. Pool.** A trans-membrane segment inside the ribosome exit tunnel triggers RAMP4 recruitment to the Sec61p translocase. *J Cell Biol* **185**, 889-902 (2009).
34 **O. Hori, M. Miyazaki, T. Tamatani, K. Ozawa, K. Takano, M. Okabe, M. Ikawa, E. Hartmann, P.**

Mai, D. M. Stern, Y. Kitao & S. Ogawa. Deletion of SERP1/RAMP4, a component of the endoplasmic reticulum (ER) translocation sites, leads to ER stress. *Mol Cell Biol* **26**, 4257-4267 (2006).

35 **M. Uhlen, P. Oksvold, L. Fagerberg, E. Lundberg, K. Jonasson, M. Forsberg, M. Zwahlen, C. Kampf, K. Wester, S. Hober, H. Wernerus, L. Bjorling & F. Ponten.** Towards a knowledge-based Human Protein Atlas. *Nat Biotechnol* **28**, 1248-1250 (2010).

36 **C. UniProt.** UniProt: the Universal Protein Knowledgebase in 2023. *Nucleic Acids Res* **51**, D523-D531 (2023).

37 **J. Jumper, R. Evans, A. Pritzel, T. Green, M. Figurnov, O. Ronneberger, K. Tunyasuvunakool, R. Bates, A. Zidek, A. Potapenko, A. Bridgland, C. Meyer, S. A. A. Kohl, A. J. Ballard, A. Cowie, B. Romera-Paredes, S. Nikolov, R. Jain, J. Adler, T. Back, S. Petersen, D. Reiman, E. Clancy, M. Zielinski, M. Steinegger, M. Pacholska, T. Berghammer, S. Bodenstein, D. Silver, O. Vinyals, A. W. Senior, K. Kavukcuoglu, P. Kohli & D. Hassabis.** Highly accurate protein structure prediction with AlphaFold. *Nature* **596**, 583-589 (2021).

38 **M. Mirdita, K. Schutze, Y. Moriwaki, L. Heo, S. Ovchinnikov & M. Steinegger.** ColabFold: making protein folding accessible to all. *Nat Methods* **19**, 679-682 (2022).

39 **H. Khatter, A. G. Myasnikov, S. K. Natchiar & B. P. Klaholz.** Structure of the human 80S ribosome. *Nature* **520**, 640-645 (2015).

40 **D. Nguyen, R. Stutz, S. Schorr, S. Lang, S. Pfeffer, H. H. Freeze, F. Forster, V. Helms, J. Dudek & R. Zimmermann.** Proteomics reveals signal peptide features determining the client specificity in human TRAP-dependent ER protein import. *Nat Commun* **9**, 3765 (2018).

41 **R. D. Fons, B. A. Bogert & R. S. Hegde.** Substrate-specific function of the translocon-associated protein complex during translocation across the ER membrane. *J Cell Biol* **160**, 529-539 (2003).

42 **V. Goder & M. Spiess.** Topogenesis of membrane proteins: determinants and dynamics. *FEBS Lett* **504**, 87-93 (2001).

43 **E. Hartmann, D. Gorlich, S. Kostka, A. Otto, R. Kraft, S. Knespel, E. Burger, T. A. Rapoport & S. Prehn.** A tetrameric complex of membrane proteins in the endoplasmic reticulum. *Eur J Biochem* **214**, 375-381 (1993).

44 **S. Pfeffer, J. Dudek, M. Schaffer, B. G. Ng, S. Albert, J. M. Plitzko, W. Baumeister, R. Zimmermann, H. H. Freeze, B. D. Engel & F. Forster.** Dissecting the molecular organization of the translocon-associated protein complex. *Nat Commun* **8**, 14516 (2017).

45 **Y. D. Ivanov, A. Taldaev, A. V. Lisitsa, E. A. Ponomarenko & A. I. Archakov.** Prediction of Monomeric and Dimeric Structures of CYP102A1 Using AlphaFold2 and AlphaFold Multimer and Assessment of Point Mutation Effect on the Efficiency of Intra- and Interprotein Electron Transfer. *Molecules* **27** (2022).

46 **M. Jaskolowski, A. Jomaa, M. Gamerdinger, S. Shrestha, M. Leibundgut, E. Deuerling & N. Ban.** Molecular basis of the TRAP complex function in ER protein biogenesis. *bioRxiv*, 2022.2010.2004.510795 (2022).

47 **S. Karki, M. Javanainen, D. Tranter, S. Rehan, J. T. Huiskonen, L. Happonen & V. O. Paavilainen.** Molecular view of ER membrane remodeling by the Sec61/TRAP translocon. *bioRxiv*, 2022.2009.2030.510141 (2022).

48 **E. Pauwels, N. R. Shewakramani, B. De Wijngaert, A. Camps, B. Provinciael, J. Stroobants, K.-U. Kalies, E. Hartmann, P. Maes, K. Vermeire & K. Das.** Structural insights into TRAP association with ribosome-Sec61 complex, and translocon inhibition by a CADA derivative. *bioRxiv*, 2022.2009.2028.509949 (2022).

49 **K. Braunger, S. Pfeffer, S. Shrimal, R. Gilmore, O. Berninghausen, E. C. Mandon, T. Becker, F. Forster & R. Beckmann.** Structural basis for coupling protein transport and N-glycosylation at the mammalian endoplasmic reticulum. *Science* **360**, 215-219 (2018).

50 **S. Itskanov & E. Park.** Structure of the posttranslational Sec protein-translocation channel complex from yeast. *Science* **363**, 84-87 (2019).

51 **X. Wu, C. Cabanos & T. A. Rapoport.** Structure of the post-translational protein translocation machinery of the ER membrane. *Nature* **566**, 136-139 (2019).

52 **M. Wiedmann, T. V. Kurzchalia, E. Hartmann & T. A. Rapoport.** A signal sequence receptor in the endoplasmic reticulum membrane. *Nature* **328**, 830-833 (1987).

53 **X. Li, O. A. Itani, L. Haataja, K. J. Dumas, J. Yang, J. Cha, S. Flibotte, H. J. Shih, C. E. Delaney, J. Xu, L. Qi, P. Arvan, M. Liu & P. J. Hu.** Requirement for translocon-associated protein (TRAP) alpha in insulin biogenesis. *Sci Adv* **5**, eaax0292 (2019).

54 **T. Kriegler, G. Kiburg & T. Hessa.** Translocon-Associated Protein Complex (TRAP) is Crucial for Co-Translational Translocation of Pre-Proinsulin. *J Mol Biol* **432**, 166694 (2020).

55 **T. Kriegler, S. Lang, L. Notari & T. Hessa.** Prion Protein Translocation Mechanism Revealed by Pulling Force Studies. *J Mol Biol* **432**, 4447-4465 (2020).

56 **P. T. McGilvray, S. A. Anghel, A. Sundaram, F. Zhong, M. J. Trnka, J. R. Fuller, H. Hu, A. L. Burlingame & R. J. Keenan.** An ER translocon for multi-pass membrane protein biogenesis. *Elife* **9** (2020).

57 **L. Smalinskaite, M. K. Kim, A. J. O. Lewis, R. J. Keenan & R. S. Hegde.** Mechanism of an intramembrane chaperone for multipass membrane proteins. *Nature* **611**, 161-166 (2022).

58 **A. Sundaram, M. Yamsek, F. Zhong, Y. Hooda, R. S. Hegde & R. J. Keenan.** Substrate-driven assembly of a translocon for multipass membrane proteins. *Nature* **611**, 167-172 (2022).

59 **P. J. Chitwood & R. S. Hegde.** An intramembrane chaperone complex facilitates membrane protein biogenesis. *Nature* **584**, 630-634 (2020).

60 **C. Haffner, U. Dettmer, T. Weiler & C. Haass.** The Nicastrin-like protein Nicalin regulates assembly and stability of the Nicalin-nodal modulator (NOMO) membrane protein complex. *J Biol Chem* **282**, 10632-10638 (2007).

61 **U. Dettmer, P. H. Kuhn, C. Abou-Ajram, S. F. Lichtenthaler, M. Kruger, E. Kremmer, C. Haass & C. Haffner.** Transmembrane protein 147 (TMEM147) is a novel component of the Nicalin-NOMO protein complex. *J Biol Chem* **285**, 26174-26181 (2010).

62 **N. Sommer, T. Junne, K. U. Kalies, M. Spiess & E. Hartmann.** TRAP assists membrane protein topogenesis at the mammalian ER membrane. *Biochim Biophys Acta* **1833**, 3104-3111 (2013).

63 **E. Rosemond, M. Rossi, S. M. McMillin, M. Scarselli, J. G. Donaldson & J. Wess.** Regulation of M(3) muscarinic receptor expression and function by transmembrane protein 147. *Mol Pharmacol* **79**, 251-261 (2011).

64 **S. Kamat, S. Yeola, W. Zhang, L. Bianchi & M. Driscoll.** NRA-2, a nicalin homolog, regulates neuronal death by controlling surface localization of toxic Caenorhabditis elegans DEG/ENaC channels. *J Biol Chem* **289**, 11916-11926 (2014).

65 **A. Christodoulou, G. Maimaris, A. Makrigiorgi, E. Charidemou, C. Luchtenborg, A. Ververis, R. Georgiou, C. W. Lederer, C. Haffner, B. Brugger & N. Santama.** TMEM147 interacts with lamin B receptor, regulates its localization and levels, and affects cholesterol homeostasis. *J Cell Sci* **133** (2020).

66 **G. Maimaris, A. Christodoulou, N. Santama & C. W. Lederer.** Regulation of ER Composition and Extent, and Putative Action in Protein Networks by ER/NE Protein TMEM147. *Int J Mol Sci* **22** (2021).

67 **C. G. Gahmberg & M. Tolvanen.** Why mammalian cell surface proteins are glycoproteins. *Trends Biochem Sci* **21**, 308-311 (1996).

68 **J. Breitling & M. Aebi.** N-linked protein glycosylation in the endoplasmic reticulum. *Cold Spring Harb Perspect Biol* **5**, a013359 (2013).

69 **V. K. Pandey, R. Sharma, G. K. Prajapati, T. K. Mohanta & A. K. Mishra.** N-glycosylation, a leading role in viral infection and immunity development. *Mol Biol Rep* **49**, 8109-8120 (2022).

70 **E. Mohorko, R. Glockshuber & M. Aebi.** Oligosaccharyltransferase: the central enzyme of N-linked protein glycosylation. *J Inherit Metab Dis* **34**, 869-878 (2011).

71 **S. Shrimal, N. A. Cherepanova & R. Gilmore.** DC2 and KCP2 mediate the interaction between the oligosaccharyltransferase and the ER translocon. *J Cell Biol* **216**, 3625-3638 (2017).

72 **R. Wild, J. Kowal, J. Eyring, E. M. Ngwa, M. Aebi & K. P. Locher.** Structure of the yeast oligosaccharyltransferase complex gives insight into eukaryotic N-glycosylation. *Science* **359**, 545-550 (2018).

73 **A. S. Ramirez, J. Kowal & K. P. Locher.** Cryo-electron microscopy structures of human oligosaccharyltransferase complexes OST-A and OST-B. *Science* **366**, 1372-1375 (2019).

74 **Q. P. Yang, M. F. Fu, H. Gao, K. Yamamoto, D. Hu & S. Y. Qin.** Subcellular distribution of endogenous malectin under rest and stress conditions is regulated by ribophorin I. *Glycobiology* **28**, 374-381 (2018).

75 **K. Takeda, S. Y. Qin, N. Matsumoto & K. Yamamoto.** Association of malectin with ribophorin I is crucial for attenuation of misfolded glycoprotein secretion. *Biochem Biophys Res Commun* **454**, 436-440 (2014).

76 **S. Y. Qin, D. Hu, K. Matsumoto, K. Takeda, N. Matsumoto, Y. Yamaguchi & K. Yamamoto.** Malectin forms a complex with ribophorin I for enhanced association with misfolded glycoproteins. *J Biol Chem* **287**, 38080-38089 (2012).

77 **D. B. Williams.** Beyond lectins: the calnexin/calreticulin chaperone system of the endoplasmic reticulum. *J Cell Sci* **119**, 615-623 (2006).

78 **G. Kozlov & K. Gehring.** Calnexin cycle - structural features of the ER chaperone system. *FEBS J* **287**, 4322-4340 (2020).

79 **C. Appenzeller-Herzog & L. Ellgaard.** The human PDI family: versatility packed into a single fold. *Biochim Biophys Acta* **1783**, 535-548 (2008).

80 **J. J. Galligan & D. R. Petersen.** The human protein disulfide isomerase gene family. *Hum Genomics* **6**, 6 (2012).

81 **A. Zapun, N. J. Darby, D. C. Tessier, M. Michalak, J. J. Bergeron & D. Y. Thomas.** Enhanced catalysis of ribonuclease B folding by the interaction of calnexin or calreticulin with ERp57. *J Biol Chem* **273**, 6009-6012 (1998).

82 **J. D. Oliver, H. L. Roderick, D. H. Llewellyn & S. High.** ERp57 functions as a subunit of specific complexes formed with the ER lectins calreticulin and calnexin. *Mol Biol Cell* **10**, 2573-2582 (1999).

83 **G. Jansen, P. Maattanen, A. Y. Denisov, L. Scarffe, B. Schade, H. Balghi, K. Dejgaard, L. Y. Chen, W. J. Muller, K. Gehring & D. Y. Thomas.** An interaction map of endoplasmic reticulum chaperones and foldases. *Mol Cell Proteomics* **11**, 710-723 (2012).

84 **R. Vinaik, G. Kozlov & K. Gehring.** Structure of the non-catalytic domain of the protein disulfide isomerase-related protein (PDIR) reveals function in protein binding. *PLoS One* **8**, e62021 (2013).

85 **E. F. Pettersen, T. D. Goddard, C. C. Huang, E. C. Meng, G. S. Couch, T. I. Croll, J. H. Morris & T. E. Ferrin.** UCSF ChimeraX: Structure visualization for researchers, educators, and developers. *Protein Sci* **30**, 70-82 (2021).

86 **D. J. Kelleher & R. Gilmore.** An evolving view of the eukaryotic oligosaccharyltransferase. *Glycobiology* **16**, 47R-62R (2006).

87 **A. Higa, S. Taouji, S. Lhomond, D. Jensen, M. E. Fernandez-Zapico, J. C. Simpson, J. M. Pasquet, R. Schekman & E. Chevet.** Endoplasmic reticulum stress-activated transcription factor ATF6alpha requires the disulfide isomerase PDIA5 to modulate chemoresistance. *Mol Cell Biol* **34**, 1839-1849 (2014).

88 **P. Walter & D. Ron.** The unfolded protein response: from stress pathway to homeostatic regulation. *Science* **334**, 1081-1086 (2011).

89 **H. P. Harding, Y. Zhang, A. Bertolotti, H. Zeng & D. Ron.** Perk is essential for translational regulation and cell survival during the unfolded protein response. *Mol Cell* **5**, 897-904 (2000).

90 **M. Jaud, C. Philippe, L. Van Den Berghe, C. Segura, L. Mazzolini, S. Pyronnet, H. Laurell & C. Touriol.** The PERK Branch of the Unfolded Protein Response Promotes DLL4 Expression by Activating an Alternative Translation Mechanism. *Cancers (Basel)* **11** (2019).

91 **J. Barandun, M. Hunziker, C. R. Vossbrinck & S. Klinge.** Evolutionary compaction and adaptation visualized by the structure of the dormant microsporidian ribosome. *Nat Microbiol* **4**, 1798-1804 (2019).

92 **A. Brown, M. R. Baird, M. C. Yip, J. Murray & S. Shao.** Structures of translationally inactive mammalian ribosomes. *Elife* **7** (2018).

93 **F. Leesch, L. Lorenzo-Orts, C. Pribitzer, I. Grishkovskaya, J. Roehsner, A. Chugunova, M. Matzinger, E. Roitinger, K. Belacic, S. Kandolf, T. Y. Lin, K. Mechtler, A. Meinhart, D. Haselbach & A. Pauli.** A molecular network of conserved factors keeps ribosomes dormant in the egg. *Nature* **613**, 712-720 (2023).

94 **B. J. Guan, D. Krokowski, M. Majumder, C. L. Schmotzer, S. R. Kimball, W. C. Merrick, A. E. Koromilas & M. Hatzoglou.** Translational control during endoplasmic reticulum stress beyond phosphorylation of the translation initiation factor eIF2alpha. *J Biol Chem* **289**, 12593-12611 (2014).

95 **M. D. Potter & C. V. Nicchitta.** Regulation of ribosome detachment from the mammalian endoplasmic reticulum membrane. *J Biol Chem* **275**, 33828-33835 (2000).

96 **M. D. Potter & C. V. Nicchitta.** Endoplasmic reticulum-bound ribosomes reside in stable association with the translocon following termination of protein synthesis. *J Biol Chem* **277**, 23314-23320 (2002).

97 **D. W. Reid, Q. Chen, A. S. Tay, S. Shenolikar & C. V. Nicchitta.** The unfolded protein response triggers selective mRNA release from the endoplasmic reticulum. *Cell* **158**, 1362-1374 (2014).

98 **K. Nagasawa, T. Higashi, N. Hosokawa, R. J. Kaufman & K. Nagata.** Simultaneous induction of the four subunits of the TRAP complex by ER stress accelerates ER degradation. *EMBO Rep* **8**, 483-489 (2007).

99 **C. Phoomak, W. Cui, T. J. Hayman, S. H. Yu, P. Zhao, L. Wells, R. Steet & J. N. Contessa.** The translocon-associated protein (TRAP) complex regulates quality control of N-linked glycosylation during ER stress. *Sci Adv* **7** (2021).

100 **M. E. Losfeld, B. G. Ng, M. Kircher, K. J. Buckingham, E. H. Turner, A. Eroshkin, J. D. Smith, J. Shendure, D. A. Nickerson, M. J. Bamshad, G. University of Washington Center for Mendelian & H. H. Freeze.** A new congenital disorder of glycosylation caused by a mutation in SSR4, the signal sequence receptor 4 protein of the TRAP complex. *Hum Mol Genet* **23**, 1602-1605 (2014).

101 **B. G. Ng, K. Raymond, M. Kircher, K. J. Buckingham, T. Wood, J. Shendure, D. A. Nickerson, M. J. Bamshad, G. University of Washington Center for Mendelian, J. T. Wong, F. P. Monteiro, B. H. Graham, S. Jackson, R. Sparkes, A. E. Scheuerle, S. Cathey, F. Kok, J. B. Gibson & H. H. Freeze.** Expanding the Molecular and Clinical Phenotype of SSR4-CDG. *Hum Mutat* **36**, 1048-1051 (2015).

102 **B. G. Ng, C. M. Lourenco, M. E. Losfeld, K. J. Buckingham, M. Kircher, D. A. Nickerson, J. Shendure, M. J. Bamshad, G. University of Washington Center for Mendelian & H. H. Freeze.** Mutations in the translocon-associated protein complex subunit SSR3 cause a novel congenital disorder of glycosylation. *J Inherit Metab Dis* **42**, 993-997 (2019).

103 **S. Dittner-Moormann, C. M. Lourenco, J. Reunert, R. Nishinakamura, S. S. Tanaka, C. Werner, V. Debus, K. P. Zimmer, G. Wetzel, H. Y. Naim, Y. Wada, S. Rust & T. Marquardt.** TRAPgamma-CDG shows asymmetric glycosylation and an effect on processing of proteins required in higher organisms. *J Med Genet* **58**, 213-216 (2021).

104 **S. Lang, S. Pfeffer, P. H. Lee, A. Cavalie, V. Helms, F. Forster & R. Zimmermann.** An Update on Sec61 Channel Functions, Mechanisms, and Related Diseases. *Front Physiol* **8**, 887 (2017).

105 **M. Sicking, S. Lang, F. Bochen, A. Roos, J. P. H. Drenth, M. Zakaria, R. Zimmermann & M. Linxweiler.** Complexity and Specificity of Sec61-Channelopathies: Human Diseases Affecting Gating of the Sec61 Complex. *Cells* **10** (2021).

106 **S. Shrimal, B. G. Ng, M. E. Losfeld, R. Gilmore & H. H. Freeze.** Mutations in STT3A and STT3B cause two congenital disorders of glycosylation. *Hum Mol Genet* **22**, 4638-4645 (2013).

107 **M. A. Jones, B. G. Ng, S. Bhide, E. Chin, D. Rhodenizer, P. He, M. E. Losfeld, M. He, K. Raymond, G. Berry, H. H. Freeze & M. R. Hegde.** DDOST mutations identified by whole-exome sequencing are implicated in congenital disorders of glycosylation. *Am J Hum Genet* **90**, 363-368 (2012).

108 **B. Xin, E. G. Puffenberger, S. Turben, H. Tan, A. Zhou & H. Wang.** Homozygous frameshift mutation in TMCO1 causes a syndrome with craniofacial dysmorphism, skeletal anomalies, and mental retardation. *Proc Natl Acad Sci U S A* **107**, 258-263 (2010).

109 **Y. Alanay, B. Erguner, E. Utine, O. Hacariz, P. O. Kiper, E. Z. Taskiran, F. Percin, E. Uz, M. S. Sagiroglu, B. Yuksel, K. Boduroglu & N. A. Akarsu.** TMCO1 deficiency causes autosomal recessive cerebrofaciothoracic dysplasia. *Am J Med Genet A* **164A**, 291-304 (2014).

110 **M. Morimoto, H. Waller-Evans, Z. Ammous, X. Song, K. A. Strauss, D. Pehlivan, C. Gonzaga-Jauregui, E. G. Puffenberger, C. R. Holst, E. Karaca, K. W. Brigatti, E. Maguire, Z. H. Coban-Akdemir, A. Amagata, C. C. Lau, X. Chepa-Lotrea, E. Macnamara, T. Tos, S. Isikay, M. Nehrebecky, J. D. Overton, M. Klein, T. C. Markello, J. E. Posey, D. R. Adams, E. Lloyd-Evans, J. R. Lupski, W. A. Gahl & M. C. V. Malicdan.** Bi-allelic CCDC47 Variants Cause a Disorder Characterized by Woolly Hair, Liver Dysfunction, Dysmorphic Features, and Global Developmental Delay. *Am J Hum Genet* **103**, 794-807 (2018).

111 **T. Michael Yates, O. H. Ng, A. C. Offiah, J. Willoughby, J. N. Berg, D. D. D. Study & D. S. Johnson.** Cerebrofaciothoracic dysplasia: Four new patients with a recurrent TMCO1 pathogenic variant. *Am J Med Genet A* **179**, 43-49 (2019).

112 **R. Sharkia, A. Zalan, A. Jabareen-Masri, H. Hengel, L. Schols, A. Kessel, A. Azem & M. Mahajnah.** A novel biallelic loss-of-function mutation in TMCO1 gene confirming and expanding the phenotype spectrum of cerebro-facio-thoracic dysplasia. *Am J Med Genet A* **179**, 1338-1345 (2019).

113 **H. Batchelor-Regan, B. Xin, A. Zhou & H. Wang.** From Disease Description and Gene Discovery to Functional Cell Pathway: A Decade-Long Journey for TMCO1. *Front Genet* **12**, 652400 (2021).

114 **Q. Thomas, M. Motta, T. Gautier, M. S. Zaki, A. Ciolfi, J. Paccaud, F. Girodon, O. Boespflug-Tanguy, T. Besnard, J. Kerkhof, H. McConkey, A. Masson, A. S. Denomme-Pichon, B. Cogne, E. Trochu, V. Vignard, F. El It, L. H. Rodan, M. A. Alkhateeb, R. A. Jamra, L. Duplomb, E. Tisserant, Y. Duffourd, A. L. Bruel, A. Jackson, S. Banka, M. McEntagart, A. Saggar, J. G. Gleeson, D. Sievert, H. Bae, B. H. Lee, K. Kwon, G. H. Seo, H. Lee, A. Saeed, N. Anjum, H. Cheema, S. Alawbathani, I.**

Khan, J. Pinto-Basto, J. Teoh, J. Wong, U. B. M. Sahari, H. Houlden, K. Zhelcheska, M. Pannetier, M. A. Awad, M. Lesieur-Sebellin, G. Barcia, J. Amiel, J. Delanne, C. Philippe, L. Faivre, S. Odent, A. Bertoli-Avella, C. Thauvin, B. Sadikovic, B. Reversade, R. Maroofian, J. Govin, M. Tartaglia & A. Vitobello. Bi-allelic loss-of-function variants in TMEM147 cause moderate to profound intellectual disability with facial dysmorphism and pseudo-Pelger-Huet anomaly. *Am J Hum Genet* **109**, 1909-1922 (2022).

115 **I. M. Abdelrazek, T. Holling, F. L. Harms, M. Alawi, T. Omar, E. Abdalla & K. Kutsche.** Craniofacial dysmorphism, skeletal anomalies, and impaired intellectual development syndrome-1 in two new patients with the same homozygous TMCO1 variant and review of the literature. *Eur J Med Genet* **66**, 104715 (2023).

116 **J. Perea, J. L. Garcia, J. Perez, D. Rueda, M. Arriba, Y. Rodriguez, M. Urioste & R. Gonzalez-Sarmiento.** NOMO-1 gene is deleted in early-onset colorectal cancer. *Oncotarget* **8**, 24429-24436 (2017).

117 **J. Perez-Garcia, A. Martel-Martel, P. Garcia-Valles, L. A. Corchete, J. L. Garcia, N. Gestoso-Uzal, R. Vidal-Tocino, O. Blanco, L. Mendez, M. Sanchez-Martin, M. Fuentes, A. B. Herrero, A. N. Holowatyj, J. Perea & R. Gonzalez-Sarmiento.** Recurrent NOMO1 Gene Deletion Is a Potential Clinical Marker in Early-Onset Colorectal Cancer and Is Involved in the Regulation of Cell Migration. *Cancers (Basel)* **14** (2022).

118 **T. Wu, N. Han, C. Zhao, X. Huang, P. Su & X. Li.** The long non-sacoding RNA TMEM147-AS1/miR-133b/ZNF587 axis regulates the Warburg effect and promotes prostatic carcinoma invasion and proliferation. *J Gene Med* **24**, e3453 (2022).

119 **S. Zheng, D. Zhao, G. Hou, S. Zhao, W. Zhang, X. Wang, L. Li, L. Lin, T. S. Tang & Y. Hu.** iASPP suppresses Gp78-mediated TMCO1 degradation to maintain Ca(2+) homeostasis and control tumor growth and drug resistance. *Proc Natl Acad Sci U S A* **119** (2022).

120 **X. Hong, H. Luo, G. Zhu, X. Guan, Y. Jia, H. Yu, X. Lv, T. Yu, H. Lan, Q. Zhang, H. Li, W. Sun, X. Huang & J. Li.** SSR2 overexpression associates with tumorigenesis and metastasis of Hepatocellular Carcinoma through modulating EMT. *J Cancer* **11**, 5578-5587 (2020).

121 **K. P. Burdon, S. Macgregor, A. W. Hewitt, S. Sharma, G. Chidlow, R. A. Mills, P. Danoy, R. Casson, A. C. Viswanathan, J. Z. Liu, J. Landers, A. K. Henders, J. Wood, E. Souzeau, A. Crawford, P. Leo, J. J. Wang, E. Rochtchina, D. R. Nyholt, N. G. Martin, G. W. Montgomery, P. Mitchell, M. A. Brown, D. A. Mackey & J. E. Craig.** Genome-wide association study identifies susceptibility loci for open angle glaucoma at TMCO1 and CDKN2B-AS1. *Nat Genet* **43**, 574-578 (2011).

122 **S. Sharma, K. P. Burdon, G. Chidlow, S. Klebe, A. Crawford, D. P. Dimasi, A. Dave, S. Martin, S. Javadiyan, J. P. Wood, R. Casson, P. Danoy, K. Griggs, A. W. Hewitt, J. Landers, P. Mitchell, D. A. Mackey & J. E. Craig.** Association of genetic variants in the TMCO1 gene with clinical parameters related to glaucoma and characterization of the protein in the eye. *Invest Ophthalmol Vis Sci* **53**, 4917-4925 (2012).

123 **A. O. Caglayan, H. Per, G. Akgumus, H. Gumus, J. Baranoski, M. Canpolat, M. Calik, A. Yikilmaz, K. Bilguvar, S. Kumandas & M. Gunel.** Whole-exome sequencing identified a patient with TMCO1 defect syndrome and expands the phenotic spectrum. *Clin Genet* **84**, 394-395 (2013).

124 **K. Thapa, K. C. Wu, A. Sarma, E. M. Grund, A. Szeto, A. J. Mendez, S. Gesta, V. K. Vishnudas, N. R. Narain & R. Sarangarajan.** Dysregulation of the calcium handling protein, CCDC47, is associated with diabetic cardiomyopathy. *Cell Biosci* **8**, 45 (2018).

125 **J. Li, C. Liu, Y. Li, Q. Zheng, Y. Xu, B. Liu, W. Sun, Y. Li, S. Ji, M. Liu, J. Zhang, D. Zhao, R. Du, Z. Liu, G. Zhong, C. Sun, Y. Wang, J. Song, S. Zhang, J. Qin, S. Ling, X. Wang & Y. Li.** TMCO1-mediated Ca(2+) leak underlies osteoblast functions via CaMKII signaling. *Nat Commun* **10**, 1589 (2019).

126 **M. Ota, Y. Tanaka, I. Nakagawa, J. J. Jiang, Y. Arima, D. Kamimura, T. Onodera, N. Iwasaki & M. Murakami.** Role of Chondrocytes in the Development of Rheumatoid Arthritis Via Transmembrane Protein 147-Mediated NF-kappaB Activation. *Arthritis Rheumatol* **72**, 931-942 (2020).

127 **B. Molloy, E. R. Jones, N. D. Linhares, P. G. Buckley, T. R. Leahy, B. Lynch, I. Knerr, M. D. King & K. M. Gorman.** Uniparental disomy screen of Irish rare disorder cohort unmasks homozygous variants of clinical significance in the TMCO1 and PRKRA genes. *Front Genet* **13**, 945296 (2022).

128 **B. J. Conti, P. K. Devaraneni, Z. Yang, L. L. David & W. R. Skach.** Cotranslational stabilization of Sec62/63 within the ER Sec61 translocon is controlled by distinct substrate-driven translocation events. *Mol Cell* **58**, 269-283 (2015).

129 **C. C. Kuo, A. W. T. Chiang, H. M. Baghdassarian & N. E. Lewis.** Dysregulation of the secretory pathway connects Alzheimer's disease genetics to aggregate formation. *Cell Syst* **12**, 873-884 e874 (2021).
130 **C. M. Wilson, C. Kraft, C. Duggan, N. Ismail, S. G. Crawshaw & S. High.** Ribophorin I associates with a subset of membrane proteins after their integration at the sec61 translocon. *J Biol Chem* **280**, 4195-4206 (2005).
131 **E. L. Snapp, N. McCaul, M. Quandte, Z. Cabartova, I. Bontjer, C. Kallgren, I. Nilsson, A. Land, G. von Heijne, R. W. Sanders & I. Braakman.** Structure and topology around the cleavage site regulate post-translational cleavage of the HIV-1 gp160 signal peptide. *Elife* **6** (2017).
132 **N. McCaul, M. Quandte, I. Bontjer, G. van Zadelhoff, A. Land, E. T. Crooks, J. M. Binley, R. W. Sanders & I. Braakman.** Intramolecular quality control: HIV-1 envelope gp160 signal-peptide cleavage as a functional folding checkpoint. *Cell Rep* **36**, 109646 (2021).
133 **H. C. Huang, Y. J. Lai, C. C. Liao, W. F. Yang, K. B. Huang, I. J. Lee, W. C. Chou, S. H. Wang, L. H. Wang, J. M. Hsu, C. P. Sun, C. T. Kuo, J. Wang, T. C. Hsiao, P. J. Yang, T. A. Lee, W. Huang, F. A. Li, C. Y. Shen, Y. L. Lin, M. H. Tao & C. W. Li.** Targeting conserved N-glycosylation blocks SARS-CoV-2 variant infection in vitro. *EBioMedicine* **74**, 103712 (2021).
134 **Y. J. Huang, H. Zhao, X. Huang, Y. Q. Deng, X. F. Li, Q. Ye, R. T. Li, Y. P. Xu, T. S. Cao & C. F. Qin.** Identification of oligosaccharyltransferase as a host target for inhibition of SARS-CoV-2 and its variants. *Cell Discov* **7**, 116 (2021).
135 **Z. Zhang, X. Wan, X. Li & C. Wan.** Effects of a Shift of the Signal Peptide Cleavage Site in Signal Peptide Variant on the Synthesis and Secretion of SARS-CoV-2 Spike Protein. *Molecules* **27** (2022).
136 **B. Kleizen, M. van Willigen, M. Mijnders, F. Peters, M. Grudniewska, T. Hillenaar, A. Thomas, L. Kooijman, K. W. Peters, R. Frizzell, P. van der Sluijs & I. Braakman.** Co-Translational Folding of the First Transmembrane Domain of ABC-Transporter CFTR is Supported by Assembly with the First Cytosolic Domain. *J Mol Biol* **433**, 166955 (2021).
137 **H. Shishido, J. S. Yoon, Z. Yang & W. R. Skach.** CFTR trafficking mutations disrupt cotranslational protein folding by targeting biosynthetic intermediates. *Nat Commun* **11**, 4258 (2020).
138 **B. Kleizen, T. van Vlijmen, H. R. de Jonge & I. Braakman.** Folding of CFTR is predominantly cotranslational. *Mol Cell* **20**, 277-287 (2005).

Summary

The ribosome-associated endoplasmic reticulum (ER) translocon machinery is the entry point of the secretory pathway and governs translocation, signal peptide (SP) insertion and cleavage, multispanning membrane protein insertion, N-glycosylation, glycoprotein processing, and protein folding and assembly. To specialize for translocation of specific protein subsets or to facilitate different co-translational processes, various accessory factors need to associate with the translocon. Recently, cryo-electron microscopy (cryo-EM) provided valuable insights into the structure and function of many translocon-bound factors. However, these single-particle cryo-EM approaches are often associated with detergent-solubilization and purification of the target factors, which may introduce artefacts or disrupt interactions to weak binding partners. Cryo-electron tomography (cryo-ET) studies, which do not rely on extensive purification procedures and enable visualization of protein complexes in their native membrane environment, remain scarce.

This thesis aims to explore the close-to-native molecular landscape of the ribosome-associated ER translocon. Using cryo-ET, I dissect ribosomal intermediate states, visualize ER translocon variants and novel interaction partners, and characterize their organization at the ER membrane. These results advance our understanding of various protein biogenesis processes and provide a structural basis for future investigations.

In chapter 1, I provide a concise overview of the protein biogenesis process, and describe recent developments in cryo-EM and its role in cellular and structural biology. Moreover, I introduce the scopes of the thesis.

In chapter 2, I comprehensively summarize the structurally and biochemically characterized molecular toolbox enabling protein biogenesis at the ER. I focus particularly on cryo-EM and cryo-ET structures, which provided a 'clearer picture' of the ER translocon complex.

In chapter 3, I use cryo-ET and subtomogram analysis to study soluble and ER membrane-bound ribosomal intermediate states at resolutions ranging from 6-8 Å *ex vivo*. Our data reveal eight actively translating ribosome intermediates, seven of

which I assigned to the elongation cycle, as well as two hibernating ribosome states. By analyzing the three-dimensional distribution of these particles, I characterize their polysomal organization at the ER membrane and in solution, which is consistent with the assignment of intermediates to elongating and hibernating particles. In conjunction with *in situ* cryo-ET, high-resolution single particle analysis and proteomics, I identify a previously unknown intermediate associated with elongation factor 1a (eEF1a) in the extended conformation. This observation indicates that eEF1a remains bound to the ribosome after GTP-hydrolysis and tRNA accommodation and possibly contributes to proofreading in mRNA decoding.

In chapter 4, I explore the molecular landscape of the ribosome-associated ER translocon at unprecedented detail. Using subtomogram analysis, I identify three major variants, the Sec61-TRAP, the Sec61-TRAP-OSTA, and the Sec61-multipass translocon. Tomogram segmentation and spatial neighborhood analysis demonstrate that OSTA as well as multipass variants cluster in distinct polysome chains, reflecting their substrate specificity for SP-containing and multispanning membrane proteins, respectively. Based on the reconstruction of the most abundant variant, Sec61-TRAP-OSTA, and ColabFold prediction models, we built a near-complete molecular model of this ER translocon, revealing the molecular details of TRAP and its interactions with Sec61 and an unidentified OSTA-specific transmembrane protein named T1. Reconstructions of the OSTA variant in context of translational activity, as well as in the condition of ER stress feature a SP-like density, which likely represents an unidentified translocon component. I propose that this factor is RAMP4 which associates with the lateral gate of Sec61 and with the ribosome in the cytosol, potentially playing a pivotal role in regulation of translocation and topogenesis. In the ER lumen, we found additional densities, named L1 and L2, associated with OSTA subunits STT3a, OST48, and RPN2. Structural analysis, ColabFold predictions, preliminary XL-MS data, and analysis of charge distribution on the surface of OSTA and candidate proteins suggest that PDIA5 (also known as PDIR) is a prime candidate for L2 and likely enhances glycoprotein folding at the translocon.

In chapter 5, I characterize the composition of the multipass translocon in context of translational activity. TRAP, a novel accessory factor of the multipass translocon, and PAT, an intramembrane chaperone for multispanning transmembrane domains, are variably recruited to the multipass translocon. However, PAT preferentially associates with the actively translocating multipass translocon, while TRAP is preferentially recruited to the inactive variant. Under condition of ER stress, where most particles (97%) are translationally inactive, PAT was not detected while TRAP is stoichiometrically bound to the multipass translocon, pointing to translocation-dependent roles. Moreover, focused refinement of the Sec61-TRAP-multipass translocon visualizes interactions

between TRAP and a structurally unidentified protein, most likely NOMO, a subunit of the BOS complex. This interaction is associated with conformational changes of the BOS complex and may be important for intermolecular communication to regulate specific processes during multipass membrane biogenesis.

In chapter 6, I comprehensively discuss my results in the context of recent literature. The available literature, additional model predictions, and other evidence substantiate my above postulations and provide a strong basis for future studies.

Samenvatting

De ribosoom-geassocieerde ER-translocon machine is de ingang van het secretorische pathway en beheerst translocatie, signaalpeptide (SP) insertie en klieving, insertie van multispanning membraan proteïne, N-glycosylering, glycoproteïne verwerking, en proteïne vouwing en assemblage. Om te specialiseren voor translocatie van specifieke eiwit-subsets of verschillende co-translational processen uit te voeren, moeten verschillende accessoire factoren zich associëren met de translocon. In de recente tijd zijn belangrijke structurele en mechanistische inzichten verkregen in veel van deze factoren door middel van cryo-elektronenmicroscopie (cryo-EM). Echter, deze cryo-EM single particle benaderingen gaan vaak gepaard met oplos- en zuiveringsstappen van de doelfactoren, wat artefacten kan introduceren of interacties met zwak bindende partners kan verstoren. Cryo-elektronentomografie (cryo-ET) studies, die niet afhankelijk zijn van uitgebreide zuiveringsprocedures en visualisatie van eiwitcomplexen in hun natuurlijke membraanomgeving mogelijk maken, zijn nog steeds zeldzaam.

Deze proefschrift heeft als doel het bijna-native moleculaire landschap van de ribosoom-geassocieerde ER-translocon te verkennen. Met behulp van cryo-ET ontleden we ribosomale tussenliggende staten, visualiseren we ER-translocon varianten en nieuwe interactiepartners, en karakteriseren we hun organisatie aan het ER-membraan. Deze resultaten bevorderen ons begrip van verschillende eiwitbiogeneseprocessen en bieden een structurele basis voor toekomstige onderzoeken.

In hoofdstuk 1 geef ik een beknopt overzicht van het eiwitbiogeneseproces, evenals de ontwikkelingen van cryo-EM en de rol ervan in de cel- en structuurbiologie. Bovendien introduceer ik de doelstellingen van het proefschrift.

In hoofdstuk 2 vat ik de structuur- en biochemisch gekarakteriseerde moleculaire toolbox voor eiwitbiogenese bij het ER samen. Ik richt me met name op cryo-EM- en cryo-ET-structuren, die een 'duidelijker beeld' hebben gegeven van het ER-transloconcomplex.

In hoofdstuk 3 gebruik ik cryo-ET en subtomogramanalyse om oplosbare en ER-membraangebonden ribosomale tussenliggende toestanden te bestuderen

op resoluties variërend van 6-8 Å *ex vivo*. Ik onthul acht actief vertalende ribosoomtussenliggende toestanden, waarvan ik er zeven heb toegewezen aan de elongatiecyclus, evenals twee sluimerende ribosoomtoestanden. Door de driedimensionale verdeling van de deeltjes te analyseren, karakteriseren we hun polysomale organisatie aan het ER-membraan en in oplossing, wat consistent is met mijn toewijzing van tussenliggende toestanden aan elongerende en sluimerende deeltjes. In combinatie met *in situ* cryo-ET, single particle-analyse op hoge resolutie en proteomics, identificeer ik een eerder onbekend tussenproduct dat geassocieerd is met elongatiefactor 1a (eEF1a) in de uitgebreide conformatie, wat aangeeft dat eEF1a gebonden blijft aan het ribosoom na GTP-hydrolyse en tRNA-accommodatie en mogelijk bijdraagt aan proofreading in mRNA-decodering.

In hoofdstuk 4 verken ik het moleculaire landschap van het ribosoom-geassocieerde ER-translocon in ongekend detail. Met behulp van subtomogramanalyse identificeer ik drie belangrijke varianten, de Sec61-TRAP, de Sec61-TRAP-OSTA en de Sec61-multipass-translocon. Tomogramsegmentatie en ruimtelijke buurtanalyse tonen aan dat OSTA- evenals multipass-varianten in verschillende polysomale ketens clusteren, wat hun substratenspecificiteit voor SP-bevattende en multispanningsmembraaneiwitten weerspiegelt. Op basis van mijn reconstructie van de meest voorkomende variant, Sec61-TRAP-OSTA, en ColabFold-voorspellingsmodellen, ben ik erin geslaagd om een bijna compleet model van deze ER-translocon te bouwen, waarbij de moleculaire details van TRAP en zijn interacties met Sec61 en een ongeïdentificeerd OSTA-specifiek transmembraanproteïne genaamd T1 worden onthuld. Reconstructies van de OSTA-variant in de context van translationele activiteit, of onder omstandigheden van ER-stress, bevatten een SP-achtige dichtheid, die waarschijnlijk een ongeïdentificeerd transloconcomponent vertegenwoordigt. Ik stel voor dat dit factor RAMP4 is, die zich bindt aan de laterale poort van Sec61 en aan het ribosoom in het cytosol, mogelijk een cruciale rol speelt in de regulatie van translocatie en topogenese. In het ER-lumen vond ik aanvullende dichtheden, genaamd L1 en L2, die geassocieerd zijn met OSTA-subeenheden STT3a, OST48 en RPN2. Structurele analyse, ColabFold-voorspellingen, voorlopige XL-MS-gegevens en analyse van de ladingverdeling op het oppervlak van OSTA en kandidaat-eiwitten suggereren dat PDIA5 (ook bekend als PDIR) een belangrijke kandidaat is voor L2 en waarschijnlijk de vouwing van glycoproteïnen bij het translocon versterkt.

In hoofdstuk 5 karakteriseer ik de samenstelling van de multipass translocon in de context van translationele activiteit. TRAP, een nieuwe accessoire factor van de multipass translocon, en PAT, een intramembraan chaperonne voor multispanning-transmembraan domeinen, worden verschillend gerekruteerd naar de multipass translocon. PAT associeert echter bij voorkeur met de actief translokerende multipass

translocon, terwijl TRAP wordt gerekruteerd naar de inactieve variant. Onder omstandigheden van ER-stress, waar de meeste deeltjes (97%) inactief zijn, werd PAT niet gedetecteerd terwijl TRAP stoichiometrisch gebonden is aan de multipass translocon, wat wijst op translocatieafhankelijke rollen. Bovendien visualiseer ik gerichte verfijning van de Sec61-TRAP-multipass translocon interacties tussen TRAP en een structuurlijk ongeïdentificeerd eiwit, hoogstwaarschijnlijk NOMO, een subeenheid van het BOS-complex. Deze interactie gaat gepaard met conformationele veranderingen van het BOS-complex en kan belangrijk zijn voor intermoleculaire communicatie om specifieke processen te reguleren tijdens de multipass membraanbiogenese.

In hoofdstuk 6 bespreek ik uitgebreid mijn resultaten in de context van recente literatuur. De beschikbare literatuur, aanvullende modelvoorspellingen en ander bewijsmateriaal bevestigen mijn postulaten en bieden een sterke basis voor toekomstige studies.

Zusammenfassung

Die Ribosomen-assoziierte ER-Translokon-Maschinerie markiert den Startpunkt des sekretorischen Weges und ist verantwortlich für Prozesse wie Translokation, Signalpeptid (SP)-Insertion und -Spaltung, Insertion von polytopen Membranproteinen, N-Glykosylierung, Glykoproteinprozessierung sowie Protein-Faltung und -Assemblierung. Um die Translokation spezifischer Protein-Populationen bewältigen oder ko-translationale Prozesse durchführen zu können, werden verschiedene akzessorische Faktoren zum Translokon rekrutiert. In der jüngeren Vergangenheit konnten mithilfe der Kryo-Elektronenmikroskopie (Kryo-EM) wichtige strukturelle und mechanistische Einblicke in viele dieser Faktoren gewonnen werden. Die Herangehensweise der Kryo-EM Einzelpartikelanalyse ist jedoch oft mit aufwendigen Solubilisierungs- und Aufreinigungsschritten der Zielfaktoren verbunden, die zu unerwünschten Artefakten oder zur Beeinträchtigung schwacher Proteininteraktionen führen kann. Kryo-Elektronentomographie (Kryo-ET)-basierte Studien, welche nicht zwingend auf extensive Aufreinigungen angewiesen sind und die Visualisierung von Proteinkomplexen innerhalb ihrer nativen Membranumgebung ermöglichen, sind selten.

In dieser Arbeit untersuche ich die annähernd native molekulare Landschaft des Ribosomen-assoziierten ER-Translokons. Mit Hilfe von Kryo-ET konnte ich ribosomale Zwischenzustände aufschlüsseln, verschiedene ER-Translokon-Varianten und neue Interaktionspartner visualisieren, und deren Organisation an der ER-Membran charakterisieren. Diese Ergebnisse tragen zu unserem Verständnis verschiedener Protein-Biogeneseprozesse bei und liefern eine strukturelle Grundlage für zukünftige Untersuchungen.

Im Kapitel 1 gebe ich einen prägnanten Überblick über den Prozess der Proteinbiosynthese sowie die Entwicklungen der Kryo-Elektronenmikroskopie (Kryo-EM) und ihre Rolle in der Zell- und Strukturbiologie. Zudem stelle ich die Zielsetzungen dieser Arbeit vor.

In Kapitel 2 fasse ich die strukturell und biochemisch charakterisierten molekularen Werkzeuge für die Proteinbiogenese im ER umfangreich zusammen. Dabei konzentriere

ich mich besonders auf Kryo-EM- und Kryo-ET-Strukturen, die ein „klareres Bild" des ER-Translokonkomplexes vermitteln.

In Kapitel 3 untersuche ich lösliche und ER-membrangebundene ribosomale Intermediate mittels Kryo-ET und Subtomogrammanalyse mit Auflösungen von 6-8 Å *ex vivo*. Die ergebnisse offenbaren acht aktiv translatierende Ribosomenintermediate, von denen ich sieben dem Elongationszyklus zuordnen konnte, sowie zwei hibernierende Intermediate. Mittels Analyse der dreidimensionalen Verteilung der Partikel konnte ich deren polysomale Organisation an der ER-Membran und in Lösung charakterisieren, die mit der Zuordnung von Intermediaten zu elongierenden und hibernierenden Partikeln übereinstimmt. Zusammen mit *in situ* Kryo-ET, hochauflösender Einzelpartikelanalyse und Proteomik konnte ich einen bisher unbekannten Zwischenzustand identifizieren, der mit Elongationsfaktor 1a (eEF1a) in einer ausgedehnten Konformation assoziiert ist. Diese Ergebnisse deuten darauf hin, dass eEF1a auch nach GTP-Hydrolyse und tRNA-Akkommodation an das Ribosom gebunden bleibt und möglicherweise einen weiteren Kontrollpunkt im Prozess der mRNA-Dekodierung darstellt.

In Kapitel 4 erkunde ich die molekulare Landschaft der ribosomalen ER-Translokonkomplexe in bisher unerreichtem Detailgrad. Mithilfe von Subtomogrammanalyse konnte ich drei Hauptvarianten identifizieren, das Sec61-TRAP-, das Sec61-TRAP-OSTA- und das Sec61-Multipass-Translokon. Tomogrammsegmentierung und dreidimensionale Analyse der Partikelpositionen offenbaren, dass sich OSTA- sowie Multipass-Varianten in verschiedenen Polysom-Ketten gruppieren, was deren Substratspezifität für SP-enthaltende bzw. polytope Membranproteine widerspiegelt. Basierend auf der Rekonstruktion der abundantesten Variante, Sec61-TRAP-OSTA, und ColabFold-Vorhersagemodellen, gelang es mir, ein nahezu vollständiges Modell dieses ER-Translokons zu erstellen. Dieses enthüllt die molekularen Details vom TRAP-Komplex und dessen Interaktionen mit Sec61 und einem nicht identifizierten, OSTA-spezifischen Transmembranprotein, hier als T1 bezeichnet. Rekonstruktionen der OSTA-Variante in Kontext der Translationsaktivität sowie unter ER-Stressbedingungen weisen eine SP-ähnliche Dichte auf, welche wahrscheinlich eine nicht identifizierte Translokonkomponente darstellt. Ich postuliere, dass es sich bei diesem Faktor um RAMP4 handelt, der mit der lateralen Öffnung von Sec61 und dem Ribosom im Zytoplasma interagiert und möglicherweise eine zentrale Rolle in der Regulation von Translokation und Topogenese spielt. Im ER-Lumen beobachtete ich zusätzliche Dichten, hier L1 und L2 genannt, die mit den OSTA-Untereinheiten STT3a, OST48 und RPN2 assoziieren. Strukturanalyse, ColabFold-Vorhersagen, vorläufige XL-MS-Daten und die Analyse der Ladungsverteilung auf der Oberfläche von OSTA und Kandidatenproteinen legen nahe, dass PDIA5 (auch als PDIR bekannt) der bestmögliche Kandidat für L2 ist und wahrscheinlich die Faltung von Glykoproteinen am Translokon fördert.

In Kapitel 5 charakterisiere ich die Komposition des Multipass-Translokon im Kontext der Translationsaktivität. TRAP, ein neuer akzessorischer Faktor des Multipass-Translokon, und PAT, ein Intramembran-Chaperon für polytope Transmembrandomänen, werden variabel zum Multipass-Translokon rekrutiert. PAT assoziiert jedoch bevorzugt mit dem aktiv translozierenden Multipass-Translokon, während TRAP zur inaktiven Variante rekrutiert wird. Unter ER-Stressbedingungen, bei dem die meisten Partikel (97%) inaktiv sind, wurde PAT nicht detektiert, wohingegen TRAP stöchiometrisch an das Multipass-Translokon gebunden ist. Darüber hinaus offenbart die fokussierte Alignierung des Sec61-TRAP-Multipass-Translokons Interaktionen zwischen TRAP und einem strukturell bisher nicht identifizierten Protein, wahrscheinlich NOMO, einer Untereinheit des BOS-Komplexes. Diese Interaktion ist mit Konformationsänderungen des BOS-Komplexes verbunden und ermöglicht wahrscheinlich dessen intermolekulare Kommunikation, um spezifische Prozesse bei der Biogenese von polytopen Membranproteinen regulieren zu können.

Im Kapitel 6 diskutiere ich umfassend meine Ergebnisse im Kontext der aktuellen Literatur. Die vorhandene Literatur, zusätzliche Modellvorhersagen und weitere Ergebnisse stützen meine Hypothesen und bilden eine solide Grundlage für zukünftige Studien.

Acknowledgements

Friedrich, thank you so much for giving me the opportunity to embark on my PhD journey in your group. Thank you for all your support and time you put into our projects, for providing feedback, for crafting and proofreading manuscripts, checking posters and presentations, and most importantly for the freedom you gave me. It was a great experience not only for my professional development, but also to grow as a person. I can't wait to see what exciting discoveries you make in the future!

Tzviyah, Piet, Bert, Eric, and Loes, thank you for asking all the important, critical questions and for providing constructive feedback we needed to improve our scientific work. Stuart and Menno, where would the lab be without your support. Thank you so much for always being available (even in the night and early morning) to help fixing just another microscope issue again! Mihajlo, thank you for your efforts in keeping the clusters and workstations running smoothly and for taking care of all the computational issues! Mariska, Joke, Arie, Savannah, and Louris, without you guys the lab would be a mess. Thank you for taking care of it. Bianca, Lisa, Dymph, thank you for always being available to tackle the organizational issues that arose. Chris and Hans, thank you for taking care of the EM square!

Robert, your expertise in data acquisition and processing has been invaluable, and I'll miss our endless discussions about the mysteries of organelles and the art of grid preparation. I look forward to hearing about CryoCloud's next great achievements! Lena, I enjoyed sharing and discussing all the little data processing tricks to solve the problems that almost made our heads explode. Thank you for that and good luck finishing your PhD! Marten, congrats on your recent paper and thank you so much for all the analyses you contributed to our projects. Dimi, I hope you and Marten will find the EMC in our tomography data one day. Good luck with your PhD journey! Juliette, thank you so much for all the effort and contributions to our numerous projects. I am looking forward to your discoveries at MRC. Best of luck! Rodrigo, the CRISPR-expert, I am grateful for all the hard work you've put into many, many projects in the lab. I'm curious to see where your next steps will take you. Karla, queen of plants (I hope you'll win the war against those pesky bugs and keep your plants thriving), I always enjoyed your positive and motivating attitude. Stay the way you are! Good luck wrapping up your PhD. Leanne, it feels like I've rarely seen you outside of the Aquilos room. I hope you've found in your lamella what you were looking for! Good luck with your thesis! Miguel, I hope you've recovered from the headaches all these MIPs must have given you. Congrats again to this incredible work. Looking forward to your next career steps. Ravi, thank you so, so much for your hospitality whenever I visited Utrecht again and for letting my try your amazing Indian curries! I am so happy for you as you start your

position at RFI later this year and wish you all the luck with your new role. Jo and Marc, thank you for sharing your beautiful data. Keep up the great work! Eka, thank you for being always so helpful with literally everything. I truly enjoyed our conversations and long walks through the town. Best of luck in Switzerland! Gijs, the pytomGUI you built all on your own is impressive. Thank you for bearing with us bugging you all the time to implement new features! Manu, your experiments never seem to fail, and I'm genuinely curious about your secret recipe for success. Keep up the great work at Boehringer Ingelheim. Wenfei, I've been completely fascinated with all these crazy structures you've uncovered in your archaea cells. I am curious what else you'll discover about them! Dounia, thank you for always being open-minded and funny. Stay as you are. Elisa, Franziska, Nicoleta, Jitse, Ramon, and Wouter, best of luck with your ongoing projects!

Zuletzt möchte ich meiner Familie danken, meinen Eltern, meiner Schwester, ihrem Mann und ihren zwei kleinen Würmchen, und meinen Freunden. Vielen Dank für Eure Unterstützung, Geduld und Zusprüche und dafür, dass Ihr immer an mich geglaubt habt.

Mein größter Dank geht an den allerwichtigsten Menschen in meinem Leben, mein kleines Pandabärchen, Lisa. Danke, dass Du immer für mich da warst, ob in Holland, oder aus der Ferne. Ich freue mich auf die aufregende Zeit, die uns bevorsteht, denn ohne dich wäre mein Leben nur halb so toll.

About the author

Maximilian Gemmer was born in Dachau, Germany on 16th of April, 1992 and raised in Berlin, Germany. He earned his Bachelor of Science in biochemistry from Greifswald University in 2014, where his studies focused on the functionalization of nucleobases under the guidance of Prof. Sabine Müller. In 2016, he continued his academic pursuits, attaining a Master of Science in biochemistry at Greifswald University. During this time, he focused on the structural and functional characterization of a bacterial master regulator, under supervision of PD. Sebastiaan Werten and Prof. Carola Schulzke. In 2017 he started his PhD in the Structural Biochemistry group at Utrecht University, under supervision of Prof. Friedrich Förster.